Ministry of Higher Education and Scientific Research
University of Babylon
College of Materials Engineering
Department of Metallurgical Engineering

Effect of Ta, In, Zr, and Y_2O_3 on Corrosion and Mechanical Properties of CuAlMn Shape Memory Alloy

A Thesis

Submitted to the Council of the Faculty of Materials Engineering/ University of Babylon in Partial Fulfillment of the Requirements for the Degree of Doctor of Philosophy in Materials Engineering /Metallurgical.

By

Duaa Amer Ali Nsaif

(M.Sc. Metallurgical Engineering, 2016)

Supervised by

Prof. Dr. Ali Hubi Haleem

Prof. Dr. Haydar H.J. Jamal Al Deen

2022 A.D **1444 A.H.**

وزارة التعليم العالي والبحث العلمي
جـــامـــــعة بـــــابـــل
كـــــلية هندســـــة المـــواد
قســـم هندســـة المعـــادن

تاثير التنتاليوم، الانديوم، الزركونيوم و أوكسيد اليتيريوم على التاكل والخواص الميكانيكيه لسبيكه CuAlMn ذاكره الشكل

اطروحة

مقدمة إلى قسم هندسة المعادن في كلية هندسة المواد/ جامعة بابل وهي جزء من متطلبات نيل درجة الدكتوراه فلسفة هندسة المواد/ معادن

من قبل
دعاء عامر علي نصيف

إشراف
أ.د. علي هوبي حليم
أ. د. حيدر حسن جابر

1444هـ **2022م**

بسم الله الرحمن الرحيم

" وَلَقَدْ آتَيْنَا دَاوُودَ وَسُلَيْمَانَ
عِلْماً وَقَالا الْحَمْدُ لله الَّذي
فَضَّلَنا عَلى كَثيرٍ مِنْ عِبادِهِ
الْمُؤْمِنينَ "

صَدَقَ اللهِ العَلِيِّ العَظِيمْ

النمل" 15 "

Supervisors Certificate

We certify that this thesis entitled " ***Effect of Ta, In, Zr, and Y_2O_3 on Corrosion and Mechanical Properties of Cu-Al-Mn Shape Memory Alloy*** " is prepared by **(Duaa Amer Ali)**

Under our supervision at the Department of Metallurgical Engineering/ College of Materials Engineering/ University of Babylon in partial fulfillment of the requirements for the Degree of Ph.D. in Material's Engineering/Metallurgical.

Signature:

Name of Supervisor:

Prof. Dr. Ali Hubi Haleem

Date: / / 2022

Signature:

Name of Supervisor:

Prof. Dr. Haydar H.J. Jamal Al Deen

Date: / / 2022

DEDICATION

To…

My Family

You deserve more than my life, Duaa!

A acknowledgment

Praise be to Allah, Lord of the Creation.

Graduate life would not have been the same without the people who have generously helped me. On this very page, I would like to express my deep gratitude to them.

My first and foremost thanks go to my supervisors them guidance

throughout the course of my postgraduate studies and them suggestions and comments on my research were invaluable. I have learnt and benefitted from his valuable knowledge.

thanks to the dean of materials engineering collage for his support.

I also would like to thank the staff of Metallurgical Engineering laboratories at the University of Babylon. The support and understanding of my family is deeply appreciated. Their love has

been for me a powerful source of inspiration and energy, support

and encouragement that have made all of this possible.

Abstract

The Copper-Aluminium-Manganese (Cu-Al-Mn) shape memory alloys (SMAs) have several industrial applications, such as seismic dampers in buildings and bridges. As a result of the nature of their work, these alloys suffer from corrosion due to the saline media, thereby leading to failures in machine parts.

In this context, the aim of the current study is to improved Cu - 8% Al - 9% Mn, produce by using powder metallurgy, which has the ability to resist corrosion and absorb vibrations. Accordingly, powders that have the ability to improve corrosion resistance were added to the alloy, such as Indium (In), Tantalum (Ta) and Yttrium Oxide (Y_2O_3) ceramic particles in proportions of 1%, 2% and 3% respectively, and Zirconium (Zr) in proportions of 0.6%, 1% and 2%.

Linear Polarization Test, Erosion-Corrosion, X-ray Diffraction (XRD), Differential Scanning Calorimetric (DSC) and Microstructural analysis were used to study the effects of these quaternary additions on the microstructures. The effect of aging heat treatment at 300^0C on previous tests was also considered. The damping behavior of the alloys was studied using a vibration instrument (Accelerometers National Instrument).

The purity and particle size were measured for all powders. Subsequently, the compacted samples Cu–8%Al–9%Mn-X (Ta, Zr, and Y_2O_3) were heat-treated, through two stages of sintering in a vacuum atmosphere with 10^{-4} torr at 550°C for 2 hr., and then at 950°C for 4 hr., respectively.

For Cu–8%Al–9%Mn-X In was heat-treated through three stages of sintering in a vacuum atmosphere with 10^{-4} torr at 109.5 °C for 1 hr., followed by heating to 550°C and stay for 2 hr., and the third stage heating to 950°C for 4 hr., respectively.

The lowest porosity achieved after sintering was 8.98% and 8.96% for 2 wt.% Ta and 1 wt.% In respectively, whereas the highest density of 8.26 g/cm^3 was achieved, upon the addition of 3% Y_2O_3 ceramic particles. From SEM and XRD observations it can be observed that the kinds of martensitic phases were β_1` from the DO_3 parent phase. Furthermore, the addition of 3%Ta, 2%In, and 3 %Y_2O_3 can enhance the SME of ternary alloy, by about 103% with 3% Ta, by 80% with addition of 2% In, and by 35% with addition of 3% Y_2O_3. The highest improvements in shape memory effect were achieved by the addition of 2% Zr wt. with 119%. The addition of Tantalum decreases the transformation temperature, Austenite finish (A_f). The best addition for Vickers hardness after sintering and after aging heat treatment belongs to 3% Y_2O_3.

The corrosion rate was found to be 3.12*10^{-3} mm/y, upon adding 2% Ta, as compared with base alloy with corrosion rate 3.58 mm/y after sintering, while after aging, the corrosion rate was 2.6 mm/y for base alloy, and the lower corrosion rate corresponded to 2% Zr with 8.303*10^$^{-4}$ mm/y. The maximum improvement in erosion resistance after sintering belong to Cu-8Al-9Mn-1%Y_2O_3 with erosion rate (0.023 g. cm^{-2}.hr^{-1}) and improvement % (192) but after Aging heat treatment the minimum erosion rate belong to Cu-8Al-9Mn-3% Y_2O_3 with erosion rate (0.0074g. cm-2.hr-1) and improvement reach (1548) %.

The damping capacity logarithmic decrement (δ) of the alloys increases with the addition of alloying element. The maximum damping ratio corresponded to 0.6% Zr, with logarithmic decrement δ equal to 0.162, as compared to the base alloy with δ equal to 0.066.

الخلاصه

ان لسبيكه نحاس - المنيوم – منغنيز الذاكره الشكل تطبيقات صناعيه متعدده منها استخدامها كماصات للاهتزازات في الطرق والجسور وغيرها و كنتيجه لطبيعه عملها فانها تعاني من تاكل شديد في الاوساط الملحيه تودي الى حصول فشل في هذه الاجزاء.

الهدف من الدراسه الحاليه هو انتاج سبيكه (نحاس –% 8 المنيوم –% 9 منغنيز) الذاكره الشكل باضافه مواد لها القابليه على مقاومه التاكل وامتصاص الاهتزازات بطريقه تكنلوجيا المساحيق. لذلك تم اضافه عناصر لها القابليه على تحسين مقاومه التاكل مثل (الانديوم ، التنتاليوم) واوكسيد اليتيريوم(حبيبات سيراميكيه) بنسب 1، 2 و 3 % و الزركونيوم بنسب 0.6، 1و 2% . في هذه الدراسة تم إنتاج سبائك ذاكرة الشكل(نحاس – المنيوم – منغنيز) Cu – Al – Mn (نحاس- المنيوم -منغنيز-X) حيث تمثل X (التنتاليوم , الزركونيوم , الانديوم و اوكسيد اليتيريوم) باستخدام ميتالورجيا المساحيق لتعزيز أداء سبائك ذاكرة الشكل ذات اساس من النحاس (نحاس المنيوم منغنيز) ومن ثم تم دراسه تأثير عناصر السبائك على درجات حرارة التحول المارتنسايتي، والتغيرات في البنيه المجهريه Microstructuresوالقدرة على امتصاص الاهتزازت Damping capacityوالتآكل وتآكل التعريه Erosion corrosion والصلادهhardness وخاصيه الذاكره الشكل shape effects تمت دراسة درجات حرارة التحول المارتنسايتي بواسطة جهاز المسعر الحراري DSC. تمت دراسة سلوك التخميد للسبائك باستخدام جهازقياس الاهتزاز Accelerometers national instrument.

حيث تم قياس الحجم الحبيبي و النقاوه للمساحيق الأولية (نحاس، المنيوم ، منغنيز، التنتاليوم ، الزركونيوم ، الانديوم و اوكسيد اليتيريوم) باستخدام جهاز قياس الحجم الحبيبي ومقياس الاشعه المفلوره (XRF) على التوالي .

خطوات تحضير العينات تشمل الخلط حيث تم خلط المساحيق باستخدام مطحنة الكرة الكوكبية ومن ثم ضغطها بضغط 750 ميجا باسكال (الذي يمثل الضغط الامثل) للحصول على المكبوسه الخضراء و بعد ذلك تمت معالجة العينات المضغوطة حرارياً بمرحلتين من التلبيد بالنسبة للعينة الاساسية و العينة الاساسية مع اضافة (تنتالوم ، الزركونيوم و اوكسيد اليتيريوم) في جو مفرغ من الهواء باستخدام غاز الاركون الخامل بضغط (10^{-4} تور) عند(550 درجة مئوية) لمدة (ساعتان) و(950 درجة مئوية) لمدة (4 ساعات) على التوالي . اما بالنسبه لاضافة الانديوم فتمت عمليه التلبيد كالتالي التسخين من درجه حراره الغرفه الى (109.6 درجه

مئويه) لمده ساعه ثم التسخين لل (550 درجه مئويه) لمده ساعتان ثم الصعود الى(950 درجة مئوية) لمدة (4 ساعات) على التوالي . و بعد اتمام عمليه التلبيد بنجاح تم اجراء المعامله المحلوليه لجميع العينات الملبدة عن طريق تسخين العينة حتى(900) درجة مئوية لمدة (30 دقيقة) متبوعة بخطوة التبريد أولاً في الماء الساخن (≈100 درجة مئوية) ثم في الماء المثلج عند (3-4) درجة مئوية. بعد ذلك تم إجراء المعالجة الحرارية (التخمير) للعينات في (300) درجة مئوية لمدة (ساعة واحدة) متبوعة بالتبريد السريع في الماء المثلج.

تم عرض النتائج وتبين أن أفضل ضغط كان الضغط (750 ميجا باسكال) الذي يعطي اعلى كثافة خضراء وأدنى مساميه خضراء و أظهرت نتائج XRD للعينات الملبدة أن المساحيق المعدنية (نحاس ، الالمنيوم و المنغنيز) تتحول إلى اطوار ولا يوجد معدن نقي . أدنى نسبه مسامية بعد التلبيد بلغت % 8.98 و% 8.96 عند اضافه 2% تنتاليوم و% 1 انديوم على توالي. بينما تم تحقيق أعلى كثافة ($8.26\ g/cm^3$)عند إضافة 3% Y_2O_3 من خلال فحص SEM و XRD لسبيكه (Cu-8٪ Al-9٪ Mn) يمكن ملاحظه ان نوع الماتنسايت المتكون هو (مارتينسيت β1) من DO_3 الطور الأم و يمكن الاستنتاج أن إضافة التنتالوم والإنديوم والزركونيوم وأكسيد الإيتريوم لا تؤثر بشكل كبير على ألاطوار المتكونه في فحص الاشعه السينيه XRD.

اما بالنسبة لتأثير المعالجة الحرارية (التخمير) من خلال النتائج تبين انه اقل معدل تأكل يصل الى ($3.12 * 10^{-3}$ mm/y) عند إضافة% 2 تنتاليوم مقارنة بالسبيكة الأساسية مع معدل تآكل (3.58 mm/y) بعد التلبيد بينما بعد التخمير معدل التآكل(2.6 mm/y) للسبيكه الأساسية واقل معدل تآكل عند اضافه% 2 زركونيوم يصل الى($8.303 * 10^{-4}$ mm/y). افضل مقاومه لتاكل التعريه بعد التلبيد تعود لسبيكه Cu-8Al-9Mn-1%Y_2O_3 بمعدل مقاومه تعريه يصل الى ($0.013\ g.\ cm^{-2}.hr^{-1}$) اما بعد التخمير فان افضل مقاومه تعريه ظهرت في سبيكه Cu-8Al-9Mn-3% Y_2O_3 بمعدل تاكل تعريه وصل الى .0.0017g). ($cm^{-2}.hr^{-1}$ تزداد سعة التخميد اللوغاريتمي (δ) للسبائك مع إضافة العناصر (التنتاليوم , الزركونيوم , الانديوم) و اوكسيد اليتيريوم واقصى نسبة تخميد عند اضافة % 0.6 من الزركونيوم مع سعة تخميد تصل الى 0.162 مقارنة بالسبيكة الأساسية ذات سعة تخميد تصل الى 0.066.

Table of contents

List of Figures

List of Table

List of symbols and abbreviations

Symbols	Meaning	units
ASTM	American Society For Testing And Materials	
A_f	Austenite finishing temperature	°C
A_s	Austenite starting temperature	°C
A	Austenite phase	
B	Bain strain	
BCC	Body center cubic	
C.R	Corrosion Rate	mm/y mpy
DSC	Differential Scanning Calorimeter	
d	Diameter	mm
E_{corr}	Corrosion potential	mV
E	Modulus of elasticity	Gpa
I_{corr}	Corrosion Current Density	$\mu A/cm^2$
LOM	Light Optical Microscope	
L	Length	mm
M	Martensite phase	
M_s	Martensite starting temperature	°C
M_f	Martensite finish temperature	°C
mV	Millivolt	mV
O.C.P	Open-Circuit Potential	mV
OWSME	One-way shape memory effect	
PM	Powder metallurgy	
p	Load	N
SMA	Shape memory alloy	
SME	Shape memory effect	%
SE	Super elastic	
s	strain	
TWSME	Two-ways shape memory effect	
TMT	Thermoelastic Martensitic Transformation	

t	Time	min or hr.
wt.	Weight Percentage	%
XRF	X-ray Fluorescent	
XRD	X-ray Diffraction	

List of Latin and Greek symbol

Symbols	**Meaning**	**units**
P	Porosity	%
ɵ	Brage angle	Degree
β	high temperature disordered phase, body-centered cubic structure	
ρ	Density	g/cm^3 or Kg/m^3
2H	Orthorhombic martensite structure	
6R	monoclnic martensite structure	
18R	monoclinic martensite structure	
α	primary solid solution of Cu, face-centered cubic structure	

Chapter 1

Introduction

1.1 General View

The technical importance of most engineering materials is based on their mechanical, electrical, or magnetic properties, which should normally be as independent as possible from environmental influences. Besides these conventional materials there is another group of materials that are not interesting so much for their properties under certain conditions, but much more for how they react to changes in these conditions. This group of materials is known as functional materials. Characteristic for shape-memory materials is an unconventional, unique correlation of strain, stress and temperature, which is based on crystallographic reversible thermoelastic martensitic transformation [1].

The basis for the shape memory and superelastic properties of SMAs is a martensitic phase transformation in the microstructure. Martensitic transformations are diffusionless solid-to-solid phase transformations. The parent phase, called austenite, is stable at higher temperatures and small strains, and the product martensite, is stable at lower temperatures and high strains. The two phases have different crystal structures. The austenite crystal structure has higher symmetry, whereas the martensite structure has lower symmetry. The following phenomena can distinguish in to [2,3]:

- One-way shape memory effect (OWSME).
- Two way shape memory effect (TWSME).
- Pseudoelasticity (PE) or superelasticity (SE).

1.2. Shape Memory Alloy System

Shape memory alloys (SMAs) or “smart alloys” are a unique class of materials that can change their form (shape or size), and can return back to their original

form with applied heat, stress, or magnetic field. Shape memory materials range from metals (alloys), polymers, ceramics, composites and even hybrid systems. Shape memory alloys can be categorized into [4, 5]:

- Bulk Shape Memory Alloys.
- **S**hape Memory Material Thin Film (SMMTF).

1.3. Copper Based Shape Memory Alloys

Copper-based SMAs are commercially attractive mainly for their low cost as compared with the Ni–Ti based alloys. The alloy systems with potential for SM behavior can be grouped into three categories, the Cu–Zn, Cu–Al, and Cu–Sn[6,7].

However, the base alloys suffer from bad cold workability and martensite stabilization; hence ternary quaternary additions in various amounts have been tried by different investigators to improve upon the properties and remove the drawbacks. (i) Cu–Al–Ni: Improved mechanical properties (ii) Cu–Al–Mn: For high ductility (iii) Cu–Zn–Al: Good or high transformation temperatures (iv) Cu–Sn: Increased transformation temperatures [8,9].

Cu-Al-Mn material systems are a class of Cu-based SMAs, highly explored because of their good mechanical behaviour (strength, ductility or cold workability). Several works have been published on the potential for utilization of Cu-Al-Mn SMAs in aerospace, industrial safety, medical, electrical devices and civil engineering applications. Extensive research into Cu-Al-Mn SMA systems have revealed that the alloys exhibit one -way and two-way SME, Superelasticity, low thermal expansion, and high damping characteristics [10].

There are several reasons behind adding the alloying elements to Cu-based shape memory alloys, including to (1) refine the grain size, (2) accommodate the transformation temperature, (3) improve the workability of these alloys, since they are difficult to process, due to a large grain size having formed during the solidification process, and (4) to enhance the service life of copper shape memory alloys in applications [11-16].

1.4. Shape Memory Applications

Shape memory alloy have found their unique roles in all fields of industrial operations in the last few years. In comparison to rival technologies, the most important characteristic of their shapes memory actuation technicality can be as follows [17,18]:

a. Shapes memory actuators, using the one or two way memory effect.

Shape memory alloys (SMA) are currently used in a variety of industries, including valves for cooling circuit, fire detections, clamp systems, and many others as show in Figure 1.1. The following are the main reasons for using SMA as an actuation mechanism:

- creation of clean, silent, spark-free and zero-gravity working conditions.
- High Power/weight (or power/volume's ratios).

b. Shape memory alloys embedded in smart materials.

Smart materials or adaptive composites like proposed by Rogers, perform generally three important functions: controller, sensor and actuator. Those functions can be obtained by combining different types of functional materials in one structure. Shape memory alloys can contribute very effectively in the

development of those smart materials. Three kinds of applications based specifically on shape memory alloys are now being developed [19]:

- Active Strain Energy Tuning (ASET)
- Active Modal Modification (AMM)
- Active Shape Control (ASC)

c. Biomedical applications

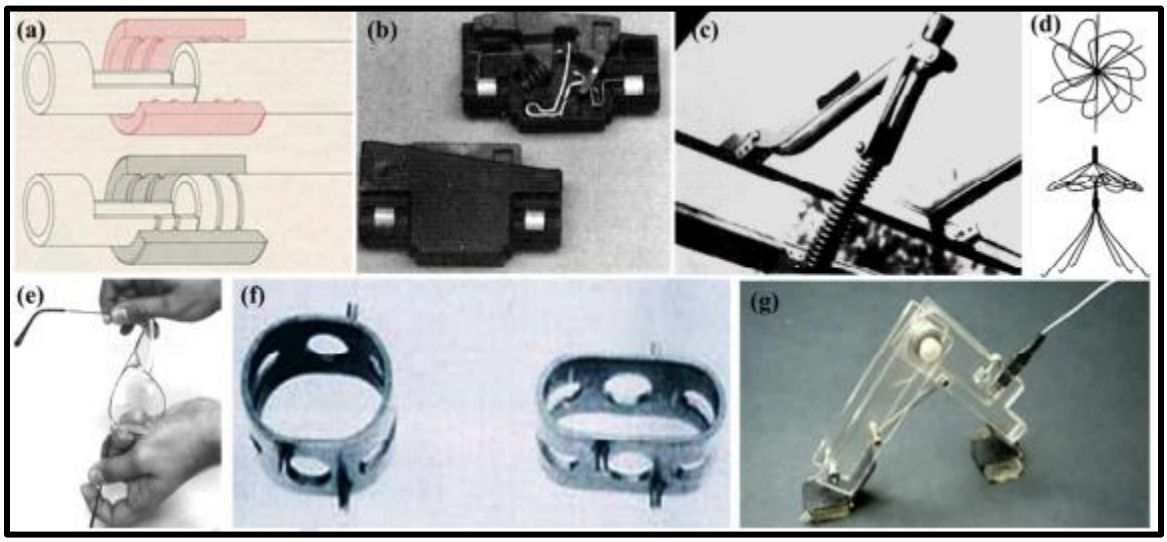

Figure (1.1): Applications of shape memory alloys: (a) Hydraulic tube-couplings (b) Electric circuit breaker, (c) thermal actuator, (d) Simon filter, (e) eye glass frame, (f) spacer and (g) robotic arm [19].

1.5 Implementation of Cu –Al –Mn Based SMAs

CuAlMn alloys have been used in medical and electrical devices, micromachines, and energy-storage technical implementations because of their high thermal and electrical conductivities [24]. The following implementation was the main implementation of CuAlMn alloys:

- Medical-grade guidewire [24].
- Concrete beam reinforcement element [22].
- Absorbent dampening material [20, 21].
- Automotive parts and actuators [19].

Figure (1-2) Application of CuAlMn SMAs [23].

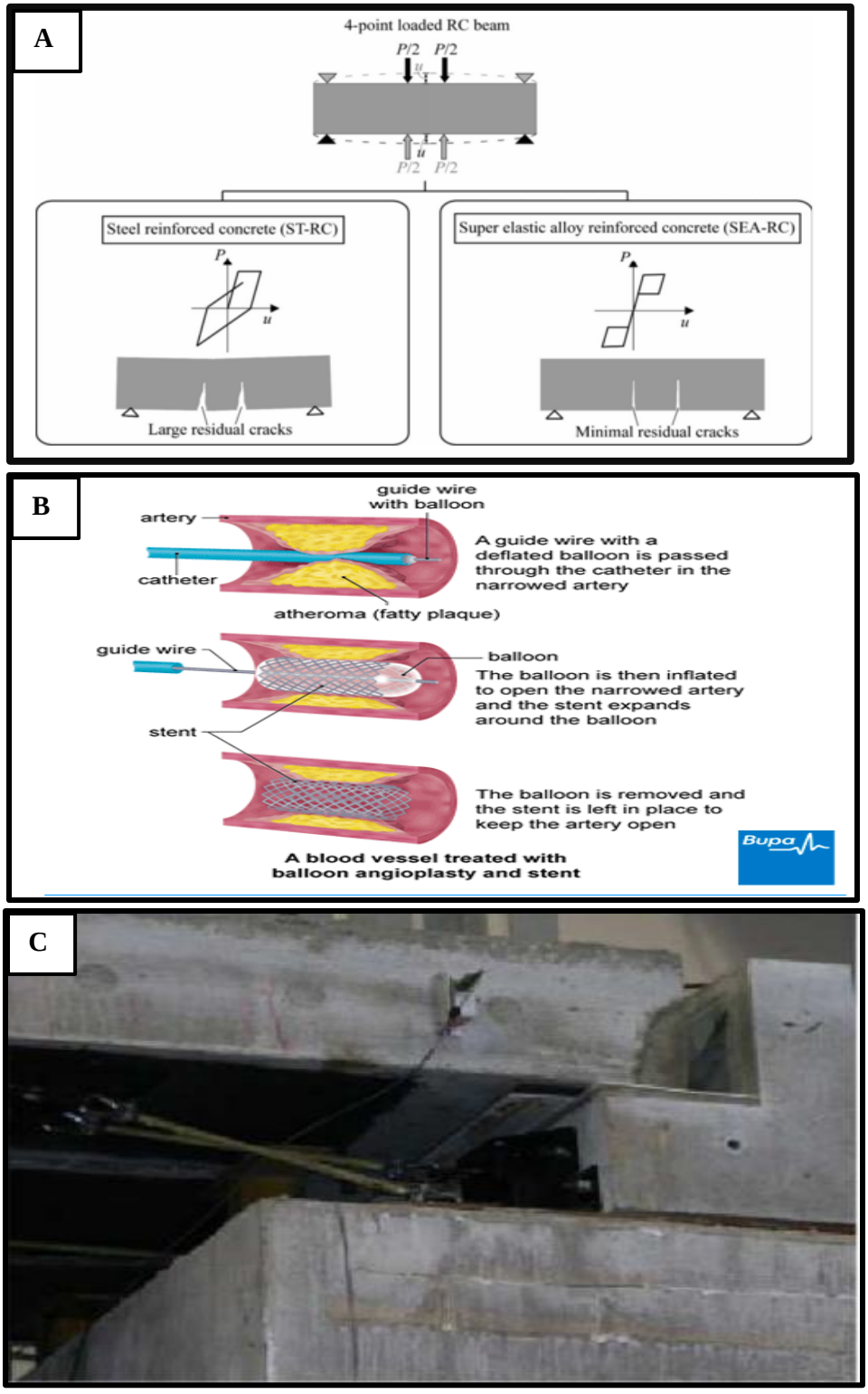

Figures (1.2): Application of CuAlMn system of (A) Concrete beam reinforcement element (B)Medical-grade guidewire,(C) Absorbent dampening material

1.6 Aim of the work

The current study aims to improved alloy (Copper - 8% Aluminum - 9% Manganese) shape memory produce by powder technology that can resist corrosion and absorb vibrations (used as a seismic damper in buildings and bridges). This aim can achieve by using the following procedures:

1. Addition Tantalum, Indium, Zirconium, and Yttrium oxide with three different ratios.
2. Inspect the influence of alloying elements addition (Tantalum, Indium, Zirconium) and Yttrium oxide ceramic particle in different amounts on the Mechanical properties, damping capacity, and corrosion resistance of Cu-Al-Mn shape memory alloys.

1.7 Layout of Thesis

The material contained in this thesis is presented as five chapters. They are the following:

Chapter 1 Introduction

Presents the introduction to the topic, states the aims and objectives and outlines the method of this research project.

Chapter 2 Theoretical background and Literature Review

Highlights the theoretical background where the concept and the details related to this subject have been explained and Highlights a review of previous literature published on the behaviour of CuAlMn shape memory alloys and the effect of alloy additives on behaviour

Chapter 3 Experimental procedure

This chapter describe the detailed of experimental procedure, the procedure of manufacture the sample by powder metallurgy and heat treatment and the methods of investigation.

Chapter 4 Results and Discussions

The results of effects of Tantalum, Zirconium, yttrium oxide and Indium on mechanical and physical and corrosion behaviour of Cu-based alloy shape memory alloy.

Chapter 5 Conclusions and Recommendations

Highlights the major results and the main contributions of this research and makes some recommendations for further research.

Chapter 2

Theoretical part and literature review

2.1 Introduction

The shape memory effects was discovered first in 1932 by a Swedish physicist, Arne Olander, namely, the pseudoplastic behavior of the Au-Cd alloys. The alloys was plastically distorted once it was cooled and returned to its original shapes once it was heated. Later in1938, Greninger and Mooradian spotted the same effect also in Cu-Zn and Cu-Al. The basic phenomenon of the memory effects governed by the thermoelastice performances of the martensite phase was reported a decade later by Kurdjumov and Khandros and later, Chang and Read detected memory effect in AuCd alloys. In 1961, Muldaver and Feder used an AgCd alloys in a thermally actuated, electrical and took the first patent for a shapes memory alloy.

in 1962 William J. Buehler and his co–workers at the Naval Ordnance Laboratory discovered shapes memory effects in an alloy of Nickels and Titanium, which can be considered the major breakthrough in the field of shapes memory materials. This metal later became known as Nitinol, an acronym for Nickel-Titanium Naval Ordnances Laboratory [25,26].

2.2 The Shape Memory Alloys Definition

Shape memory alloy (SMAs) are a type of alloy that display many unique properties, including shapes memory and super elastic effects. In its low temperature phase, SMAs exhibit the shapes memory effect (SME) [27].

Generally, these material can be plastically deformed at some relatively low temperature and upon exposure to some higher temperature will go back to their shapes prior to the deformation. A material that shows shapes memory only upon heating is referred to as having a one-way shapes memory. Some materials

also undergo a shape change upon cooling. This is called two-way shapes memory [28, 29].

However, when that material is heated to above its transitions temperature, it undergoes a change in crystalline structures, which causes it to go back to its un deformed shapes. SMAs in the super-elastic state are capable of recovering their previous shapes after the removal of even relatively high applied strains. In this effect, the deformation from an applied load is not plastic and shapes recovery is achieved isothermally on unloading [25, 30].

2.2.1 Crystallographic Aspects of SMAs

The crystalline structure of a material dictates the material overall behavior. For this reason, it is important to have a basic understanding of the crystallographic and microscopic aspects of shapes memory alloys (SMAs). This is true even for those looking to use them in large scale applications. The SME is typically made possible by a SMA's ability to exist in two distinct crystallographic structures: the high-temperature phase, called austenite (named after the English metallurgist Williams Chandler Austen) and the lower-temperatures phases, called martensite (named after the Germane metallographer Adolf Martens).

Particularly, it is the transition from the less-symmetric martensite to the more-symmetric austenite that allows the material to return to its original shapes. The less-symmetric twinned microstructure of the martensite phase allows the SMA to form with several rhombus variants, thus accommodating different macroscopic geometries generated by applied stresses. However, there are no variants in the austenite phase and, therefore, when returned to austenite the material must return to its original microstructure, eliminating the geometry accommodated by the rhombus variants of the martensite [30].

In general, the martensite is a relatively soft and easily deformed phases, stable at lower temperatures and under higher stresses, while the austenite is the stronger phase, stable at high temperatures and low stresses. The unique abilities of SMAs to recover their forms is in part due to the ordered crystalline structure between the austenitic and martensitic phases and involves rearranging of atoms within the crystal lattice. The martensitic transition is associated with an inelastic distortion of the crystal lattice with no diffusive process involved. The phase transition results from a cooperative and collective motions of atoms on distances lesser than the lattice parameters [31].

The martensitic transition can occur at low temperatures with very limited atomic mobility. This fact leads to the lack of diffusion within the transitional time scale of the martensitic transition. Without diffusion, they almost immediately make martensitic transition (a first-order transition). When a memory alloy forms a martensitic phase change, it changes from its high symmetry phase to its low symmetry martensitic phase (usually cubic) (highly twinned monoclinic structure). This order allows a displacement of the material (without diffusion) through martensitic phases, either through stress or temperature changes (thermal induced martensite) rather than the diffusion of solid-state metal transitions. This means that not only thermal input but also mechanical input is supplied with energy required for the martensitic transition can. If only one crystal of the origin phase is cooled down below Mf, the martensite variations are generally generated with a total of 24 crystallographic habits. However, there is only one possible origin (austenite) orientation, with the single defined structure and forms reverting to all martensitic configuration on heating above AF [32,33].

Twinning is the mechanisms by which single martensite variants deform, and it is defined as a mirrors symmetry displacement of atoms across a specific atom plane, the twinning plane. Most metals deformed due to slip or dislocation, but shapes memory alloys react to stress by simply shifting the crystal structure's orientation through twin boundary movement. Deformations, on the other hand, would result in classic plastic deformations by slip, which is irreversible and thus has no memory. Figure (2.1) gives an overview of the martensitic phase transition in shapes-memory alloys effects [1,35].

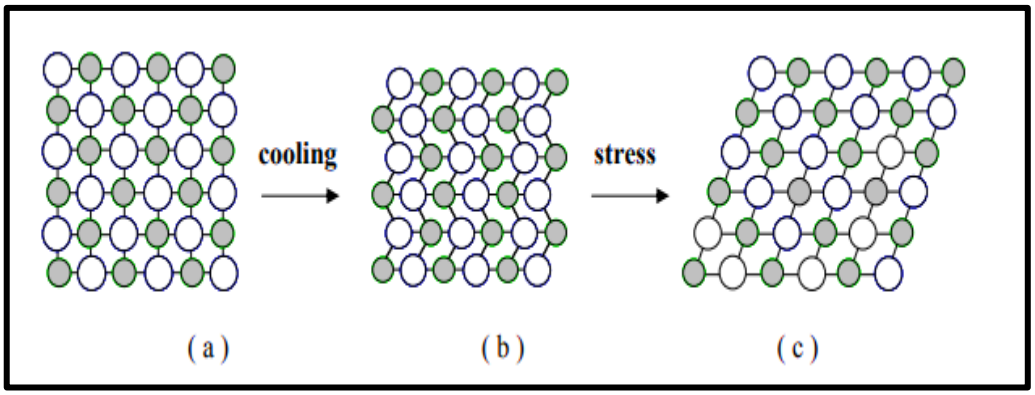

Figure (2.1): Schematic illustration of the mechanism of the shape-memory effect: (a) atomic configuration on {110}- type planes of parent austenite phase, (b) twinned martensite phase occurring thermally on cooling, (c) detwinned martensite occurring with deformation [35]

During the deformation from austenite phase to martensite phase at temperature below the martensitic finish temperature (Mf), the alloys start in the twinned martensite condition. When the alloys are cooled back down to below Mf the twinned martensite, structure are restored. It should be notedthat the transition between origin phase and self-accommodating martensite results in no macroscopic shapes different. Thus, a one-way shapes memory is achieved. Figure (2.1) can also explain the origin of the super elastic effect. In this case, the alloys is deformed at a temperature above Af and the martensite transition is entirely stress-induced. The symmetrical origin phase is changed into the

lower symmetry, deformed martensite phase directly. Upon unloading, the decreasing stresses and surrounding elasticity of the matrix results in the martensite plates shrinking back and the origin phase structurebeing restored [32,35].

The driving force for phase transition inshapes memory alloy is the chemical free energy between the phases. When the difference in chemicals free energies is enough to nucleate the other phase, transition will start and continue as the energy for growing is supplied by further rise in chemical energy differences. Ordinary metals are unable to reverse deformation caused by dislocation motion and atomic planes rolling over one another, resulting in a new crystal position and a permanent change in crystalline order. SMAs deform by detwinning, which adjusts the tilt orientation of twins and does not induce dislocation movement, unlike normal metals [32].

2.2.2 Martensitic Transformation

Shape memory comes from a particular kind of phase transition that produces the structure known as martensite. Martensite comes from the solid-state procedure of displacive transition. Solid-state transition are typically of two kinds: diffusional and displacive [36].

The new phase can be created by randomly moving atoms over long distances in a **diffusional transition**. Since the new phase that is formed has a different chemical compositions than the matrix from which it is formed, long-range diffusion is needed. The diffusional transition is dependent on both time and temperature since this type of transition necessitates atomic migration [36].

Displacive transition, otherwise, do not need great atomic migration; in this status the atom is rearranged into a new and more stable atomic structure. This

rearranging, is done without change the chemical nature of the matrix. These transitions are also referred to as a thermal transition. The martensite phase in SMA is not the typical martensite phase found in steel. The martensite phase here is a comparatively ductile and soft phase, but this term was used to refer to steels [36, 37]. The origin and martensite phases are shown in Figure (2-2).

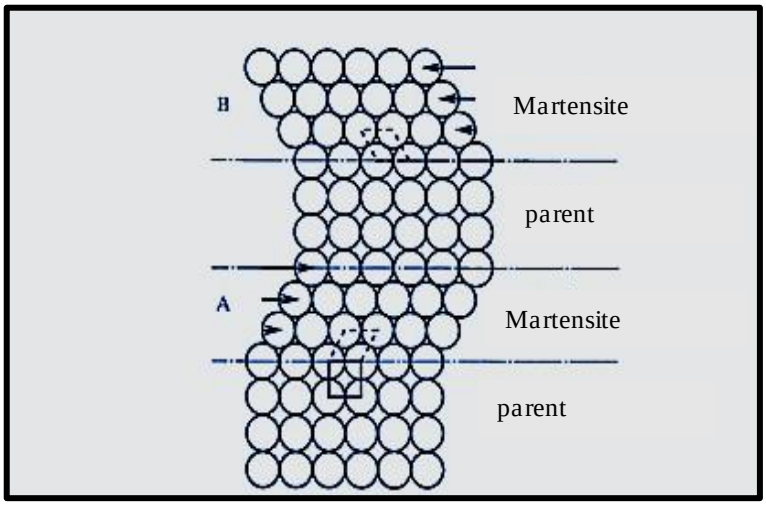

Figure (2-2): Parent and martensite phase [38]

The phase transition from Austenite to Martensite is occur in two parts: The Bain strain and the lattice invariant shear (LIS) or lattice accommodation. The Bain strain, referred to as lattice deformation, consists of all atomic movements that are required to form the new phase from the old (Figure 2-3a).

Martensitic transition is defined as a lattice deformation involving shearing deformation and resulting cooperative atomic movement. In order to minimize the strain through nucleation and growth two types of LIS technique could occur dislocation slip (Figure 2-3c) or twinning (Fig. 2-3d) [38].

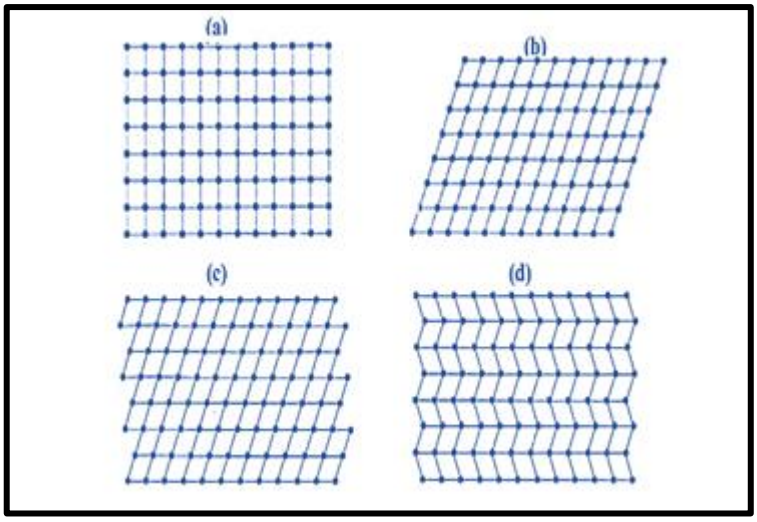

Figure (2-3): Transformation from austenite to martensite in two-dimensions; (a) being completely austenitic, (b) Bain strain, (c) LIS, accommodation by slip and (d) LIS, accommodation by twinning [38].

Martensite transition can be also categorized in two categories: non thermoelastic and thermoelastic [39]. What differentiate shapes memory alloys from conventional materials is their ability to form thermoelastic martensite. For thermoelastic martensite transition, the transition temperature hysterias are little, the interface between origin and martensite is animated and the transition is crystallo-graphically reversible due to a much minimal driving force [40].

2.3 Copper Based Shapes Memory Alloy

2.3.1 Metallurgical Properties of CuAlMn Alloys

The most popular Copper-based are Cu-Zn-Al, Cu-Al-Ni, and Cu-Al-Mn shape memory alloys.

The major benefit of these alloys over NiTi is that they are comparatively cheap and can be formed using traditional metallurgical methods. Actuators, safety valves, and pipe couplings may all benefit from copper-based SMAs. Copper-based SM has good rigidity and a high damping capability [41].

The transformation from a body centered cubic ordered origin phase to a mixture of monoclinic and orthorhombic martensitic phases is seen in many Cu-based SMAs. To enhance the characteristic features of synthesized alloys, different elements such as (Al, Zn, Cr, Ni, Sn, Pb, Nb, Be) can be applied to the elemental copper [42].

Aluminum bronze is a kind of bronze in which aluminum is applied to copper as the primary alloying element. It can be used in a wide range of engineering systems, with a number of alloys finding use in various industries. Many forms of Aluminum bronze, as per ISO 428, contain 4-10% Wt.% Aluminum, as well as many other alloying elements such as Iron, Nickel, Manganese, and Silicon in varying amounts [42].

Aluminum bronze has a chemo-mechanical combination that outperforms many other alloy sequences, making it the material of choice for essential applications. Aluminum enhances the mechanical characteristics of copper by maintaining a face center cubic (FCC), thus improving the casting and heating characteristics of the base metal. Other alloying components, such as magnesium, iron, and tantalum, strengthen mechanical properties and alter microstructure. Nickel and Manganese help to avoid rust, while iron helps to refine grain [43].

Figure (2.4) shows the recovery of forms by heating the pre-bound 17% specimen, in which recovery of forms is nearly perfect [44].

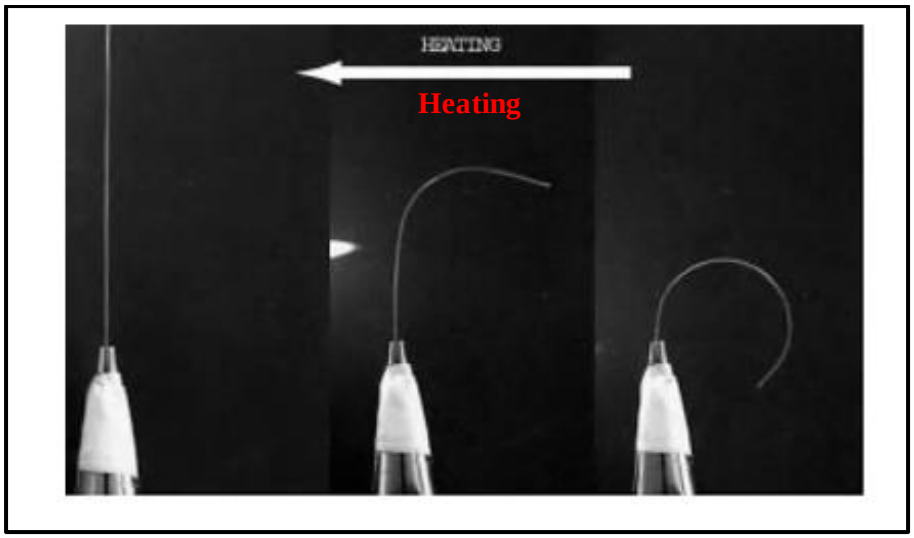

Figure (2.4): Shape memory effect of Cu-Al-Mn alloy, where the bent sheet regains the original straight shape by heating.

When the Al content is 14wt%, the Ms temperature of CuAl alloys is a little above room temperature. Alloys containing more than 14 wt.% Al are suspectable to the precipitation of a second phase γ_2 that does not undergo phase transition. Good electrical and thermal conductivity along makes Cu-based shapes memories alloys an attractive alternative to NiTi alloys [45].

Figure (2.5) shows the Cu-A1 binary phase diagram [phase β_2]in which both systems performed their shapes memory structures in the domain of β-phases, moreover, the third elemental addition to the binary and/or ternary is aimed to modify and control the transition temperatures in comprehensive range in meet the applications necessities, i.e., T ≈ 100–370°C. From above, it was proven that the transitions temperatures are highly sensitive to the composition of alloys[46]

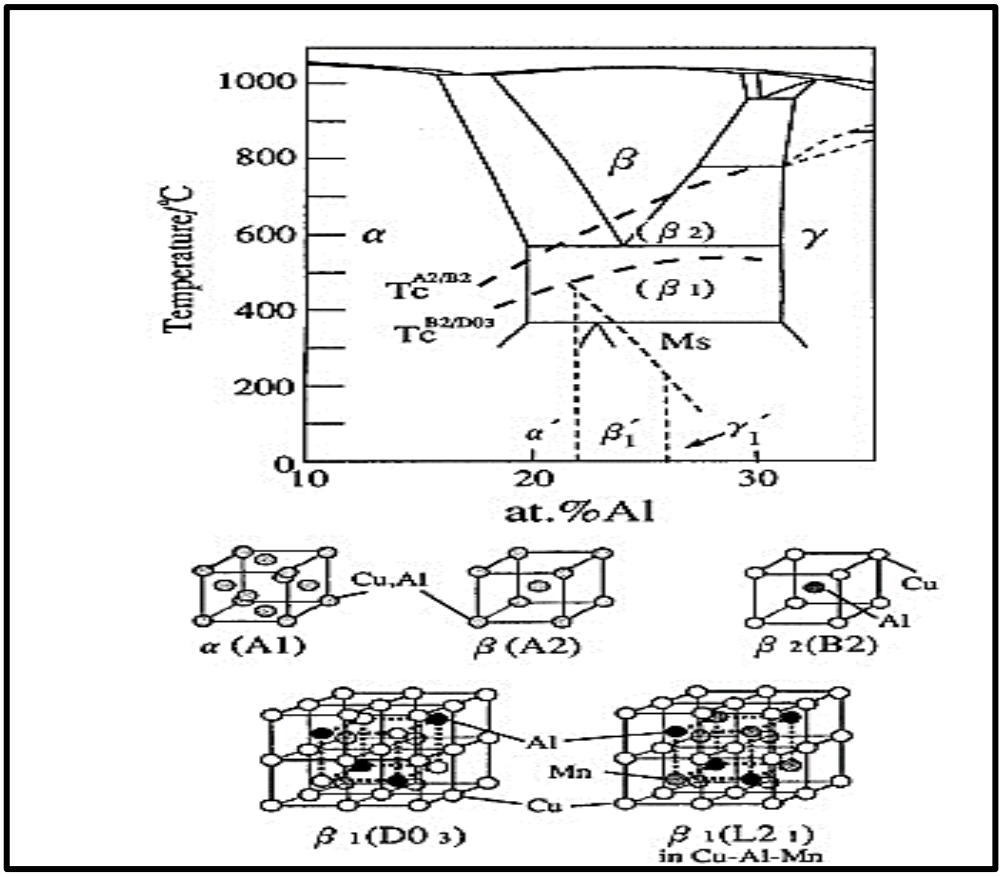

Figure (2.5): Phase diagram of Cu-Al system with $A_2 \leftrightarrow B_2$ and $B_2 \leftrightarrow Do_3$ order disorder transition temperatures and Ms temperature

Because of the composition of the alloys in Cu–A1-based alloys, the presence of different martensitic structures, like a) α` b) β`, and c) γ`, has increased the interest in working with these alloys. In the presence of Cu_3Al, two ordering mechanisms are possible in these alloys. The metastable β-phases undergoes a two-stage disorder ↔ order transition: $A_2 \leftrightarrow B_2$ and $B_2 \leftrightarrow L_{21}$ (DO_3) once rapidly cooled [47]. The α-phase and the β-phase have some crystal structure differences that are significant for the thermal activation of the driving force [48].

2.3.2 Characteristic of CuAlMn Based Shapes Memory Alloys and Their Application

Because of the crystallographic reversible thermoelastic martensitic transformation, shapes memory alloys (SMAs) exhibit peculiar properties as a thermal memory effect, super elasticity (SE). Cu based SMAs, such as Cu-Al-Ni, Cu-Zn-Al and Cu-Al-Mn, are commonly studied systems, because of their ease of fabrication and lower manufacturing costs. Cu-Al-Ni and Cu-Zn-Al, on the other hand, have some drawbacks in technical applications, which can be explained by their brittle existence, and cold workability due to the high degree oforder, and even high elastic anisotropy in the β-phase [49].

Cu-Al-Mn SMAs show extra ductility due to their origin phase with an L_{21} structure that show low degree of order with a low Al concentration of less than 18 wt.%. For the Cu–Al–Mn SMAs, the disordered-phase is stable at high temperatures, but during a quenching cycle, the disordered-phase transforms into the $\beta(A_2) \rightarrow \beta_2(B_2) \rightarrow \beta_1(L_{21})$ ordered phase. Moreover, Cu-Al-Mn alloys exhibit a shapes memory effect (SME) based on $\beta_1(L_{21})$ to monoclinic martensitic transition above16 at% Al [50]. Variant's kind of martensite ά (3 R), $\beta 1^{`}$ (18 R) and $\grave{\gamma}_1$ (2H) depended on the amount of Aluminum and Manganese present, form in the various composition ranges of the alloy. ά (3R) martensite is predominant at lower Aluminum contents, whereas at higher amounts of it, $\grave{\gamma}_1$(2H) martensite is formed. In the intermediate concentration range, both and $\beta_1^{`}$(18R) martensite co-exist [51,52].

The additions of manganese to binary CuA1 alloys stabilizes the BCC process by lowering the temperature range of stability of the phase and expanding the composition range over which it occurs. It increases the ductility of alloys by lowering the degree of order in the initial process [53,54].

These alloy transition temperatures are extremely sensitive to variations in Al and Mn concentrations. The transition temperatures of the alloys reduction as the Al and Mn contents rise. Because of the shapes memory effect, Cu–A1–Mn alloys have good strain recovery and super elasticity [24, 55].

Cu-Al-Mn shapes memory alloys (SMA) have good strength and very high damping and shapes memory effects as compared to common metals. Cu - Al - Mn shapes memory alloys are less expensive to manufacture than TiNi shapes memory alloys since vacuum casting is not needed [57]. CuAlMn properties are shown in Table (2-1) [24].

Table (2-1): Shape memory characteristics for CuAlMn, NiTi, CuZnAl and CuAlNi

Alloys	Transformation Temp.	SE%	OWSME	TWSME
CuAlMn	-200 to 150	7.5	10	3.2
NiTi	-40 to 100	8	8	5
CuZnAl	-200 to 120	2	5	2
CuAlNi	-200 to 170	2	5	2

In recent times, the need for materials with high damping capacity, in such fields as automotive, aerospace and structure, has spurred the research and development of high damping materials. Damping occurs in materials when there is a loss of energy in the process of converting one form of energy into another. Among the different means available to achieve damping, much importance has been attached to the use of shape memory alloys (SMAs) because of their unique microstructure, leading to good damping capacity. Shape memory alloys exhibit high damping capacity or internal friction due to thermoelastic martensitic transformation, which is related to the hysteretic movement of interfaces, i.e., martensitic variant interfaces and twin boundaries.

The high density of mobile twins in the martensitic phase and mobile interfaces between the parent phase and martensite leads to internal friction. considerable amount of energy is absorbed due to internal friction, which gives rise to high damping in shape memory alloys [58].

In recent years, the addition element method for grains refinement has gotten a lot of attention because it has the advantage of a slight quantity of addition, high refining efficiency, and a simple synthetic process. B, V, Cr, Mg, and Ti elements were found to effectively refine the grains of Cu-Al-Mn SMAs and enhance their various properties [59].

2.3.3 Phase diagram of (Cu-Al-Mn)

Traditional Cu-based shapes-memory alloys as Cu-Al-Be or Cu-Zn-Al are identical to this alloy framework (Cu-Al-Mn). Cu-Al-Mn is characterized by its magnetic properties, which are a significant feature. Cu-Al-Mn is para-magnetic at high temperatures and converts to a magnetic glassy phase at temperatures well below the martensitic transition, whereas most shapes-memory alloys are diamagnetic. The relative stability of the bcc and close-packed phases in Cu-Al-Mn could be influenced by such a distinct magnetic action [60]. Its pseudo elastic strain is significantly greater, and its energy dissipation behaviors are significantly stronger, over a significantly larger number of cycles than as compared to the Cu-Al-Be alloy [61].

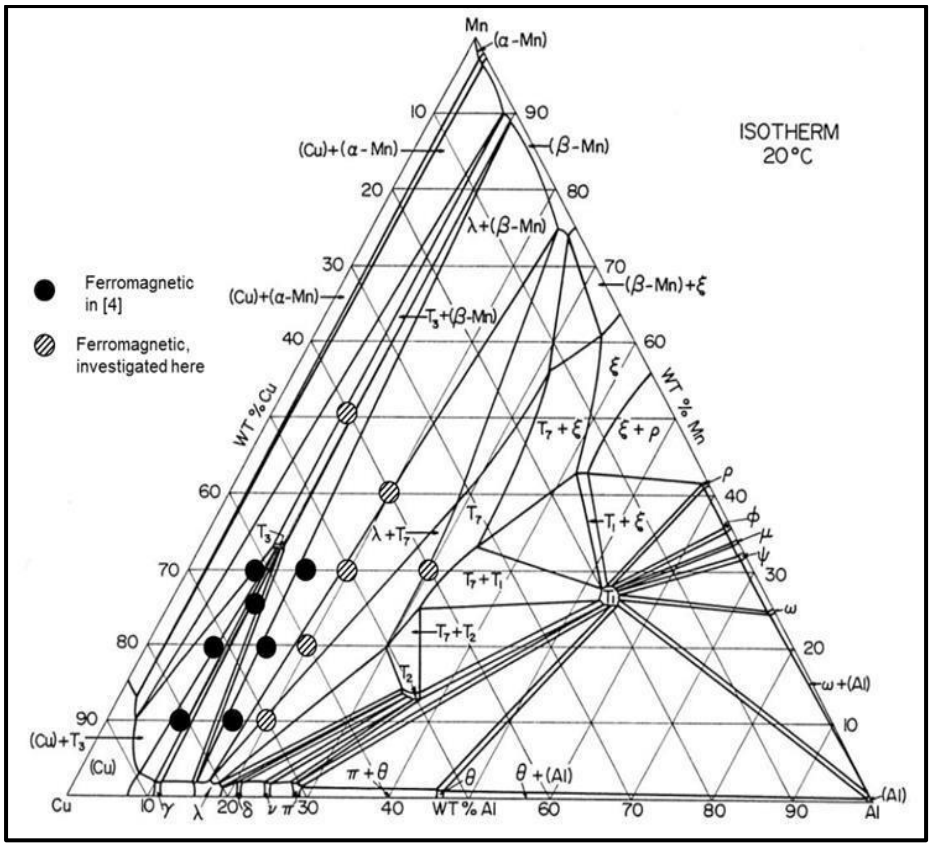

Figure (2.6): Ternary phase diagram of CuAlMn at 20°C [62]

The disoriented β-phased is a stable at high temperatures in these types of memory alloy and after quenching it turns into the martensitic phase. However, changing the alloying elements fraction can significantly alter phase stability; for example, raising the Aland Mn content in Cu-Al-Mn SMAs, the prevalent martensite phase, can significantly alter the phase's stability temperature range and transition temperatures. That is, in these alloying systems, careful chemical composition control is critical, and more attention is needed during the processing routes [63].

Figure (2.7a and b) shows an isothermal part diagram at 800 °C and a vertical part diagram of the Cu-Al-10 wt.-%Mn section respectively. It can be seen that the single phase β region is expanded by the supplement of Mn and that the

transition temperatures associated with two types of order–disorder transitions, A_2 to B_2 and B_2 to L_{21}, in the β phase region drastically decrease with decreasing Al content.

This vertical diagram in Figure (2.7b) suggests that the grade of order in the β origin phase may lower with reduce Al contents. Actually, in the high Al composition ranges >16 at. %Al, the ordering to the L_{21} structure cannot be suppressed by quenching from the disordered A_2 phase region, and the L_{21} phase transforms into a 6M structure with (6) layered modulation.

However, in the low Al composition range, 16 wt.%, the ordering from the A_2 to the L_{21} structure can be suppressed by fast cooling and the martensitic transition from the A_2 to the 2 M (disordered F.C.C) structure occurs at low temperature [56].

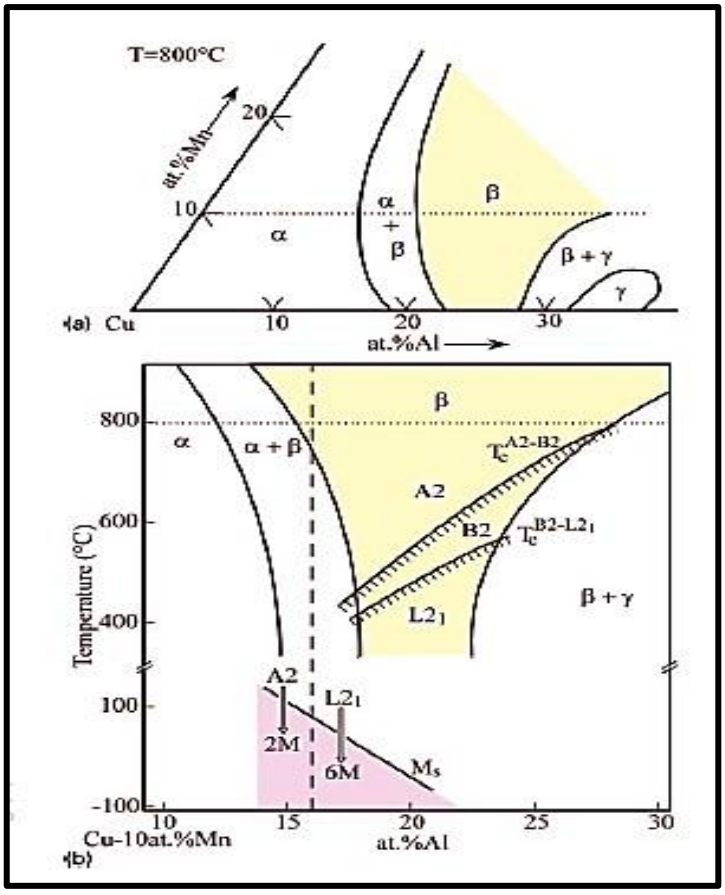

Figure (2.7a and b): isothermal section diagram at 800°C and (b) vertical section diagram in Cu– Al–10 at. -%Mn ternary system with A_2/B_2 and B_2/L_{21} order–disorder transformation and martensitic transformation starting Ms

2.3.4 Austenite Phase and Martensite Phase

Shape memory alloys have a solid-state phase transition in which both the starting phase (austenite, or original phase) and the martensite phase, which has a monoclinic lattice structure, occur at low temperatures. Under low to no stress, martensite is formed by a displacive thermal transition from the higher temperature austenite process. These two phases consist of a body-centered cubic structure for austenite, and a face-centered cubic structure for martensite.

The martensitic thermo-plastic transition is the transition between these two phases. The temperature, applied mechanical load, and thermo-mechanical

background of the material all influence the stable process at any given time [55].

Temperatures, streses and strain are correlated following the relation depicted in Figure(2.8), that also highlights the shapes memoryeffect of such alloy.

In (0) the materials are kept at lower temperatures in an undeformed and unstressed state presenting a randomly organized twinned martensite. The return to an un-stressed condition is associated with a high hysteresis and a residual strain (2) since the reorientation occurred in (1) is caused by an aporigin plastic deformation. In (3) the As is reached and martensitc starts moving into austenitc, while in (4) the process are completed.By continuing growing the temperature no other effects are gained (5).

If from this point a load is applied again, a different behavior is shown this time: the higher temperature maintained the alloys in austenitic phase so that the response is much stiffer and linear (6). An higher stress leads to the appearance of a plateau that is justified by a stress-induced microstructural change: austenite is transformed into detwinned martensite (7). But since martensite is not stable at large temperatures when the load is taken away, the reverse transition occurs (8) until the alloys is again fully in austenitic phase (9).

Point (10) concludes the transition cycle at large temperatures, thus describe the SE effect [65].

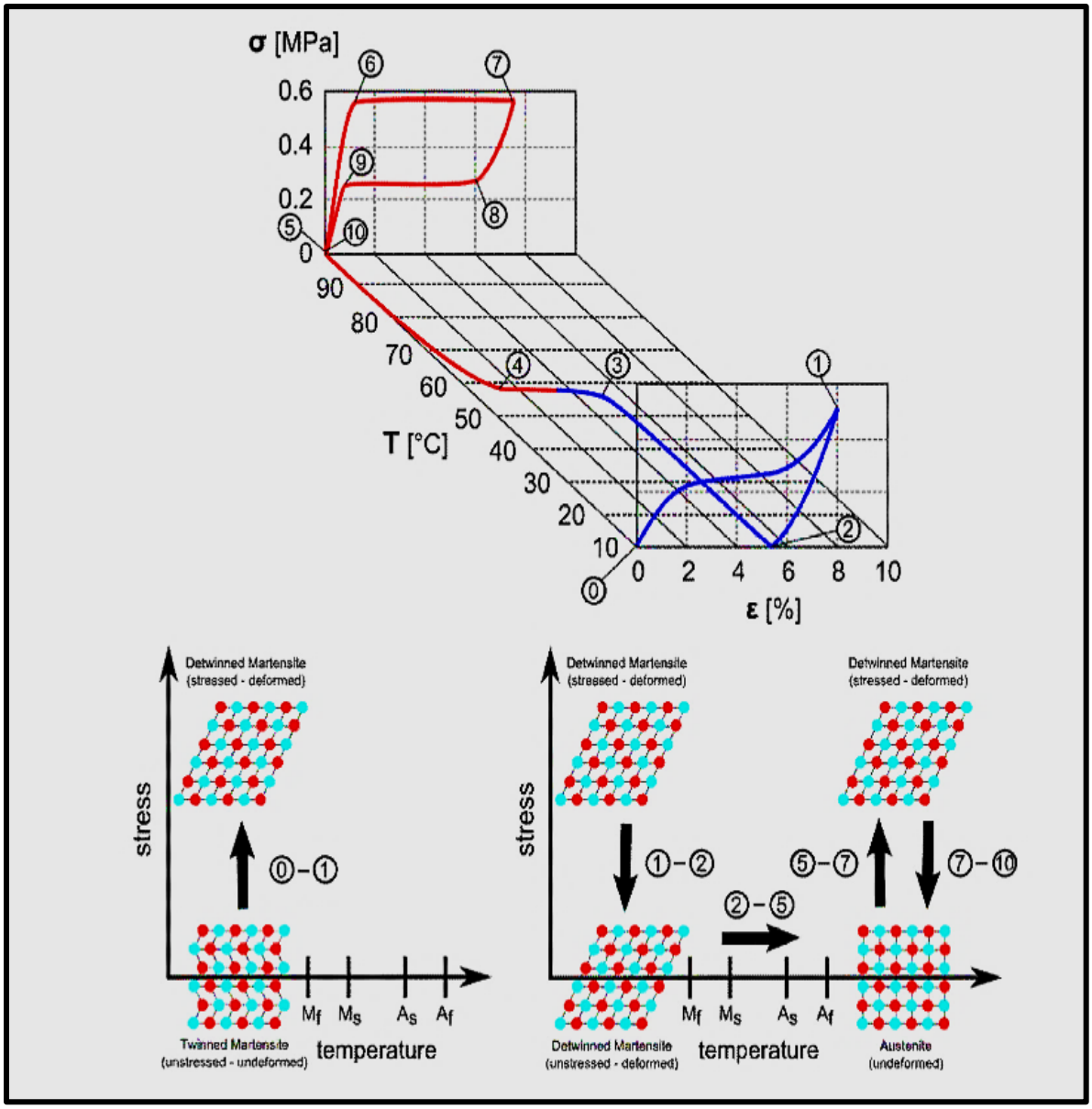

Figure (2.8): Thermo-mechanical behavior of a SMA showing the dependency among temperature, T, stress, σ, and strain, ε, and the related crystal structures.

2.4. The Shapes Memory Effects

The shapes memory effect (SME) is a property which covers two basic requirements: thermoelastic martensitic transition and twinning as a deformation mode. The deformation processes that are mainly responsible for shapes memory effect are deformation of martensite or stress-induced martensitic transition. As discussed earlier, the deformation of martensite

should occur by twinning to realize the shapes memory effect, because slip is an irreversible process. The martensitic transition occurs in self-accommodating manner to keep the same shapes upon cooling (upon transition) and to minimize the energy change. Further deformation proceeds with twin boundary motion which is the reorientation process of one martensite variant to another.

2.4.1. One-Way and Two-Way Shapes Memory Effect

In its martensite phase, a de-twin structures transform into the original phase structure after heat is supplied in an austinite phase, the One-way SME (OWSME), is described as an inverted transition process. In other words, OWSME materials can be remembered only when heat is applied to their deformation forms [69]. Figure (2-9) show the mechanism of the One-way SME (OWSME).

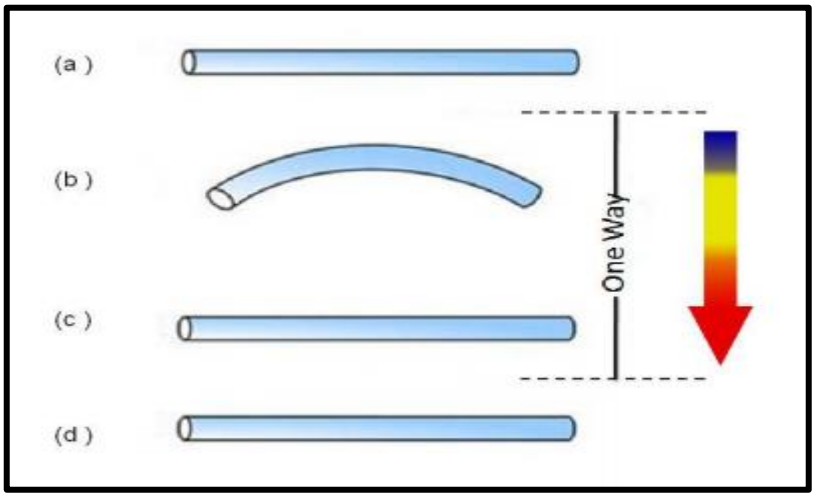

Figure (2.9): Macroscopically Mechanism of One Way Shape Memory Effect: (a) Martensite, (b) Loaded and Deformed in martensite phase T≤ Mf, (c) Heated above T G As (austenite),(d) Cooling to martensite T≤ Mf.[68]

However, in the two-way SME (TWSME) response, the material has the capability to remember both its origin phase (austenite) and deformed phase (martensite) shapes through a spontaneous form change mechanism. The primary variation between the OWSME and the TWSME is that the shapes

variation which occurs in the latest is created without external stresses. Figure (2-10) show the mechanism of the two-way SME (TWSME) [69,70].

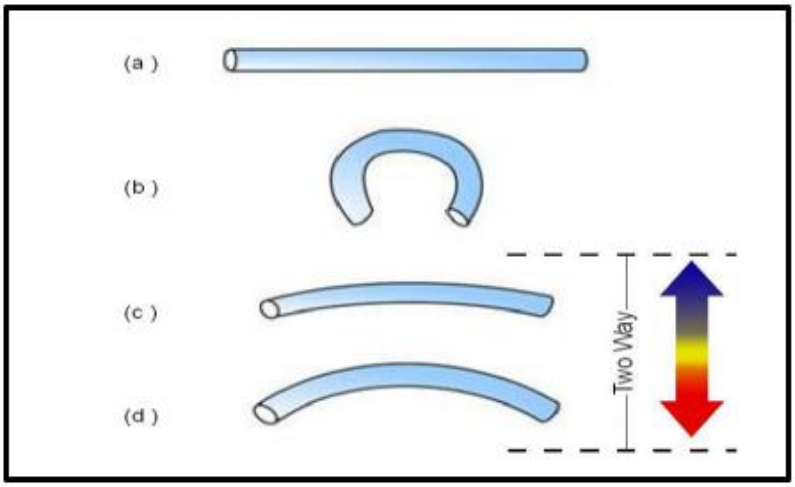

Figure (2.10): Macroscopically Mechanism of Two Way Shape Memory Effect: (a) Martensite state, (b) Several deformation with an irreversible amount, (c) Heated, (d) Cooled.[68]

2.4.2. Superelastic Effect

The superelastic effect is described as the recovery of large strain as a result of the stress-induced martensitic phase transformations under constant temperature. SMA is in its austenite phase at relatively high temperatures (temperatures above A_f). When a sufficiently high stress is applied to the material in the austenite phase, the SMA transforms into the detwinned martensite. When the load is released, a reverse transformation to the austenite state takes place, which results in complete shape recovery and a substantial hysteretic loop. A temperature diagram demonstrating the superelastic effect of SMAs is shown in Figure 2.11. Also, if the temperature is above a critical temperature termed Md(c-d), the material is stabilized in the austenite phase and the martensitic transformations cannot be induced by an applied load [71].

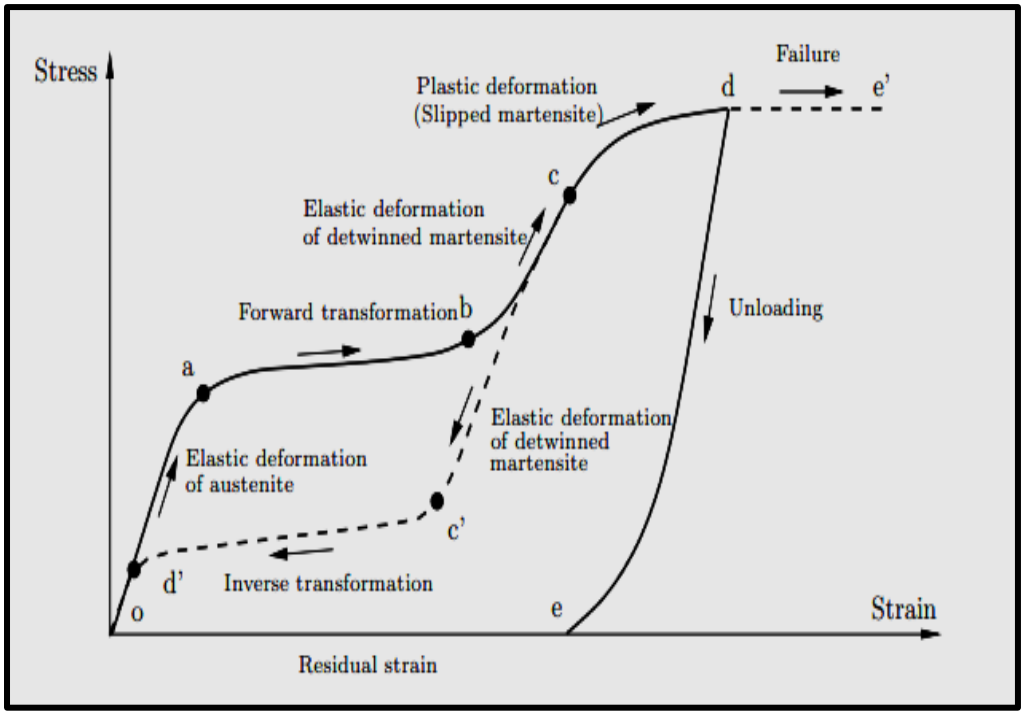

Figure 2.11: ***Superelastic Effect***

2.5 Copper Based Shapes Memory Alloys Fabricated by Powder Metallurgy

It is difficult to control the grains sizes of Cu base SMAs by conventional casting method and with the desired chemical compositions. Generally, the change in composition will change the temperature transition of coarse grains and will weaken alloys mechanical properties.

Mechanical alloying (MA) and powder metallurgy (P/M) with a hot isostatic press (HIP) has been documented as a method for fabricating Cu-based SMAs. It's easier to make near-net shapes alloys with P/M, and it gives you more control over the composition and grain sizes (coarse grains do not favor high mechanical properties) [73, 74].

Other fabrication methods such as casting, stamping, or machining are several times more expensive than the P/M process. P/M is the choice when strength,

wear strength or the high temperatures of the die casting alloys are higher than their capacity. P/M provides greater accuracy and eliminates most or all of the casting finishing operations required. It prevents casting defects like holes, inclusions of hands. However, the P/M process is economical only when production rates are higher, since the tooling cost is quite appreciable [75].

Powder metallurgy exhibits characteristics such as low costs, a large supply of raw materials, simpler processing equipment, low energy consumption, and fast processing [76].

2.5.1 The steps of powder metallurgy PM process

1. Mixing Proses
2. Powder Compaction
3. Sintering of Compacted Powder

2.5.2 **Liquid-Phase Sintering:** is a process for forming high performance, multiple-phase components from powders. It involves sintering under conditions where solid grains coexist with a wetting liquid. In systems involving mixed powders, liquid formation is possible because of the differing melting ranges of the components. Common systems involving liquid-phase formation during sintering include copper-cobalt, tungsten-copper, tungsten-nickel-iron, tungsten-silver, copper-tin, iron-copper, tungsten carbide/cobalt, and copper-phosphorus. Because of the faster sintering and superior properties, liquid phase sintering is applied to 70% of all P/M alloys. Heating of a mixed-phase system begins with a mixture of elemental powders. When the liquid forms, it flows and wets the solid particles and begins acting on the solid phase. Melt penetration between the solid particles can cause swelling of the compact,

especially if the green density is high, and the particles are coarse. The mechanism of sintering process is shown in the Figure (2.12) [84,85].

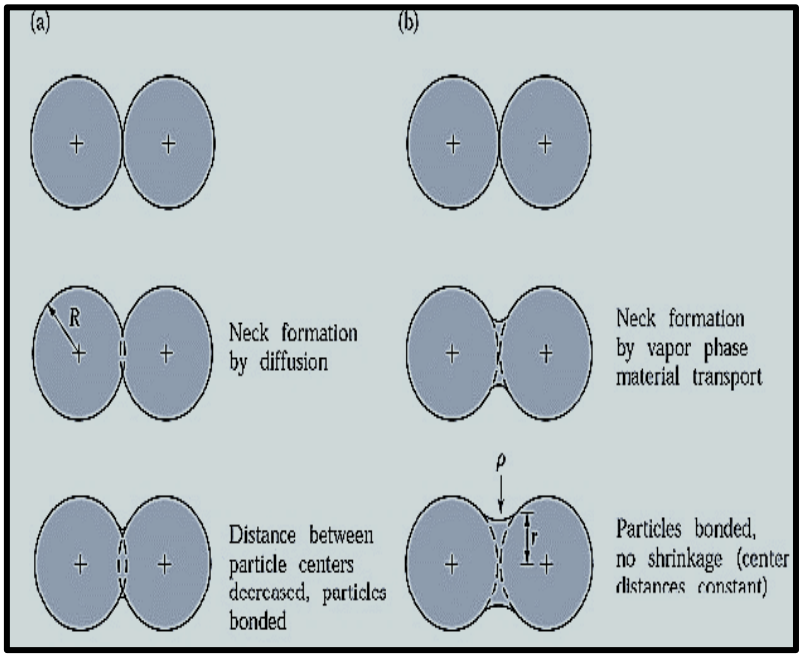

Figure (2.12) The mechanisms for sintering metal powders: a-solid-state material transport; b-liquid-phase material transport [83].

Sintering in solid state is classified into three stages [72,79]:

- Adhesion out shrinkage: During the sintering processing, when the powder compact is heated to a certain temperature, initial bonding hand neck growth occurs quickly.
- Densification and grain growth: This is where the majority of the shrinkage occurs, as further pore rounding occurs, forming a network of pores and allowing hand grain growth to continue. Volume diffusion of voids from the interior towards the surface results in closed pores with increasing pore size and less total pores.
- Elimination of the last isolated pores: This is where it happens. In the vicinity of the gain boundary, the periodization of isolated pores gradually increases, and pore shrinkage has been occulted more quickly.

2.6 Corrosion Behavior of Cu Base Alloy

Copper is different from most other metals in that it combines corrosion resistance with high electrical and heat conductivity, formability, machinability, and strength when alloyed, except for high temperatures[94].

In a saline sea water system, most metals and alloys behave abnormally. Corrosions is one of the most common issues in marine applications, and it has an effect on the material intrinsic properties. In general, corrosions inhibitor or copper alloys with other elements are used (Zn, Sn, Ni, Al, Mn, Ag and Ti etc.) and the combinations of both have been practiced to prevent corrosion of Cu. Aluminum is one of the attractive alloying elements used to inhibit corrosions of coppers-based alloys, which forms a protective layers on the surfaces of Copper [86].

In a chloride medium, Copper and its alloys are extremely corrosion resistant. As a result, these materials are commonly used in industrial applications including heat exchangers and mobile devices. These materials high corrosion resistance is due to two factors. To begin with the standard potential of Cu|Cu in an acidic medium is higher than the hydrogen evolution potential. In the absence of dissolved oxygen, Copper spontaneous corrosion potential can be found in the immunity zone. Second, in neutral medium, corrosion products form a uniform and adherent film on the metal surface that serves as a protective layer against the aggressive medium. Despite this self-protective effect, Copper and Copper alloys can be damaged in a variety of circumstances [87].

The formation of a protective passive layer of Cu_2O and Al_2O_3 on the surface of Cu-Al alloys when exposed to corrosion environment is primarily responsible for their corrosion resistance. The higher tolerance of Aluminum

for oxygen in salt solutions than copper leads to the formations of these stable passive layers on Cu-Al alloys [88].

2.6.2 Factors Affecting Corrosion Mechanisms:

Many of the variables in seawater can affect marines corrosionand the effective mechanisms directly or indirectly. However, only the main point will be highlighted [89,90].

2.6.2.1. Oxygen

The oxidation mechanism, which is involved in most corrosions processes, is dissolving oxygen, due to the high pH of natural seawater. This is valid for all metals, with the exception of those with a much negative standard potential, such as magnesium, where water reduction may also be involved [89,90].

2.6.2.2 Chloride

The high chloride (Cl^-)content is critical in the formations of metal ions complexes, such as those with copper, iron, and other metals, which influences the corrosion reaction both qualitatively and quantitatively. Potential outcome is an acceleration of the metals oxidation rates, which has been observed frequently when complex intermediates can be produced. One example is copper corrosion, where the chloride ion, according to some scholars, is specifically involved in the oxidation process [89, 91]:

$$Cu^{2+} + 2Cl^- \rightarrow CuCl_2 + 1\ e^- \quad \textbf{(2.1)}$$

$$CuCl_2 + H_2O \rightarrow Cu_2O + 4Cl^- + 2H^+ \quad \textbf{(2.2)}$$

2.6.2.3 Calcium and magnesium

Seawater has a large pH and this tends to increase locally when oxygen is reduced at the metal surface of calcium and magnesium oxide, hydroxide, and salt, giving rise to the formations layer know as calcareous layer [93].

2.6.2.4 Organics compound

Like in the chloride ions case, many organics compound can be involved in the formations of quite stable metals ions complexed [89].

2.6.2.5. Specific conductivity

Basic conductivity is relatively large. In the case of general corrosions, it is possible that seawater corrosions will affect general corrosion as well as localized corrosion incurrent will begin to increases with increased conductivity, and this is especially true for localized corrosion processes since there is a real currents flow through the solution in these cases [92].

2.7 Erosion-corrosion

Erosion corrosion is the acceleration or increase in rate of deterioration or attack on a metal because of relative movement between a corrosive fluid and the metal surfaces. Generally, this movement is quite rapid and mechanical wear effects or abrasion are involved. Metal is removed from the surface as dissolved ions, or it forms solid corrosion products that are mechanically swept from the metal surface. Sometimes movement of the environment decreases corrosion, particularly when localized attack occurs under stagnant conditions, but this is not erosion corrosion because deterioration is not increased.

Erosion corrosion is characterized in appearance by grooves, gullies, waves, rounded holes, and valleys and usually exhibits a directional pattern [93,94]. In

many cases, failures because of erosion corrosion occur in a relatively short time and they are unexpected largely because evaluation corrosion tests were run under static conditions or because the erosion effects were not considered. Figures (2.13 A and B) shows a sketch representing erosion corrosion of a heat-exchanger tube handling water [94].

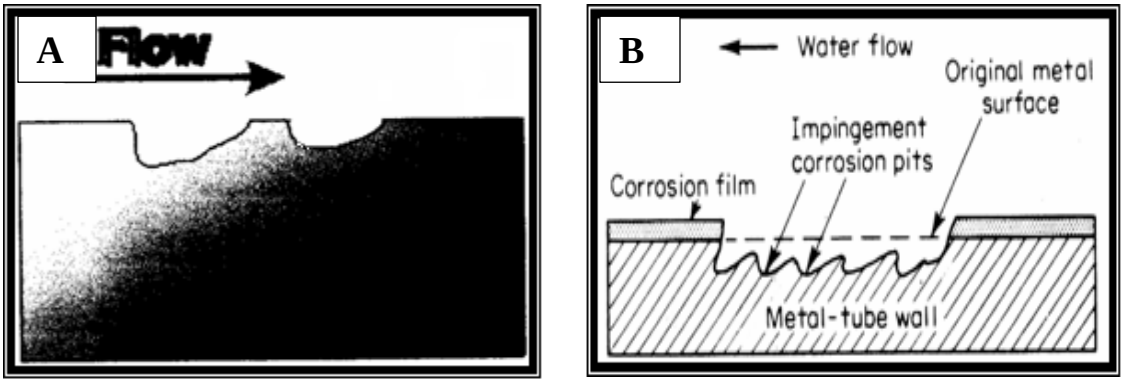

Figure (2.13): Erosion-corrosion for piping systems (A) Condenser tube wall (B) Effect of flow direction on erosion-corrosion [94]

Most metals and alloys are susceptible to erosion-corrosion damage. Many depend upon the development of a surface film of some sort (passivity) for resistance to corrosion. Examples are aluminum, lead, and stainless steels. Erosion corrosion results when these protective surfaces are damaged or worn and the metal and alloy are attacked at a rapid rate. Metals that are soft and readily damaged or worn mechanically. such as copper and lead, are quite susceptible to erosion corrosion. Many types of corrosive mediums could cause erosion corrosion. These include gases, aqueous solutions. organic systems. and liquid metals. For example, hot gases may oxidize a metal and then at high velocity blow off an otherwise protective scale [96].

Solids in suspension in liquids (slurries) are particularly destructive from the standpoint of erosion corrosion. All types of equipment exposed to moving fluids are subject to erosion corrosion: Some of these are piping systems,

particularly bends. elbows, and tees: valves: pumps: blowers centrifugal: impellers: agitators; agitated vessels: heat-exchanger tubing such as heaters and condensers; measuring devices such as an orifice: turbine blades: nozzles; ducts and vapor lines; scrapers; cutters: wear plates: grinders; mills; baffles; and equipment subject to spray [95].

Where the fluid does not contain solids and in smooth pipes, the tolerable flow rate will be relatively high but turbulence must usually be expected and flow limits determined. In addition to reducing flow rates, the introduction of turbulence sources such as sharp curves and irregularities around joints is very important as shown in Figure (2.14) below [97].

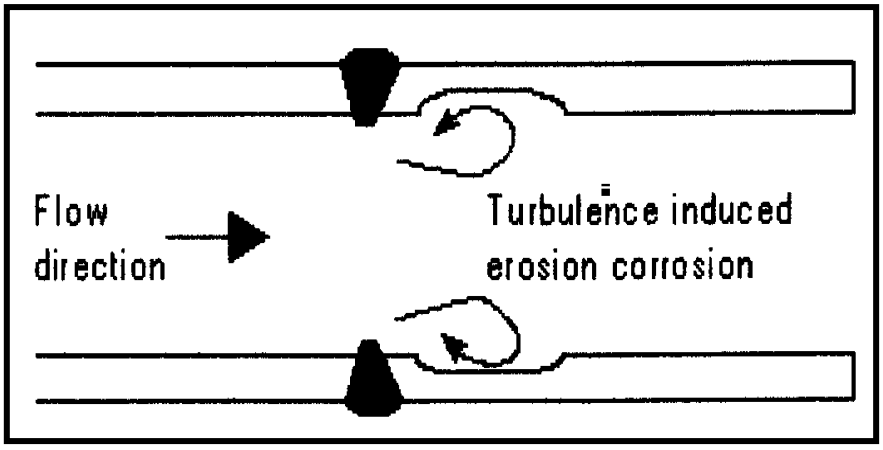

Figure (2.14): Illustrating turbulence induced erosion-corrosion in steel pipes joint [97]

2.7.1 Factors Influencing Erosion-Corrosion

Since corrosion is involved in the erosion-corrosion process all of the factors that affect corrosion should be considered [97,98].

2.7.1.1 Surfaces film

The structure and properties of the protective film that form on certain metals or alloys are critical in terms of erosion-corrosion resistance. The capability of these films to protect the metal depends on the speed or the ease of forming

when exposed to the environment, its mechanical damage or erosion resistance and its rates of reform when destroyed or damaged.

A film that is hard, thick, adherent, and continuous can provide better protection than one that is easily removed or worn off by mechanical means. Under stress, a brittle films that cracks or spalls cannot be protective. The nature of the protective film forming on a certain metal depression sometimes. Often the quality of the protective film forming on a particular metal will depend on its particular environment and therefore will decide its erosion-corrosion resistance by that fluid [96].

2.7.1.2 Velocity

Environmental speed plays a major role in erosion-corrosion. The dynamics of corrosion reactions are often influenced by velocity. It has high erosion effects and especially if the solution has suspended solids. Increasing in velocity usually results in increased attack, particularly if there are high rates of flow. At low velocities, erosion-corrosion can occur on metals and alloys that are fully resistant to a specific environment. Increased speed can increase or decrease attack depending on its effect on the mechanism of corrosion involved. It can increase the attack on steel by increasing its supply to the metal surface by adding oxygen, carbon dioxide, or sulphide hydrogen or by increasing its speed by reducing the thickness of the stagnant surface film [98].The erosion rate is affected by the velocity of the slurry and the kinetic energy of the sand particles in the slurry, which increases the impact force of the particles on the metal surface. Consequently, increased environmental speed leads to an increase in solid patient impact energy [96].

Reactants, intermediate products and corrosion products are either carried to or away from the metal surface. The shear and compressive stresses produced by

the flowing medium, as well as the impact of particles or bubble implosion if the medium contains solid or gaseous phases, harm the surface films at the metal/medium interface. Corrosion occurs as a result of these acts in the following ways [96,98].

1. Erosion-corrosions.
2. Cavitation corrosions.

2.7.1.3 Turbulence

Turbulence or unstable flow conditions cause a lot of erosion-corrosion failures. Turbulence causes a greater liquid turbulence than for laminar flux at the surface of the metal. The best example of this kind of failure is perhaps at the inlet ends for tubing in condensers and other similar heat exchangers in the shell and tube. It is referred to as corrosion inlet tube. Erosion-corrosion can be caused by ledges, crevices, deposits, sharp changes in cross section, and other obstructions that disrupt the laminar flow pattern [98].

2.7.1.4 Impingement

Impingement is to blame for a lot of failures. The metal fails when the water is forced to change its direction of flow, but the vertical and horizontal runs of pipe are largely unchanged. Other applications where impingement conditions occur include steam turbine blades, especially in the exhaust or wet-steam ends; entrainment separators; bends; external components of aircraft; sections in front of inlet pipes in tanks; cyclones; and any other application where impingement conditions exist. Solids in the liquid, as well as gas bubbles, increase the impingement effect. The presence of air bubbles aids in the acceleration of impingement attack [96].

The susceptibility to impingement attack is increased by dissolved (O_2) or (Cl^-) in the water and a low pH. If the liquid contains gas bubbles or solids, or if a gas flow contains droplets, impingement corrosion may occur in bends.

Droplets or bubbles hammer against the surface of metal and can quickly fail when conditions are unfavorable. Figure (2.15) show bending impression and the main flow direction show in Figure (2.16) [99,100].

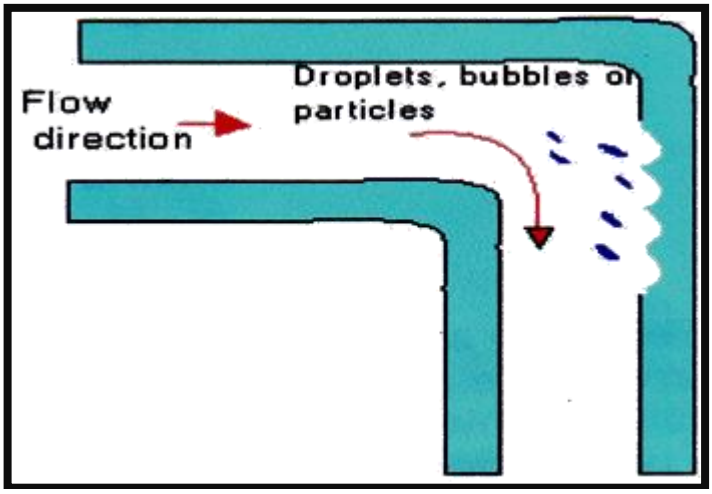

Figure (2.15): Cross section of elbow pipe or elbow -joint pipe (impingement in a bend) [100].

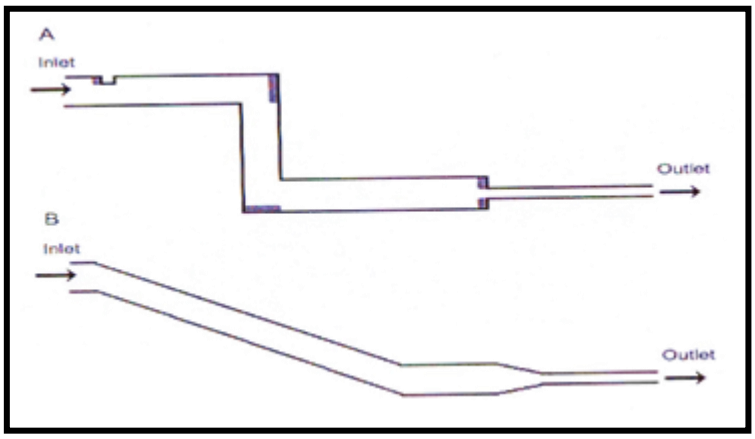

Figure (2.16): The pipe (A) shown above is leaking due to erosion-corrosion

A: Indicates the most probable location for leaks.

B: This is one example of a way to redesign the pipe to eliminate or minimize erosions-corrosion [100]

There are some methods used to prevent or minimize corrosion in the metals and alloys [92]:

1 - Material selection.

2 -Alteration of environment.

3-Coatings.

4-Suitable Design.

5-Anodic and cathodic protection inhibitors.

Methods for Calculation of Corrosion Rate may be determined by (mdd) and give the value expressed in (mpy and verse vesa according to the equation (2-4):

$$R\ (mpy) = \frac{1.44}{\rho} * R\ (mdd) \quad \textbf{.....(2.4)}$$

Also determine in electrochemical methods by (corrosion current density) and translate to other expression by the equation (2-4):

$$C.R\ (mpy) = \frac{0.13 \times Icorr \times E.W}{A \times \rho} \quad \textbf{.....(2.5)}$$

Where: weight of corroded material in (mg).

ρ = density in (g/cm^3).

A=area of corrosion in (in^2) in (mpy) while in (mm/yr.) the area expressed in (cm^2) where (1 mil = 0.00 1 in).

E.W = equivalent weight.

$$E.W = \frac{1}{NEQ} \quad \text{.....(2.6)}$$

$$NEQ = \frac{fi\ .ni}{ai} \quad \text{.....(2.7)}$$

fi= mass fraction, ni= valence electron and ai= atomic weight.

2.8 Damping

Damping is the capacity of a mechanical system to reduce intensity of a vibratory process. The damping capacity can be due to interactions without side systems, or due to internal performance-related interactions. The damping effect for a vibratory process is achieved by transforming (dissipating) mechanical energy of the vibratory motion in toother types of energy, most frequently heat, which can be evacuated from the system.

2.8.1 Damping Parameters

The damping parameters like damping capacity, loss factor, damping ratio and quality factor provides an insight about the damping behavior of material or systems. Modelling the damping behavior requires identification of appropriate damping parameters relevant for the model under consideration. However, the contribution of individual types of damping like material, structural and fluid damping is difficult to estimate from the overall measurement due to the resulting interacting effects of various damping types.

The measurement approaches used to estimate the damping parameters are broadly classified according to time and frequency based response of the system[161].

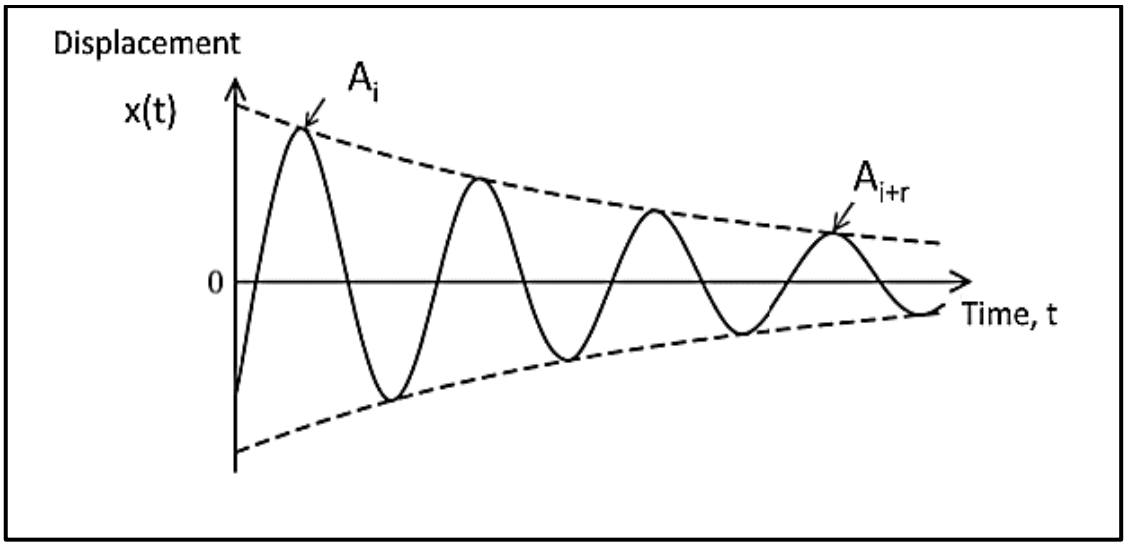

Figure 2.17: The response of the system under impact loading

Logarithmic decrement is a commonly used time-based response method to estimate the damping parameters of a single degree-of-freedom oscillatory system with low damping.

The logarithmic decrement δ is the natural logarithm of the ratio of the amplitudes of two successive cycles of the damped free vibration;

$\delta = \ln (A_i/A_{i+r})$

2.8.2 Internal friction in the thermoelastic martensitic phase

The high damping capacity of the thermoelastic martensitic phase is related to the hysteretic movement of particular behaviour has been related to a decrease in the interfaces (martensite variant interfaces, twin boundaries). Many alloy systems exhibit such a thermoelastic martenresitic transformation. The most studied and well-known systems are Cu–Zn–Al, Cu–Al–Ni and Ni–Ti alloys. These systems are designed to eliminate or at least to reduce structural damage on buildings and infrastructure by limiting the transmitted displacement (Seismic Isolation techniques) or by absorbing the energy of the seismic event

(Energy Dissipation techniques). One energy dissipation technique consists on using dampers based on Shape Memory Alloy (SMA).

Shape memory alloys have many interesting properties that can be exploited in these applications, namely their Superelasticity, high fatigue resistance, near strain-rate independence (in certain conditions related to temperature control). The damping capacity comes from two mechanisms: martensite variations reorientation which exhibit the SME and stress-induced Martensitic transformation of the austenite phase which exhibit the superelasticity [161].

Superelasticity is the main property explored in this type of devices and represents the material's capability to change between metallurgical phases (austenitic and martensitic phases) due to stress application cycles. This property allows SMA based dampers to withstand very large strains (when compared to dampers based on other metallic materials) without any residual deformation upon unloading, while dissipating energy during the loading/unloading cycles. Using SMAs for passive structure control relies on the SMA's damping capacity ,which represents its ability to dissipate vibration energy of structures subject to dynamic loading[162].

2. 9 Literature Survey

In 2001 Sutou et. al. [56] Studied the effect of grains refinmen on the mechanical and shapes memory (SM) properties of alloy was investigated "By using a special induction melting technique, single-phase β alloys of the Cu-Al17%–Mn 10%–V (0.1, 0.5, 1) or Cu-Al-Mn-Cr (0.5, 1, 2) quaternary systems were prepared. Added V or Cr to the Cu-Al-Mn ternary alloys in excess of 0.5 at. % V or l at. % Cr were effective in this case "Refining the grain phase β` to under 200 um. With the increasing content of V or Cr, the Ms. temperature

decreased, but the grain refinement did not improve the SM and pseudo elastic properties. The temperature of the Cu-Al-Mn Alloys martensitic transitions decrease with the size of grain.

In 2008 Mallik and Sampath [109] Investigated the effect of Aluminum and Manganeseconcentrations on the shapes memory properties of Cu–Al–Mn shapes memory alloys. Variations in Aluminums and Manganese content have a significant effect on the transition temperatures, shapes memory and super elastic behavior of these SMAs. The Martensite morphology changes as the Aluminum and Manganese concentrations in the alloys rise, and the transition temperatures fall. In the composition spectrum of the alloys chosen, the Martensitic phase is dominant. These alloys contain two types of martensite, namely (18R) and (2H), both of which have a high density of twins. All**o**ys with a lower Aluminums content and a higher manganese content have a higher manganese content show good super elasticity.

In 2008 Mallik and Sampath [110]: Studied Cu-Al-Mn shapes memory alloy with 10–15 wt.% Al and 0–10 wt.% Mn prepared by ingot metallurgy. When the Cu/Al ratio or the volume of Aluminums is kept constant, the alloys damping ability reductions with a rise in manganese . Although ageing the alloys at 300°C raises their transition temperatures, it lowers their damping ability due to the formation of precipitates. Owing to the formations of aluminums-rich precipitates, the alloys aged at 500°C do not exhibit the Austenite to Martensite transitions and thus have low damping ability. The transition temperatures decrease with an increases in either Aluminums or Manganes concentrations of the alloys.

In 2009 Mallik and Sampath [51]: Studied transition temperatures, shapes memory effects, and super-elasticity of Cu–Al–Mn shapes memory

alloys. These alloys are extremely sensitives to composition changes. Ternary alloys are memory alloys with a ternary form. The quaternary element such as "Zn, Si, Fe, Pb, Ni, Mg, Cr, and Ti" were added to the ternary (base) alloys in various quantities (1, 2 and 3 wt.%) for the current analysis. Transition temperatures were found to be increased by quaternary additions of Zn and Ni, but decreased by "Fe, Cr, Ti, Si, and Mg". With the addition of quaternary elements, the super-elasticity of Cu–Al–Mn SMAs decreases by around 2-3%. Due to solid solution or precipitation hardening in the origin phase matrix, a higher stress is required to form stress induced martensite leading to decrease super-elasticity.

In 2009 Faisel, et. al [156]: Studied corrosion-erosion of (Cu-9.5%Al) prepare by powder metallurgy technique. They found an increase in weight loss for corrosion-erosion tests with phase transition before and after heat treatment using simple immersion method and erosion-corrosion of (Cu-9.5%Al) prepared by powder metallurgy technique. The findings show that adding alloy elements (Ni, Mn, Fe, Si) to alloys increases corrosion resistance, wear resistance, and corrosion resistance. The shift in weight over time indicates a stable case after exposure to corrosion media. Alloys (Cu-Al-Ni-Mn-Fe-Si) also have a low rate of corrosion in seawater, strong wear resistance, and a high compressive pressure.

In 2010 Jiao et. al. [107]: Studied the effects of solution temperatures on martensite transitions temperature, damping capacity and shapes memory's effects of a Cu-7.66Al–9.52Mn alloys was investigation by resistivity temperature method, reversal torsions pendulum methods and bend test. The results showed the shapes memory effects of Cu-7.66Al–9.52Mn improved with increasing the solution temperatures up to 1073K, over which it increased

slowly with the temperatures. Its damping capacity also increased with increasing temperatures upto 1098 K, but it decreases with further increasing temperatures. The shapes memory effect in Cu based alloys was mainly determined by the amount of the martensite, while their damping capacity was affected by the amount and the thickness of the martensite plates.

In 2011 Montecinos and Simison [93]: Investigated the corrosion behavior of a shape memory Cu–11.40Al–0.55Be (wt.%) polycrystalline alloy in 3.5% NaCl has been characterized in view of its application in bridges as seismic dampers. Samples with two different microstructures were employed: single phaseβ and β matrix with γ_2 dendritic precipitates. They were found that the Chloride environment could produce a de-aluminization attack on the studied alloy. The corrosion behavior was affected by the alloy microstructural conditions. The single-phase microstructure suffered matrix dealloying (aluminum preferential dissolution) on the whole surface. In the two-phase microstructure, preferential dissolution of γ_2 dendritic precipitates occurred, which seems to protect matrix from dealloying.

In 2013 Canbay and Karagoz [112] Prepared Cu-based shapes memory alloys by arc melting. The Cu-based polycrystalline quaternary alloys CuAlMn– X (X = Mg, Fe) were produced in this study. The characteristic transition temperature can be controlled by the variations in the Aluminum and Manganese content. Additionally, the effect of magnesium and iron on the transition temperatures and thermodynamic parameters was investigated in the Cu–Al–Mn ternary system. The additions of the magnesium decrease the characteristic transition temperatures of the Cu–Al–Mn system, but that of the iron increases. Due to the low solubility of the magnesium, it forms precipitates in the matrix.

In 2013 Takhakh et. Al [123]: Studied the effects of Ta addition to Cu-Al-Ni shape memory alloy. Cu-Al-Ni specimens using powder metallurgy technique with vacuum sintering environment, three rang of Ta powder weight percentage (0.3,0.6,0.9) % has been added. Micro hardness and sliding wear resist have been tested followed by X-ray diffraction, SEM and EDX for micro structure observation. Using different Ta powder weight percentage will not affect on X-ray diffraction results or the shape memory effect. There is a nonlinear increment in HV (85 to 168) with the increasing the weight percentage of Ta that result to alloy enhancement with the addition of Ta particle to the structure.

In 2014 Canbay and Keskin [104]: Studied Cu–Al–Mn, Cu–Al–Mn–V and Cu–Al–Mn–Cd shape memory alloys were produced by arc melting. They have investigated the effects of the alloying elements on the characteristic transformation temperatures, variations in structure and microstructure. The characterization of the transformation temperatures was studied by the differential scanning calorimetry. It was observed that the addition of the vanadium and cadmium decreases the characteristic transformation temperatures. The structural changes of the samples were studied by X-ray diffraction measurements and optical microscope observations. The crystal structure of the martensite shape memory alloys was identified as M18 at room temperature. The crystallite sizes of the alloys were determined. V-type martensite with different orientations were detected. Microhardness value of the alloys were found between 194 and 211 Hv.

In 2014 Xiao et. al. [105]: Mechanical alloying and powder metallurgy were used to create ductile Cu–Al–Mn–Ti–B shapes memory's alloys with high fatigue strength. The composition of the mixture (wt.%) was (81.9 % Cu, 8.0 % Al, 9.6% Mn, 0.33 % Ti, 0.17 % B). The size of the crystallite grains decreases

as milling time increases. At room temperature, the aged alloys had a martensite structures and a shapes memory recovery of 92%.

In 2015 Kumar et. al. [108]: Studied Cu-12.5wt.% Al-5wt.% Mn-2wt.% X [X=Zn, Si, Mg, Cr]. Liquid metallurgy was used to prepare the samples. All of the alloys have a grains structures with (α+ β) phases in the homogenized state, which is a requirement for Martensite formations on quenching, suggesting that all of the alloys have the ability to exhibit shape memory behavior. The formation of martensite can be seen in the majority of quenched samples, but with varying morphologies. The plate- or spear-like martensite process [the zig-zag phase] is observed in the precipitated martensite. The martensitic phases of Al_2Cu_3 [β`] and $Al_4Cu_9$ [γ`] have been clearly identified in the XRD of the quenched samples.

In 2017 Yang et. al. [106]: Investigated the effects of Vanadium and Manganese content on Cu–Al–Mn. The findings show that during deformation, stress-induced 2H martensite from L_{21} origin stabilizes in all Cu-Al-Mn-V alloys. The super-elasticity and shape memory effect can be broken down into three categories. Situation 1 alloys (wt.%) with excellent super-elasticity strains of up to 5.4 % and 3.9 % respectively include (Cu 63.7, Al 25.3, V 1.9, Mn 9.1) and (Cu 63.7, Al 25.8, V 2.2, Mn 8.3) alloys (wt.%). (Cu 63.8, Al 25.4, V 4.2, Mn 6.6 and Cu 63.0, Al 26.2, V 4.7, Mn 6.1) alloys are situation 2, and exhibit good shapes memory effects being up to 3.5% and 3.9% respectively. The super-elasticity and shape memory effect of (62.8%Cu, 26.2%Al, 2.6%V, 8.4%Mn) alloys, which are in situation 3, are in the middle of the two. The SE properties of the Cu–Al–Mn–V alloys vary. With increasing V material, the SE strain and relative recovery rate gradually decreases.

In 2018 Kozuh et. al. [130]: Prepared bars of Cu-8.3%Al-9.4%Mn shape memory alloys by continuous casting technique. The samples were characterized using optical microscopy and scanning electron microscopy along with EDX analysis. The continuous cast alloy revealed some martensitic phase, which, after quenching, led to the microstructure that is completely martensite. Quenching of samples had an effect on several mechanical properties and change in morphology of fracture. Hardness in cast and quenched state gives similar values (235 HV and 223 HV). In ageing condition, the value of hardness in all samples increases. After ageing at 100 °C, hardness was 274 HV, while after ageing at 200 °C and 300 °C, hardness values significantly increase (432 HV and 332 HV). Increase in hardness values can be caused by the second phase particle presence. These changes in mechanical properties can be due to change in grain size and microstructure.

2.9.1 Summary of literatures

From the review of literatures, it is clear that many researchers have studied about CuAlMn shapes memory alloys, some researchers studied the effect of alloying elements addition on the mechanical properties, electrochemical, corrosion behavior and shape memory effects, also others studied the erosion-corrosion of these alloys show in Table (2.2) comparison between some researches and this study.

Table (2.2) comparison between some researches and this study.

Reference	Alloy composition	Addition alloying	Results
[104]	Cu - 21%Al-3.7%Mn	(0.45, 0.37) V and (0.6, 0.43) Cd	The martensites occurred in the samples are V-type and needle-type martensites. Hv increase from (149 to 211and 256 when addition Cd and V respectively
[105]	Cu, 8.0 % Al, 9.6% Mn, x Ti, xB	0.71% B, 0.33% Ti	A_s and A_f after aging about 45 and 55 respectively. martensite 18R after aging. shape memory recovery reach 92%
[106]	Cu–12.8% Al–9.1Mn	(1.9 - 4.5) % V	The SME gradually increase with the increase of V content. V- 4.0 and V - 4.5 alloys exhibit good SMEs, being up to the largest value of 3.5% and 3.9% respectively
[107]	Cu–7.66% Al–9.5%Mn	…….	Maximum Logarithmic decrement of Samples reach 0.16 at solution treatment 1098K
[56]	Cu-Al17%–Mn 10%	(0.1, 0.5, 1) V, (0.5, 1, 2) Cr	Microstructure contain (β and precipitate), A_s and A_f about (81, 97) respectively and decrease with addition Cr and V
[108]	Cu-12.5 wt.% Al-5 wt.% Mn	2.% (Zn, Si, Mg, Cr)	Grain structure with (α+β) phases is visible in the homogenized condition of all the alloys. The martensitic phases of

			Cu_3Al and Al_4Cu_9. Hv. hardness increase from 250 to 475 when addition Mg element.
[109]	Cu–(10-15)% Al- (0-5)%Mn	--------	transition temperatures As and Af about 95 and 117 respectively. lath type martensite $\beta`_1$. SE about (3-8)%.
[110]	Cu-(10-15) % Al-(0-5) % Mn		A_s and A_f about (58 and 80)°C respectively. damping capacity IF about 0.16.
[51]	Cu–12.5%Al–5%Mn	Zn, Si, Fe, Pb, Ni, Mg, Cr and Ti	Transition temperatures A_s and A_f about 50 and 56 °C respectively. An increase of 4–8% in strain recovery by SME was observed in the alloys with the quaternary alloying additions.
[112]	Cu-12%Al-5%Mn	(1.69 and 1.1) %Mg, (1 and 1.3) %Fe	transition temperatures As and Af (382.41 and 405.51) K respectively and decrease with alloy addition
[113]	Cu, Cu-Al and Cu-Al-Ag	4.3% Al, 4.7% Ag	electrochemical behaviors
[156]	Cu-9.5%Al	3%Si, 5%Ni, 1%Mn, 4%Fe	increase in corrosion resistance about (113.3 – 566.6%). Also high resistance in corrosion/erosion of two alloys are

			calculated. When the heat treatment are carried out, the improvement ratio is (488.9%),and the hardness have (185HV) value.
[130]	Cu-8.3%Al-9.4%Mn	ageing at 300 °C	Hv increase after aging in 300C from 235to 332. The V-shape martensite.
[123]	Cu-Al-Ni	(0.3, 0.6, 0.9) %Ta	Micro hardness increase from (85-168)Hv with increase Ta form (0.3 to 0.9)%wt.. no effect of Ta addition to the martensitic phase.
[93]	Cu–11.40Al–0.55Be		corrosion behavior in 3.5% NaCl (electrochemical tests)
The Current research	Cu-8%Al-9%Mn	(1, 2, and 3) wt. % Ta, In, Y_2O_3 and (0.6, 1, 2) % Zr	Shape memory effects, linear polarization, density, porosity, erosion corrosion, damping capacity, transformation temperatures, Micro-structures, hardness before and after aging heat treatments at 300◦C

The originality of present work is:

1. The alloy Cu8%Al9%Mn shape memory used as industrial application (a seismic damper in buildings and bridges).
2. Addition Tantalum, Indium, Zirconium, and Yttrium oxide with three different ratios.

Chapter 3

Experimental Work

3. 1. Introduction

This chapter deals with the materials and devices used in the current study as well as the practical method applied for the manufacturing of shape memory alloys and the main components of the powders (Copper, Aluminium, Manganese, and the additional powder), using powder technology. Heat treatment (including quenching and aging) was used for shape memory alloys. The microstructure was explored using an optical microscope, scanning electron microscope (SEM), and energy dispersive x-ray spectroscopy (EDX). X-ray diffraction (XRD) was employed to detect the phases. A differential scanning calorimeter (DSC) was utilised for the transformation temperature of martensite and austenite. The shape memory effect was obtained by Vickers hardness. The corrosion testing was done in 3.5% NaCl. Most steps of the sample preparation and specimens test were performed at the laboratories of the Metallurgical Engineering and Ceramic and Building Materials Department/Faculty of the Materials Engineering-University of Babylon.

3.2. Materials

The powders, i.e., Cu, Al, Mn, Zr, In, Ta, and Y_2O_3 used in this research to prepare shape memory alloy with an average particle size origin are shown in Table 3.1. Chemical composition analysis was done for all powders used in this thesis in order to ensure their purity. Figure 3.l shows the summary of all the programs used in the present work.

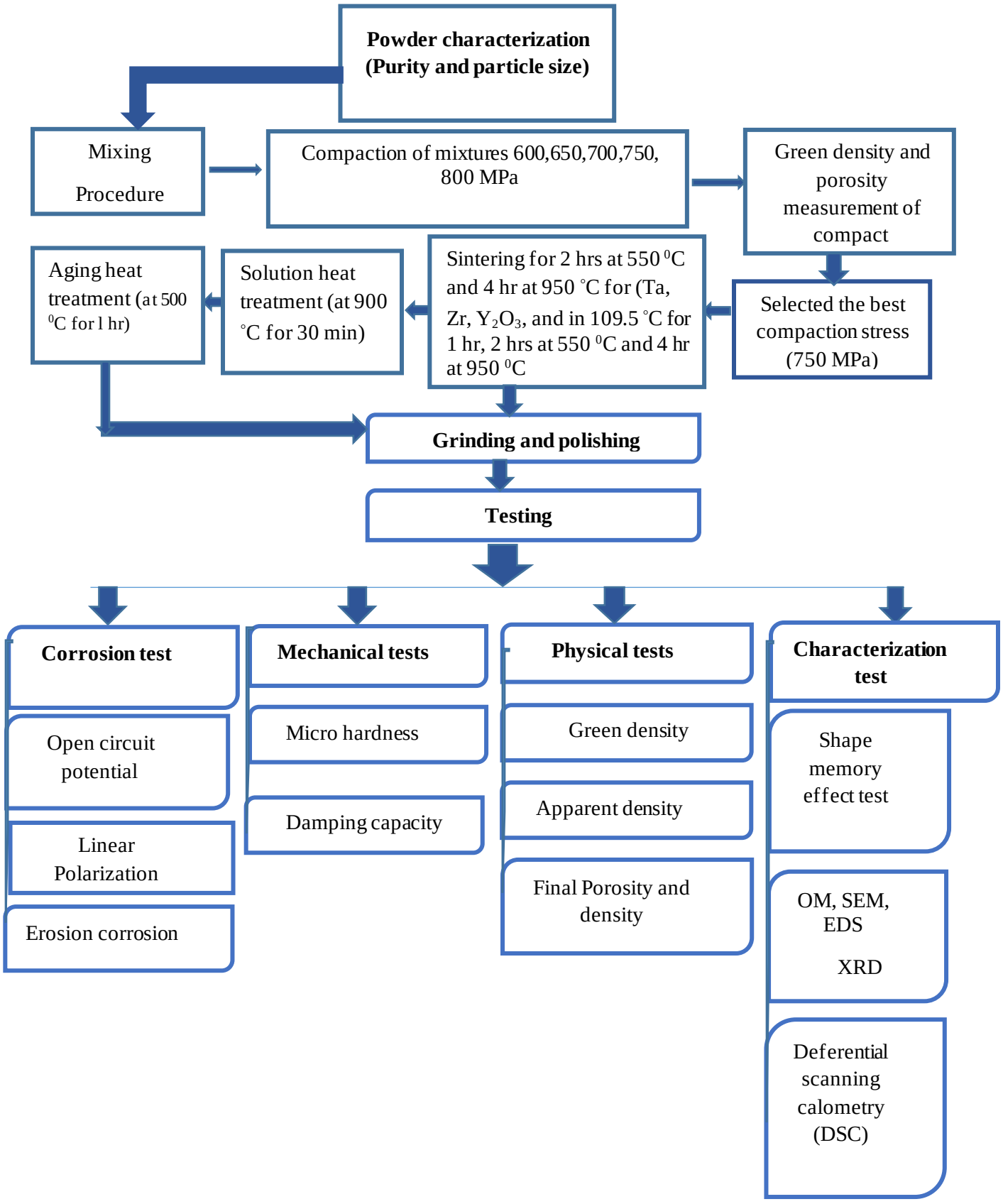

Figure 3.l: The summary of the overall procedure

3.3. Particle Size

Particle size analyzer type ("Bettersize2000" LASER PARTICLE SIZE ANALYZER), as shown in Figure (3.2), was used to determine the particle size of Cu, Al, Mn, In, Zr, Ta, and Y_2O_3 powders. Half gram (0.5 gm) of each element powder was poured inside the device chamber along with distilled water (free of minerals/solids). The water was used as a medium to keep these particles of element powder in a suspension state. The device separated these particles according to their size. The tests were carried out at the University of Babylon/College of Materials Engineering/Ceramic and Building Materials labs. Table 3. l shows the average particle size of the used powders approved in the preparation of the samples.

Table 3.l: Powders Specifications

Powders	Average particle size (µm)	Supplier
Copper	4.827	India/CDH/Centra Drug House (P) ltd.
Aluminium	l9.38	=
Manganese	l9.09	=
Tantalum	ll.74	=
Zirconium	l4.23	=
Indium	l8.46	=
Yttrium oxide	8.55	=

Figure 3.2: Laser particle size analyzer

Figure 3.3 shows the results of the particle size analysis.

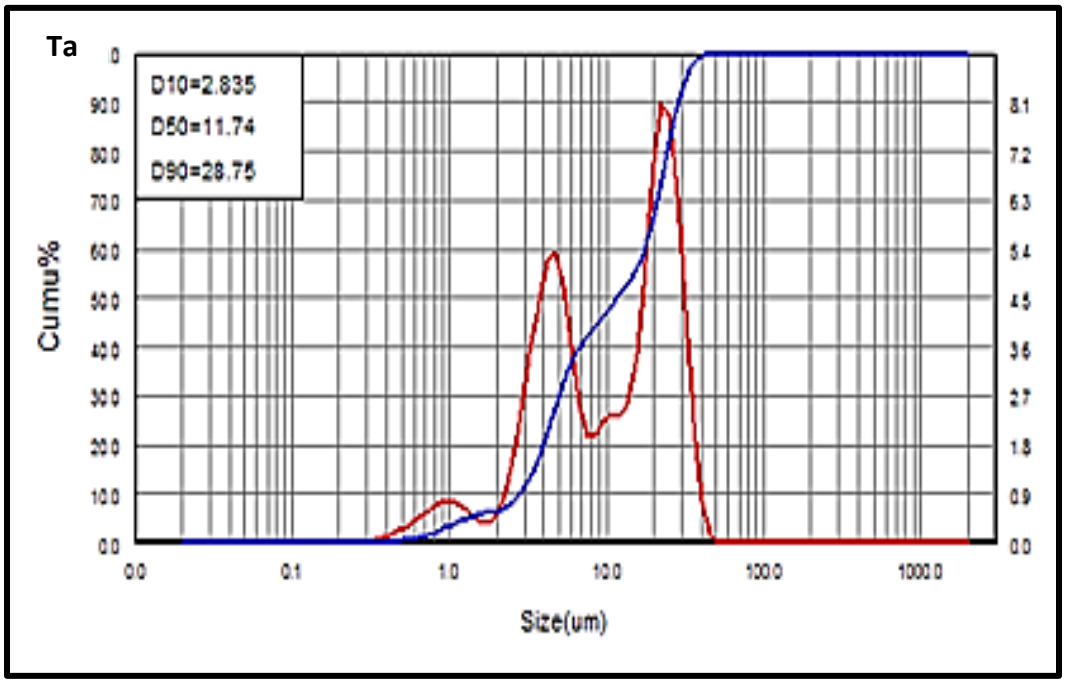

Figure 3.3: Particle size analyzer

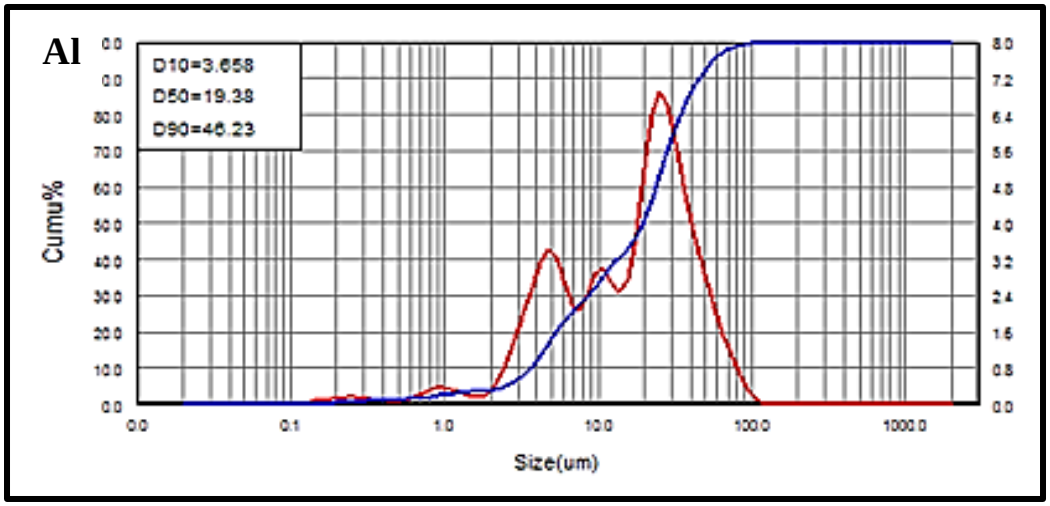

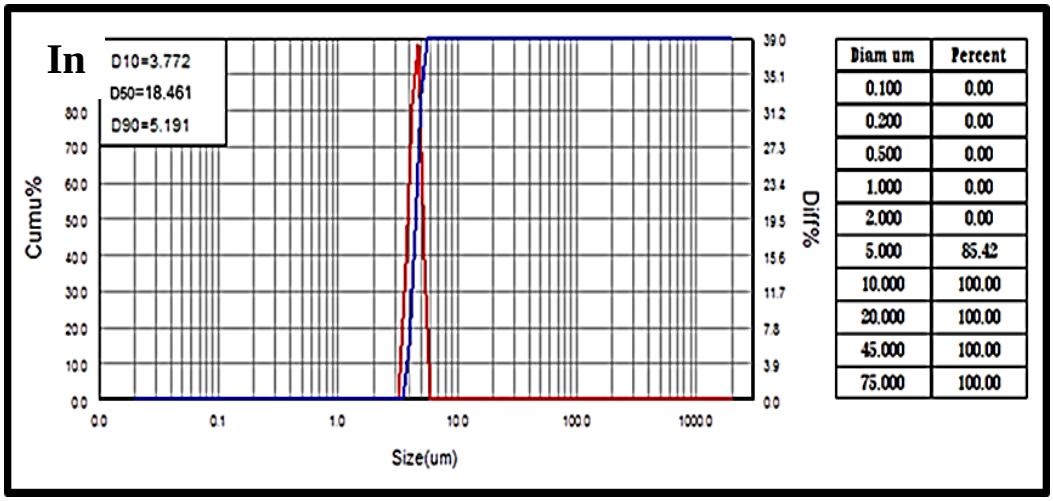

Diam um	Percent
0.100	0.00
0.200	0.00
0.500	0.00
1.000	0.00
2.000	0.00
5.000	85.42
10.000	100.00
20.000	100.00
45.000	100.00
75.000	100.00

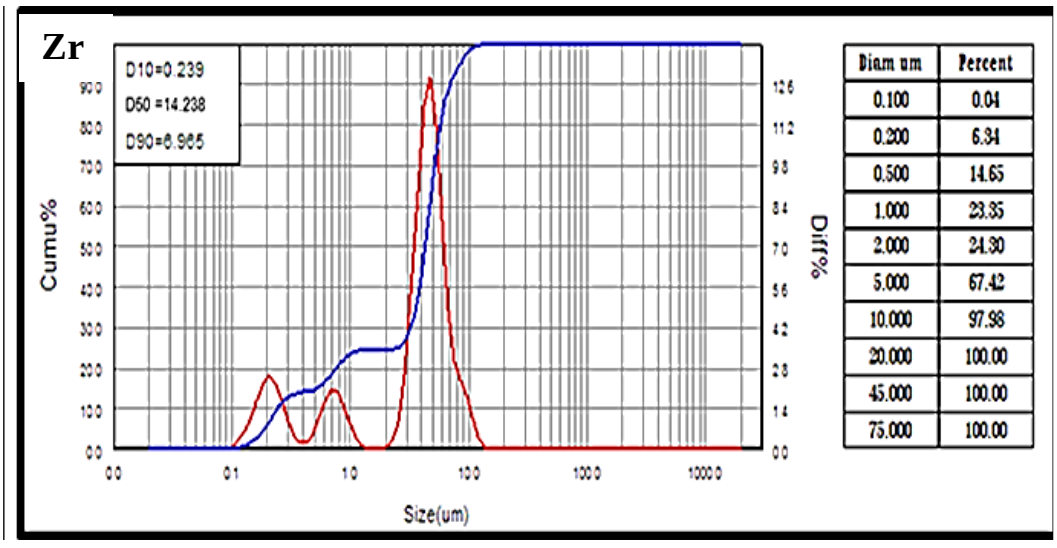

Diam um	Percent
0.100	0.04
0.200	6.34
0.500	14.65
1.000	23.35
2.000	24.30
5.000	67.42
10.000	97.98
20.000	100.00
45.000	100.00
75.000	100.00

Figure 3.3: Contd.

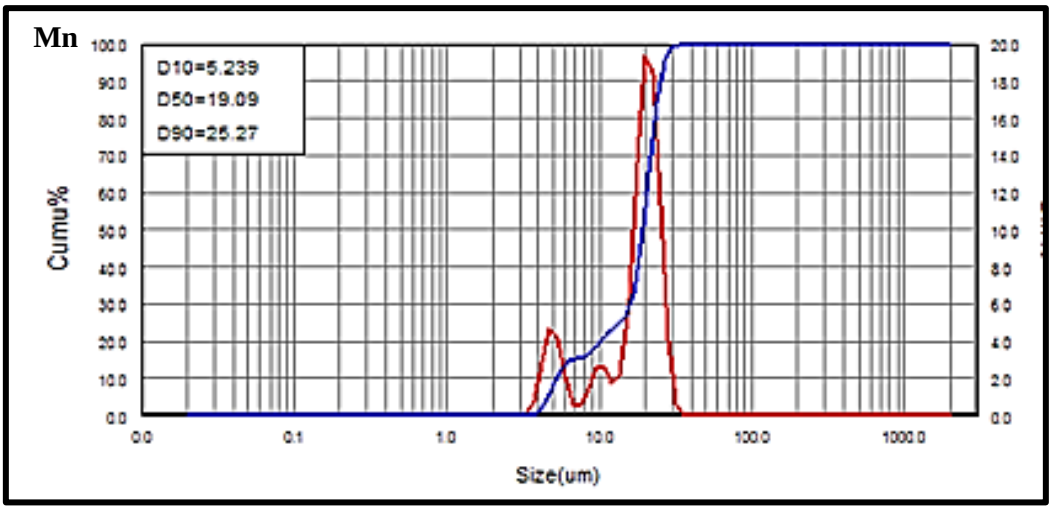

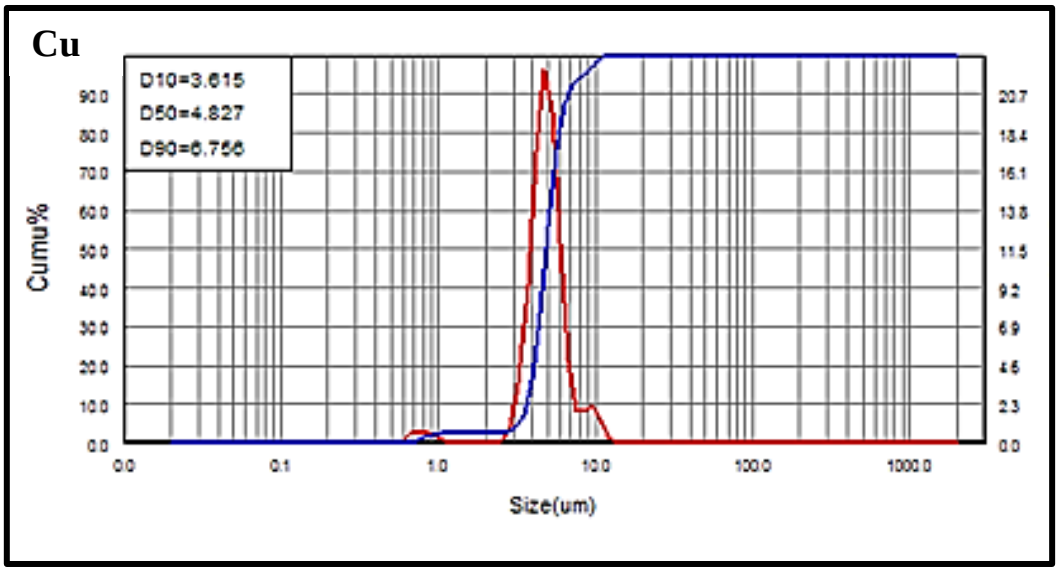

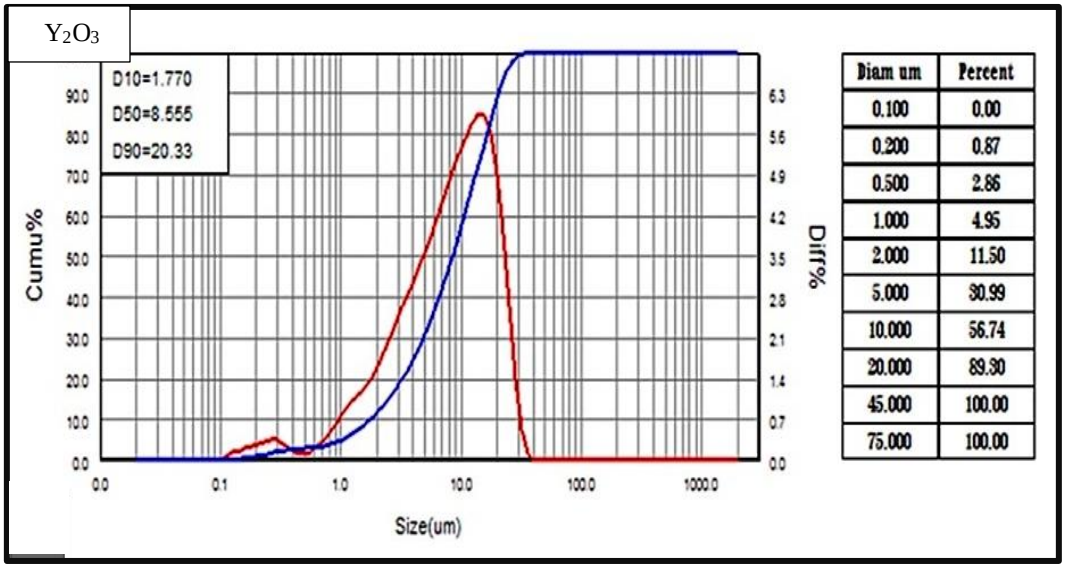

Diam um	Percent
0.100	0.00
0.200	0.87
0.500	2.86
1.000	4.95
2.000	11.50
5.000	30.99
10.000	56.74
20.000	89.30
45.000	100.00
75.000	100.00

Figure 3.3: Contd.

3.4. Chemical Composition

This test has been demonstrated to investigate the purity of elemental powders as shown in Tables 3.2. The tests were carried out at the Ministry of Science and Technology/Department of Materials Research via a spectro- analyzer model (SPECTROMAXx).

Table 3. 2: Purity for base powder of the alloy

Element	Cu	S	Fe	Sn	Pb	Zn
Percent%	99.95	0.003	0.016	0.004	0.023	0.001
Element	Al	Fe	Zn	W	S	Ni
Percent%	99.967	0.004	0.002	0.001	0.007	0.02
Element	Mn	Fe	W	Cu	Sn	Ni
Percent%	99.964	0.001	0.006	0.024	0.001	0.004
Element	Ta	Pb	S	C	Si	
Percent%	99.88	0.04	0.02	0.01	0.05	
Element	Zr	Cr	Si	C	Fe	S
Percent%	99.97	0.006	0.004	0.003	0.002	0.015
Element	In	C	Mn	Fe	S	Sn
Percent%	99.987	0.002	0.001	0.003	0.006	0.001
Element	Y_2O_3	Pb	Mn	C	V	Zn
Percent%	99.93	0.001	0.004	0.056	0.001	0.005

3.5. Preparation of Samples

The preparation of the base alloy (Cu-Al-Mn) SMAs with 8 wt.% of Aluminium and 9 wt.% of Manganese through mixing, compacting, and sintering process. The experiment was done to study the effects of the added elements, i.e., (Ta, Zr, In), and Y_2O_3 ceramic particles on the mechanical and corrosion behaviour of the base alloy. Table 3. 3 shows the samples used for the Cu-Al-Mn experiment and the added elements' percentages.

Table 3. 3: Chemical composition of alloys under study

Synthesized Composition	Code	Cu wt.%	Al wt.%	Mn wt.%	Ta wt.%	In wt.%	Zr wt.%	Y_2O_3 wt.%
Cu-8Al-9Mn	A	83	8	9	-	-	-	-
Cu-8Al-9Mn-1%Ta	B1	82	8	9	1	-	-	-
Cu-8Al-9Mn-2%Ta	B2	8l	8	9	2	-	-	-
Cu-8Al-9Mn-3%Ta	B3	80	8	9	3	-	-	-
Cu-8Al-9Mn-1%In	C1	82	8	9	-	1	-	-
Cu-8Al-9Mn-2%In	C2	81	8	9	-	2	-	-
Cu-8Al-9Mn-3%In	C3	80	8	9	-	3	-	-
Cu-8Al-9Mn-0.6%Zr	D1	82.4	8	9	-	-	0.6	-
Cu-8Al-9Mn-1%Zr	D2	82	8	9	-	-	l	-
Cu-8Al-9Mn-2%Zr	D3	8l	8	9	-	-	2	-
Cu-8Al-9Mn-1%Y_2O_3	E1	82	8	9	-	-	-	1
Cu-8Al-9Mn-2%Y_2O_3	E2	8l	8	9	-	-	-	2
Cu-8Al-9Mn-3%Y_2O_3	E3	80	8	9	-	-	-	3

3.5.1. Mixing Procedure

The mixing of element powders of base alloy and additional powders was done using Planetary Automatic Ball Mill type (FRITSCH Pulaeristte Germany) as shown in Figure 3.4. Stainless-steel balls with different diameters (10 mm & 5 mm) was used. These balls are used to grind and mix element powders for 4 hours at 300 rpm. The wet mixing was done using 0.5 cc of ethyl alcohol to every 25 g of the powder mixture. The wetting mixing was used to minimize the temperature generated by friction between the balls with the walls and powder.

Figure 3. 4: Bench-Top Planetary Automatic

3.5.2. Compaction of Mixed Powder

The compaction of the mixed powder (base alloy element and addition powders) was done using an electrical uniaxial hydraulic press type (Soil Test, Inc. USA) as shown in Figure 3.5A & C.

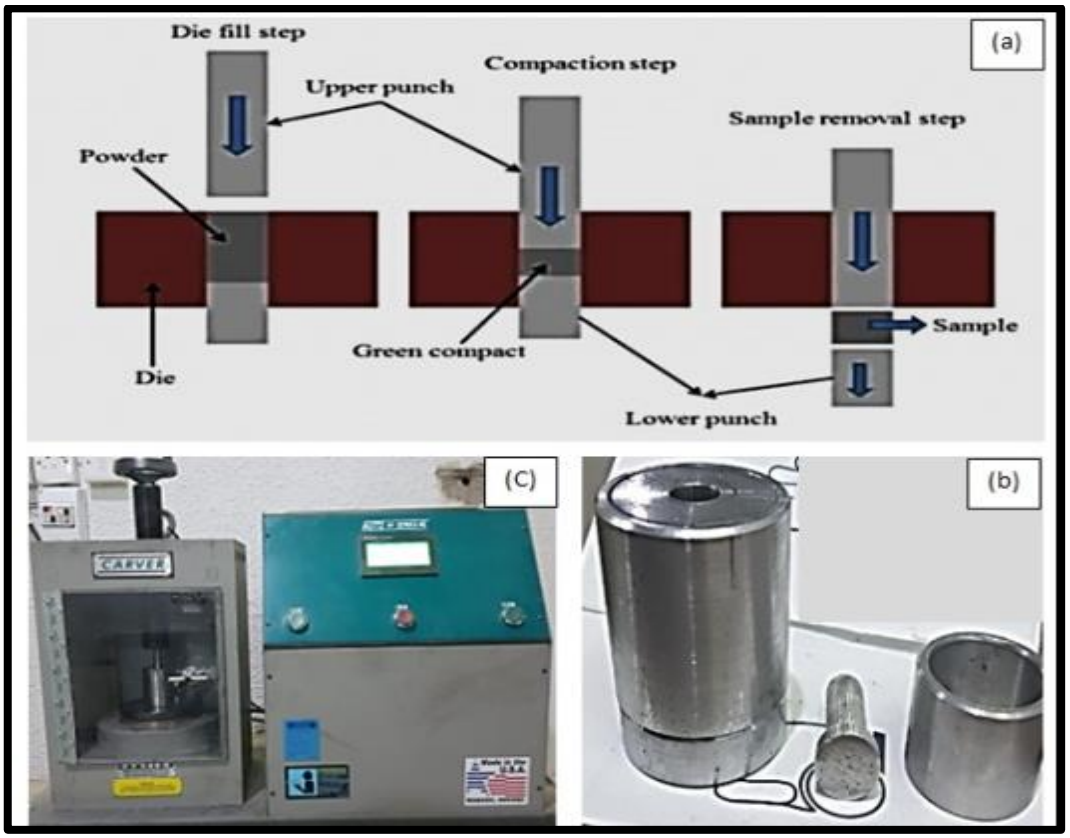

Figure 3.5: A) Schematic representation of the uniaxial pressing; B) Stainless steel dies; C) Uniaxial hydraulic press.

The device was used to create a green sample of mixed powder with specific dimensions, i.e., D = 12 mm, t = 5 mm. The device consists of a single action die made from tool steel as shown in Figure 3.5B.

The graphite is used as a lubricant in order to minimize the friction between the punch and the die wall as well as the friction between the green compact and the die wall and also to avoid the cracks formed from the ejection of the green compact.

Various compression stresses, (600, 650, 700, 750, 800 MPa) with loading rate 1 ton/min and hold time 2 min have been used in order to determine the optimum compression stress that causes the highest green density and lowest

green porosity [123,160]. Between these limits, samples were defect-free and had sufficient green strength for handling.

3.5.3. Sintering of green sample

The final step of preparing experiment samples was the sintering: Sintering is a heat treatment process applied to the compact sample to get the optimum strength and integrity. The apparatus (furnace) used for sintering consists of Quartz Tube and Argon gas stream supply as shown in Figure 3.11. Argon gas was supplied to the tube to avoid the oxidation of samples (inert gas ambient surrounding the test sample). The heat rate was 20 ˚C/min.

1- **First sintering attempt:** Heating green compacts from room temperature (25 to 550 °C). Soaked for 2 hrs and heated from 550 to 950 °C. Soaked for 2hrs at 950 °C and slow cooled in a furnace. Crushing and breaking of specimens, incomplete sintering process, as shown in Figure 3.6.

Figure 3.6: CuAlMn after first attempt of sintering crushing and breaking of specimens

2- **Second attempt:** Heating green compacts from room temperature (25 ◦C) to 550 °C. Soaked for 2hrs at 550 °C and heated at 550 to 950 °C. Soaked

for 3hrs at 950 °C and slow cooled in a furnace [158,160]. X-ray diffraction peaks show incomplete phase transformation.

All specimens sintered were preserved and kept inside the furnace for the cooling process, which was set to room temperature (25 °C).

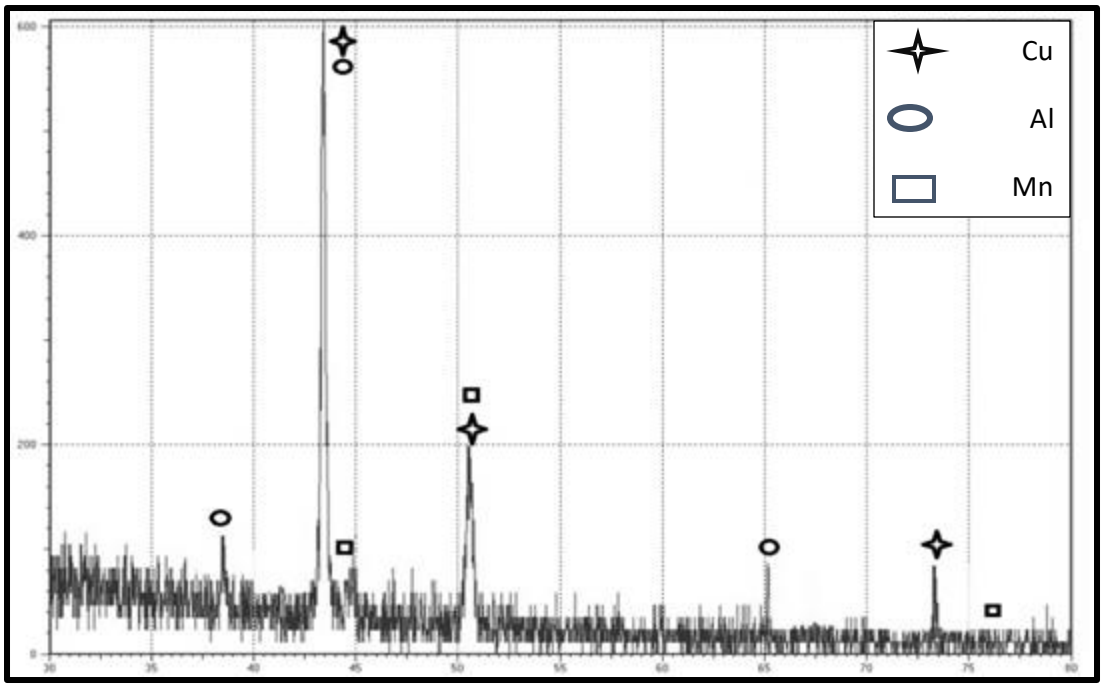

Figure 3.7: XRD after second attempt

3. Third attempt sintering: The sintering process for CuAlMn and CuAlMn-X (Ta, Zr and Y_2O_3), as shown in Figure 3.8, was performed as follows:

1. Heated from room temperature to 550 °C and soaked for 2 hrs.
2. Heated from 550 °C to 950 °C and soaked for 4 hrs.
3. Slow cooling in the furnace with continuous vacuum to room temperature (25 °C). The heat rate was 20 ˚C/min.

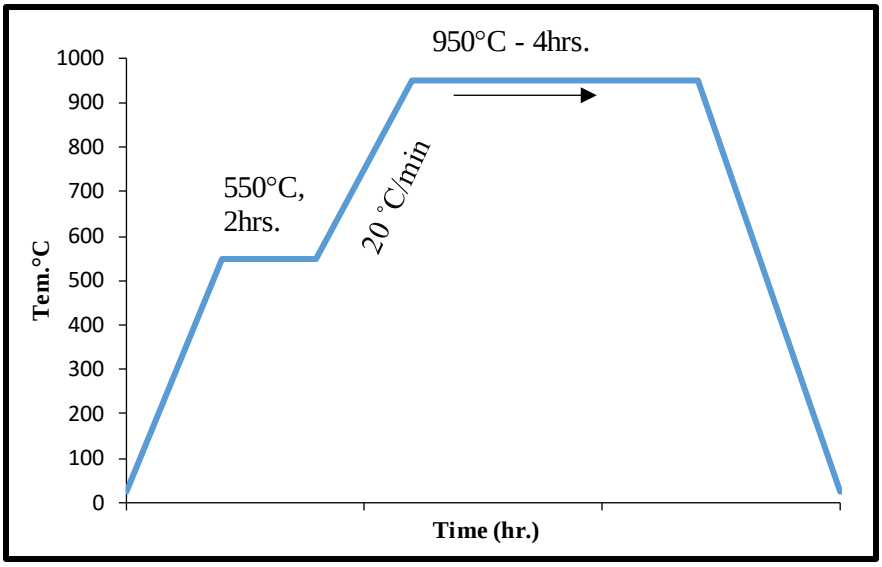

Figure 3.8: Sintering time Vs temperature for CuAlMn-X (Ta, Zr and Y_2O_3)

1- First sintering attempt for CuAlMn-In: Green compacts (CuAlMn- x% In) were heated from room temperature (25 °C) to 550 °C, soaked for 2hrs at 550 °C and heated from 550 °C to 950 °C, and soaked for 3 hrs at 950 °C and slow cooled in furnace. The exit of molten metal from the specimens and the occurrence of cleavage in the specimens is shown in Figure 3.9.

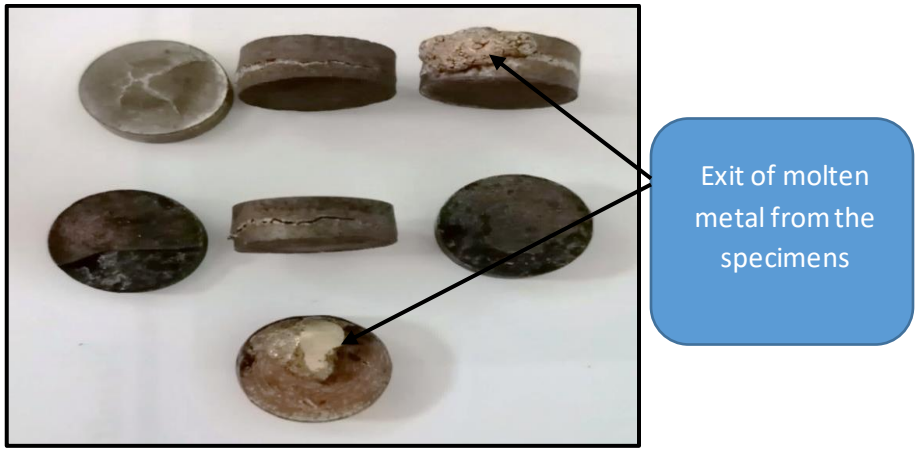

Figure 3.9: Specimens CuAlMn-x In alloys after attempt in sintering

2- Second attempt: The sintering process for CuAlMn-In the heat rate used was 20 ˚C/min, which was maintained through the entire sintering cycle of 7 hrs, as shown in Figure 3.10.

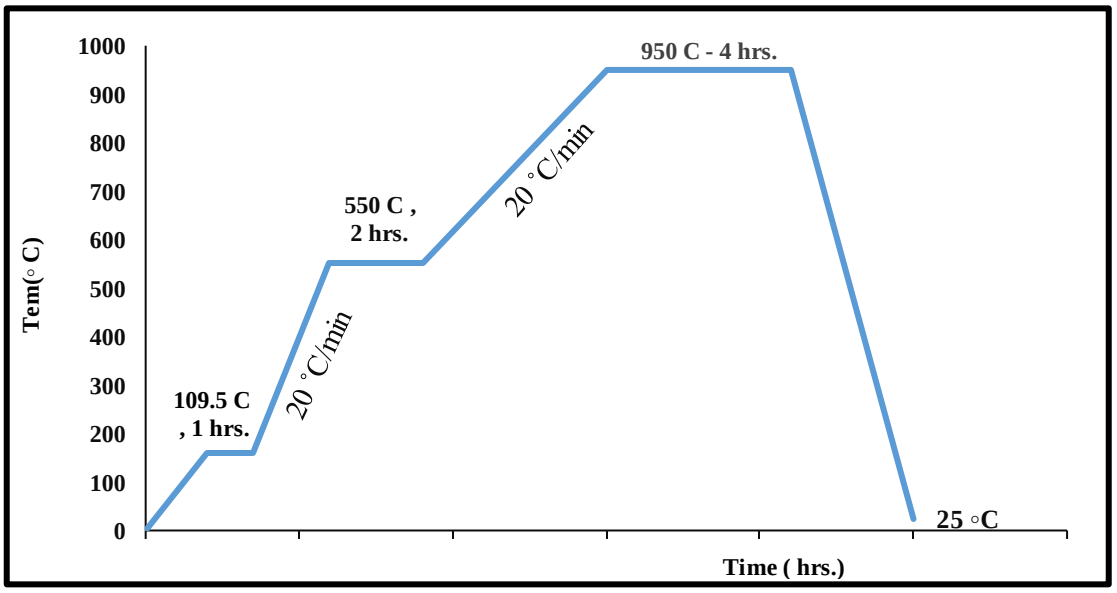

Figure 3.10: Sintering time vs temperature for CuAlMnIn

It was performed as follows:

1. Heated from room temperature to 109.5 °C and soaked for 1 hr.
2. Heated from 109.5 °C temperature to 550 °C and soaked for 2 hrs.
3. Heated from 550 °C to 950 °C and soaked for 4 hrs.
4. Slow cooled in the furnace with continuous vacuum to room temperature (25 °C). Heat rate 20 ˚C/min

The electrical furnace was used to sinter the specimen, as shown in Figure 3.11 A, and the final shape of success sinter specimen is shown in Figure 3.11B.

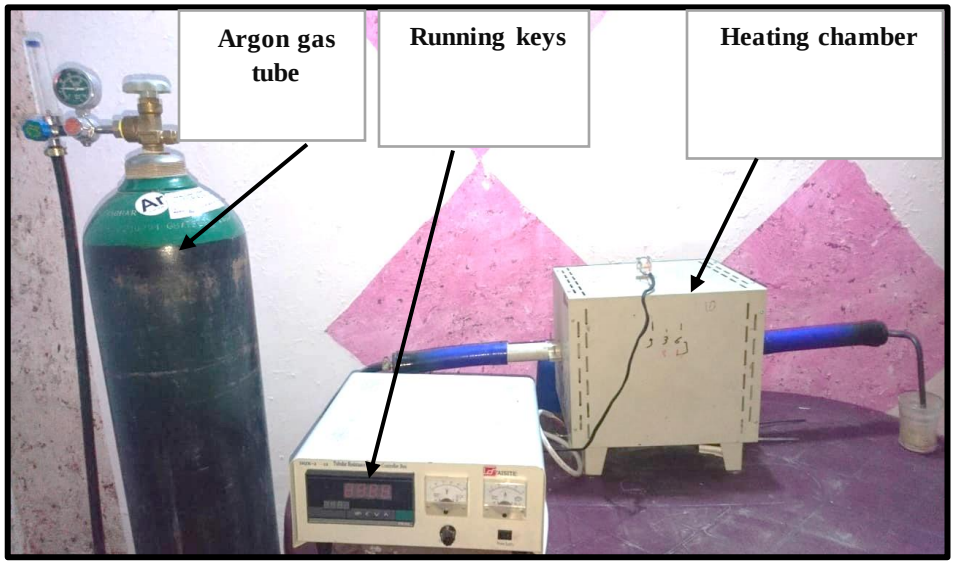

Figure 3.11: (A) Sintering furnace

Figure 3.11: (B) Specimens after sintering

3.6. Heat Treatment after Sintering

3.6.1. Solution heat treatment (Betatized)

Sintered specimens subjected to solution heat treatment is shown in Figure 3.12. The temperature was raised from 25 °C (room temperature) to 900 °C for 30 min with the heat rate 20 ˚C/min, and then rapid cooling was applied to 100

°C and maintained for 10 min. And then the process was cooled down to 3–4 °C using ice water. The purpose of step quenching is reducing the tendency of the formation of quenching cracks and restricting the formation of martensite plates by excess dislocations trapped in fast cooling from high temperatures [52]. Figure 3.12 explains the quenching process and furnace used for this treatment.

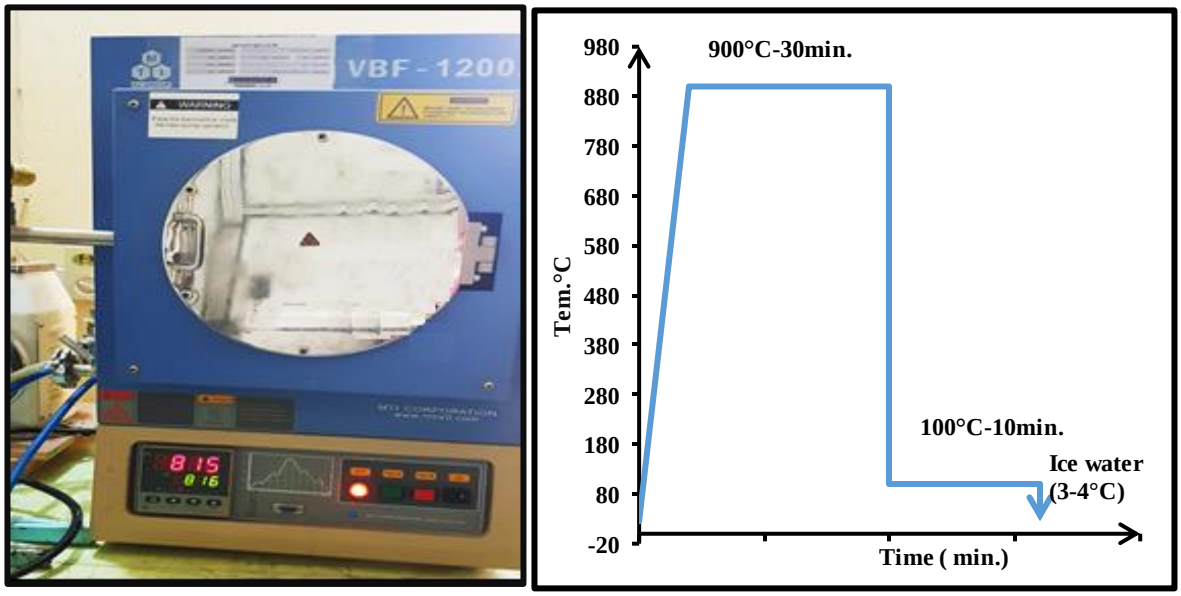

Figure 3.12: (A) Electrical furnace for heat treatment, (B) Quenching procurer.

3.6.2. Ageing heat treatment

Figure 3.13 explains the solution heat treatment program. A specimen of varying alloy element contents was subjected to post-quench isothermal ageing in the austenitic phase of the alloy at 300 °C for l h [110]. The heat rate used was 20˚C/min. After ageing, the specimen were quenched into ice water 3–4 °C. The specimen were further studied for their microstructure, transformation temperatures, and corrosion resistance.

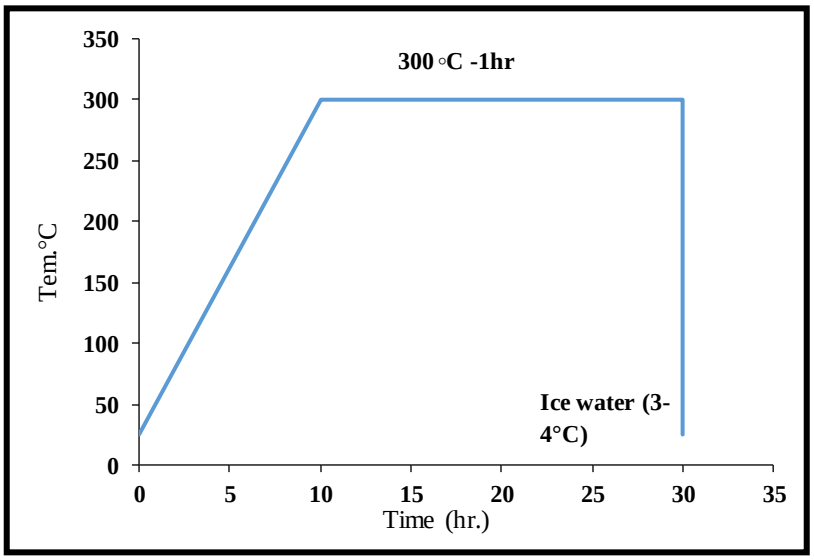

Figure 3.13: Thermal cyclic of aging heat treatment process

3.7. Differential Scanning Calorimeter (DSC) Tests

The Differential Scanning Calorimeter test was conducted to examine the thermal behaviour of the martensitic transformation. This technique is based on the detection and quantification of the exothermic and endothermic phenomenon of a specimen being tested.

The instrument is made of two resistors and two crucibles: the specimen to be analysed are inserted into one of the crucibles, and both crucibles are connected to the thermocouples. The components are connected to a computer.

The quantities of a specimen required for analysis are generally a few milligrams, and the velocity of heating and the cooling rate depends on the ability to operate the instrument used. The DSC measures the difference of the heat flows in the specimen and the reference while both are under the same program-controlled temperature. For this experiment, a specimen of weight 5–l0 mg was heated up to 400 °C and then cooled to 0 °C, with a cooling/heating rate of 10 °C/min. The cooling agent used in the DSC was liquid Argon.

The DSC test was carried out at Iran Polymer and Petrochemical Institute-Tehran, Iran. The device used was type NETZSCH DSC as shown in Figure 3.14.

Figure 3.14: DSC equipment

3.8. Heat Treatment for Shape Memory Effect

In order to obtain shape memory effect, which is determined by cold working, Brinell hardness indenter was used. The temperature used was 200 °C for 1 hr [129], which is the Af (austenite finish temperature). This temperature is used according to the DSC test result. This heat treatment was done for all specimens after aging heat treatment.

3.9. Shape Memory Effects

The shape memory effect can be determined from the Brinell impression using Brinell hardness test with load 31.25 Kg and holding time 10 sec [129]. The test was done for all sintering specimens. The heat treatment temperature used

was 200 °C and it was estimated from the DSC test result. The diameter of the ball impression before and after the heat treatment was determined using Brinell hardness device, as shown in Figure 3.15. The shape memory effect can then be calculated from the equation below [129].

Shape memory effect (SME%) $= \frac{Db - Da}{Db} \times l00\%$ .....(3-1)

Da = diameter of impression in µm (after heat treatment for shapes memory effect).

Db = diameter of impression in µm (before heat treatment for shape memory effect).

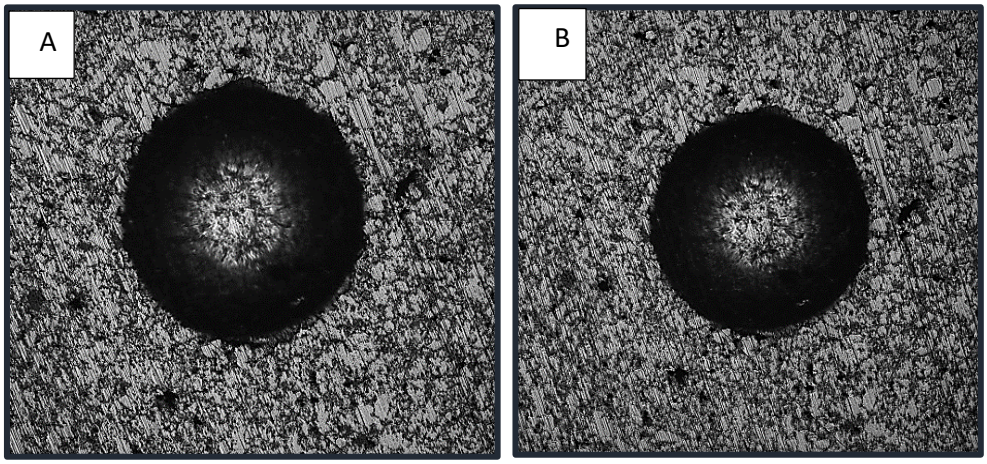

Figure 3.15: Macrostructures of Cu-Al-Mn shape memory alloy A) before shape effects heat treatment and b) after heat treatment

3.10. Green Porosity and Density

The green density of Cu-Al-Mn and Cu-Al-Mn- x% X(Ta, Zr, In, and Y_2O_3) were calculated by measuring the dimensions of the specimen after compacting, weighing the specimen and using the following relationship [116]:

$$\rho g = \frac{Mg}{\boldsymbol{Vg}} \ldots\ldots\ldots\ldots\ldots\ldots\ldots\ldots\ldots (3-2)$$

ρ_g: green density of sample in (g/cm^3)

M_g: mass(g).

V_g: volume (cm^3)

The green porosity calculation of the samples was obtained by estimating the theoretical density of the mixture (Copper, Aluminium, Manganese, Tantalum, Zirconium, Indium powder, and yttrium oxide ceramic powder) and using the following Eq. (3-3):

$$p\,g = 1 - (\frac{\rho\,g}{\rho\,th}) \times 100 \ldots\ldots\ldots\ldots\ldots\ldots\ldots\ldots\ldots\ldots (3-3)$$

where P_g is the green porosity of the sample, and

ρ_{th} is the theoretical density of the mixture (g/cm^3).

The theoretical density of alloys is determined by their percentage ratios, according to the following relationship [116]:

$$\rho_{th} = (W_1\% * \rho_1 + W_2\,\% * \rho_2 + W_2\,\% * \rho_3 + \ldots\ldots\ldots\ldots) \ldots\ldots\ldots\ldots\ldots (3.4)$$

where

$\rho_1, \rho_2, \rho_2, \ldots..$ are the theoretical density

$W_1, W_2, W_3, \ldots\ldots.$are the weight percentage of powder.

3.11. Final Density and Porosity

Since density is mass/volume, the precise method to measure the volume of water displaced by the immersed objects is Archimedes principle. The density and porosity of sintered part are calculated according to ASTM- B 328-96 [116]:

i. The specimen is dried using temperature up to 100 °C for 6 hrs in argon atmosphere and then cooled to room temperature. The weight of the dry specimen is measured as mass A.

ii. At room temperature, using a suitable vacuum pump, the pressure was reduced over the immersed specimen in oil with a viscosity of 22 cst at 37 °C for no more than (7kPa) pressure for 30 min. By weighing the fully impregnated sample in air, mass B was found.

iii. Weigh the fully impregnated specimen in water (Mass F).

For this study, the temperature was 30 °C, and the density of water (ρW) at this temperature was 0.9956 g/cm^3. Density (ρ) is computed according to the following equation [116]:

$$\rho = \left(\frac{A}{B-F}\right) * \rho w \quad \text{.....(3.5)}$$

and the porosity can be measured by

$$P = \left[\frac{B-A}{(B-F)D_o} \times 100\right]\rho w \quad \text{.....(3.6)}$$

where ρ_o = density of oil g/cm^3 =0.7702 g/cm^3

3.12. Microstructural Characterization

3.12.1. X-ray Diffraction (XRD)

Crystal structures and phases of the alloys were determined using X-ray diffraction device types (Shimadzu XRD-6000 X-Ray diffractometer) in the Ministry of Science and Technology Baghdad Governate, Iraq. X-Ray diffraction identification of all phases with crystal structure and lattice parameter and angles. X-Ray diffraction using radiation CuKα with wavelength (λ = l.5409 A) 40 KV, 30 mA at room temperature, and angles starting and finishing at 2θ = 20°–80° range were indexed by comparison with the standard charts.

3.12.2. Scanning Electron Microscope Observation (SEM)

Scanning electron microscope observation was used to reveal the microstructures of etched specimen for quenched and aged conditions of the base alloy and for higher addition amounts of Ta, Zr, In, and Y_2O_3. The images were captured with different magnification power. This test was conducted in Lab. Razi Metallurgical Research Center, Iran using SEM model (TESCAN S8000, USA).

3.12.3. Optical microstructure

An optical Microstructure test was done for sintered and aged specimen with different magnification power (100X, 200X, 400X, 800X) using light optical microscope type 1280 XEQMM300TUSB. The photos were captured using high-resolution camera fixed on the microscope as shown in Figure 3.16.

The specimens were prepared as following for optical microstructure:

1. Grinding using sheets of SiC: l80, 400, 600,800 and l000 grade.
2. Polished using diamond (grain size l μm) on a polishing wheel cloth and washed in water and dried in warm air. The tests were carried out to the sintered and aging heat-treated specimen of 12 mm diameter and 5 mm thickness. These specimens were then cleaned with water and alcohol, and then dried with hot air.
3. The specimens were then etched with etching solution (2.5 g $FeCl_3$ and 48 ml methanol in 10 ml HCl) [130].
4. After that, the specimens were ready for microscopic observation analysis.

Figure 3.16: Specimen used for microstructure observation

3.13. Microhardness Measurement

Vickers hardness was achieved to understand the effect of the alloys elements and heat treatment on the Cu-Al-Mn shape memory alloys. A digital microhardness tester (Type TH7l5, Beijing, Time High Technology ltd) is shown in Figure 3.l7. The amount of load was about 500 gm for 15 seconds at a regular distance of 0.25 mm [129].

For the microhardness test, the specimens were prepared as follows:

1. Grinded using sheets of SiC: l80, 400, 600,800 and l000 grade.
2. Polished using diamond (grain size l μm) on a polishing wheel cloth and washed in water and dried in warm air. The tests were carried out to the sintered and aging heat treated specimen of 12 mm diameter and 5 mm thickness. The hardness was recorded as an average of five readings for each specimen.

Figure 3.17: Micro hardness device

3.14. Erosion/Corrosion Test

Erosion is a mechanical process, like the removal of part of the material from the surfaces because of the collision or gases and liquid effects. The erosion-corrosion apparatus was designed during this study depending on ASTM G 73-98 as shown in Figure 3.18.

The tank's diameter is 30 cm and height is 50 cm. The corrosion media were delivered directly at high pressure in vertical direction of the specimen through a jet nozzle with d = 0.75 mm by a pump that sucks the different media from a plastic tank (chamber) with ¾ horsepower, single-phase electric motor made from Teflon (chemical pump), with the distance between the sample and nozzle being 10 mm. The chemical pump is resistant to the slurry and chemical solution.

The pipe joints and valves connected to the chamber with chemical pump are made from PVC plastic [150].

All alloys' examined temperature was 25–30 ^{o}C wherever 3.5% NaCl (seawater) caused erosion-corrosion, falling from the nozzle at an angle of 90° (the impact angle between the line of water and surface of specimen).

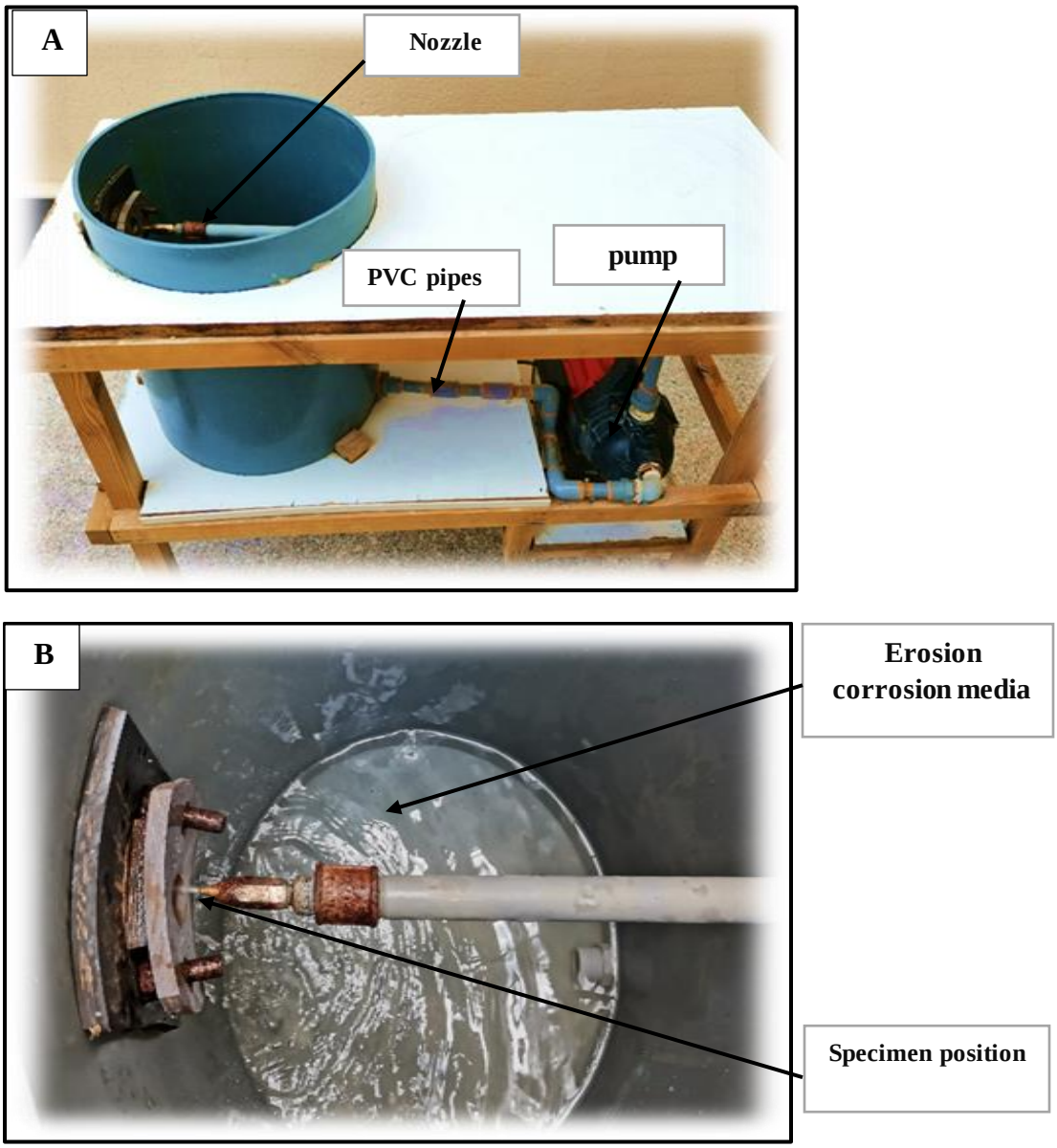

Figure 3.18: (A)The erosion-corrosion device, (B) Jet nozzle

It is possible to calculate the change in weight and then get the erosion rate according to equations 3.7 and 3.8.

$Change\ in\ weight\ (\Delta w) = original\ weight\ (wo) - weight\ after$ corrosion ……(3.7)

$$Erosion\ rate\ \left(\frac{mg}{hr.cm2}\right) = \frac{\Delta W}{time\ of\ exposure\ *\ Area} \ldots\ldots\ldots\ldots\ldots (3.8)$$

The chamber was filled with 3.5% natural salt/litre of water. The particle size for salt was 3.908 μm, and the chemical composition for salt is shown in Table 3.4 (tested in Iran- instrument model:PW41X0L00).

Table 3.4: Chemicals composition for salt that was used in the test

Elements	**Si**	**Fe**	**Mn**	**Mg**	**Sn**	**Co**	**Sb**	**Na**	**Al**	**Cl**
Percent%	0.052	0.334	0.021	0.010	0.006	0.003	0.006	38.628	0.124	59.621

3.15. Electrochemical Tests

3.15.1. Open circuit potential

Open-Circuit Potential (O.C.P), also known as equilibrium potential, is the potential of an electrode measured with respect to a reference electrode in the absence of current (under open-circuit conditions) according to ASTM G3-l4. It is simply a valuable technique that determines the potential difference between the working (specimen) and a reference electrode. The O.C.P. (voltage versus time) was recorded every five minutes for a specimen in the corrosion solution. The potential was measured of open circuit potential (OCP) as a function of time till steady-state potentials.

3.15.2. Linear Polarization Test

A corrosion cell consists of the working electrode, which is CuAlMn –X (Ta, In, Zr, and Y_2O_3), with three different weight percentages. The reference electrode used in this study was the saturated calomel electrode (SCE). The auxiliary electrode used in the electrochemical cell was platinum. The working electrode (W.E) was the specimens. The linear polarization was carried out according to ASTM G5-94 [117].

A 1-liter beaker consisting of working, counter, and reference electrodes as shown in Figure 3.19 – a magnetic stirrer (type Heidolph, MR Hei Standard\W-Germany) – was used. Constant potentials (anodic or cathodic) were imposed on the specimen using the potentiostat (lIDA INSTRUMENT-Germany). This potentiostat can induce constant potentials ranging from (± l V), which is the potential of the standard calomel electrode (SCE) used in this study.

Linear polarization tests were used to obtain the microcell corrosion rates. In the tests, cell current readings were taken during a short, slow sweep of the potential. The sweep was taken from (± 250) mV relative to open circuit potential (OCP). The scan rate defines the speed of potential sweep in mV /sec. In the above range, the current density versus voltage curve is almost nearly linear. A linear data fitting of the standard model gives an estimate of the polarization resistance, which is used to calculate the corrosion current density (i_{corr}) and corrosion rate.

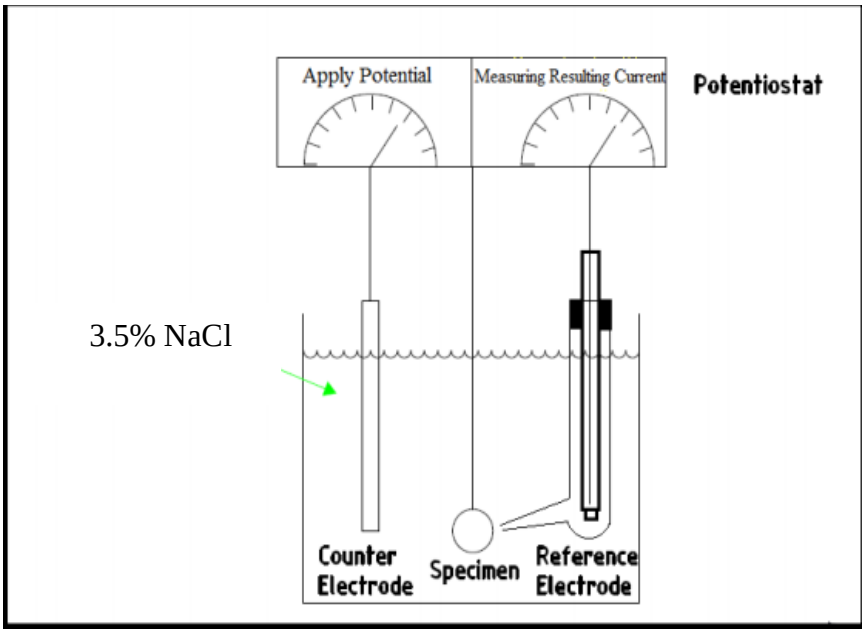

Figure 3.l9: The schematic diagram of electrochemical system.

The general equation applied for the determination of corrosion rate by current density in solution on the alloy during electrochemical reactions are [159, 160]:

$$\boldsymbol{corrosion\ rate\ (mpy) = \frac{0.13 * I\ corr * (E.W)}{\rho}} \text{.....(3.9)}$$

where, 0.13 = metric and time conversion factor.

Icorr = density of the corrosion current (μA/ cm²).

E.W = equivalent weight.

ρ = density of alloy (g/cm³).

mpy = Corrosion rate (mils per year).

3.16. Damping Capacity Measurement

ASTM E756-05 provides a test method for measuring the vibration-damping properties of materials including Young's modulus (E) or the shear modulus (G) [111].

A simple experiment to investigate the damping properties of the specimen was done by generating the free vibration on the specimen and then recording it using a sensor as shown in Figure 3.20B. The researchers should keep the surroundings quiet during testing because the sensor is very sensitive to external sounds and vibrations. Damping capacity was done for sintered and aged specimens using Accelerometers national instrument, as shown in Figure 3.20A.

The specimen was placed in a clamped position (a plastic base part No.1 which contains an aluminium base with an inner diameter of 14 mm and an outer diameter of 17 mm as shown in Figure 3.21, in which the specimens were placed, and a plastic tube part No. (2) to be installed directly above the specimen to be tested, through which a metal ball was dropped. Furthermore, a metal ball was dropped to generate a free vibration on the specimen, which was recorded by a sensor installed on the free side of the specimen connected by Accelerometers national instrument.

The Accelerometers were connected by a LabView soft program installed in the computer to convert the form of vibration data from analogue into digital signals and to transform them into frequency domain.

The test was conducted at the University of Babylon College of Engineering/Department of Mechanical Engineering.

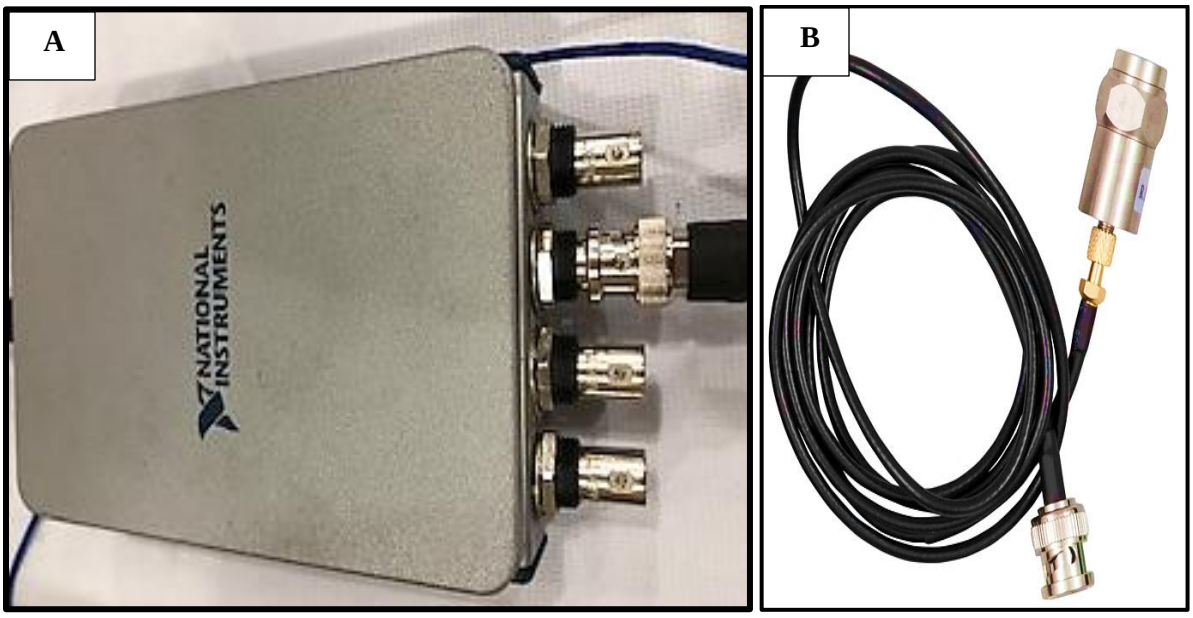

Figure 3.20: (A)Accelerometers national instrument, (B) Vibration Sensor

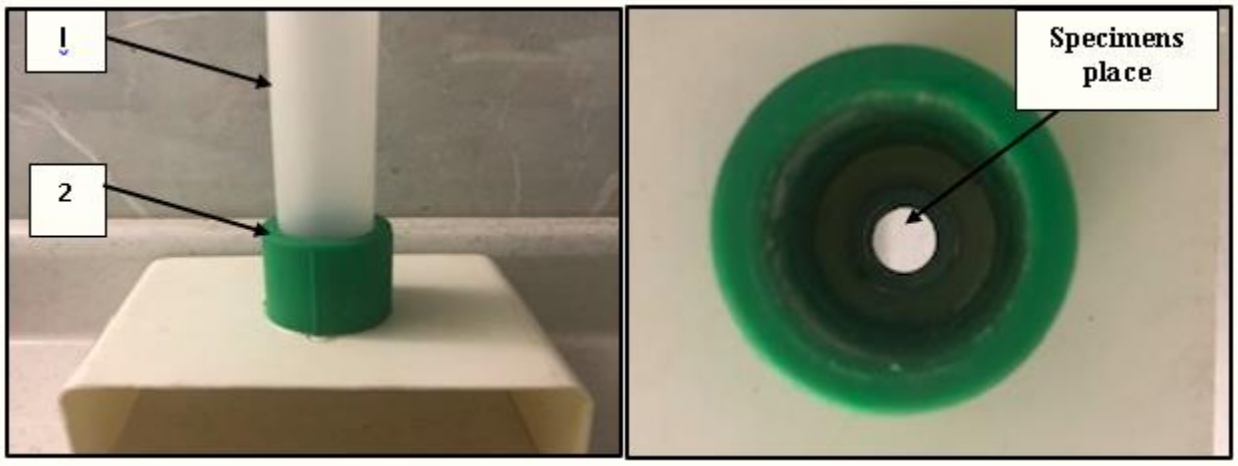

Figure 3.21: Specimen's holder

The damping properties of the beam are expressed by damping ratio (ξ), which can be identified by analysing the wave using the logarithmic decrement (δ) [111].

Chapter 4

Results and Discussion

4.1. Introduction

In this chapter, the experimental results of this study are discussed in consecutive forms. The experimental results include some physical and mechanical properties. Physical properties such as particle size analysis, apparent density and apparent porosity before and after sintering. While, mechanical properties include the microhardness, and damping capacity of each CuAlMn-X (Ta, Zr, In, and Y_2O_3) shape memory alloys. Electrochemical tests results after sintering and after the aging heat treatments have been presented and microstructures (optical and SEM). The results of all tests are presented below.

4.2. Physical Properties Tests

4.2.1. Apparent Density of Powders

Apparent density of elemental powders and ceramic powder (weight per unit volume of powders) used to prepare mixtures of alloys have been measured and shown in Figure (4.1).

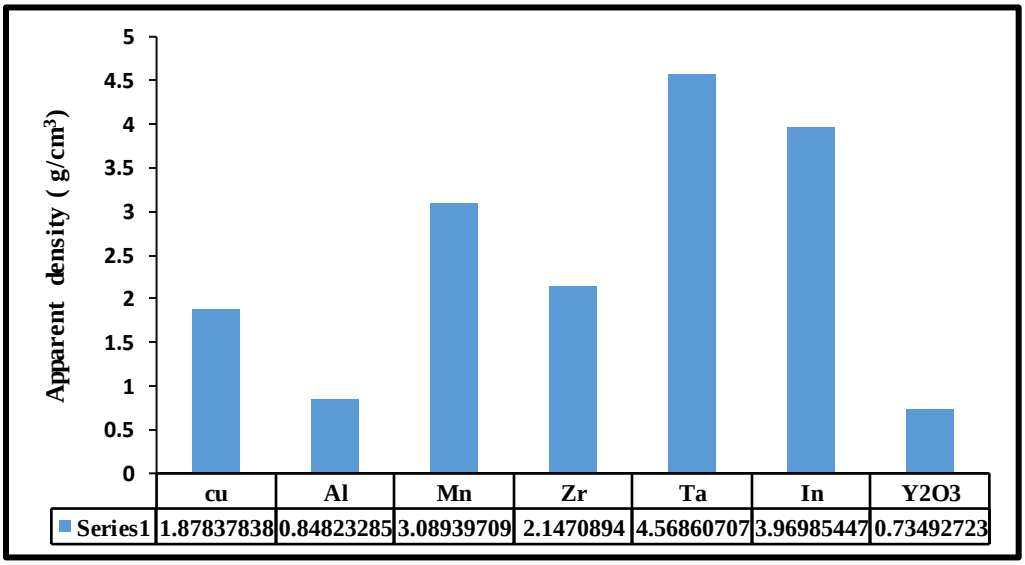

Figure (4.1) Apparent density of powders

The apparent density of Tantalum (4.56 gm/cm^3) and Indium (3.96 gm/cm^3) is the highest density compared with other powders due to the high density of the solid material for both. Factors affect apparent density such as particle size and its distribution, surface area, particle shape, the roughness of individual particles, and particle arrangement as well as the density of the solid material. Apparent density is controlled by mixing various sizes of particles and the measured apparent density of powders [119].

4.2.2. Compacting Pressure, Green Density and Green porosity

Different compacting stresses have been taken in order to determine the best compacting stress that can be applied to compact all alloys. The test has been done for alloy (A).

The green density increases with increasing compacting pressure from 600 MPa to 800 MPa Jassim Salman et. al. [120] as shown in Figure (4.2).

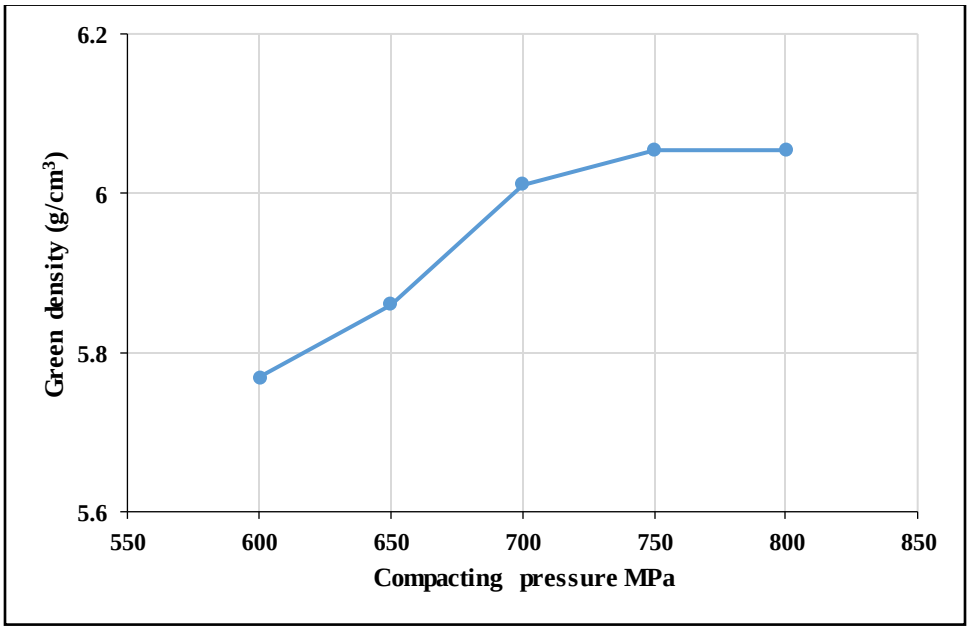

Figure (4.2) Green density-compacting pressure relation for base alloy A

Three stages occur during the compaction process the first stage powder particles are rearranged. In the second stage, elastic and plastic deformation of the particles have been taken place [120].

Green porosity has been shown in Figure (4.3) for green compacts for base alloys. With the increasing compacting pressure, the density of the powder mass increases because the total amount of porosity in the mass decreases.

The best compacting stress can be determined by evaluating the maximum green density as well as lowest green porosity in the point in which any increase in compression stress doesn't lead to increase green density and decrease green porosity as shown in Figure (4.3).

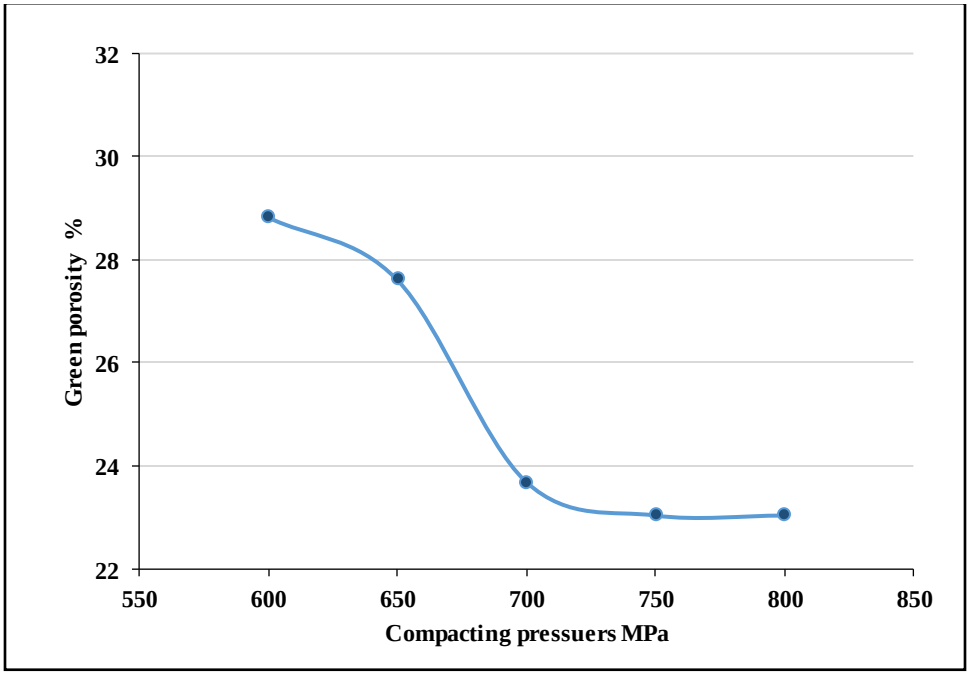

Figure (4.3) Green porosity-compacting pressure relation for base alloy A

From the Figures (4. 2-3) it can be seen that the best compacting pressure 750 MPa. Which gave the maximum green density as well as lowest green porosity.

4.2.3. Effect of Ta, Zr, In and Y_2O_3 on Green Density

The effect of the Tantalum addition on the green density (density before sintering) of CuAlMn alloy is shown in Figure (4.4). The green density increasing with increasing the percentage of the added Ta. This is due to the high density of Ta element (4.56 gm/cm^3) compared to Cu (1.87 gm/cm^3).

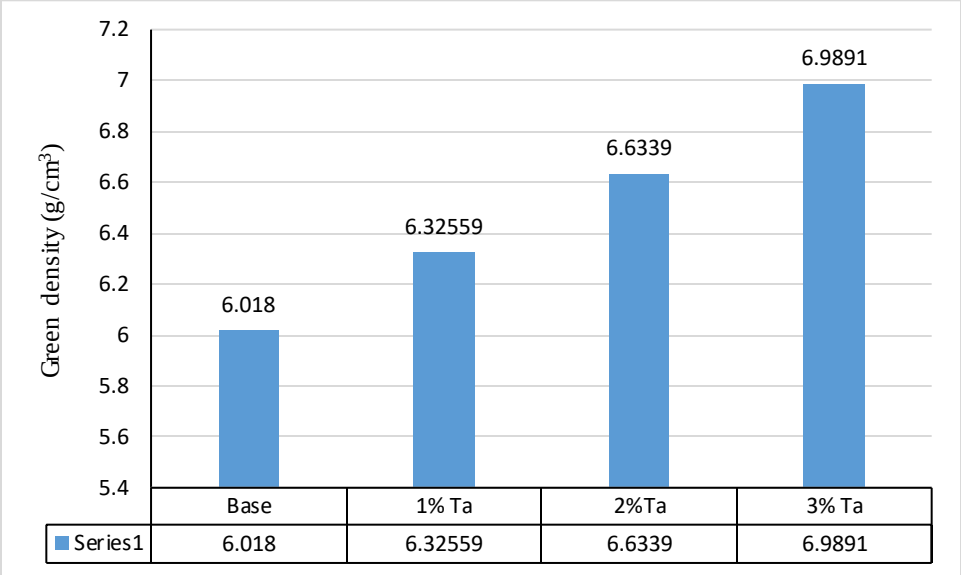

Figure (4.4): Effect of Ta on the green density of CuAlMn SMAs

The effect of the Indium addition on the green density of CuAlMn alloy is shown in Figure (4.5). The green density increasing with increasing the percentage of the added Indium. This is due to the high density of In element (3.96 g/cm^3) compared to Cu (1.87 g/cm^3).

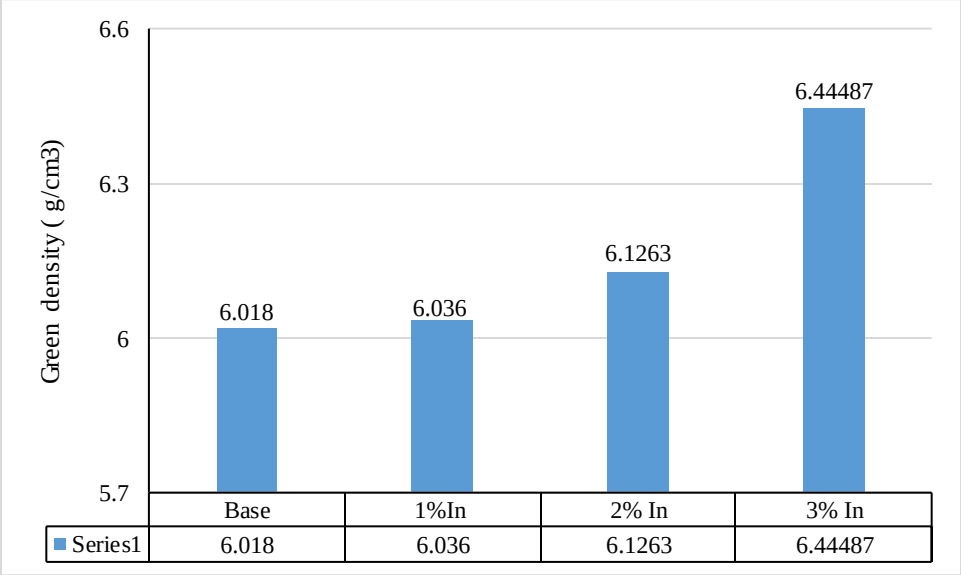

Figure (4.5): Effect of Indium on the green density of CuAlMn SMAs

The effect of the Y_2O_3 addition on the green density of CuAlMn alloy is shown in Figure (4.6). The green density decreases with increasing the percentage of the added Y_2O_3 powder as the density of Y_2O_3 (0.73 gm/cm^3) compared to Cu (1.87 gm/cm^3).

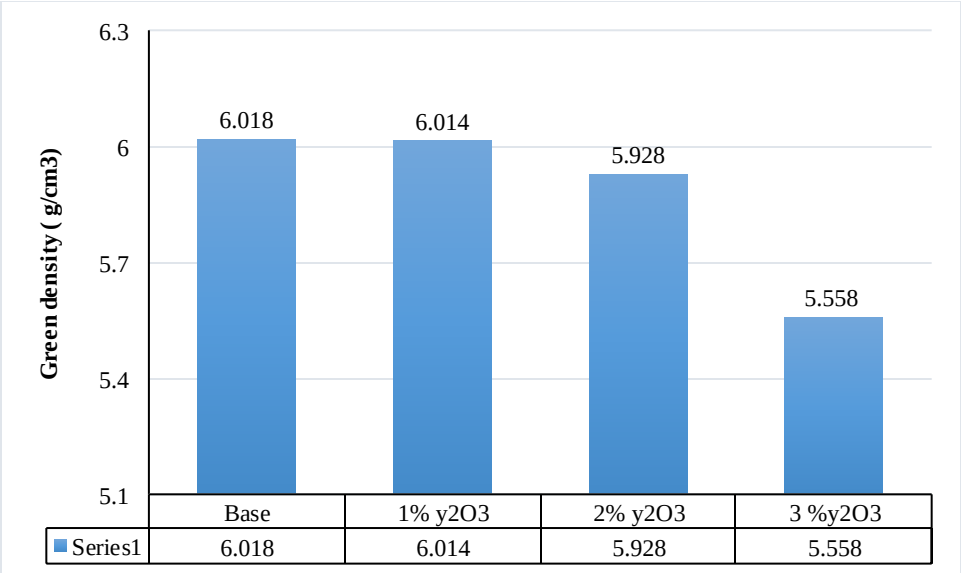

Figure (4.6): Effect of Y_2O_3 on the green density of CuAlMn SMAs

The effect of the Zirconium addition on the green density of Cu-Al-Mn alloy is shown in Figure (4.7). The reason for the increasing of the green density is due to the relatively high density of the Zirconium addition (2.14 g/cm^3).

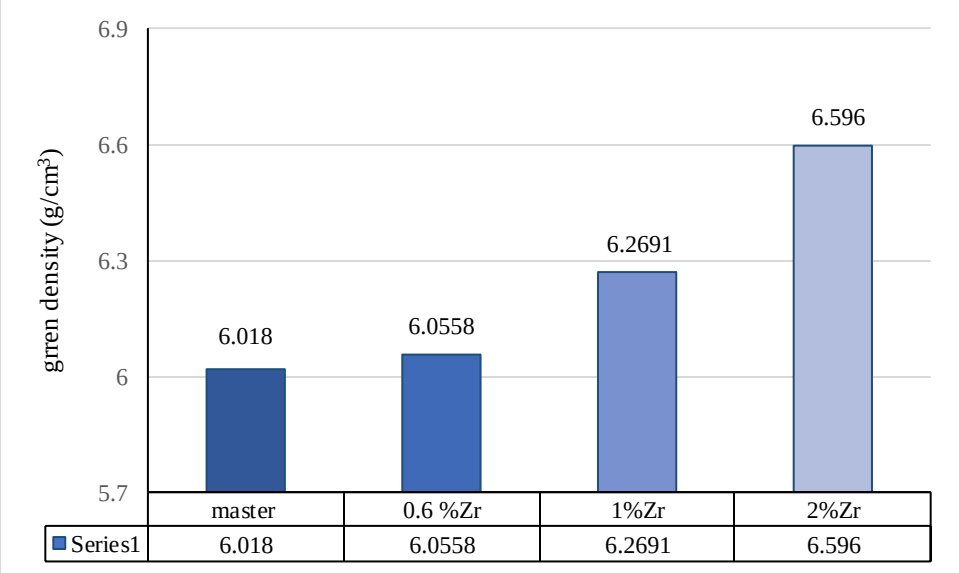

Figure (4.7): Effect of Zr on the green density of CuAlMn SMAs

4.2.4. Effect of Ta, Zr, In and Y_2O_3 on Porosity of Cu-Al-Mn Shape Memory Alloys after Sintering

The effect of Tantalum, Zirconium, and Y_2O_3(ceramic particles) on the porosity after sintering of the Cu-Al-Mn shape memory alloys shows in Figures (4. 8-11). These additives have a clear effect on the final density of CuAlMn. As they (Ta, Zr, Y_2O_3) decrease in the final porosity values of the alloy. The difference in particle size of element as shown in Table (3.1) (4.827, l9.38, l9.09 µm) for Cu, Al, and Mn respectively, while (11.74, 14.23, 14.23 µm) for Ta, Zr, and Y_2O_3 respectively. The small particle enters between vacancy between the largest practical and cause reduce porosity in alloy.

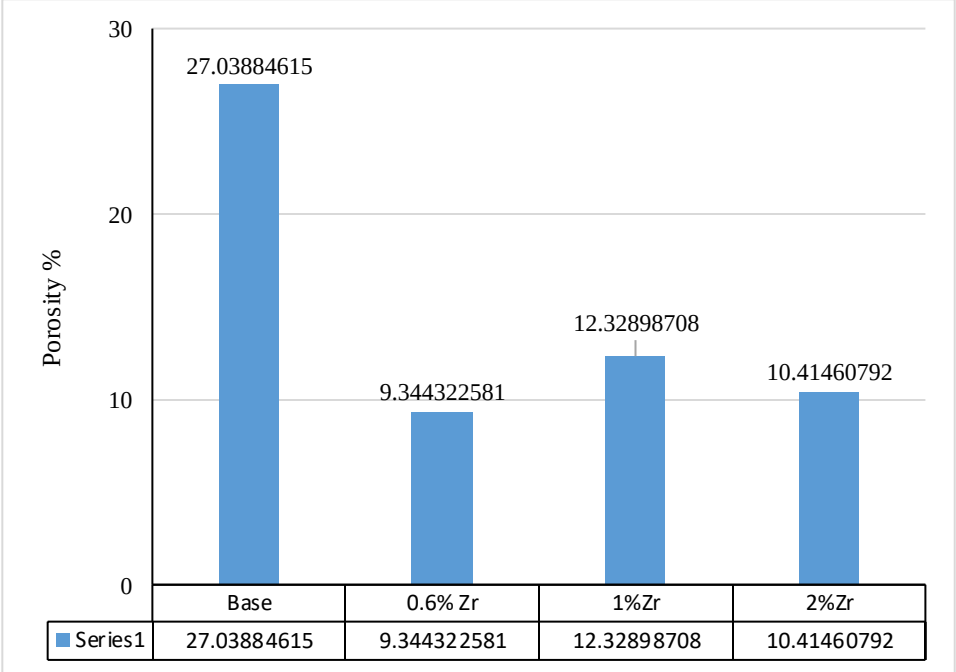

Figure (4. 8): Effect of Zirconium on the porosity of CuAlMn

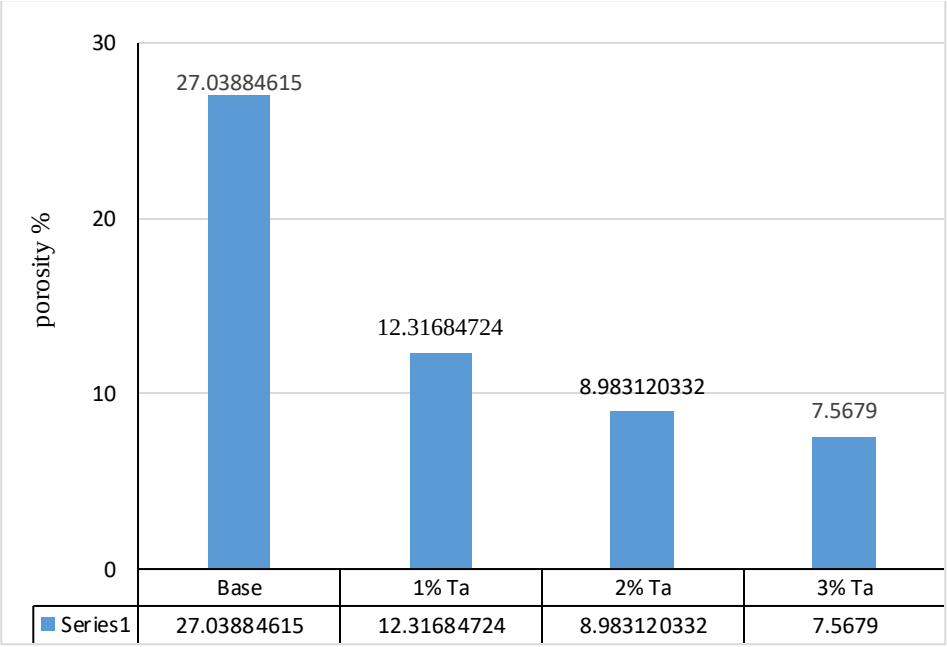

Figure (4.9): Effect of Tantalum on the porosity of CuAlMn

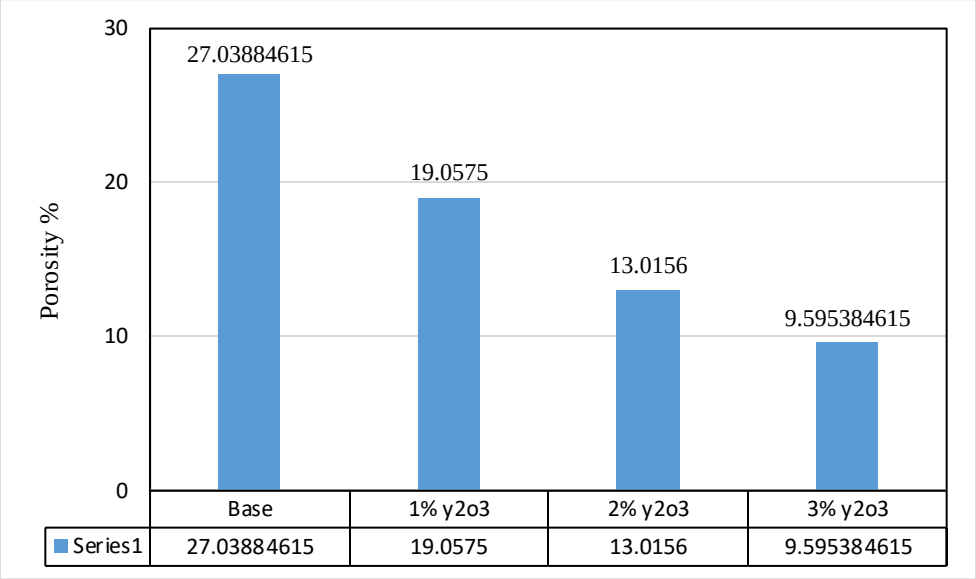

Figure (4.10): Effect of Y_2O_3 on the porosity of CuAlMn

As for Indium, the porosity after sintering has decrease when addition % In element from (1 to 3)% wt.. The final porosity values of the CuAlMn shape memory alloys as shown in Figure (4.11).

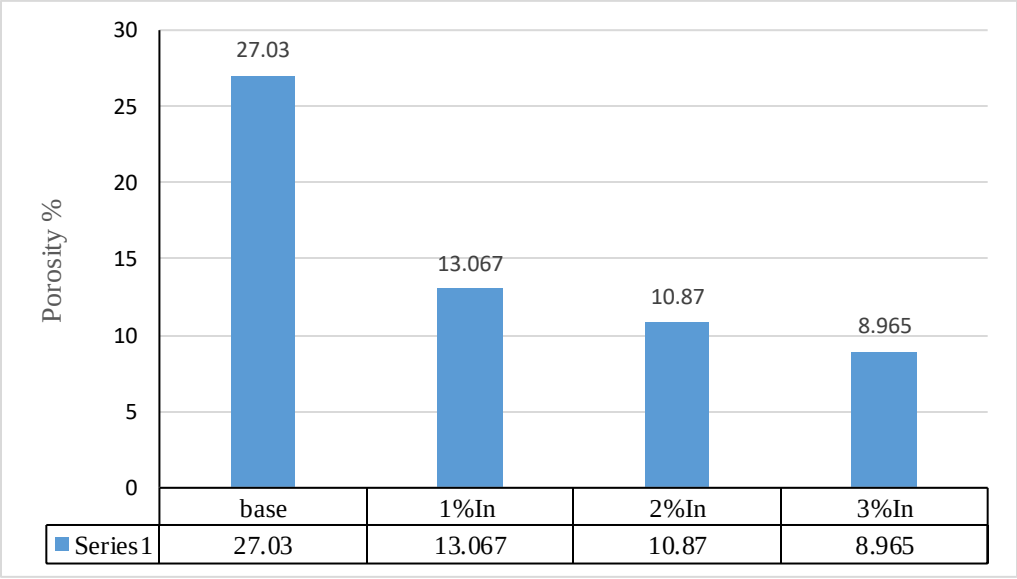

Figure (4.11): Effect of Indium on the Porosity of CuAlMn

4.2.5. Effect of Ta, Zr, In and Y_2O_3 on Density after Sintering of Cu-Al-Mn Shape Memory Alloys

The effect of Tantalum, Zirconium, Indium and Y_2O_3 on the density after sintering of the Cu-Al-Mn shape memory alloys have been shown in Figures (4.12-15).

From the results of the density values (after sintering), we notice an increase in the density value with an increase in the percentage of Tantalum from (1-3) % wt. as show in Figure (4.12). As Tantalum can be diffusion into the Cu lattice to form a supersaturated Cu rich solid solution and produce a grain refinement. The result agrees with K. A. Darling et. al. [121].

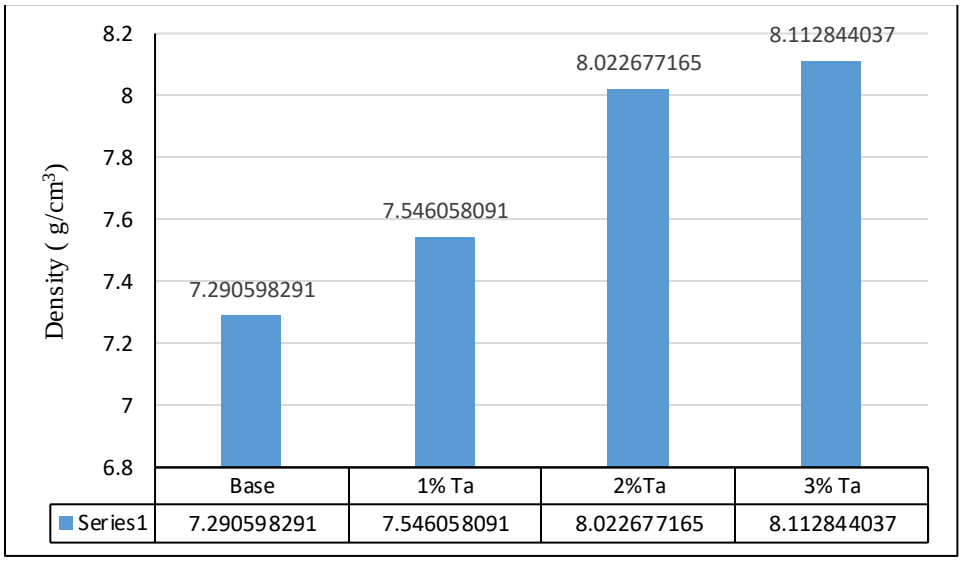

Figure (4.12): Effect of Ta on the density of CuAlMn

When adding Zirconium, the density value increases and the highest density value was at 1% Zirconium, then decreased when adding a higher percentage of Zirconium 2% as show in Figures (4.13).

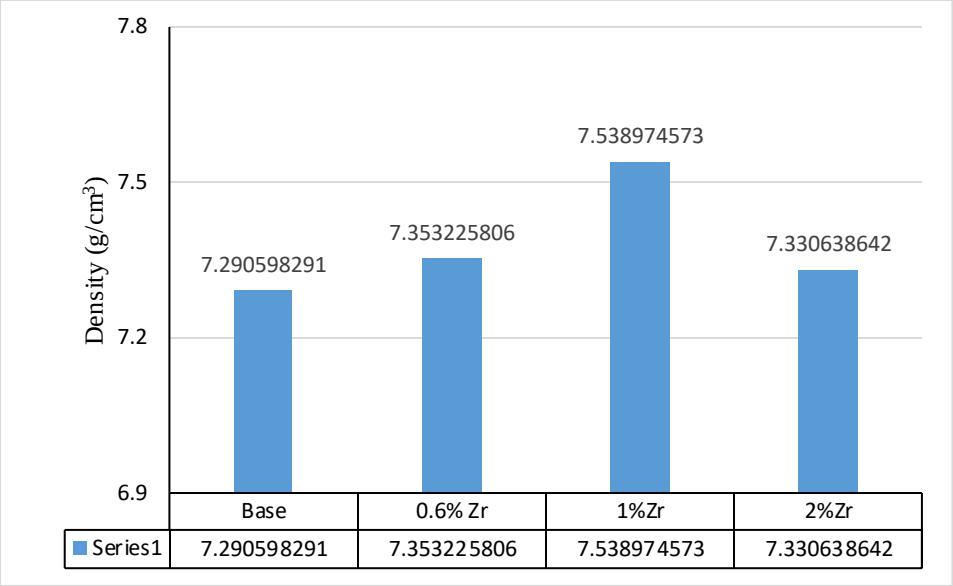

Figure (4.13): Effect of Zr on the final density of CuAlMn

As for the behavior of the alloy when adding Y_2O_3 as show in Figure (4.14) we notice an increase in the final density values (7.43, 7.58 and 8.23) g/cm^3 with an increase in the percentage of Y_2O_3 from (1 to 3) % wt. respectively. The increase in density after sintering regarded to reduction in porosity.

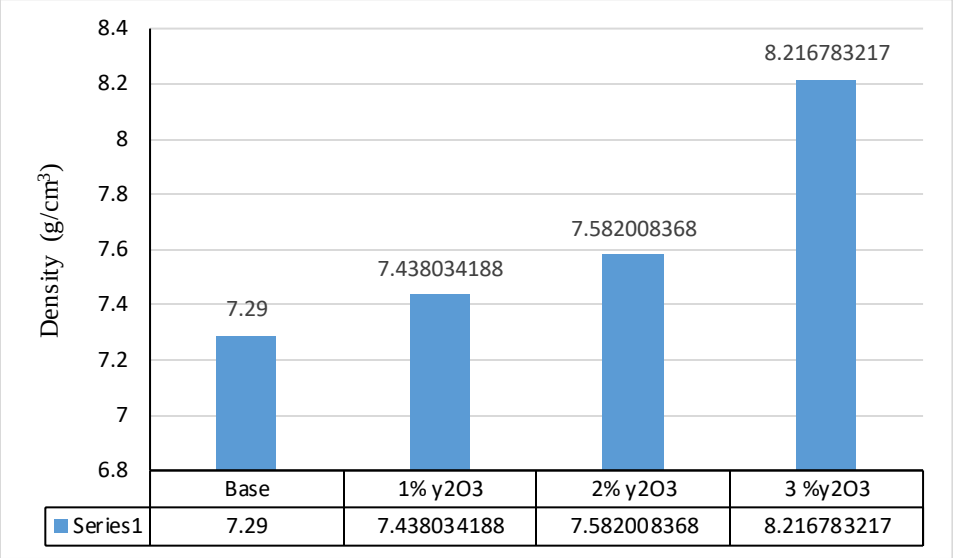

Figure (4.14): Effect of Y_2O_3 on the density of CuAlMn

While with regard to Indium, we notice increase the density values (7.48,7.86 and 7.90) g/cm^3 with an increase in the element's percentage from (1 to 3) % wt. as shown in Figure (4.15).

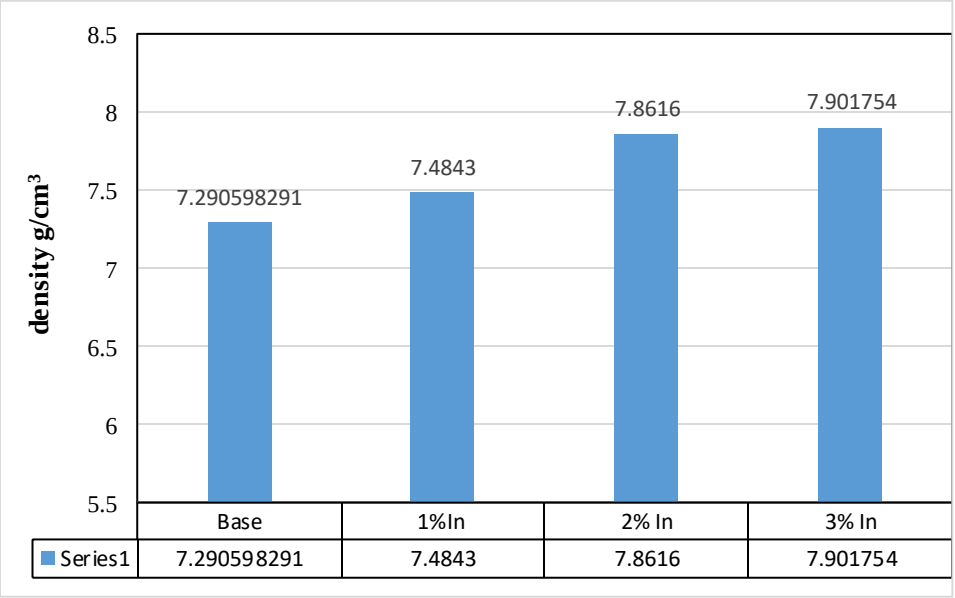

Figure (4.15): Effect of In on the density of CuAlMn

4.3. X-Ray Diffraction

The X-ray diffraction analysis has been used for compacted, sintered, and Aged specimen, and the results of X-Ray diffraction have been shown in the followings:

4.3.1. X-ray Diffraction Patterns for Compacted Green Sample

XRD results of compacted green alloys have been presented. X-ray diffraction test has been done for compacts alloy (A) as shown in Figure (4.16).

The X-ray peaks for the elements depend on the intensity, and theta degree. In Figure (4.16) represents the X-ray diffraction patterns for compacts which appear the peaks for Copper, Aluminum, and Manganese. Aluminum appears in 2θ= (38.8, 45.042, 65.62) while Copper in 2θ= (43.94, 51.020, 74.66), Manganese exists in (43.94 ,45.3, 50.6).

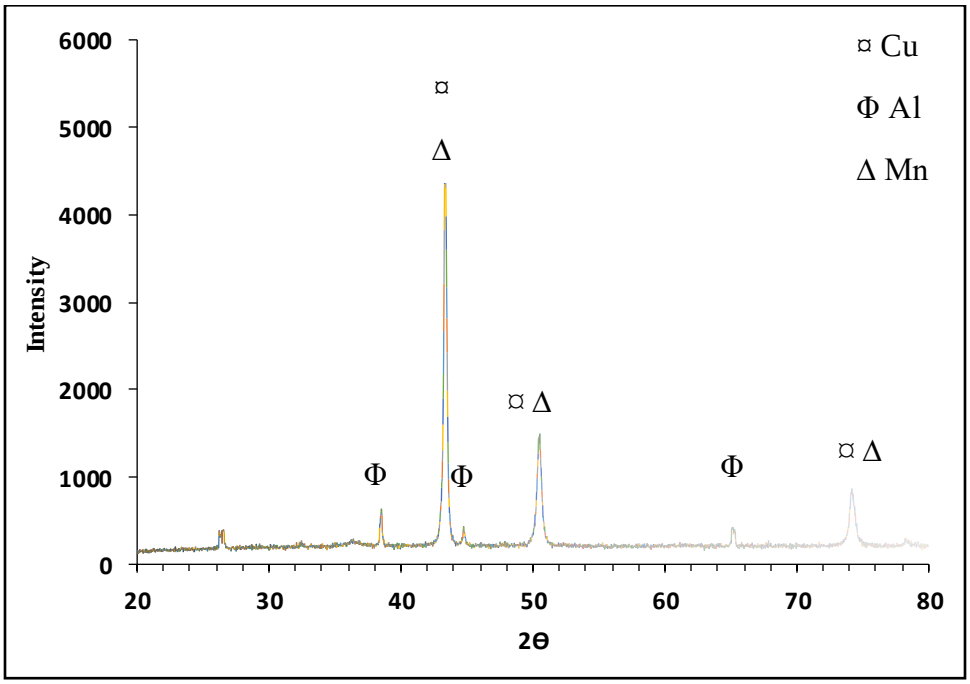

Figure (4.16) :X-ray diffraction for compacted sample A

4.3.2. X-ray diffraction Patterns for sintered specimens

XRD results of sintered green alloys Cu-8%Al-9%Mn and CuAlMn-X (Ta, In, Zr and Y_2O_3) at 950 °C have been presented in Figure (4.17).

Three phases were observed, namely α-Cu, γ-Al_4Cu_9 and β- Cu_3Al. Similar X-ray diffraction patterns result were obtained for Guofei Zhanga et. al. [122].

From Figure (4.17) it was seen that the formation of phases indicates the form of the Cu- α solid solution and β phase. There was no change observed in the phases observed in result with additives. The XRD is not sensitive to compounds form by the addition of Ta, Zr, In, and Y_2O_3 as it not sensitive to an amount less than 6%.

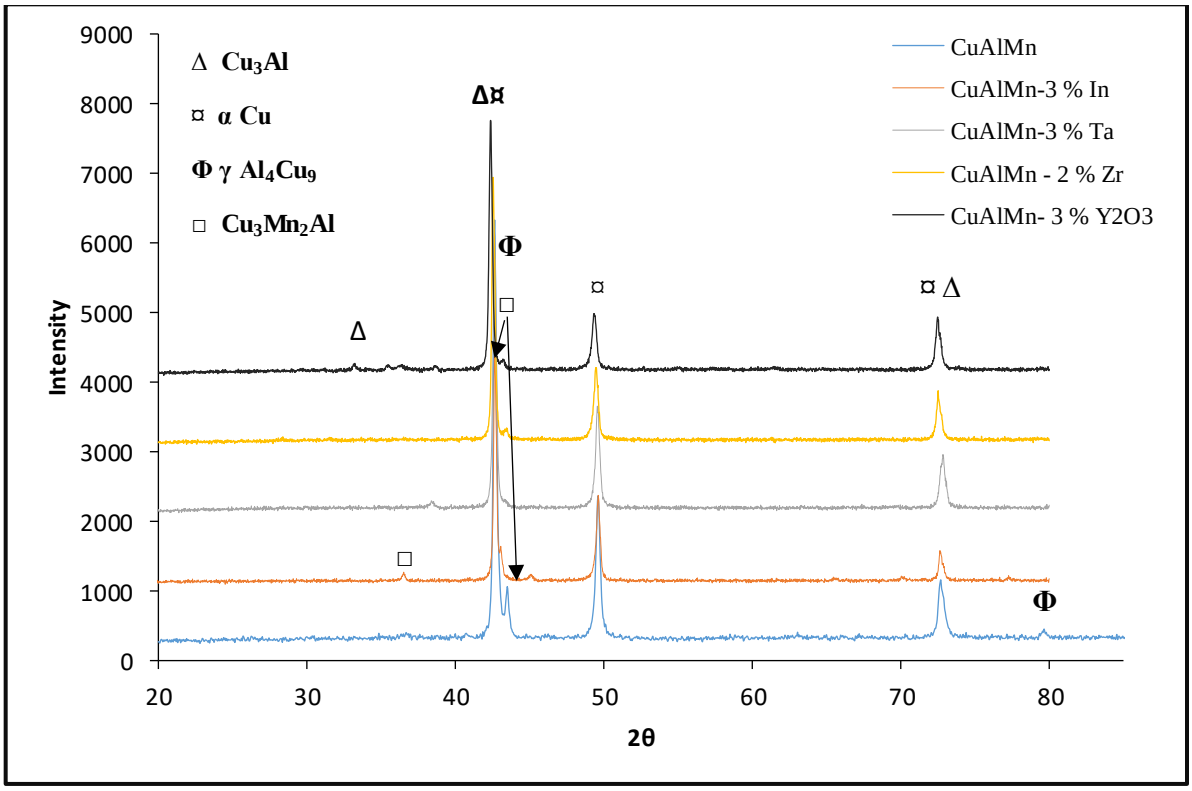

Figure (4.17) :X-ray diffraction for sintered specimens (A, B3, C3, D3, E3)

4.3.3. X-ray Diffraction Patterns for Quenched Specimens

The different types of martensite formed in the alloys were determined by X-ray diffraction analysis of the polycrystalline specimens. The X-ray diffraction patterns of the alloys (A, B3, C3, D3, and E3) after solution and quenching heat treatment are shown in Figure (4.18). The peaks in the patterns were identified based on literature U.S. Mallik and V. Sampath [110] and Jiao Yu, et. al. [124]. The variation in the intensity of the diffraction peaks of martensite phase depends on the extent of austenite to martensite transformation. Here, it can be concluded that the addition of Tantalum, Indium, Zirconium, and Y_2O_3 are not significantly affect XRD patterns. There was no change observed in the type of martensitic phase with additives, but the thickness of the martensite plate decreased, As can be seen from Figure (4.17). The main diffraction peaks observed at room temperature belong to M 18R (β̀1 martensite). In all the alloys β̀1 (Cu_3Al) martensite are present [52,53,125]

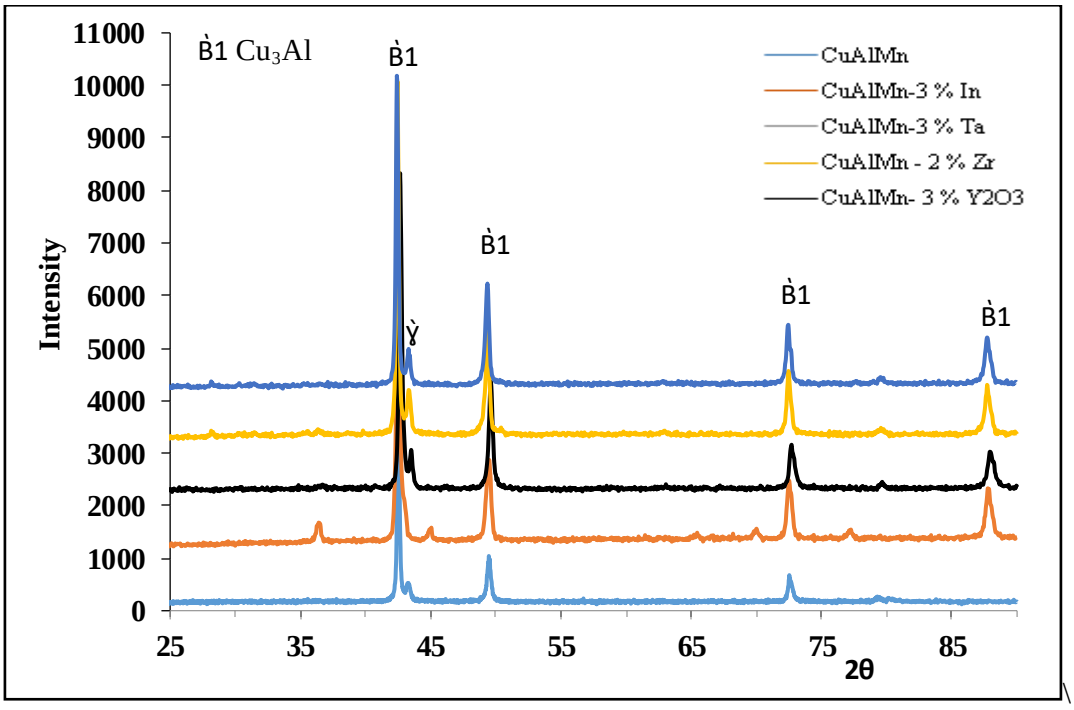

Figure (4.18) :X-Ray diffraction for aged specimens (A, B3, C3, D3, E3)

4.4. Light Optical Microscope (LOM) Observation of the Alloys

The microstructure image of the alloys A, B1, B2, E3 have been taken by light optical microscope in sintered and aged conditions as shown in Figures below.

4.4.1. Light Optical Microscope after Sintering

The morphology transition in the microstructure of green compact to that of sintered compacts is a function on sintering time and temperature. The most common types of features in the microstructures in metallic materials are the boundaries between crystalline grain s and/or the boundaries between different solid phases in multiphase alloys.

Figures (4.19-22) show the microstructures of the alloy, it has been shown that the two-phase morphology (α+β) without any appearance of the martensitic plates. Phase (α) were existing as (FCC primary solid solution of Cu) the (α) phase is represented by the bright areas in the microstructure. While the (β) phase is represented by the dark areas in the microstructure. The porosity after the sintering process is low and the pores were small and this will lead to better properties for shape memory alloy [50].

Figure (4.19 A-D) shows the microstructure of alloys CuAlMn-x % In (1, 2, and 3) wt%. after sintering. The Indium additions will be at grain boundaries, make the grains of (α) phase small gradually with increasing Indium percentage [126].

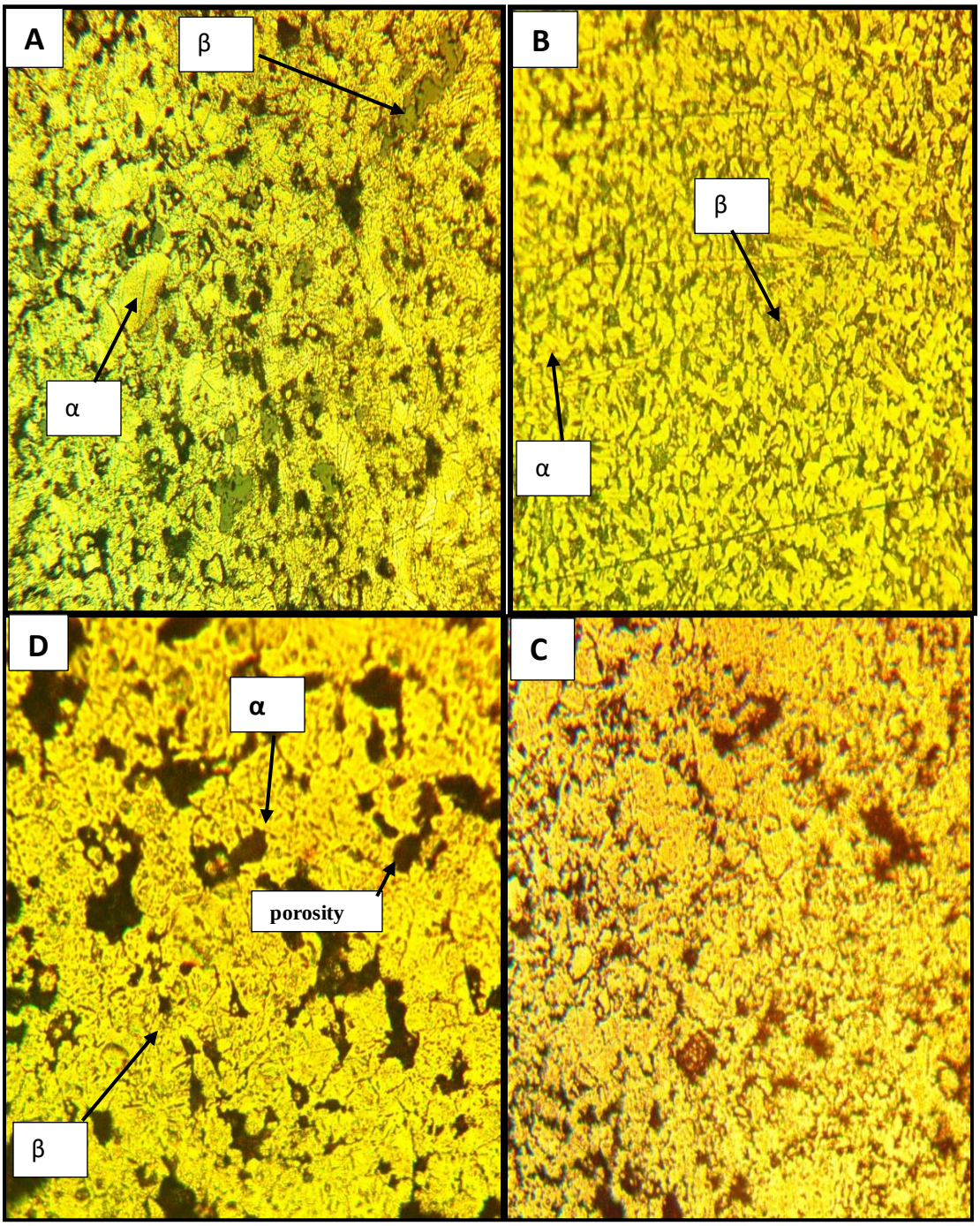

Figurers (4.19 A-D): Optical microstructure of CuAlMn- x% In alloys after sintering for (A) alloy A, (B) alloy D1, (C) alloy D2, (D) alloy D3. 10X

Figure (4.20 A- D) show the microstructure of alloys CuAlMn-x %Ta (1, 2 and 3) %wt. after sintering.

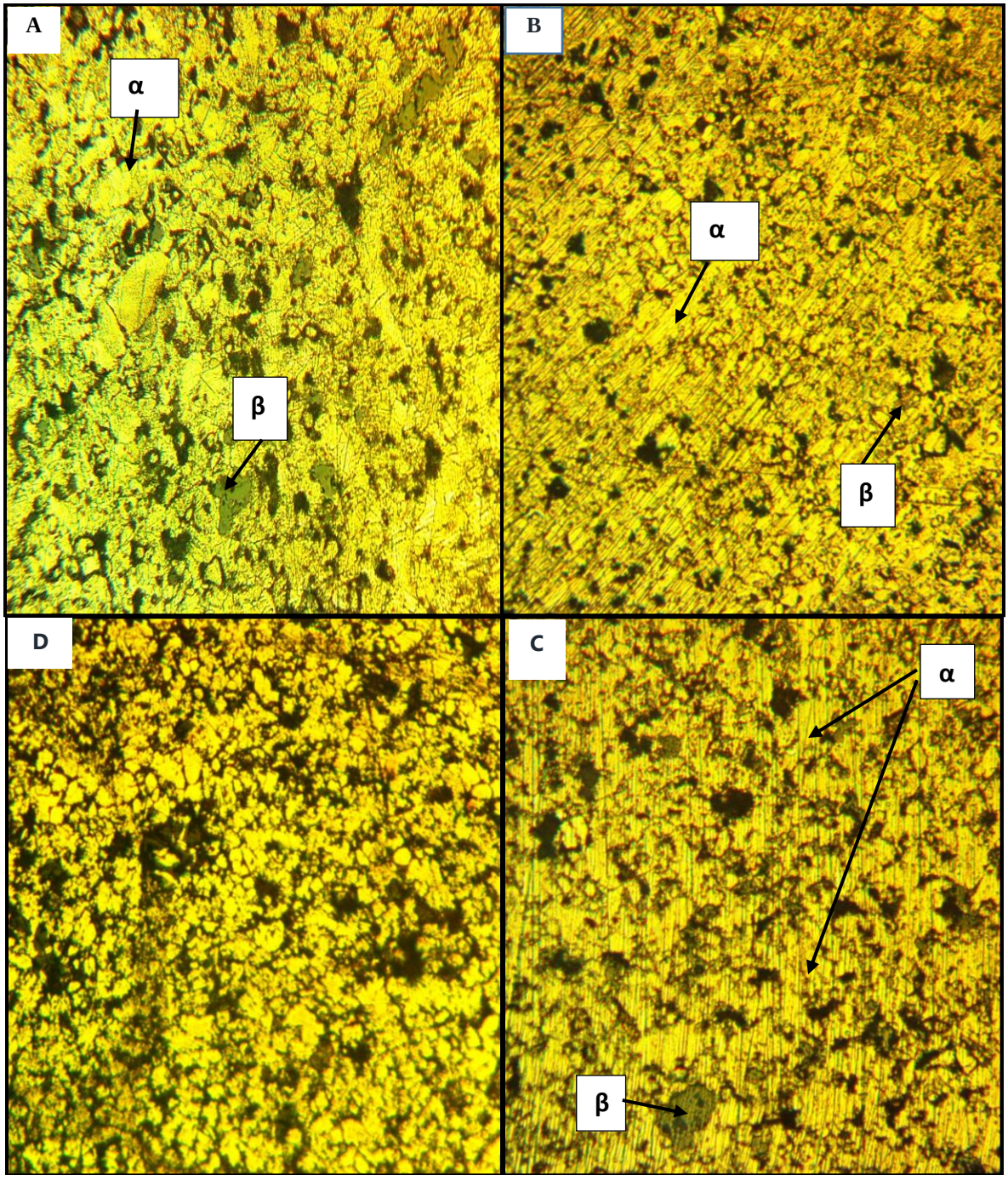

Figures (4.20): Optical microstructures of CuAlMn- x% Ta alloys after sintering for (A) alloy A, (B) alloy B1, (C) alloy B2, (D) alloy B3

Figure (4.21A-D) shows the microstructure of alloys CuAlMn-x %Zr (0.6, 1, and 2) %wt. after sintering.

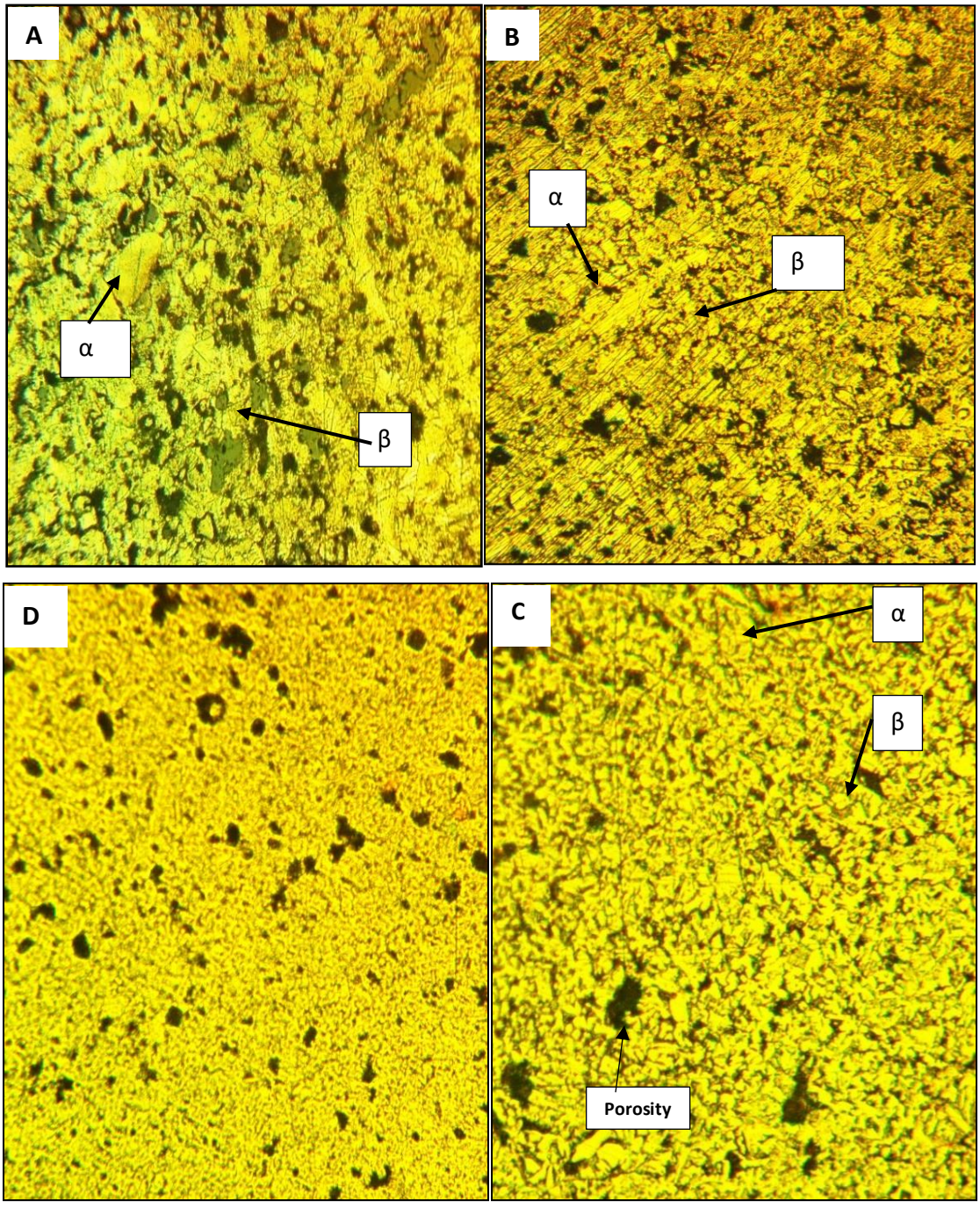

Figures (4.21 A-D): OM of CuAlMn- x% Zr alloys after sintering for (A) alloy A, (B) alloy B1, (C) alloy B2, (D) alloy B3

Figure (4.22) is showing the microstructure of composite material CuAlMn-x %Y_2O_3 (1, 2, and 3) % wt. after sintering.

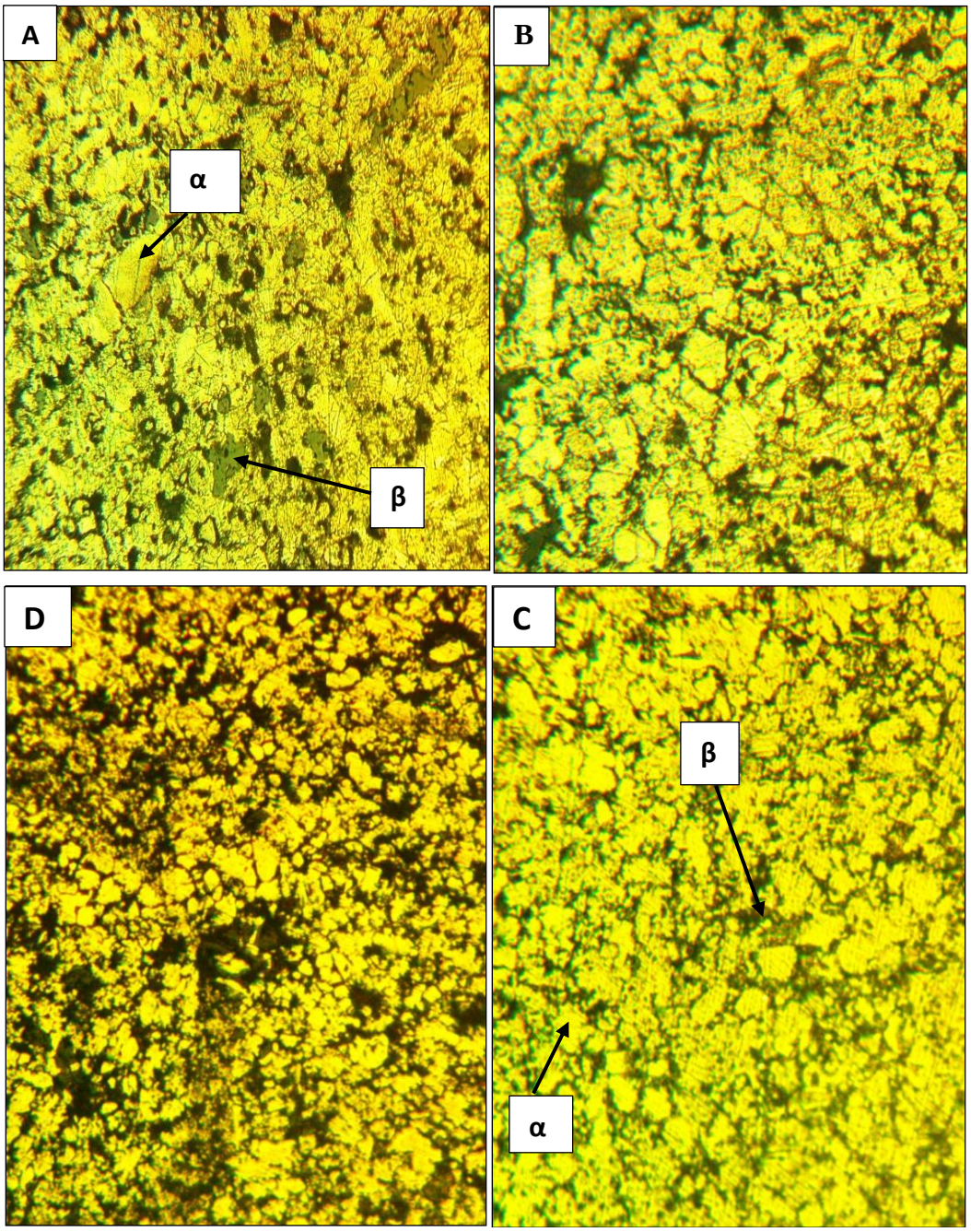

Figures (4.22): OM of CuAlMn- x% Y_2O_3 composite material after sintering for (A) alloy A, (B) alloy E1, (C) alloy E2, (D) alloy E3

Figures (4. 19-22) shown that the Ta, Zr, In and Y_2O_3 addition to Cu-8%Al-9%Mn shape memory alloys have a significant effect in terms of grain refinement and

restricted the grain growth rate. Meanwhile, these elements (Ta, Zr, and In) have uniformly distributed into the matrix and their most effectiveness has concentrated on the formation of the second phase. The result agrees with the result of Safaa Al-Humairi and V. Sampath and U.S. Mallik [128, 52] respectively.

The grain refinement is happening due to the formation of secondary phases and also due to the dissolution of the elements in the alloy matrix [52].

Grain structure with ($\alpha + \beta$) phase prerequisite for martensite formation on quenching is observed in all the alloys, indicating a potential for exhibiting the shape memory behavior Rupa Dasgupta [9].

4.4.2. Light Optical Microscope after Quenching

The β - phase of CuAlMn shape memory alloy has a disordered bcc structure at high temperatures. During quenching the alloy experiences the ordering transitions, $\beta(A_2) \rightarrow \beta_2(B_2) \rightarrow \beta_1(L_{21})$, and then the thermoelastic martensite transformation, $\beta_1(L_{21}) \rightarrow \beta_1`$ (18R).

Regarding the CuAlMn phase diagram, Cu–8%Al–9 %Mn alloy lies in a two-phase (α and β) region when the solution temperature is 900°C. During quenching (β) phase undergoes the ordering transformation, followed by martensite transformation [107].

Figure (4.23-26) shows the microstructure of alloys Cu-Al-Mn, CuAlMn-(1, 2, 3) %Ta, CuAlMn-(1, 2, 3) % In, CuAlMn-(0.6, 1, 2) % Zr and CuAlMn-(1, 2, 3) % Y_2O_3 respectively after solution at 900°C and then aging heat treatments at 300 °C for 1hr. follow by quenching in ice water.

Figure (4.23 A-D) show the microstructures of alloys CuAlMn-x % Ta (1, 2 and 3) % wt. after quenching heat treatments.

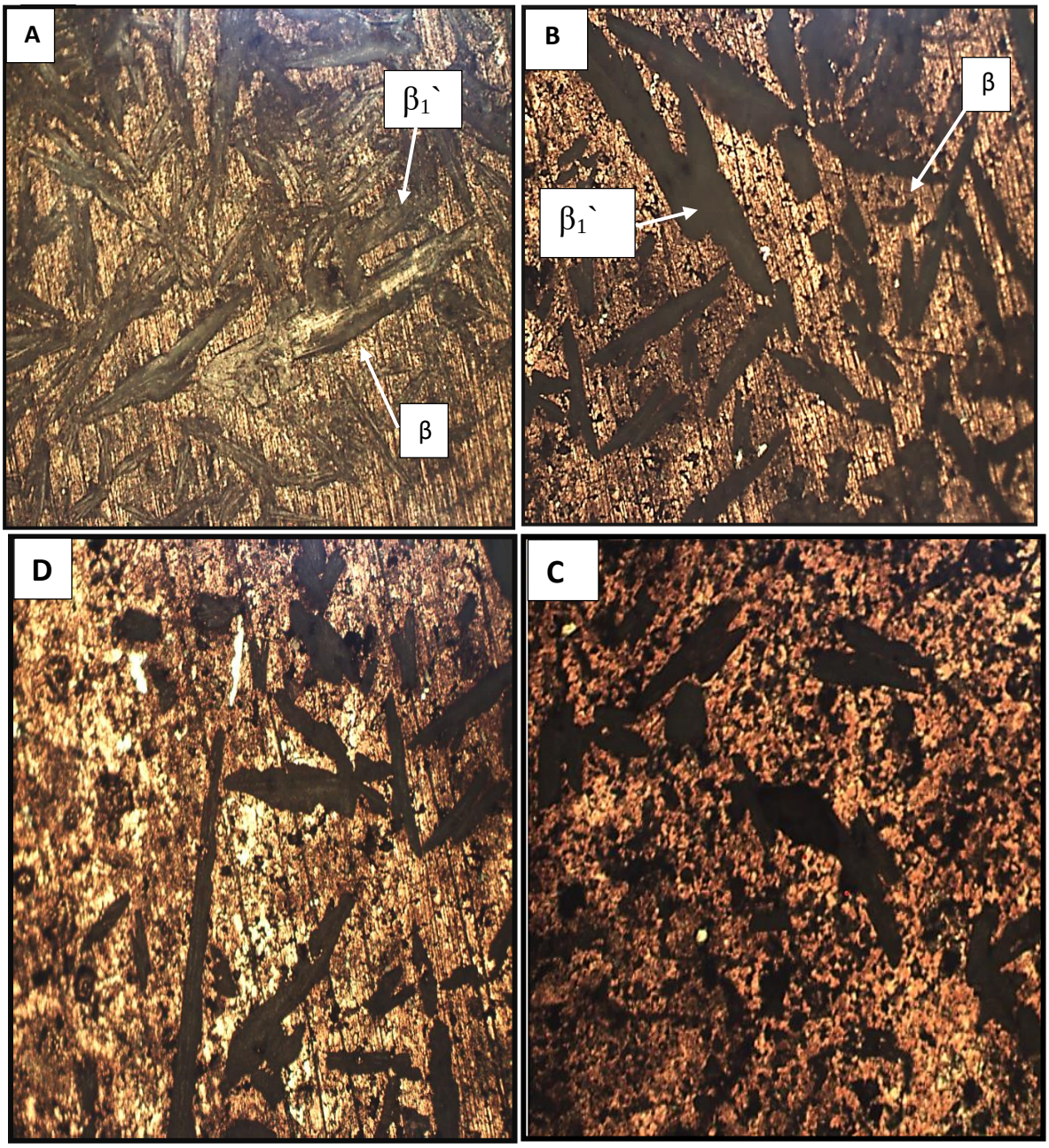

Figures (4.23A-D): optical microstructures of CuAlMn- x% Ta alloys after Aging for (A) alloy A, (B) alloy B1, (C) alloy B2, (D) alloy B3

Figure (4.24) shows the microstructure of alloys CuAlMn-x % Zr (0.6,1 and 2) % wt. after quenching heat treatments.

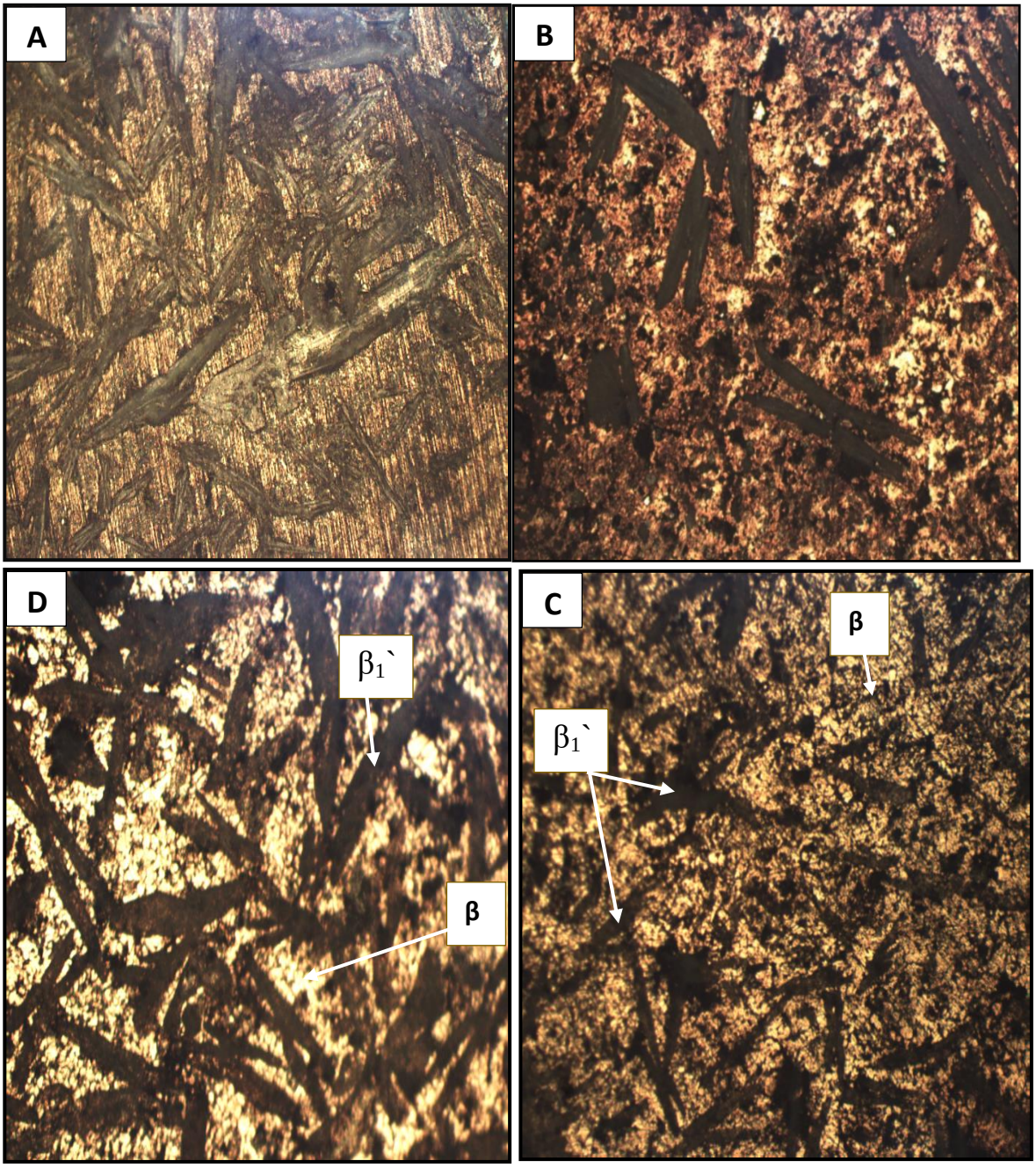

Figures (4.24A-D): Optical microstructures of CuAlMn- x% Zr alloys after Aging for (A) alloy A, (B) alloy B1, (C) alloy B2, (D) alloy B3

Figure (4.25) shows the microstructure of alloys CuAlMn-x % In (1,2 and 3) % wt. after quenching heat treatments.

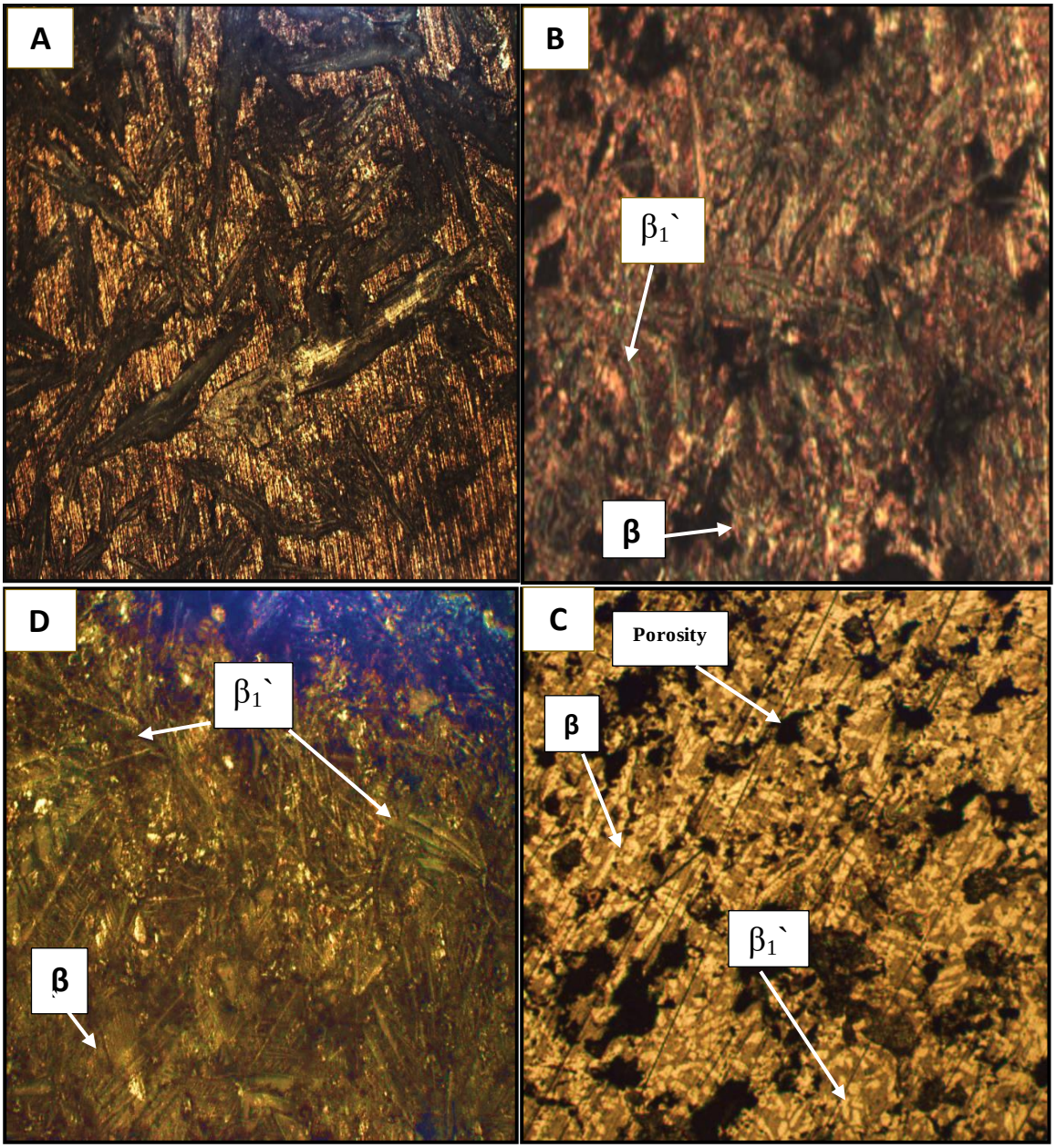

Figures (4.25A-D): Optical microstructures of CuAlMn- x% In alloys after Aging for (A) alloy A, (B) alloy D1, (C) alloy D2, (D) alloy D3

Figure (4.26 A-D) shows the microstructure of composite material CuAlMn-x % Y_2O_3(1, 2, and 3) % wt. after quenching heat treatments.

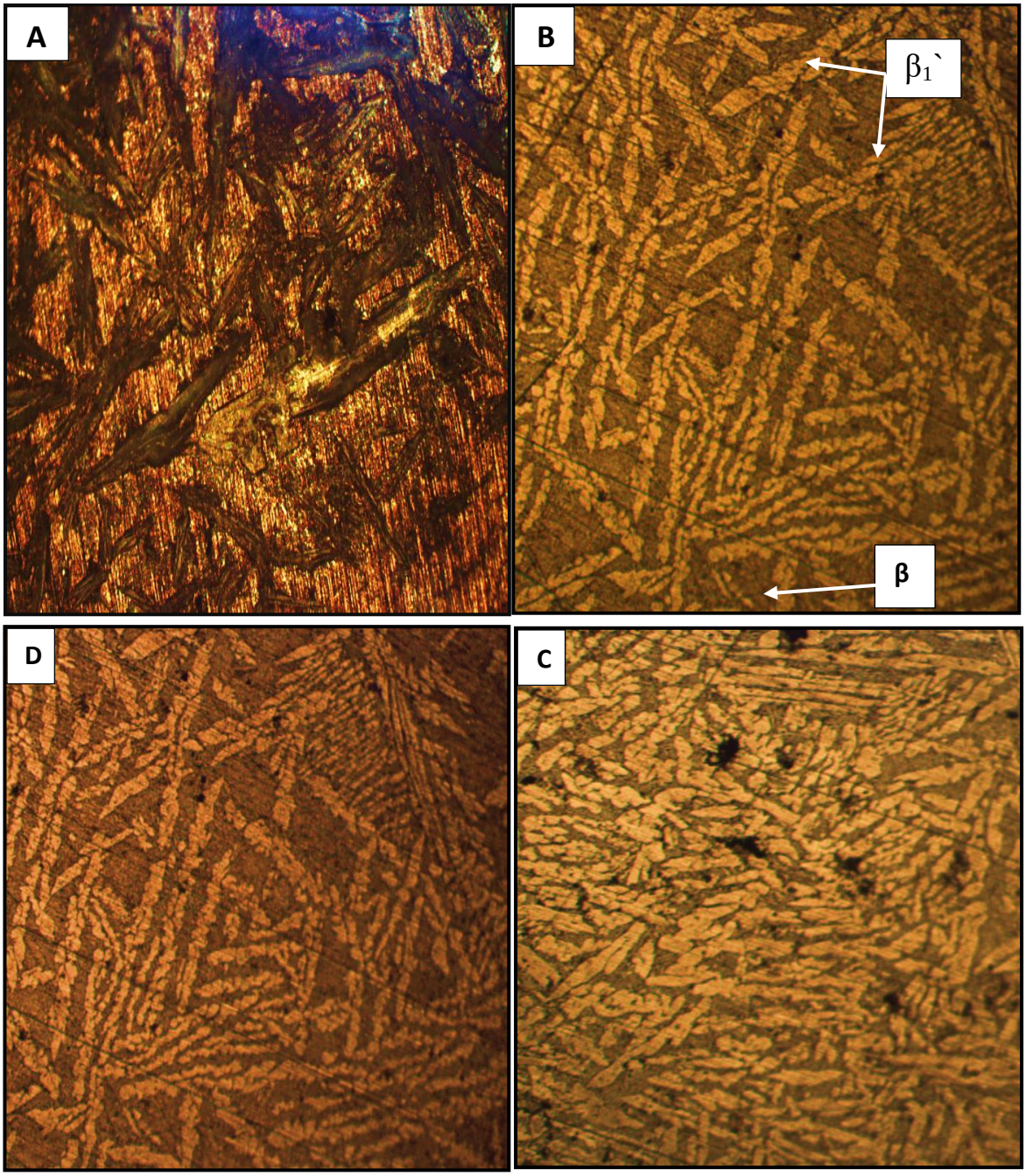

Figures (4.26A-D): Optical microstructures of CuAlMn- x% Y_2O_3 composite material after Aging for (A) alloy A, (B) alloy E1, (C) alloy E2, (D) alloy E3

Figures (4. 23-26) show OM micrographs of the Cu-Al-Mn alloy after aging heat treatment. The alloys after aging at 300˚C for 1 hr. has β_1` martensite and β parent

phase at room temperature. The results agree with others researchers Tamara H. et.al. [127] and S. Kozuh et.al.,[130]. As shown in Figs. (4. 23 - 26) the grain size of the alloy after quenching is much higher compared to those of alloy after sintering

By rapid cooling in water, the alloy undergoes ordering transitions $\beta(A_2) \rightarrow \beta_2(B_2) \rightarrow \beta_1(L_{21})$, and then martensite transformation $\beta 1\ (L_{21}) \rightarrow \beta 1'$ occurs during rapid cooling from the stable β-phase region the martensitic phase occurs below the Ms-temperature. The grains appear clearly, and martensite plates have different orientations into different grains. The martensite is formed primarily as the plate. In some fields, the V-shape martensite was noticed. This is typical self-accommodating zig-zag martensite morphology, which is characteristic for the β′ martensite in SMAs [107,130].

4.5. Scanning Electron Observations

SEM analyses and grain size of the base alloy (Cu-Al-Mn) and alloy with additives (Ta, Zr, In, and Y_2O_3) with the highest wt.% after sintering are show in Figures (4. 27 A, B, C, and D).

From Figure (4. 27 A-D) it can be seen that the microstructures contained two phases α light color and β dark color.

The alloys element changes the grain size (G. S) of alloys as shown in Figure (4. 27 A) the grain size base alloy range between (24-30) nm, but the addition of Ta element reduces the G. S to 44.8 nm as shown in Figure (4. 27 B and C).

The addition of Zr and In elements reduce the grain size (G.S) to 46.1nm and 43.9nm respectively, whoever the addition of Y_2O_3 (ceramic particles) the grain size reduces to 44.4nm as shown in Figure (4. 27 D).

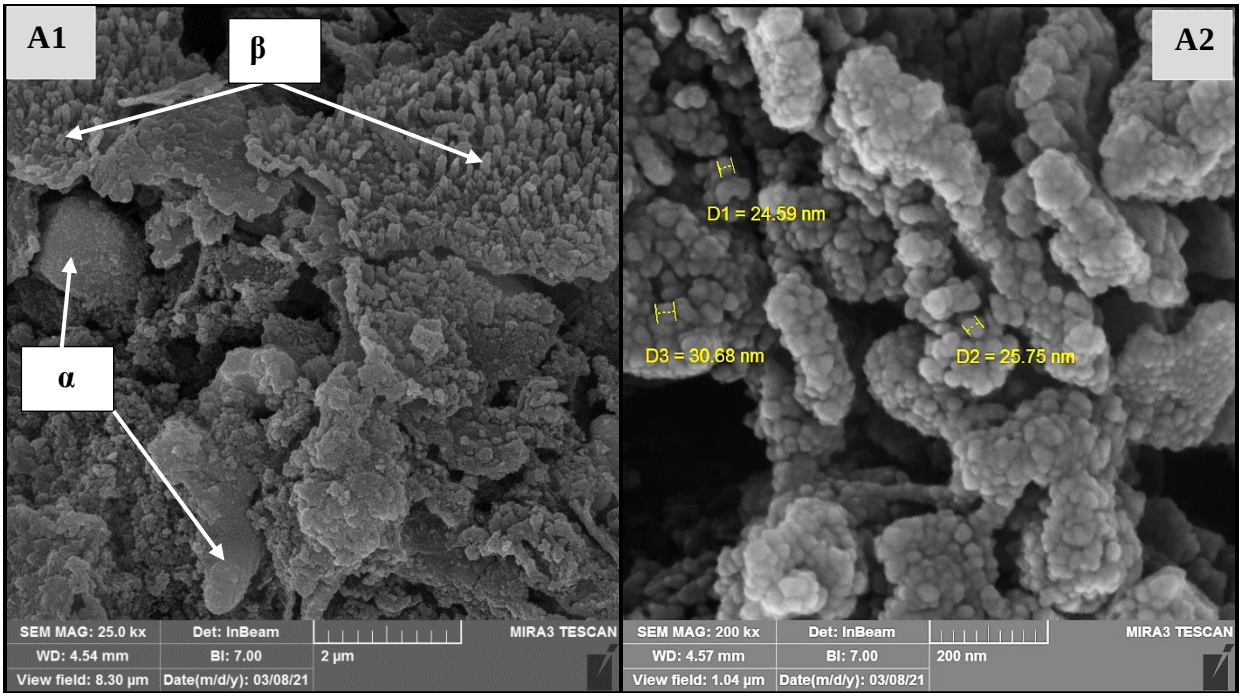

Figure (4. 27 A): SEM analyses of CuAlMn alloy with two different magnifications (A1-50KX and A2- 200KX)

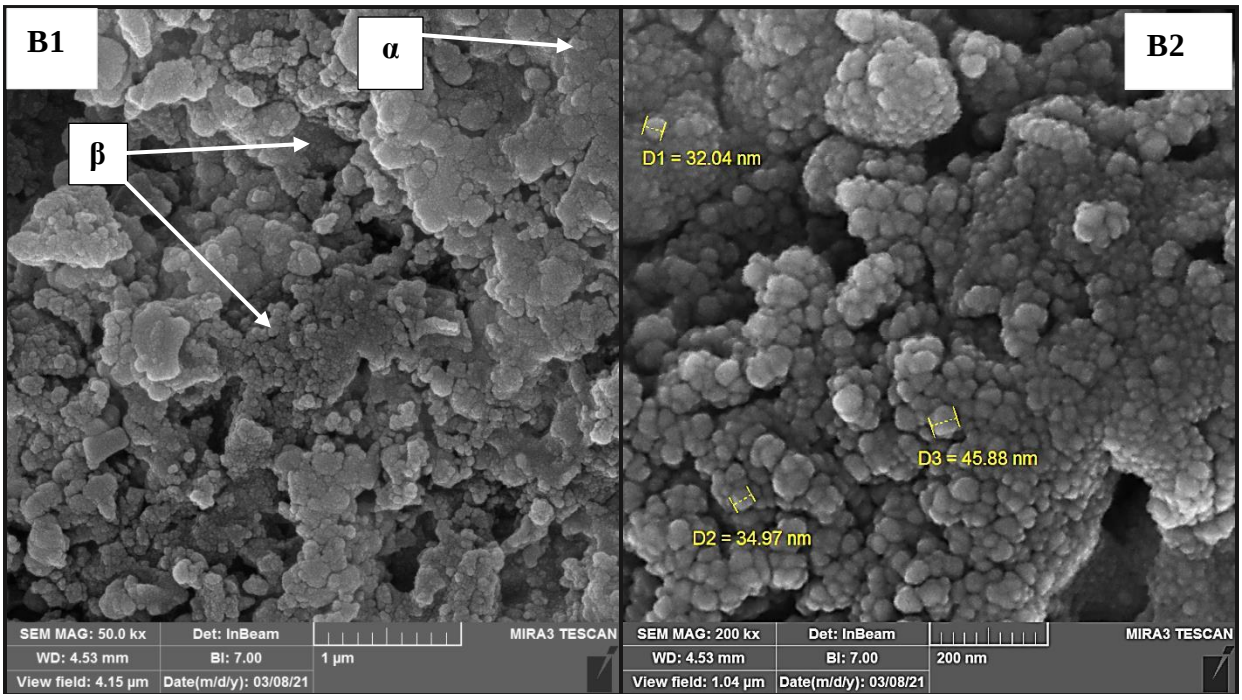

Figure (4. 27 B): SEM analyses of CuAlMn-3%Ta alloy with two different magnifications (B1 -50KX and B2 -200KX)

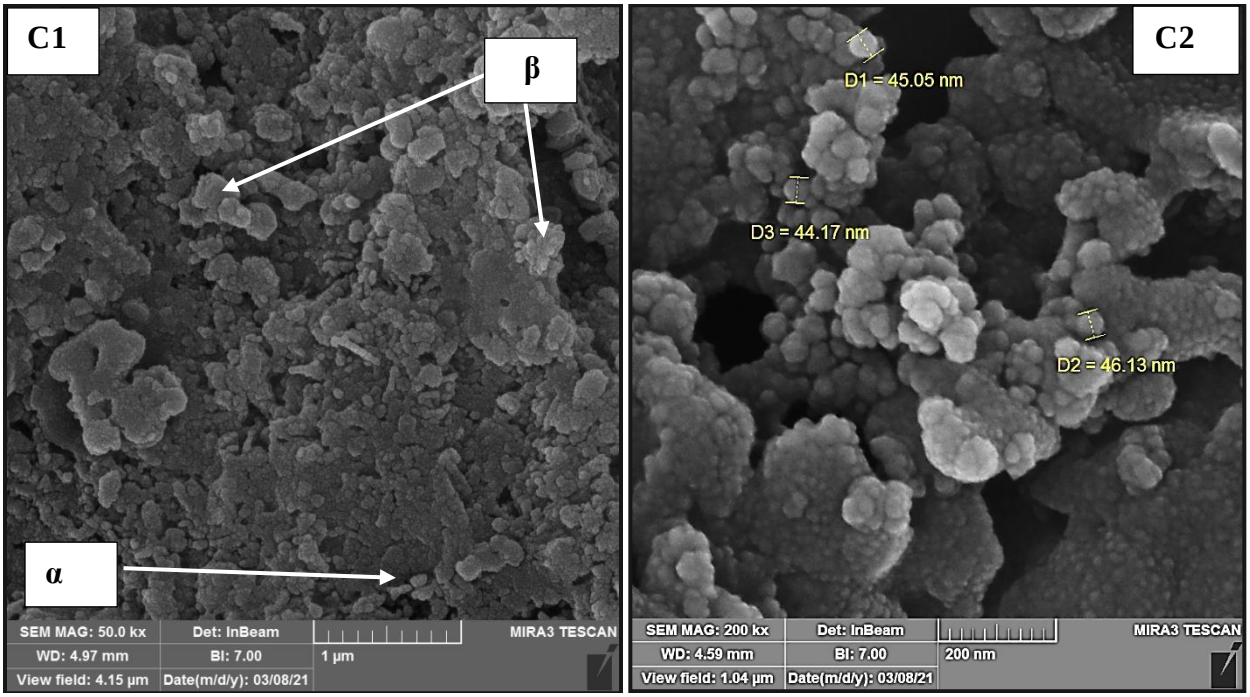

Figure (4. 27 C): SEM of CuAlMn-2% Zr alloy with two different magnification C1 50KX and C2 200KX

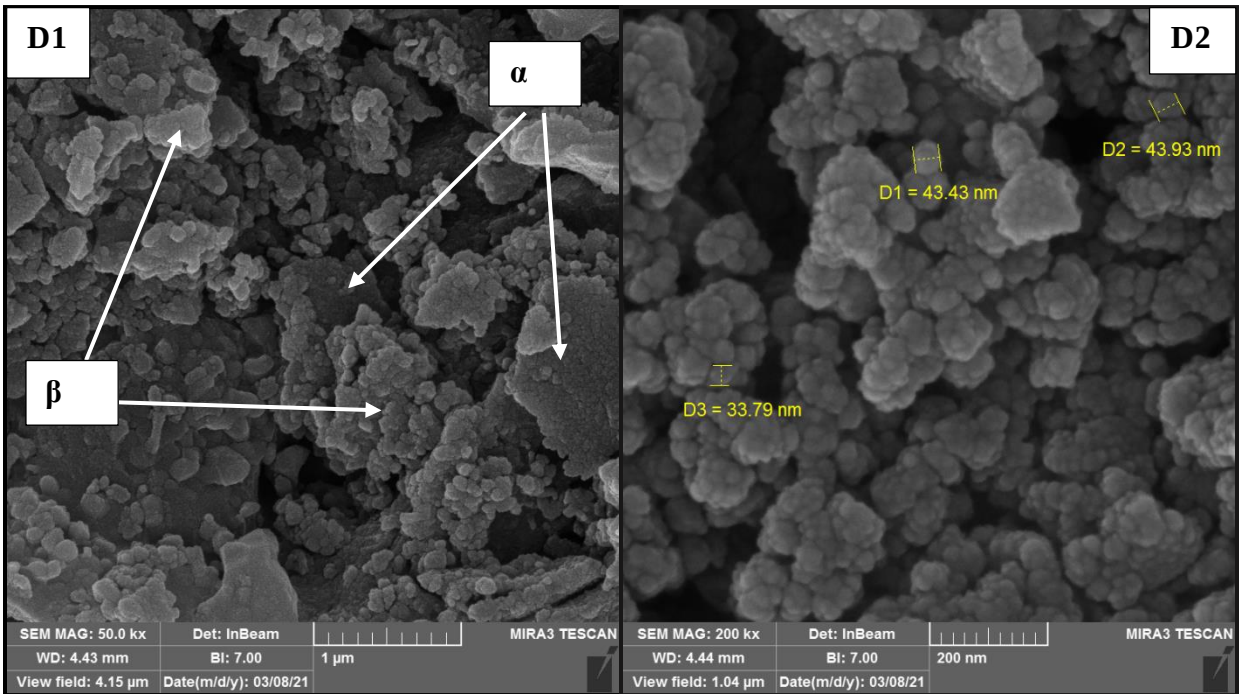

Figure (4. 27 D): SEM analyses of CuAlMn-3% In alloy with two different magnification D1- 50KX and D2- 200KX

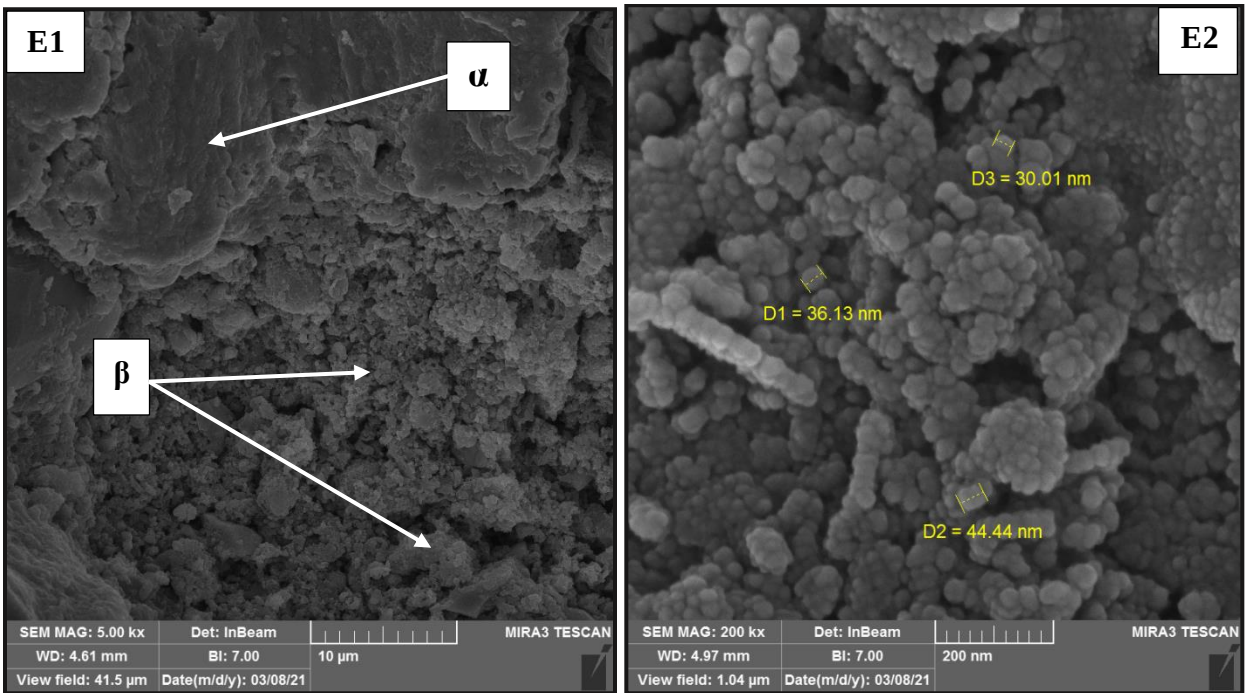

Figure (4. 27 E): SEM analyses of CuAlMn-3% Y_2O_3 alloy after sintering with two different magnification E1- 50KX and E2- 200KX

The microstructure of specimen (A, B3, C3, D3, and E3) after aging heat treatment have been tested under SEM and EDS as shown in Figure (4.28A-E). Figure (4.28A-E) refer to Scanning Electron Microscope micrograph of alloys (Cu-8%Al-9%Mn) shape memory alloy with microstructures consisted of martensite β1` phase with β matrix

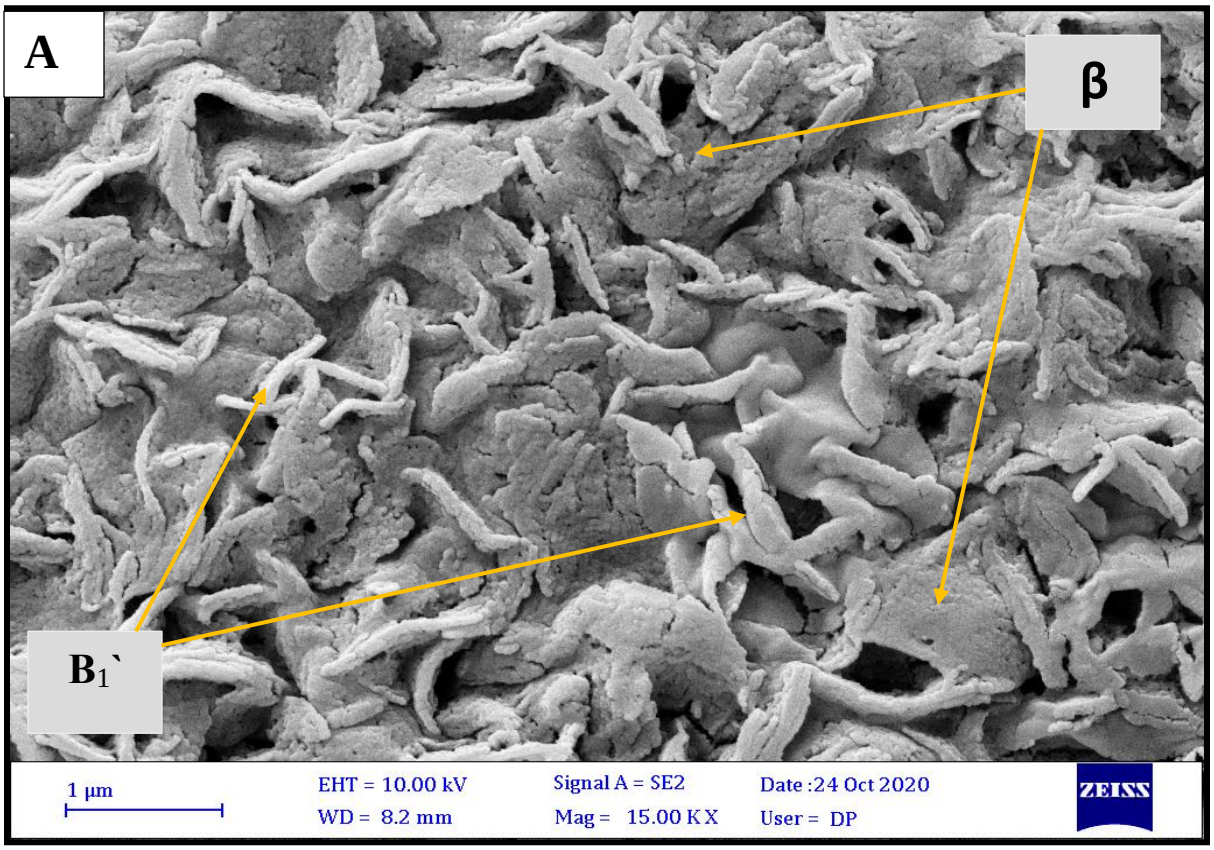

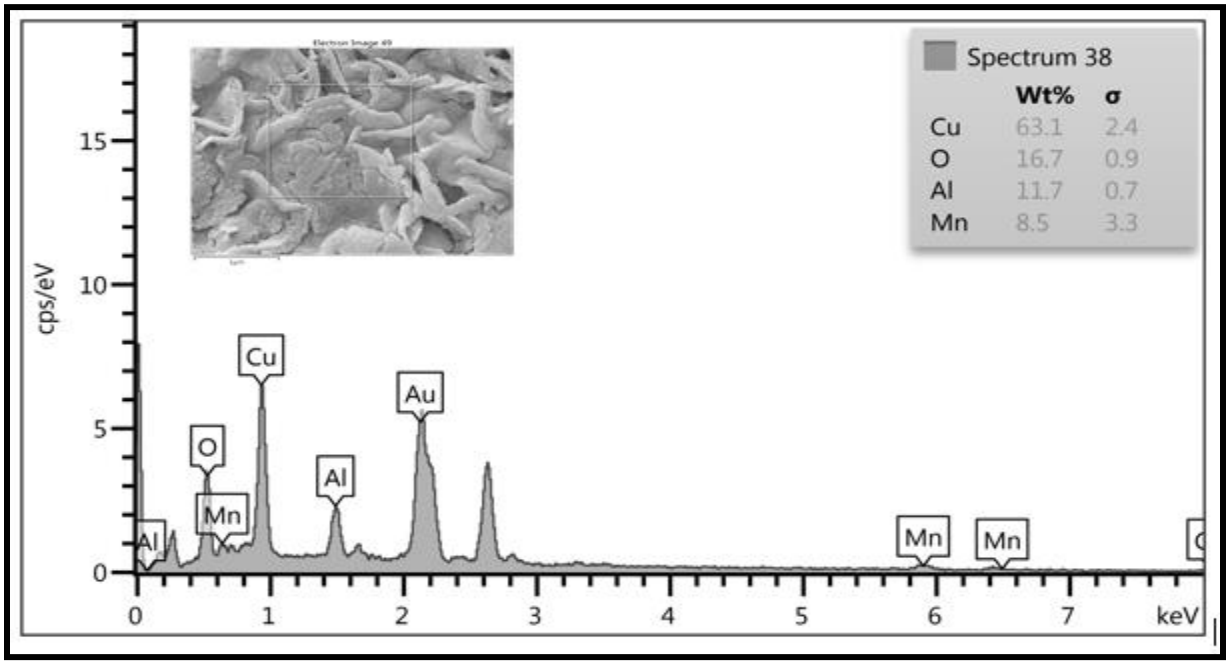

Figure (4.28 A): SEM image and EDS analysis for alloy CuAlMn after Aging process

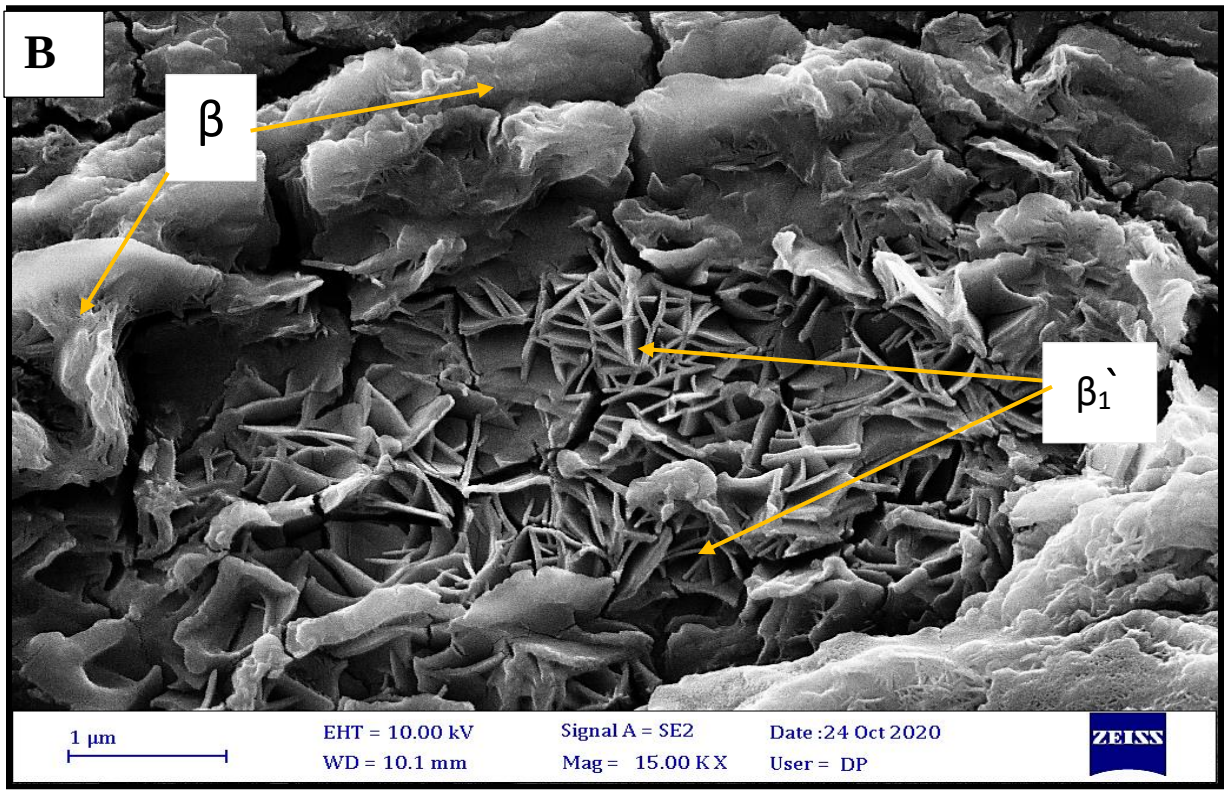

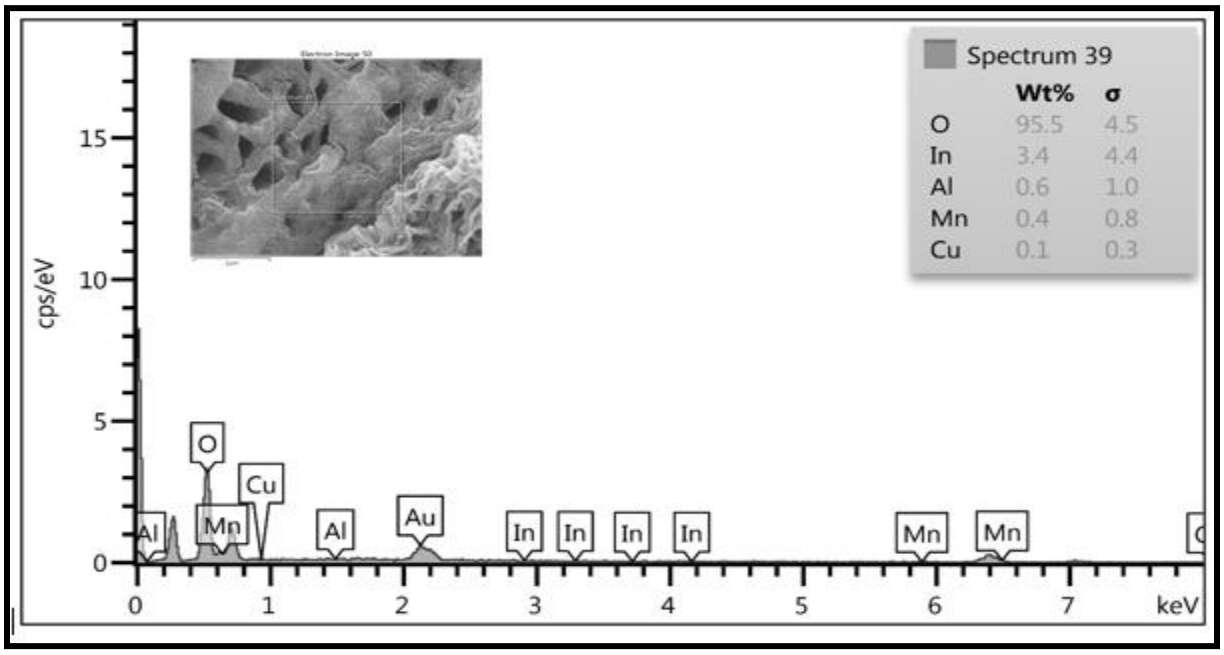

Figure (4.28B): SEM image and EDS analysis for alloy CuAlMn-3%In after Aging process

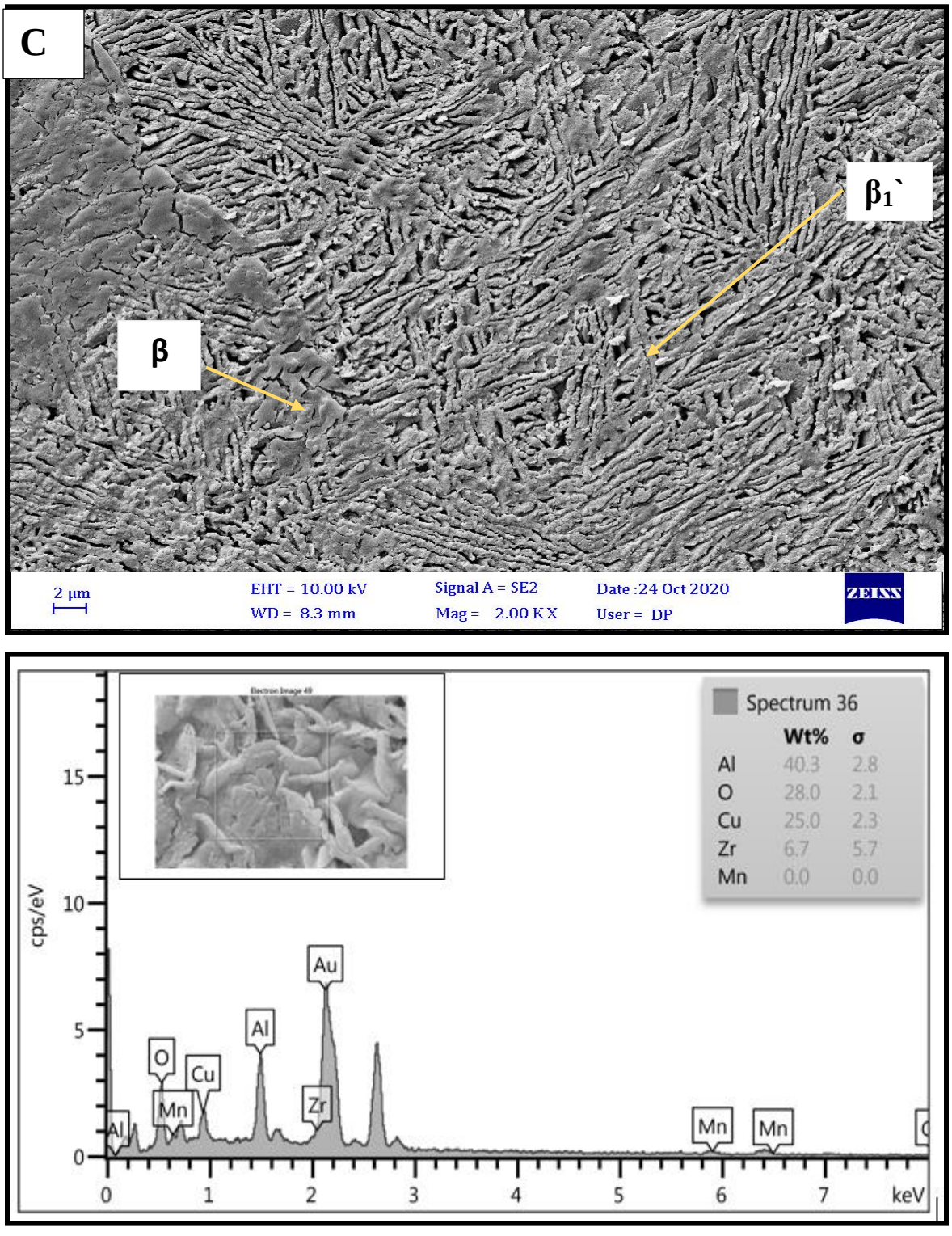

Figure (4.28 C): SEM image and EDS analysis for alloy CuAlMn-2%Zr after aging process

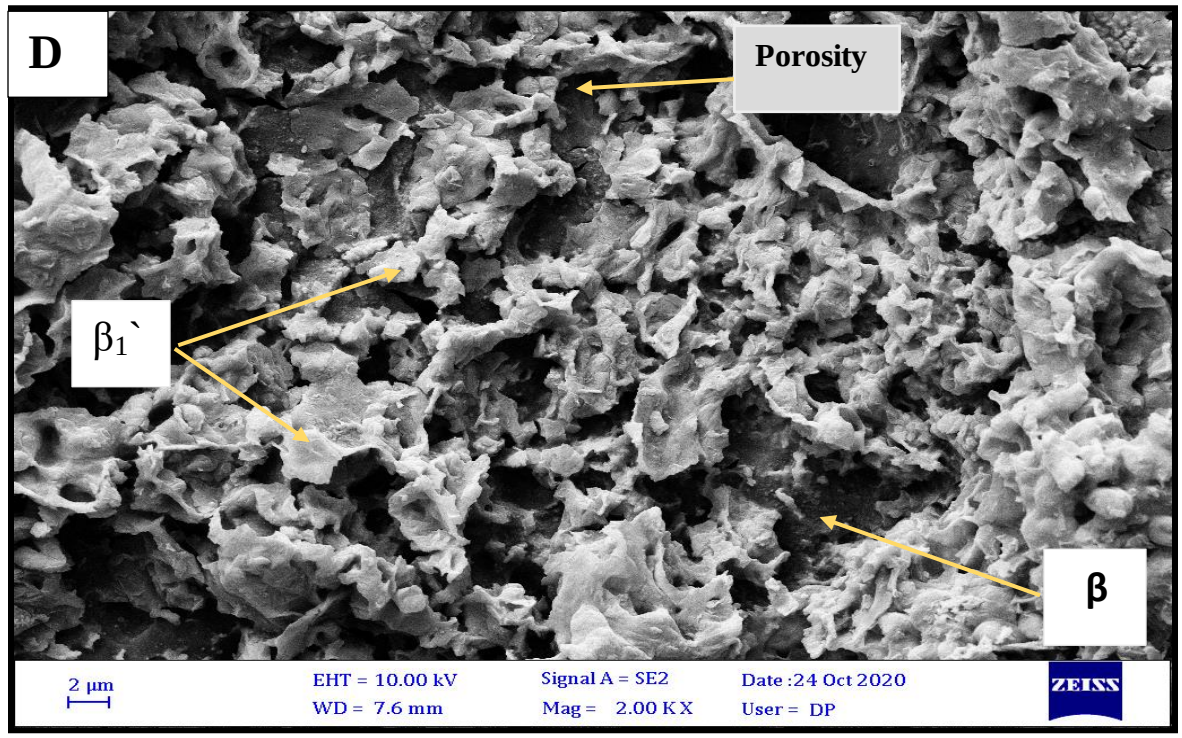

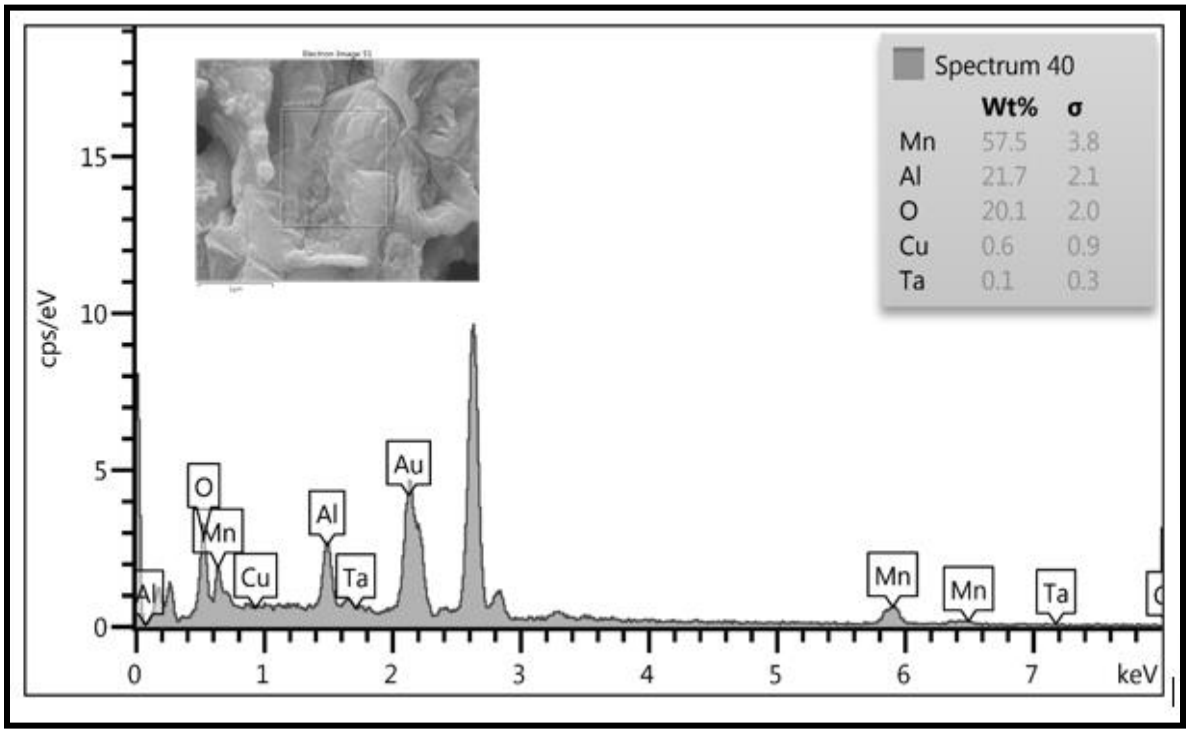

Figure (4.28 D): SEM image and EDS analysis for alloy CuAlMn-3%Ta after aging process

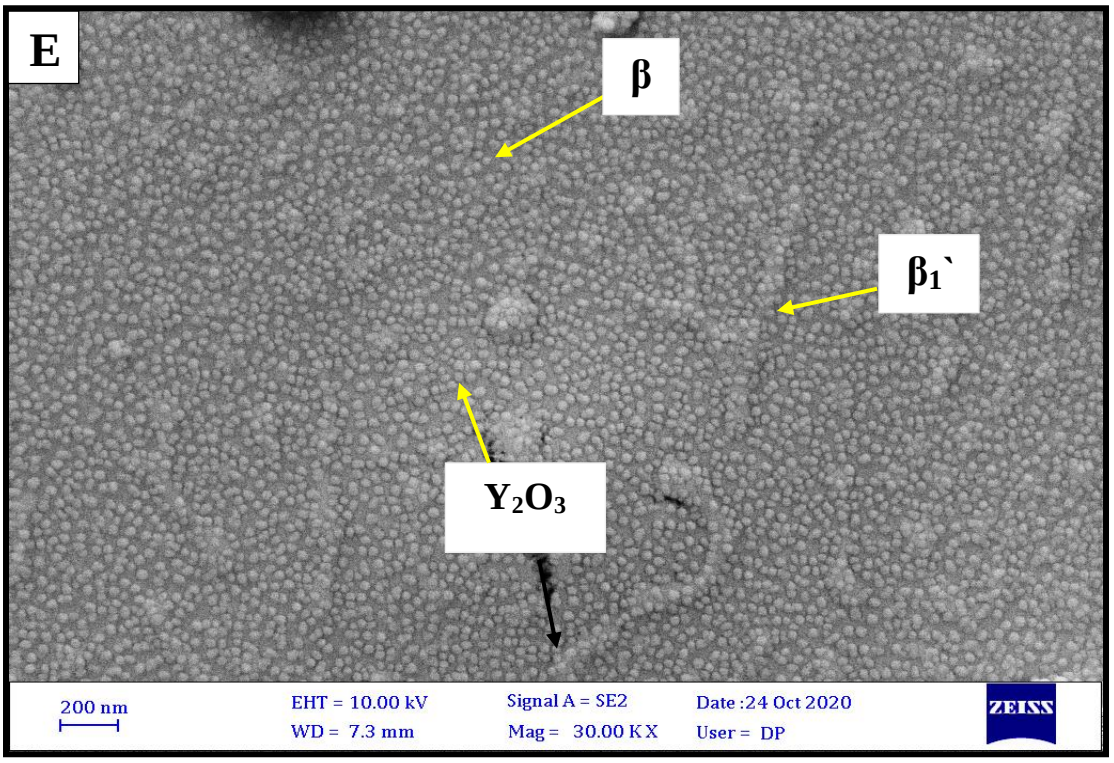

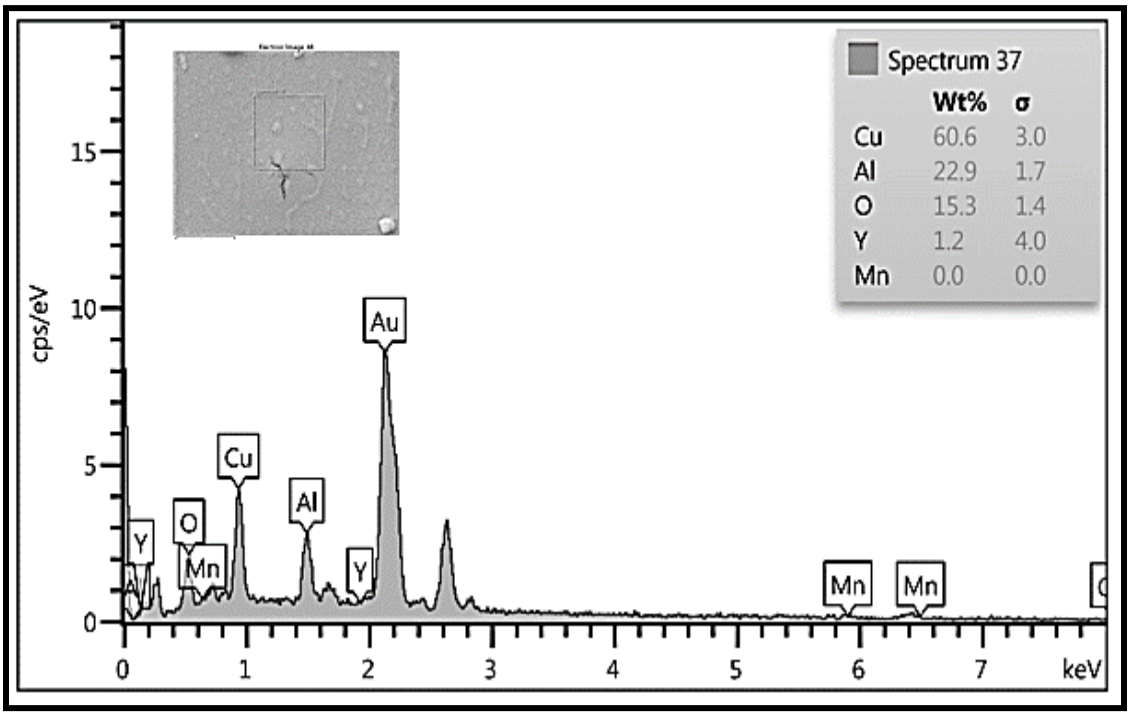

Figure (4.28E): SEM image and EDS analysis for composite material CuAlMn-3%Y_2O_3 after aging process

At the temperature of 900˚C, the Cu83Al8Mn9 alloy has martensite (β_1') and (β) parent phase with disorder bcc structure as show in Figure (4.27 A-E). The result agrees with Mirko Gojic, et. al., [132]. By rapid cooling, the alloy undergoes ordering transitions $\beta(A_2) \rightarrow \beta_2 (B_2) \rightarrow \beta_1 (L_{21})$, followed by martensite transformation $\beta_1 (L_{21}) \rightarrow \beta 1'$. The martensite microstructure after aging forms as V-shape martensite was noticed. Self-accommodating zig-zag martensite morphology is characteristic for the β_1' martensite in shape memory alloys [131].

4.6. Mechanical properties

4.6.1. Shape Memory Effects

The shape memory effect (SME%) of alloys A, B1, B2, and E3 after aging heat treatment was determined by using Brinell hardness by measuring the diameter of ball indenter after and before the heat treatment as shown in Table (4.2).

The shape memory effect in CuAlMn alloy is based on the thermoelastic martensite transformation that occurs between β phase (Do_3 or L_{21}) order structure and martensite phase (identified as 3R, 9R, and 18R). Consequently, no deterioration of SME in CuAlMn-X (Ta, Zr, In, and Y_2O_3) alloys were observed (Table 4.2). Furthermore, the addition of (Zr, In, and Y_2O_3) can increase the SME of ternary Cu-Al-Mn alloy.

The highest shape memory effect was achieved when the addition of 2% Zr and 3 wt.% Ta wt. This is because the Ta element easily diffused into the matrix and reacted with the base alloying element to form multi-variant martensite so that the enhancement of shape memory effect has been achieved.

Furthermore, the type and amount of the precipitates and intermetallic compounds might influence the shape memory effect of the alloy. It was observed that the additions of alloying elements exhibited an increase in the SME. This enhancement in the SME was attributed to the existence of the precipitates and grain refinement which was brought about by the addition of alloying element in the parent phase.

Table (4.1): The Influence of alloying elements on SME of Cu-8%Al-9%Mn SMA

Synthesized Composition	Code	D_b(μm)	D_a(μm)	SME %	Impro.
Cu-8Al-9Mn	A	616	594	3.57	-
Cu-8Al-9Mn-1%Ta	B1	618	590	4.36	22.12885
Cu-8Al-9Mn-2%Ta	B2	529.1	506	4.34	21.56863
Cu-8Al-9Mn-3%Ta	B3	523	485	7.26	103.3613
Cu-8Al-9Mn-1%In	C1	612	587	4.08	14.28571
Cu-8Al-9Mn-2%In	C2	589	551	6.45	80.67227
Cu-8Al-9Mn-3%In	C3	563	527	6.39	78.9916
Cu-8Al-9Mn-0.6%Zr	D1	555	530	4.5	26.05042
Cu-8Al-9Mn-1%Zr	D2	573	545	4.89	36.97479
Cu-8Al-9Mn-2%Zr	D3	587	541	7.83	119.3277
Cu-8Al-9Mn-1%Y_2O_3	E1	549	530	3.46	0
Cu-8Al-9Mn-2%Y_2O_3	E2	601	580	3.49	0
Cu-8Al-9Mn-3%Y_2O_3	E3	581	583	4.82	35.01401

4.6.2 Vickers Microhardness

Vickers microhardness value as a function of weight percentage of Ta, Zr, In and Y_2O_3 additions for sintered and aged specimens are shown in Figures (4. 29 -32) and Table (4.2). The hardness value for the base alloy Cu83Al8Mn9 shape memory alloy agrees with Guofei Zhanga et. al. [122].

From Figure (4. 29A-B), it was noticed that the hardness of alloy (A) in the sintered specimen is 75.7 g/μm^2 and when added (1, 2, and 3 % wt.) of Ta the hardness increasing to (77.81, 80, 86.03 g./μm^2) respectively.

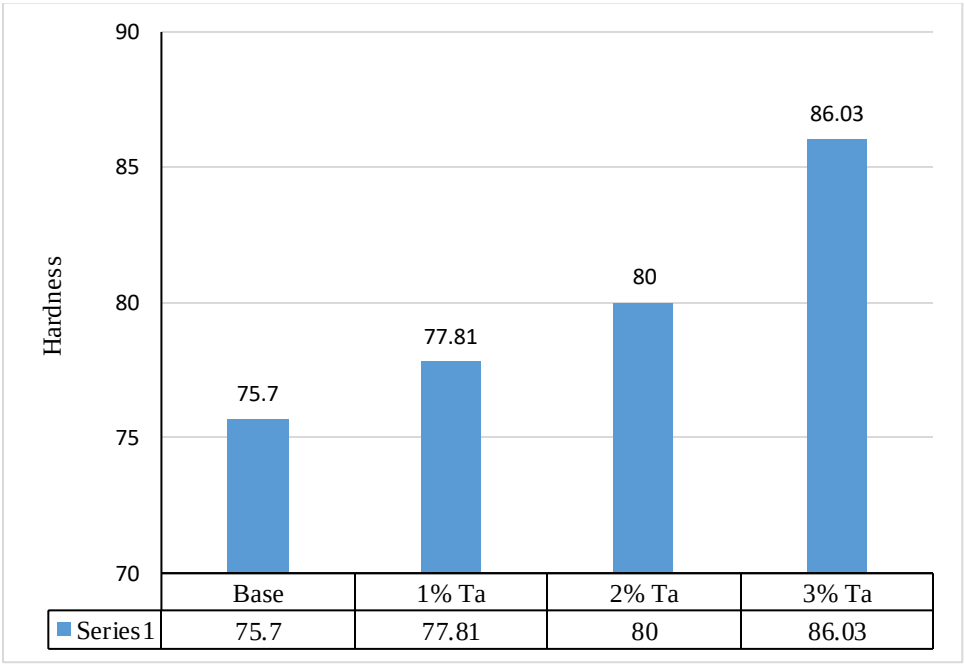

Figure (4.29A) Micro hardness measurement after sintering for alloys A, B1, B2 and B3

While in the aged specimen the hardness is 108.5 g./μm^2 for base alloy (A) and increasing to (117, 120, 126.6 g./μm^2) respectively with increase the Ta percentage addition.

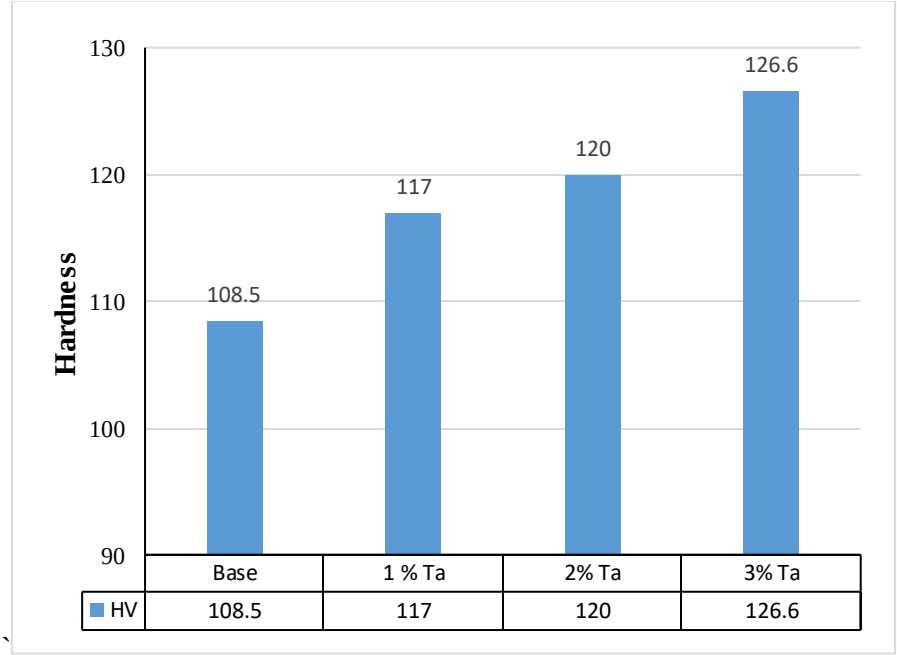

Figure (4.29B) Micro hardness measurement after aging for alloys A, B1, B2and B3

The best addition amount of Ta is 3 wt. % and this is attributed to the grains refinement which was associated with the inhibiting effects of grain growth by Ta element in solid solution. The increase in hardness value with Ta addition agrees with Ayad M. et. Al [123].

From Figure (4.30 A-B), it was noticed that the hardness of alloy (A) in the sintered specimen is 75.7 g./μm^2 and when added (1 and 2) % wt. of Zr the hardness increasing to (87.26, 95.97 g./μm^2) respectively. The best addition amount of Zr is 2%. This is attributed to the grains refinement and reduce the porosity after sintering with the addition Zr element.

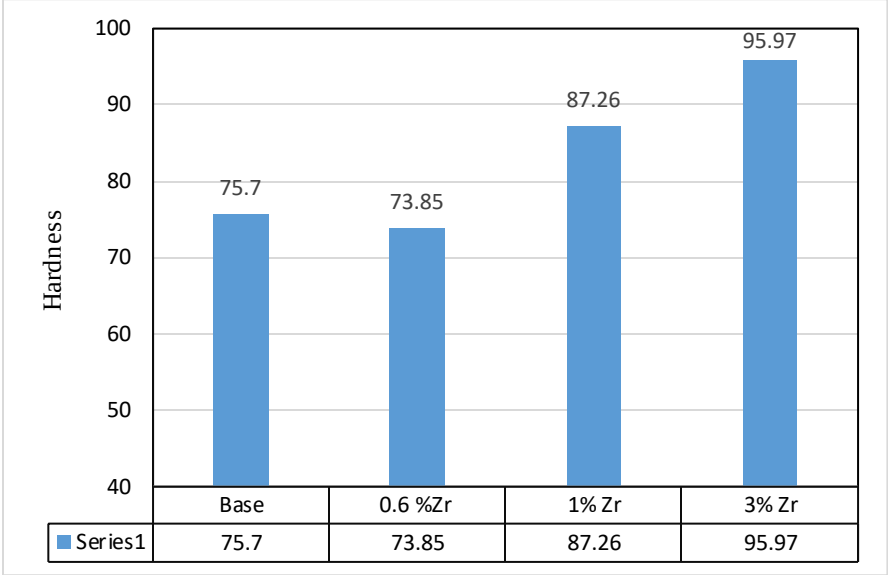

Figure (4.30A) Micro hardness measurement after sintering for alloys A, D1, D2and D3

While in the aged specimen the hardness is 108.5 g./μm^2 for alloy (A) and increasing to (109, 112, 125 g./μm^2) respectively with Zr addition. The best addition amount of Zr is 2%. This is attributed to the grain refinement of martensite phase with the addition Zr element.

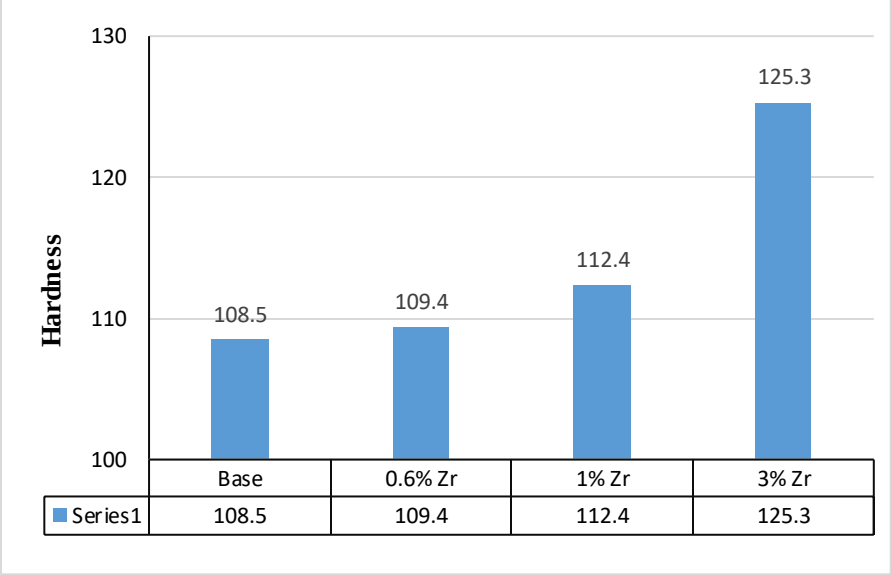

Figure (4.30B) Micro hardness measurement after Aging for alloys A, D1, D2and D3

The addition of Zr to Cu-Al-Mn SMA have decreased the grain size, therefore the value of hardness increase. This is attributed to the formation of fine precipitates that rusticated the grain growth by the pining effects, the result agrees with Safaa Al-Humairi [128].

In the Figure (4.31A-B) it was noticed that the addition of Indium with different amounts (1,2, and 3) % wt. affects the hardness of alloys as (73.1, 60.11, 86.97 g/µm^2) respectively this is at sintering condition and in the aged condition, it increases to (111, 118, 132 g/µm^2) with In addition. The Vickers hardness increased as the In content increased because of the combined effect of the solid-solution strengthening of the α-phase and the hardening of the fine martensitic phase [126].

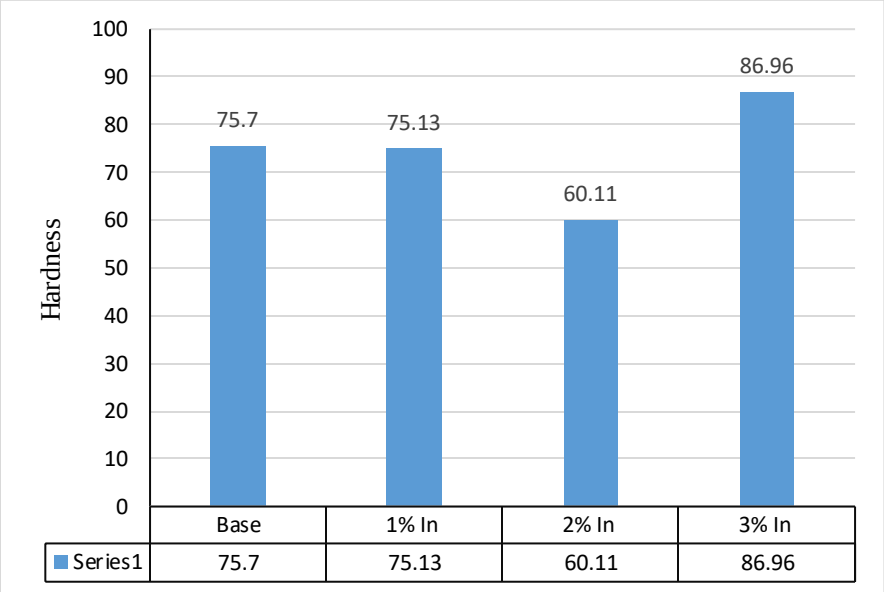

Figure (4. 31A): Micro hardness measurement after sintering for alloys A, C1, C2and C3

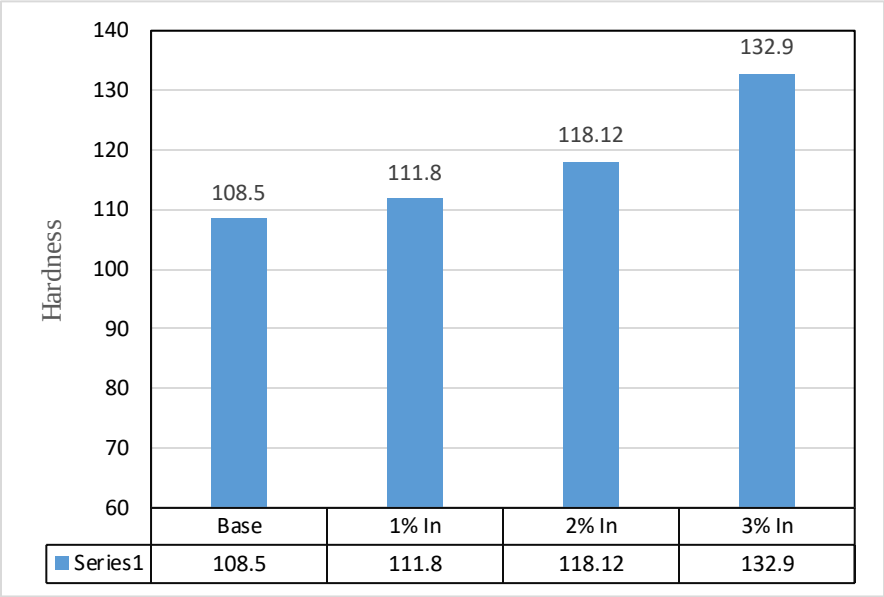

Figure (4.31B) Micro hardness measurement after Aging for alloys A, C1, C2 and C3

In Figure (4.32 A-B), The existence of hard Y_2O_3 particles within the matrix of CuAlMn composite specimens has more hardness. It was noticed that the addition amounts (1, 2, 3 % wt.) of Y_2O_3 increases the hardness of the alloys in the sintered condition to (74.04, 83.65, 113.11 g/μm^2) and the aged condition is increasing too (137, 132,143.8 g/μm^2). The higher hardness achieved was 143.8 g/μm^2 in the addition of Y_2O_3 in the aged condition. A dispersion of fine precipitates stabilizes free dislocations in the matrix and sub-grain structure, which enhances dislocation hardening.

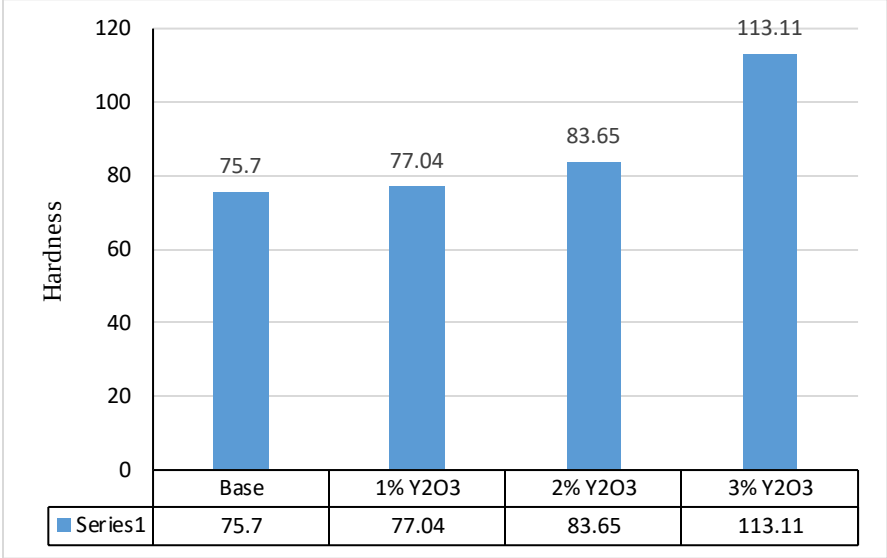

Figure (4.32A) Micro hardness measurement after sintering for alloys A, E1, E2 and E3

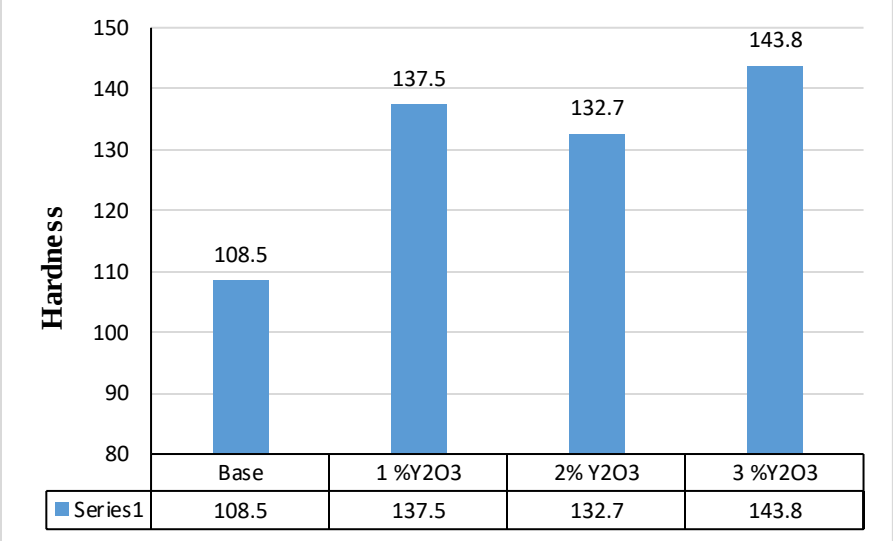

Figure (4.32B) Micro hardness measurement after Aging for alloys A, E1, E2and E3

In general, aged specimens have higher hardness as the result of precipitation hardening and presence martensite phase. Aged in martensite phase is associated with diffusion and precipitation process of an intermetallic compound that is precipitated as fine particles and distributed equally in the microstructure which acts as obstacles

prevent the dislocation movement, and the presence of martensite phase (or a mixture of both), while sintered specimens have low hardness due to the martensite phase doesn't form and presence of α phase [131].

Table (4.2): Micro hardness and improvement of alloys after sintering and aging heat treatment

Synthesized Composition	Code	Hv after sintering	Hv after aging
Cu-8Al-9Mn	A	75.7	108.5
Cu-8Al-9Mn-1%Ta	B1	77.81	117
Cu-8Al-9Mn-2%Ta	B2	80	120
Cu-8Al-9Mn-3%Ta	B3	86.03	126.6
Cu-8Al-9Mn-1%In	C1	75.13	111.8
Cu-8Al-9Mn-2%In	C2	60.11	118.12
Cu-8Al-9Mn-3%In	C3	86.96	132.9
Cu-8Al-9Mn-0.6%Zr	D1	73.85	109.4
Cu-8Al-9Mn-1%Zr	D2	87.26	112.4
Cu-8Al-9Mn-2%Zr	D3	95.97	125.3
Cu-8Al-9Mn-1%Y_2O_3	E1	77.04	137.5
Cu-8Al-9Mn-2%Y_2O_3	E2	83.65	132.7
Cu-8Al-9Mn-3%Y_2O_3	E3	113.11	143.8

From Table (4. 2) can be notes that the best improvements in hardness after sintering and after aging heat treatment belong to Cu-8Al-9Mn-3%Y_2O_3. The improvements in hardness of CuAlMn alloy after the addition of (Ta, In, Zr, and Y_2O_3) can be

attributed to the grain size reduction, solid solution strengthening, and hard intermetallic compounded [133].

4.7. Differential Scanning Calorimeter

Representative graphs of analysis for DSC analysis of Cu8%Al9%Mn, Cu8%Al9%Mn-3%Ta, Cu8%Al9%Mn-3%In, Cu8%Al9%Mn-2%Zr, Cu8%Al9%Mn-3% Y_2O_3 SMA gained on heating from 0 °C until 600°C (5 °C min) on the as Aging specimen shown in Figure (4.33).

This test is done in order to calculate the AF which is the austenite finish temperature that is used in the shape memory effect test as heat treatment temperature. A small difference is utilized on the temperature peaks of the four alloys. This fact suggests that the phase transformation temperatures are not too sensitive to the small percentage of alloys additives.

During heating, the reversal of phases has been referred to as an abrupt change in resistive lope between 77°C and 277 °C. Such Thermal event has already been associated with the corresponds to the consumption of the $\beta_3(L_{21})$-Cu_2MnAl phase for producing the $\beta_1(D0_3)$-Cu_3Al phase. Therefore, the reaction can be represented by the $\beta_3(L_{21})$-$Cu_2MnAl + \beta_1(D0_3)$-$Cu_3Al \rightarrow \beta_1`(D0_3)$ - Cu_3Al transformation [134,135, 136].

The presence of two peaks in the curves of CuAlMn-Ta, CuAlMn-Zr, CuAlMn-In , and CuAlMn-Y_2O_3 as shown in Figure (4.33 B, C, D, and E), indicates the appearance of multi stage-martensite- austinite transformation $\beta1`(18R) \rightarrow \gamma`(2H) \rightarrow \beta1(L_{21})$ during the heating process [155]. The results of DSC agree with Canan Canbay and Tercan Polat [138].

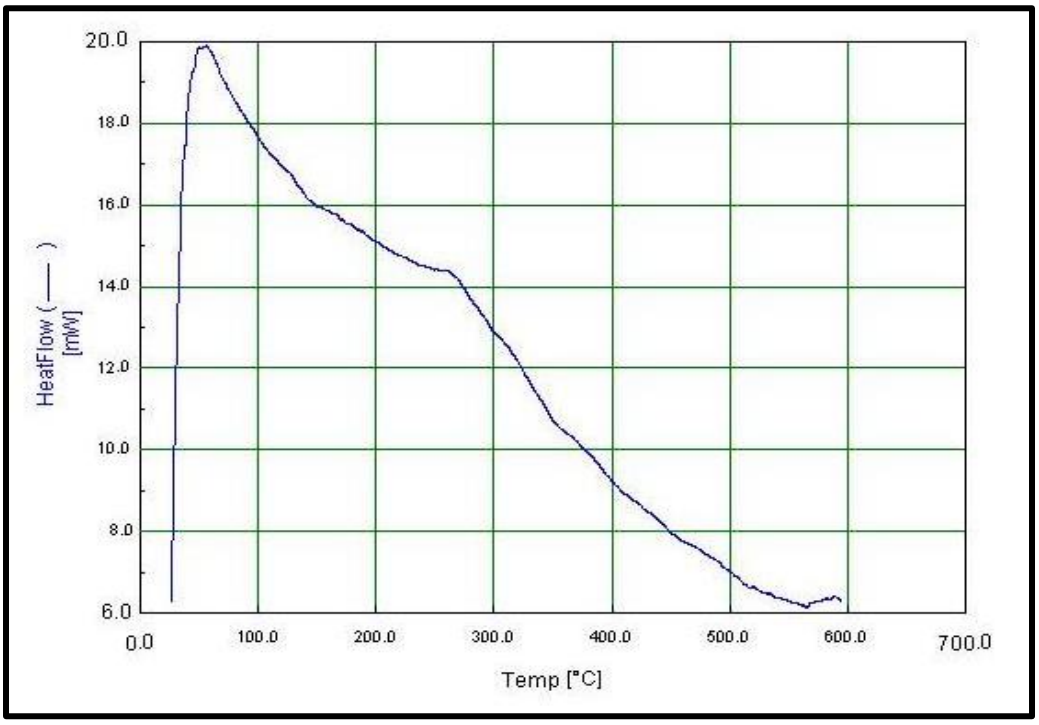

Figure 4.33 A: DSC curve of the unmodified Cu-Al-Mn alloy

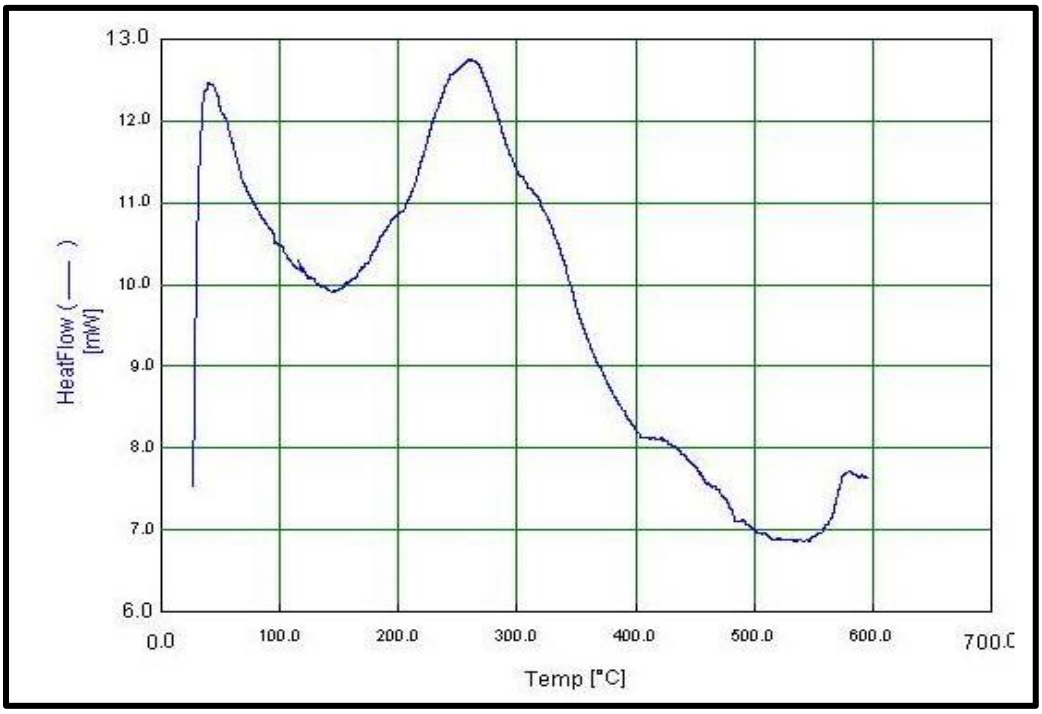

Figure 4.33 B: DSC curve of the 3 wt. %Ta modified Cu-Al-Mn alloy

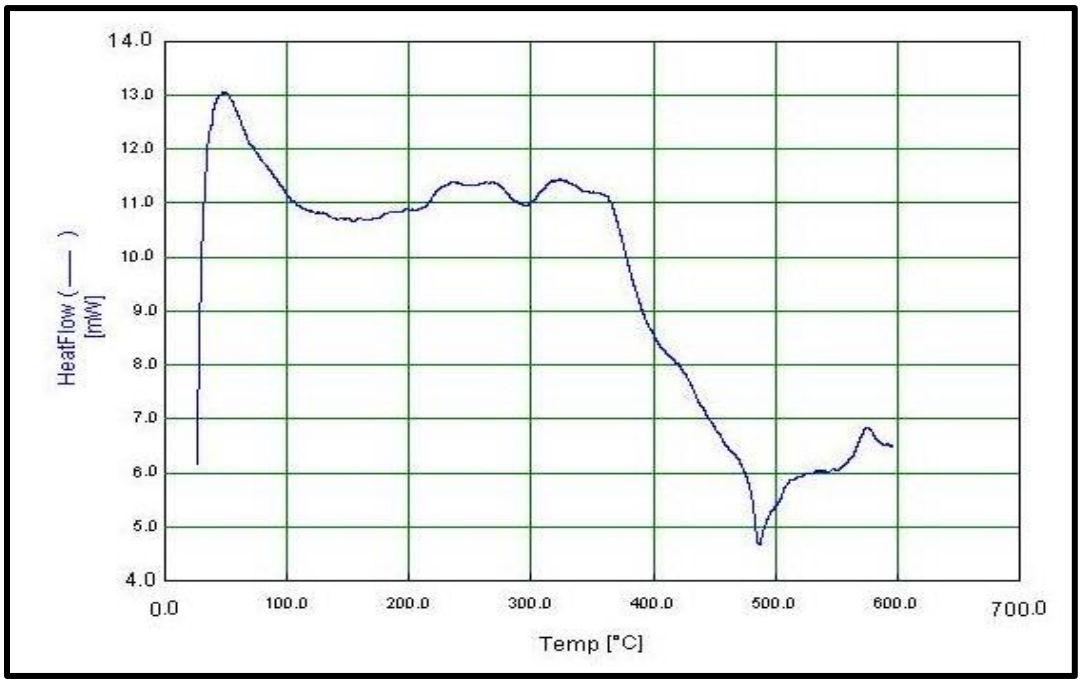

Figure 4.33 C: DSC curve of the 2 wt. % Zr modified Cu-Al-Mn- alloy

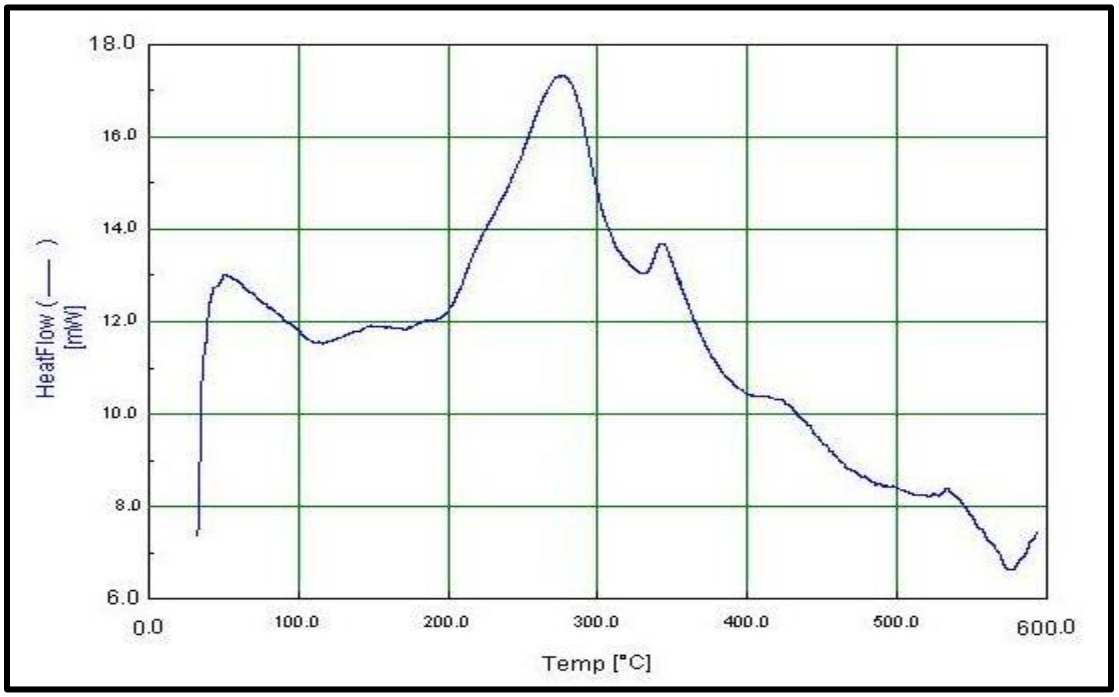

Figure 4. 33D: DSC curve of the 3 wt. %In modified Cu-Al-Mn alloy

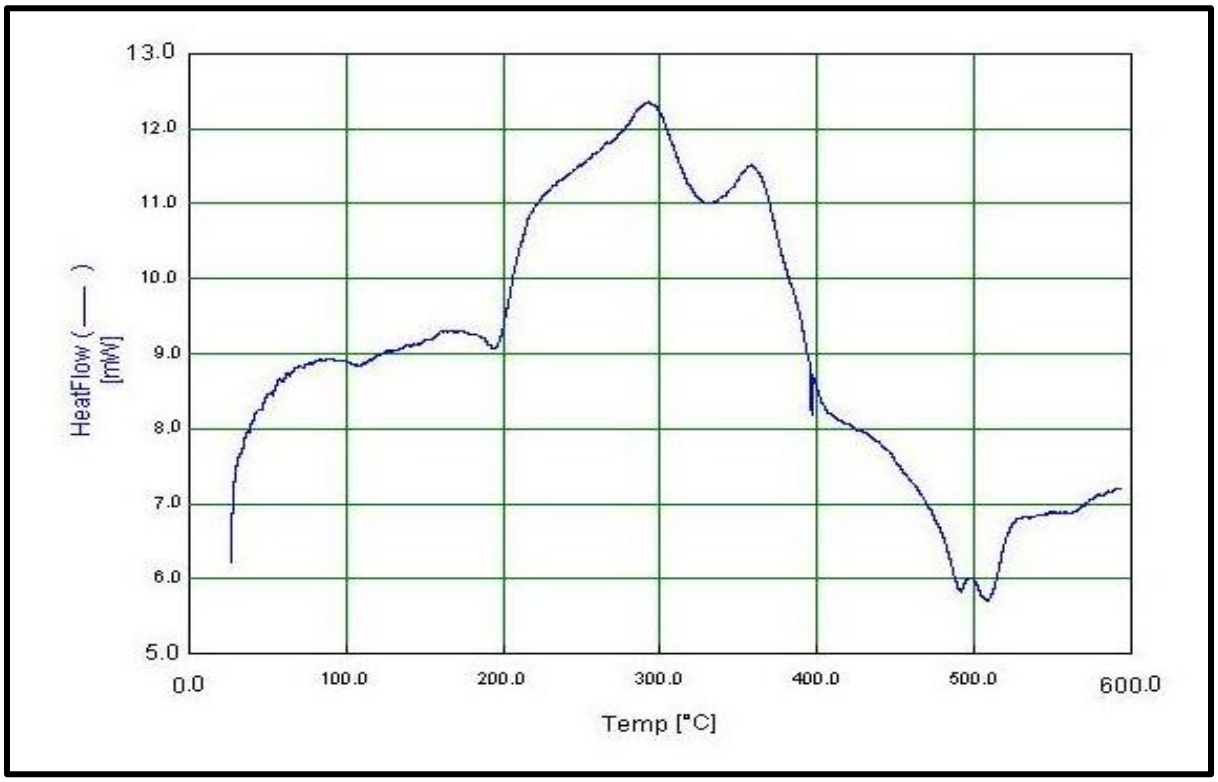

Figure 4.33 E: DSC curve of the 3 wt. % Y_2O_3 modified Cu-Al-Mn- alloy

From figures (4.33) it can be seen that the addition of Tantalum decreases the transformation temperatures (A_f) by about 75 °C. The addition of (Zirconium and Y_2O_3) decreases the transformation temperatures by 80 °C while Indium (Af) decreases 85 °C as compared with base alloy. Austinite started Temperature decreases about (5-15) °C with addition grain refinement.

The change in the transformation temperatures is attributed to the formation of precipitates, which leads to a change in the composition of the parent austenitic phase. Grain refining elements usually have very limited solubility in Cu-base shape memory alloys. Refining is largely due to the formation of small insoluble particles which either assist grain nucleation or inhibit grain growth. These elements, therefore, have only very slight effects on transformation temperature [38].

The detected (Af–As) gap is correlated with the movement of the interface between the martensite and parent phase and the consequent growth of the martensite in the alloys. So, it is observed that the difference in the (Af–As) gap occurs due to the difference in the mobility of the austenite–martensite interface [112].

4.8. Electrochemical Tests

4.8.1. Open Circuit Potential (OCP) – Time Measurements

For any closed electrical circuit, there are anodic and cathodic reactions take place. The specimens have been placed in a corrosive solution then a reaction occurs between the surface of the specimens and the corrosive medium, resulting in a potential called "open circuit potential".

The rise and fall in the potential curve mean the protective oxide layer on the surface of the metal has formed and broken out. The stability in potential value is reached (the potential value is fixed) when the anode reaction is equal to the cathodic reaction or the oxidation reaction is equal to the reduction reaction. Open circuit potential of CuAlMn (base alloy) with and without additives (Ta, In, Zr, and $Y_2O_{3,}$) with three different ratios was represented in Figures (4.34 A, B, C, and D) below.

The period from 0 up to 130 minutes and with an interval of 5 minutes were potential reported.

Table (4.3) represent the open circuit measurement and improvements% in reduce corrosion potential of alloys CuAlMn, CuAlMn-(1, 2, 3) %Ta, CuAlMn-(1, 2, and 3) %In, CuAlMn-(0.6,1, and 2) % Zr and composite specimens CuAlMn -(1, 2, and 3) % Y_2O_3 respectively after sintering.

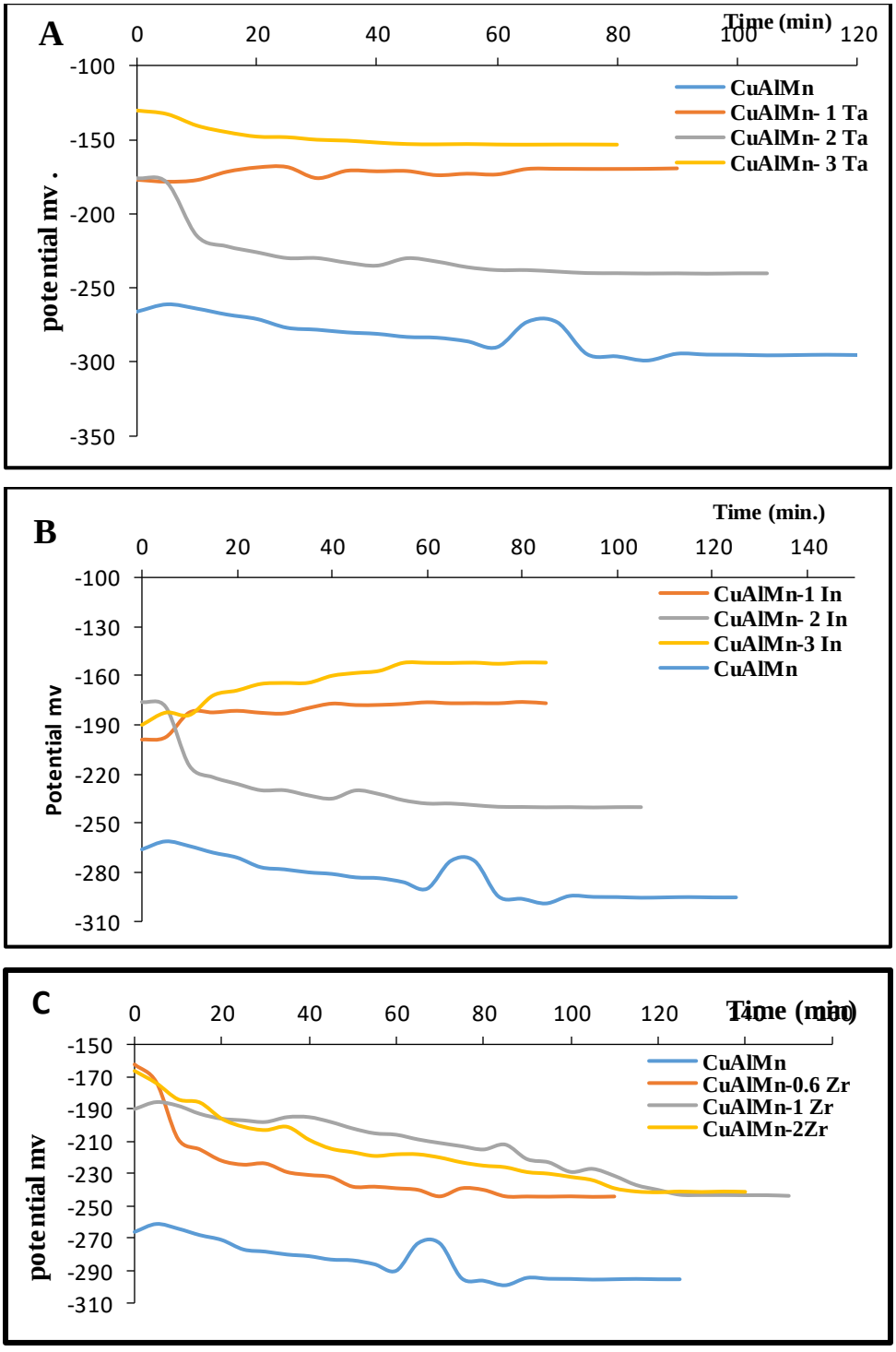

Figures (4. 34): Open circuit measurement of alloys (A) CuAlMn-(1, 2, 3) %Ta, (B) CuAlMn-(1, 2, 3) % In, (C) CuAlMn-(0.6, 1, 2) % Zr, (D) CuAlMn-(1, 2, 3) % Y_2O_3 after sintering

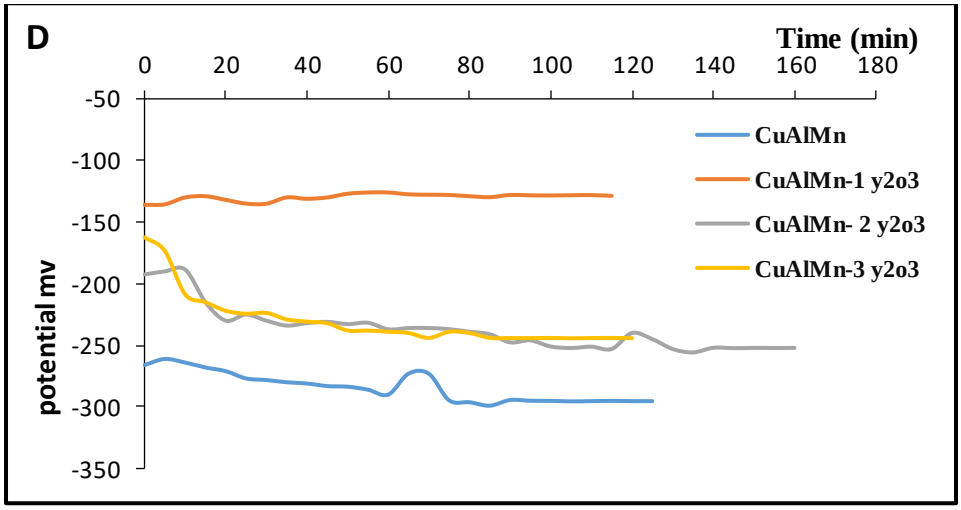

Figures (4. 34): Contend.

Table (4.3) Potential and improvement of alloys after sintering

Synthesized Composition	Code	Potential *E* (mV)
Cu-8Al-9Mn	A	-295
Cu-8Al-9Mn-1%Ta	B1	-169
Cu-8Al-9Mn-2%Ta	B2	-241
Cu-8Al-9Mn-3%Ta	B3	-153
Cu-8Al-9Mn-1%In	C1	-176
Cu-8Al-9Mn-2%In	C2	-240
Cu-8Al-9Mn-3%In	C3	-152
Cu-8Al-9Mn-0.6%Zr	D1	-244
Cu-8Al-9Mn-1%Zr	D2	-241
Cu-8Al-9Mn-2%Zr	D3	-241
Cu-8Al-9Mn-1%Y_2O_3	E1	-128
Cu-8Al-9Mn-2%Y_2O_3	E2	-252
Cu-8Al-9Mn-3%Y_2O_3	E3	-244

From Figure (4. 34A), addition (Ta) element to base alloy (CuAlMn) at three different addition ratios (1, 2 , and 3) wt. % when addition 3 % Ta, the alloy shows more nobility behavior as the potential value increases positively, the occurrence of stability in the potential value after 60 minutes from the start of the test.

The behavior of the alloys when adding Indium (In) element are shown in Figure (4.34 B), the curves show that 3 % addition by wt. of (In) element to the alloy show more nobility behavior as the potential value increases positively, the occurrence of stability in the potential value after 50 minutes from the start of the test.

Regarding the Zirconium (Zr) element addition of 1% and 2% by wt., as shown in Figure (4.34C) the alloy with (1and 2) % additives show similarity in potential behavior.

The behavior of the composite specimens differs according to the different proportions when adding yttrium oxide (Y_2O_3) as shown in Figure (4. 34D), where when adding 1% the potential value increases in the positive direction, while when increasing the percentages of addition of Y_2O_3, the potential values are directed in the negative direction.

From Table (4.4) can be noticed that the corrosion potential reduces by adding these elements (Ta, Zr, and In) and Y_2O_3 ceramic particles.

The best improvement belongs to Cu-8Al-9Mn-1%Y_2O_3 composite.

There is a difference in potential corrosion value between the CuAlMn alloy and CuAlMn-x%Zr, CuAlMn-x%Ta, CuAlMn-x%In, CuAlMn-x%Y_2O_3 composite, this means the alloy show more nobility when these additives are added.

Figures (4.35A, B, C, D) represent the open circuit measurement of alloys CuAlMn, CuAlMn-(1, 2, 3) %Ta, CuAlMn-(1, 2, 3) %In, CuAlMn-(0.6, 1, 2) % Zr and CuAlMn-(1, 2, 3) % Y_2O_3 respectively after Aging heat treatment in 300°C for 1 hr.

Table (4.5) represent the open circuit potential and improvement of alloys (A, B1, B2……E3) after Aging

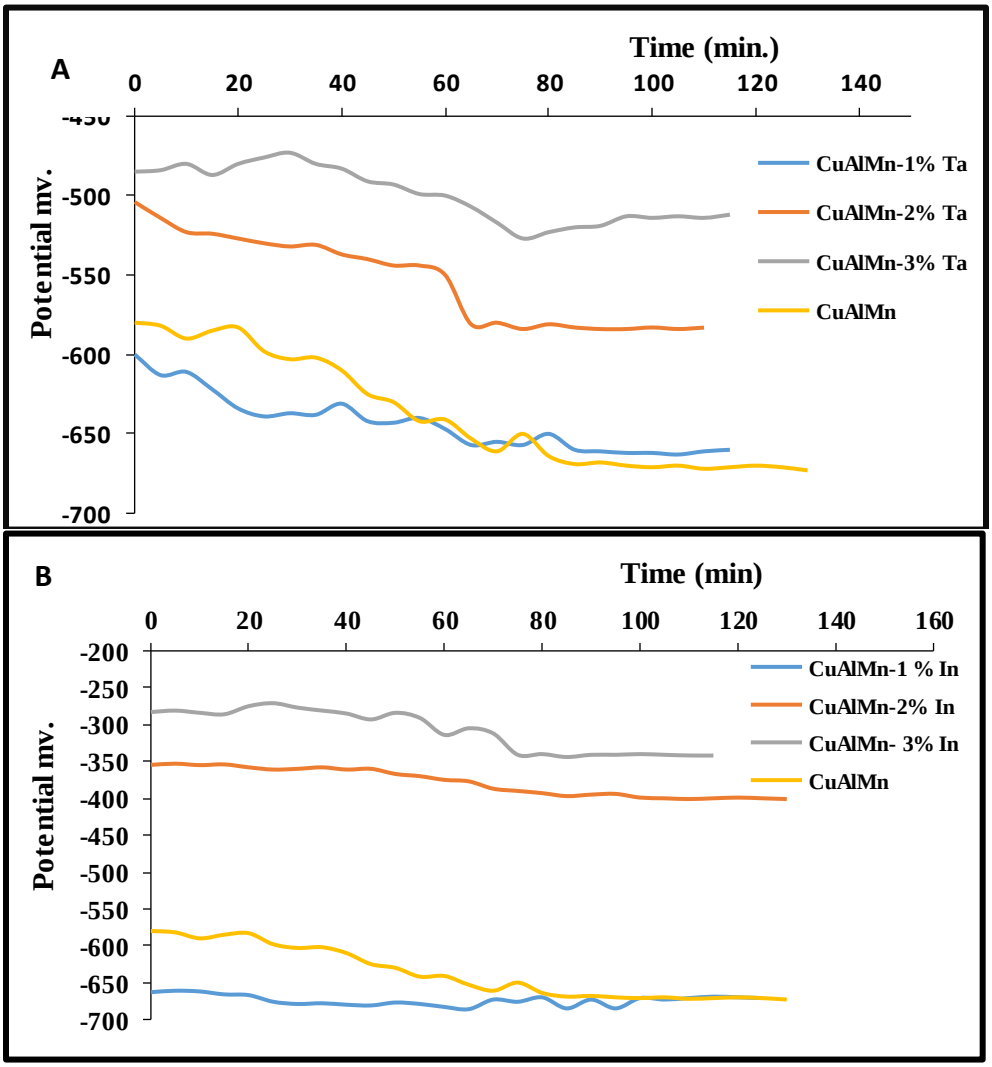

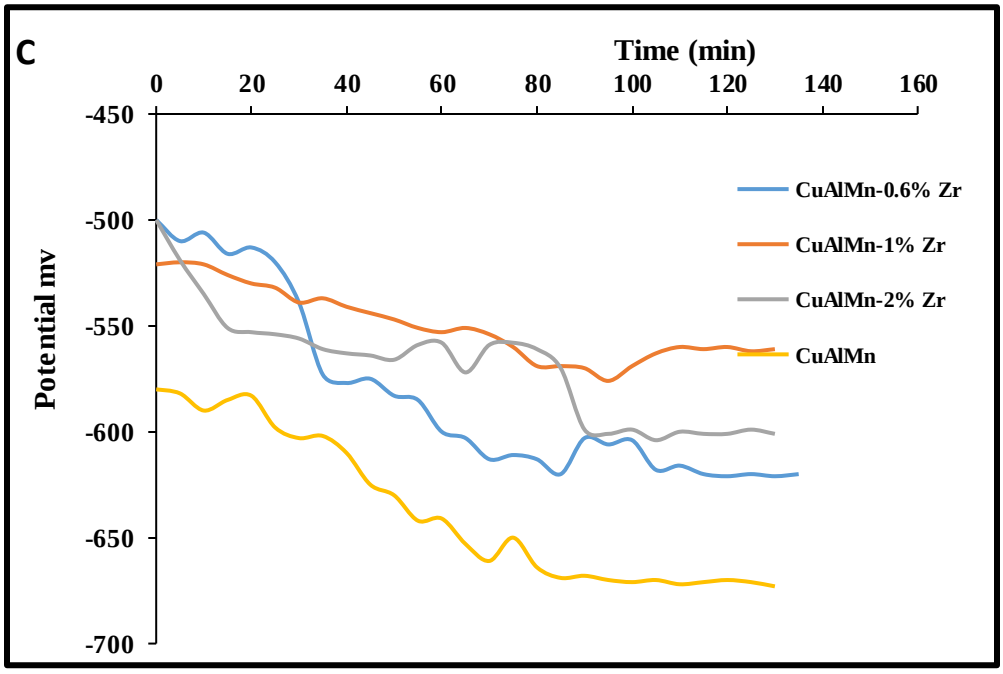

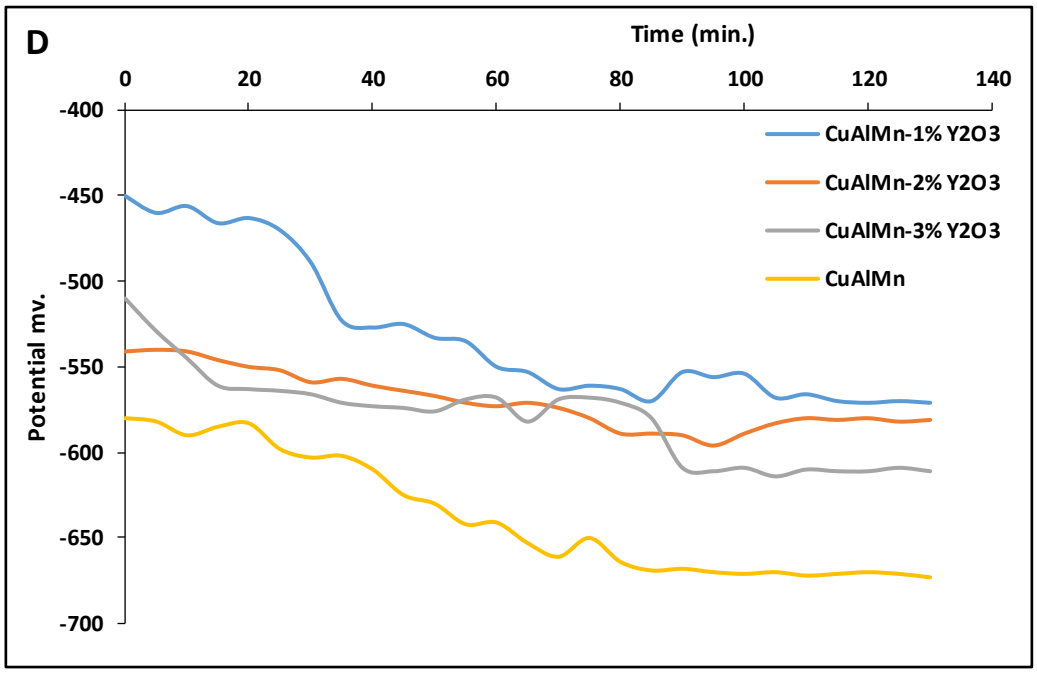

Figures (4.35): OCP measurement of alloys (A) CuAlMn-(1,2,3) %Ta, (B) CuAlMn-(1,2,3) %In, (C) CuAlMn-(0.6,1,2) % Zr, (D) CuAlMn-(1,2,3) % Y_2O_3 after aging heat treatments

Table 4.3: potential and improvement of alloys after aging

Synthesized Composition	Code	Potential *E* (mV)
Cu-8Al-9Mn	A	-671
Cu-8Al-9Mn-1%Ta	B1	-661
Cu-8Al-9Mn-2%Ta	B2	-584
Cu-8Al-9Mn-3%Ta	B3	-513
Cu-8Al-9Mn-1%In	C1	-670
Cu-8Al-9Mn-2%In	C2	-401
Cu-8Al-9Mn-3%In	C3	-341
Cu-8Al-9Mn-0.6%Zr	D1	-621
Cu-8Al-9Mn-1%Zr	D2	-661
Cu-8Al-9Mn-2%Zr	D3	-600
Cu-8Al-9Mn-1%Y_2O_3	E1	-570
Cu-8Al-9Mn-2%Y_2O_3	E2	-580
Cu-8Al-9Mn-3%Y_2O_3	E3	-611

From Figure (4.35A, B, C, and D) and Table (4. 5) can be noticed that the corrosion potential reduces by the addition of these elements (Ta, Zr, and In) and Y_2O_3. The best improvement belongs to Cu-8Al-9Mn-3%In .

4.8.2. Linear Polarization Curves

Corrosion behavior has been studied by linear polarization test for the specimens after sintering and after quenching heat treatment in (3.5 % NaCl, pH= 6.84) have been presented as the following:

4.8.2.1. Corrosion Behavior in 3.5% NaCl Solution after Sintering

The corrosion rate (mm/y), corrosion potential (E_{corr}), and corrosion current density (Icorr) of specimen were calculated from the polarization curves presented in Table (4.5). The potentiodynamic polarization behavior of the alloy in 3.5 % of NaCl solution after sintering is presented below in Figure (4.36A, B, C, and D).

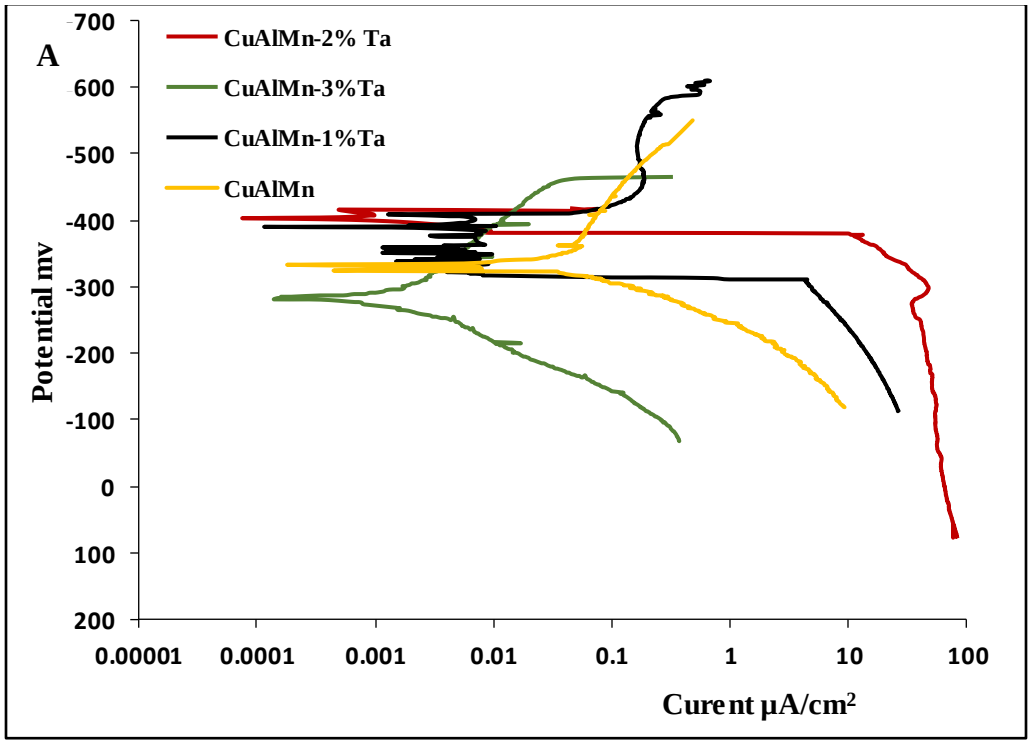

Figure (4.36): Potentiodynamic curves for CuAlMn alloy after sintering state, in 3.5% NaCl solution. A) CuAlMn (1,2,3) %wt. Ta, B) CuAlMn (0.6,2,3) %wt. Zr alloy, C) CuAlMn-(1,2,3) %wt. In, (D) CuAlMn-(1,2,3) Y_2O_3%wt.

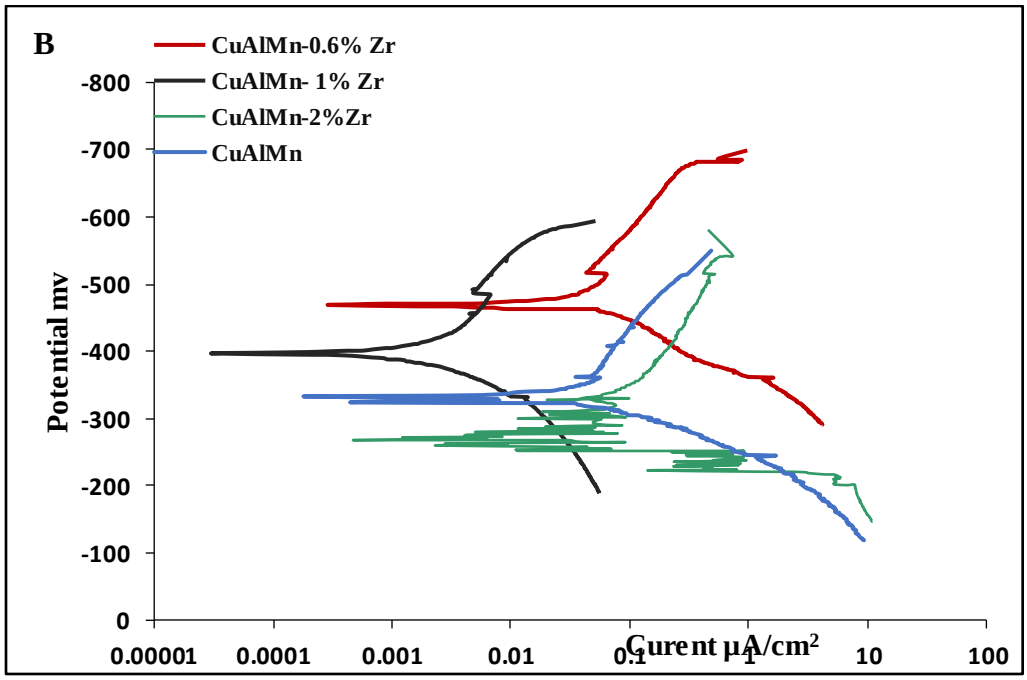

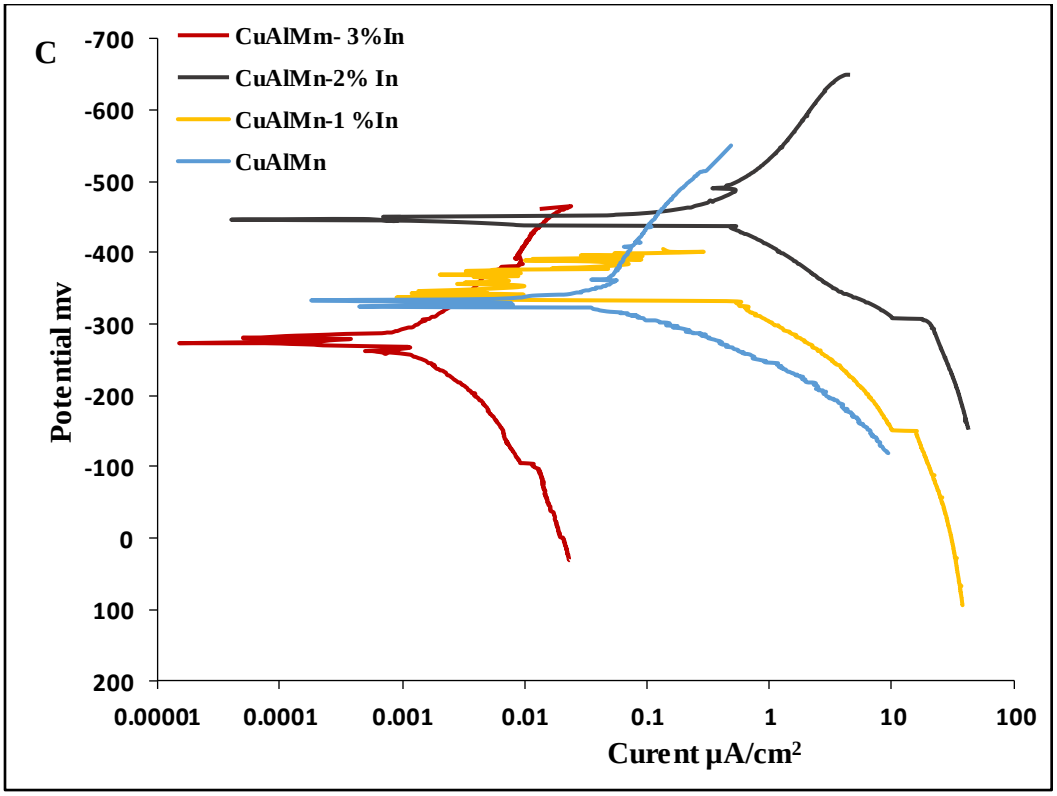

Figures (4.36): contend

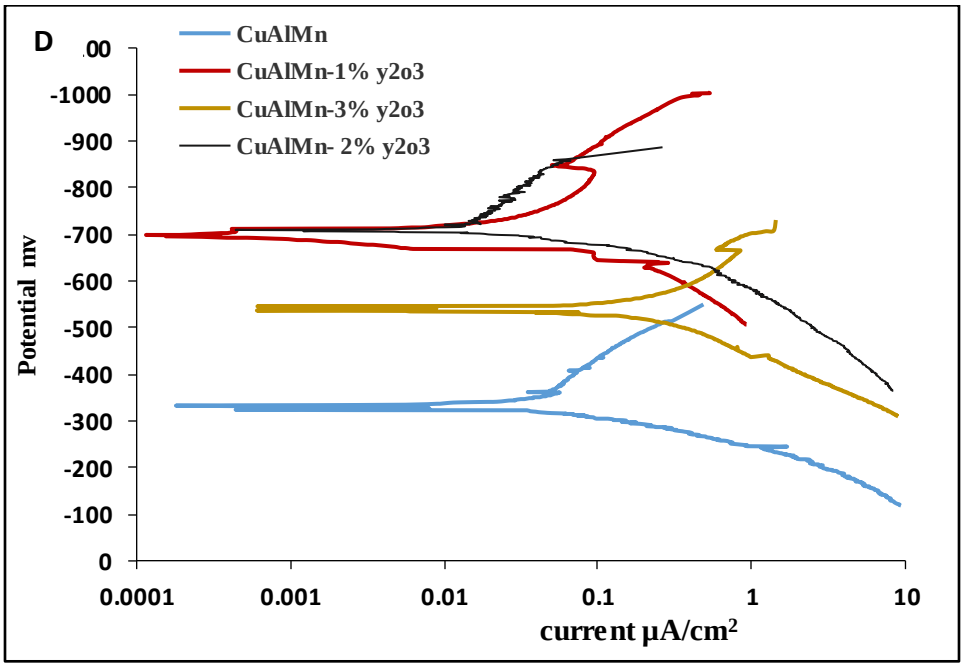

Figures (4.36): contend

Table (4.5): Electrochemical parameters of ternary Cu-Al-Mn and quaternary SMAs in 3.5 wt.% NaCl solution obtained from the polarization test

Synthesized Composition	Code	Current density Icorr (μA/cm^2)	Potential E corr (mV versus SCE)	Corrosion rate $C.R$ (mm/year)
Cu-8Al-9Mn	A	156.74	-528.5	2.801
Cu-8Al-9Mn-1%Ta	B1	2.36	-391.6	0.0419
Cu-8Al-9Mn-2%Ta	B2	136.34nA	-403.3	2.27*10^-3
Cu-8Al-9Mn-3%Ta	B3	719.86 nA	-283.1	0.0116 10^-3
Cu-8Al-9Mn-1%In	C1	411.2 nA	-356.0	8.187*10^-3
Cu-8Al-9Mn-2%In	C2	3.29	-450.9	0.0687
Cu-8Al-9Mn-3%In	C3	721.6nA	-280.6	0.0154
Cu-8Al-9Mn-0.6%Zr	D1	35.87	-450	0.625
Cu-8Al-9Mn-1%Zr	D2	1.36	-397.8	0.023
Cu-8Al-9Mn-2%Zr	D3	1.07	-307.2	0.0182

Synthesized Composition	Code	Current density Icorr (μA/cm^2)	Potential E corr (mV versus SCE)	Corrosion rate $C.R$ (mm/year)
Cu-8Al-9Mn-1%Y_2O_3	E1	4.34	-662.1	0.074
Cu-8Al-9Mn-2%Y_2O_3	E2	504.9nA	-701.8	8.47*10^-3
Cu-8Al-9Mn-3%Y_2O_3	E3	39.84	-539.8	0.617

Table (4.5) can be noticed that the corrosion rate in 3.5 wt.% NaCl solution after sintering reduce by adding these elements (Ta, Zr, and In) and Y_2O_3 ceramic particles. The best an improvement belongs to Cu-8Al-9Mn-2%Ta with improvement ratio in reducing corrosion rate about 99.91%

Tafle curves can be estimated and classified into the cathodic branch of the polarization curve represents hydrogen evolution while the anodic branch shows alloy dissolution. The anodic branch of the polarization curve can be divided into three regions: the apparent Tafel region, a region where there is a tendency of the electrode to passivity, and the third region in which the current density rises again with the positive potential changes. This anodic behavior is the characteristic of the dissolution of Copper and its alloys in sodium hydroxide solution [140].

In the Tafel-type active region, the anodic slope was around 0.35 mV/second. The current density decreases to some extent due to the formation of the corrosion products on the electrode surface, which has some protective effect and reducing the active dissolution of metals from the surface. This decrease in current density is usually explained by the formation of cuprous oxide (Cu_2O), surface adsorbed precipitates, but it can be also observed that the result of the formation of Aluminum oxide/hydroxide layer which has been found on the surface of the alloy.

The possible reactions for the formation of corrosion products ($CuC1_2$ and Cu_2O) on pure copper are as the following [139]:

$$Cu + 2C1^- \rightarrow CuCl_2^- + 1e^- \quad (4.1)$$

$$2Cu\,C1_2 + H_2O^- \rightarrow Cu_2O + 4CL^- + 2H^+ \quad (4.2)$$

$CuC1_2^-$ complex formation developed either due to the dissolution of copper or CuCl. In fact, it was proposed that cuprous chloride (CuCl) is the initial corrosion product when Cu reacts with NaCl. The stability of Cu_2O depends on the chloride ions concentration.

The corrosion surface of Cu base alloy might be composed of different products (Cu_2O, $CuC1_2$, $A1_2O_3$, $AlCl_4$, etc.). The formation of Cu_2O and $CuC1_2$ and their characteristics are explained for corrosion of pure Cu (Equation 4.1 and 4.2). Al reacts with Cl- ions and forms $AlC1_4$ as per Eq. (4.3). Since the chlorides are thermodynamically unstable in the presence of oxygen and these chlorides react with water and forms an $A1_2O_3$ oxide layer according to Eq. (4.4), which protects the sample surface [86].

$$Al + 4C1^- \rightarrow AlCl_4 + 3e- \quad (4.3)$$

$$AlCl^- + 3\,H_2O^- \rightarrow A1_2O_3 + 6H + 8C1^- \quad (4.4)$$

When Al is present on the electrode surface aluminum chloride salt is formed, which is readily dissolved as an $AlCl^+$ ion in addition to the dissolution of copper as a copper chloride complex ion. At more potentials the current density decreases to some extent due to the formation of corrosion products on the electrode surface, which have some protective effect and reduce the active dissolution. This decrease comes from the decreases in electrode potential for oxidation and a decrease in current density is

usually explained by formation of cuprous chloride (CuCl), cuprous oxide (Cu_2O) ,and Aluminum oxide [140].

4.8.2.2. Corrosion behavior in 3.5% NaCl solution after Aging Heat Treatment

The potentiodynamic polarization behavior of the alloy in 3.5% of NaCl solution after Aging heat treatment is presented below in Figures (4.37 A, B, C, D).

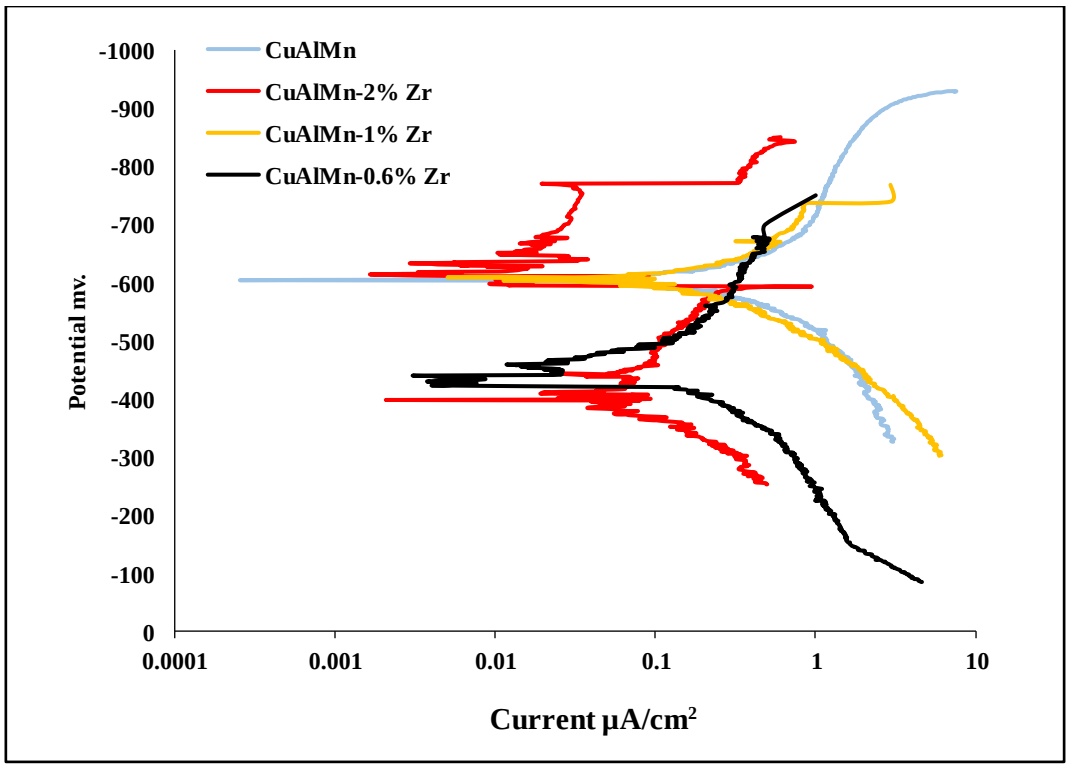

Figure (4. 37): Potentiodynamic curves for CuAlMn alloy after Aging in 3.5% NaCl solution. A) CuAlMn- (0.6, 1, 2) wt. % Zr alloy, B) CuAlMn- (1, 2, 3) %wt. Ta and C) CuAlMn - (1, 2, 3) %wt. In, D) CuAlMn--(1, 2, 3) %wt. Y_2O_3

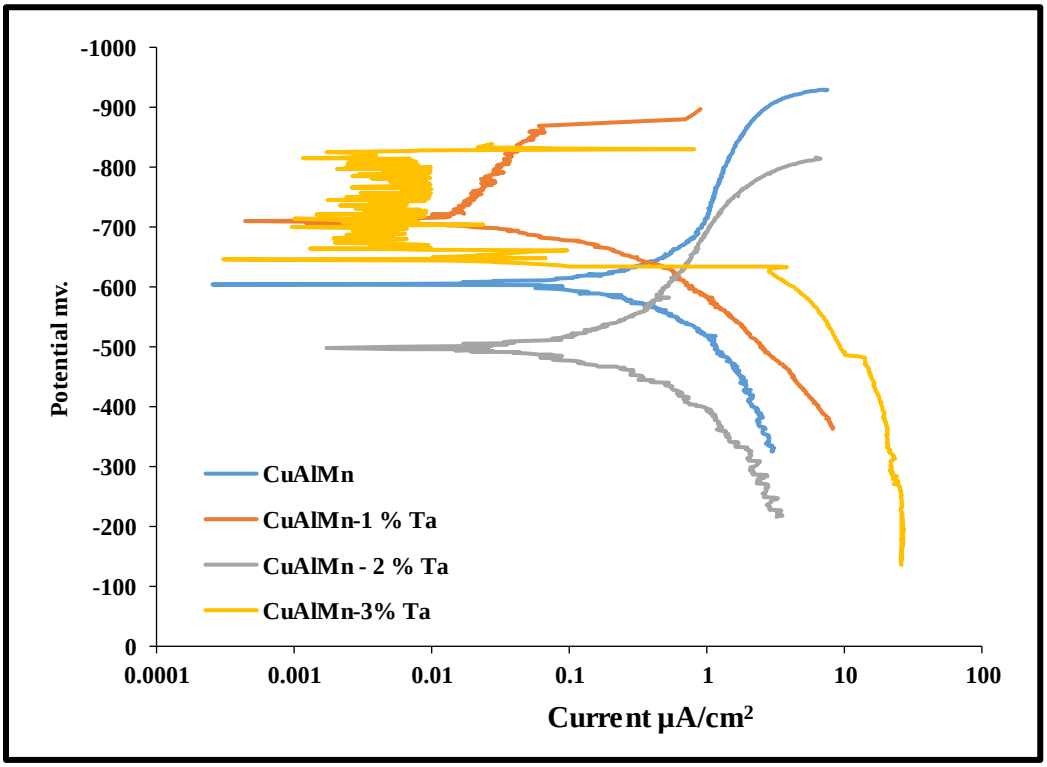

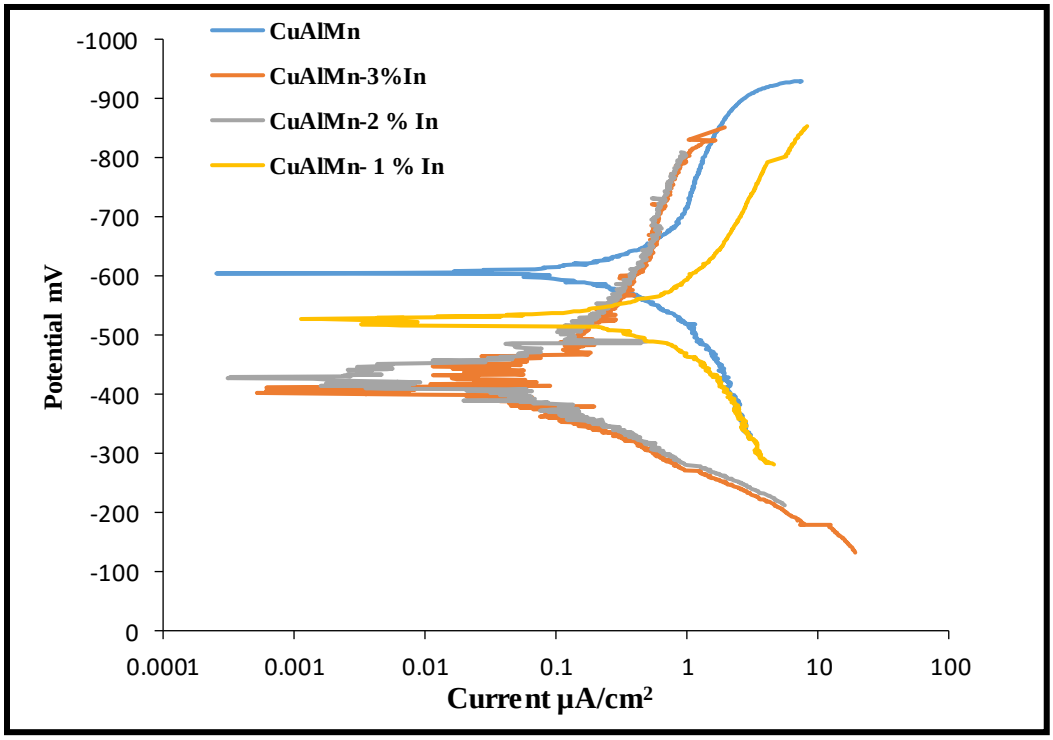

Figure (4.37): contend

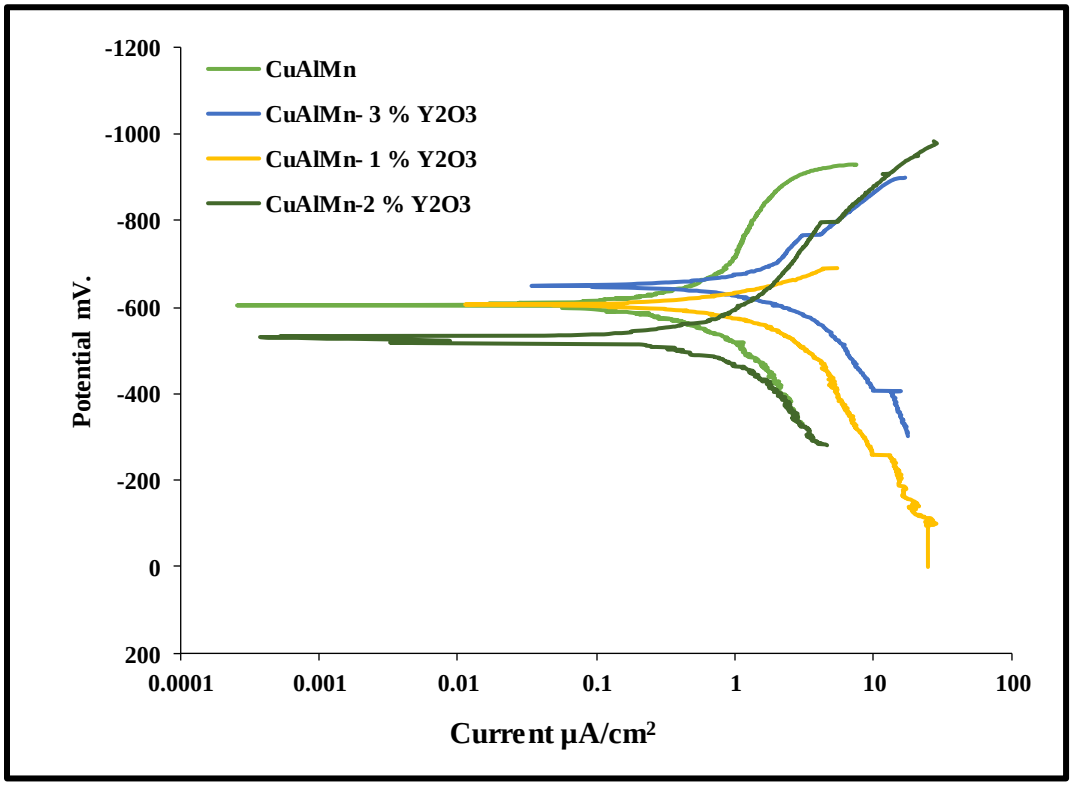

Figure (4.37): contend

Representative curves of CuAlMn-2% wt. Zr and CuAlMn-3% wt. Ta is shown in Figures (4.37A and B) respectively. The first almost linear part corresponds to the apparent Tafel region and a critical current density (i_c) is reached, then the electrode presents a tendency to passivate with a decrease in the current. After that, the current rises again with the increase of the potential until the scanning is reversed in the limiting current region. This is the typical anodic behavior for the dissolution of Copper and Copper alloys in chloride solutions [140,141].

Table (4.6): Current density I_{corr} ($\mu A/cm^2$), potential and corrosion rate $C.R$ (mm/y) of alloys (A, B1, B2, B3 ……. E3) shape memory alloys after aging

Synthesized Composition	Code	Current density I_{corr} ($\mu A/cm^2$)	Potential E_{corr} (mV)	Corrosion rate $C.R$ (mm/year)
Cu-8Al-9Mn	A	115.92	-602	2.06
Cu-8Al-9Mn-1%Ta	B1	11.55	-711.6	0.205
Cu-8Al-9Mn-2%Ta	B2	10.11	-420.10	0.182
Cu-8Al-9Mn-3%Ta	B3	3.24	-643.5	0.0575
Cu-8Al-9Mn-1%In	C1	39.84	-539.8	0.777
Cu-8Al-9Mn-2%In	C2	13.41	-430.6	0.280
Cu-8Al-9Mn-3%In	C3	28.70	-498.3	0.611
Cu-8Al-9Mn-0.6%Zr	D1	35.87	-458.2	0.625
Cu-8Al-9Mn-1%Zr	D2	75.85	-603.3	1.29
Cu-8Al-9Mn-2%Zr	D3	36.34nA	-403	6.36*10^-4
Cu-8Al-9Mn-1%Y_2O_3	E1	85	-601.7	1.454
Cu-8Al-9Mn-2%Y_2O_3	E2	30.74	-513.10	0.5158
Cu-8Al-9Mn-3%Y_2O_3	E3	36.95	-647.6	0.572

From Table (4.7) can be noticed that the corrosion after aging reduces by adding these elements (Ta, Zr, and In) and Y_2O_3. The best an improvement belongs to Cu-8Al-9Mn-2%Zr with an improvement ratio in reducing corrosion raita about 99.68%. The very high fraction of grain boundaries in the microstructure is likely to reduce corrosion rates in two ways: (1) accelerating the passivation kinetics, and (2) reduce the intensity of galvanic couple between grain interior, and grain boundary [118].

The effects of polarization on the surface of alloys (CuAlMn, CuAlMn-3%In, CuAlMn-3% Ta, CuAlMn-3% Y_2O_3 and CuAlMn-2% Zr were shown in Figure (4.38A, B, C, D and E).

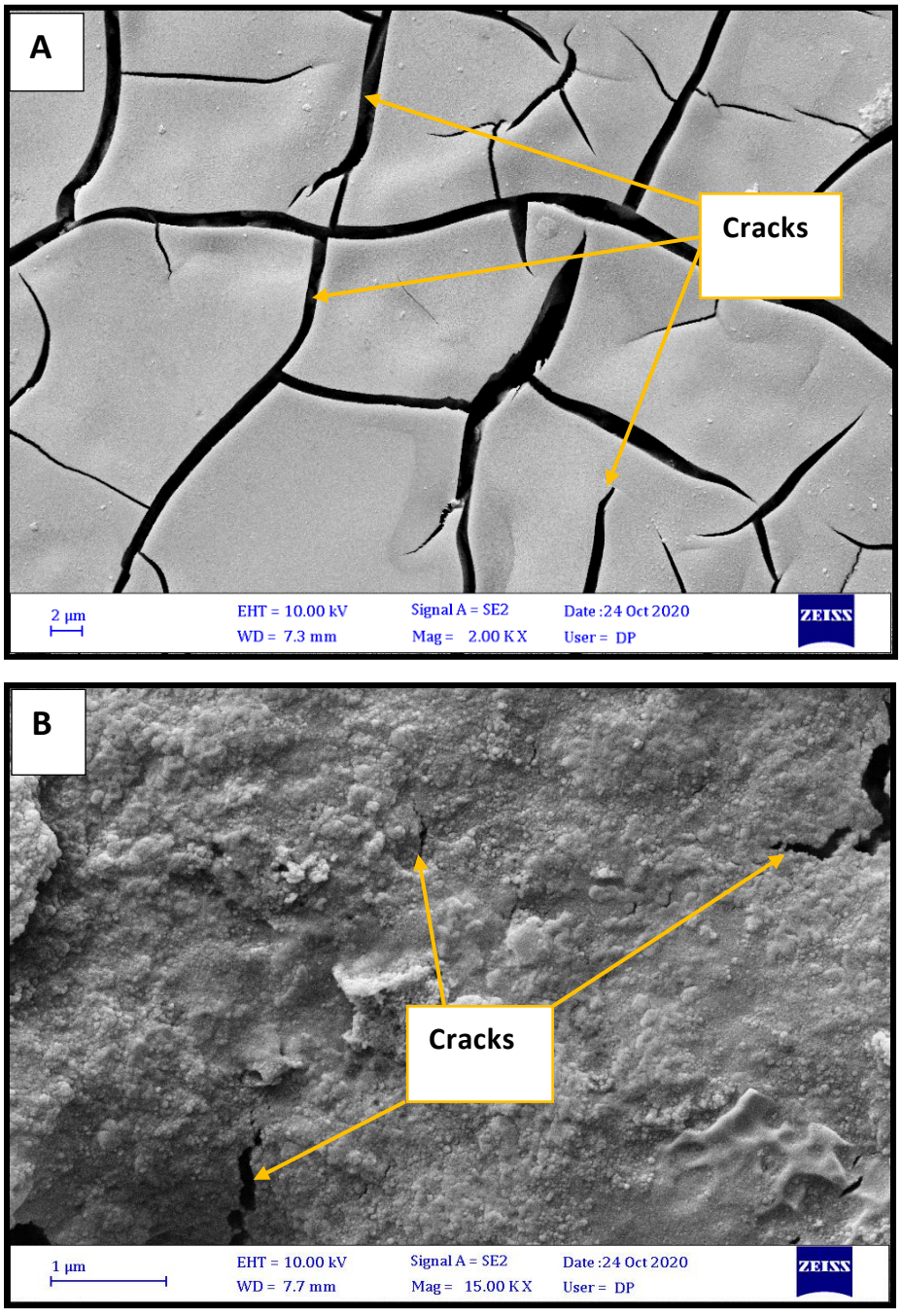

Figure (4.38): Surface morphology of alloys after polarization test (A) CuAlMn, (B) CuAlMn-3%In, (C) CuAlMn-3%Ta, (D) CuAlMn- 3%Y_2O_3, (E) CuAlMn-0.6%*Zr*

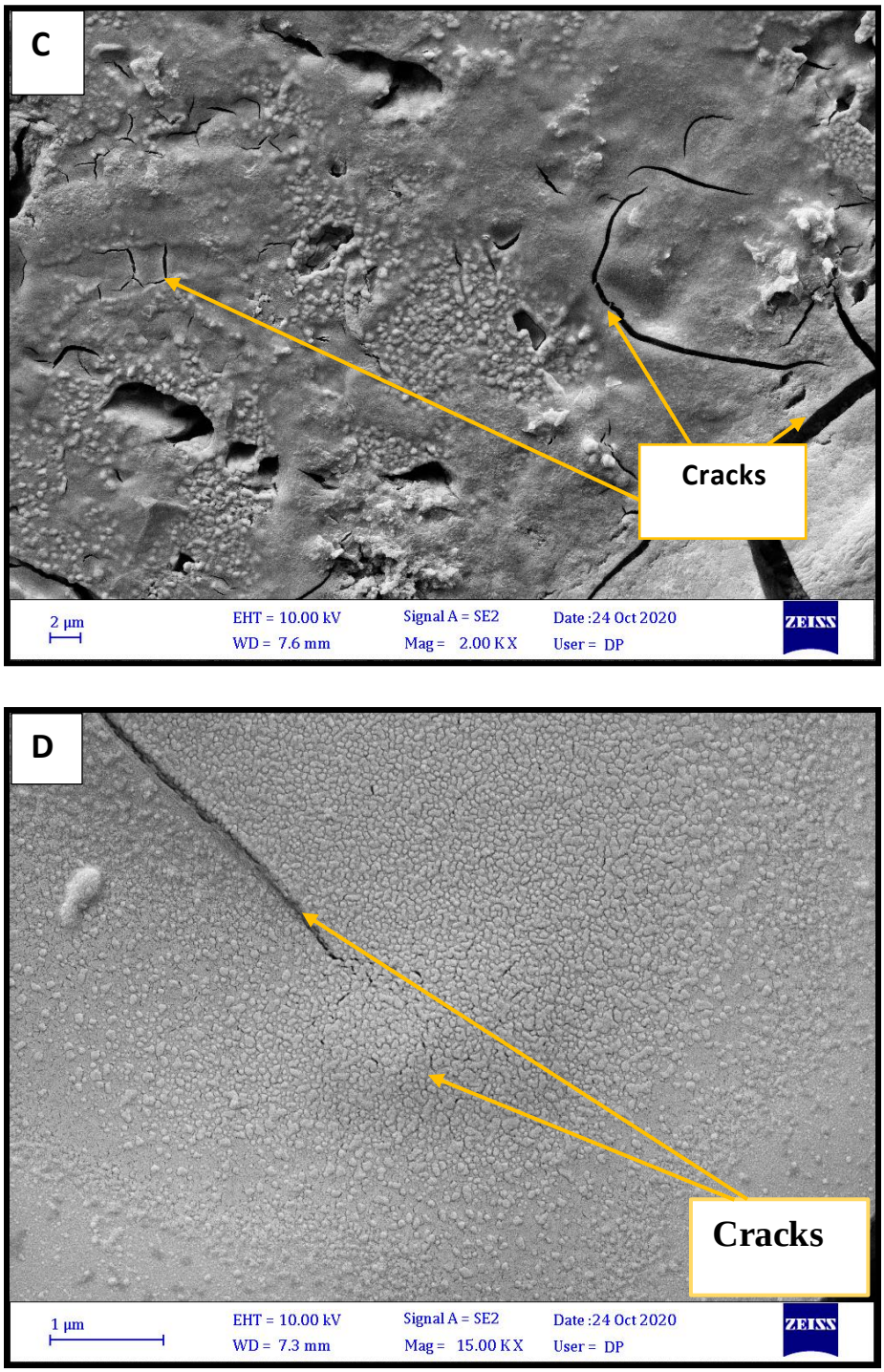

Figure (4.38): contend

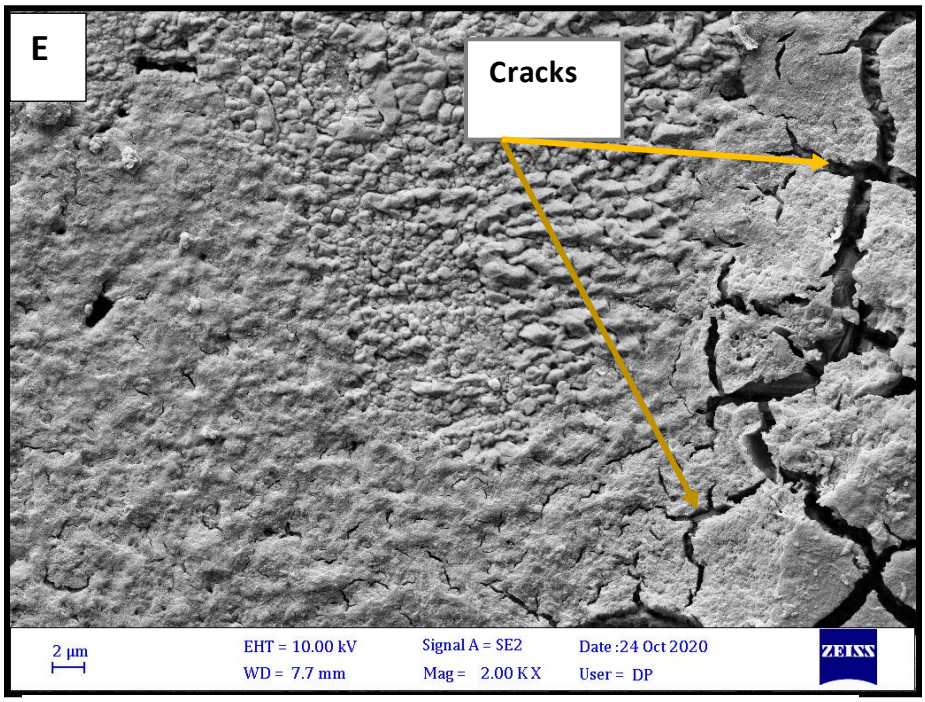

Figure (4.38): contend

From Figure (4.38) can be seen that the surface of base alloy as shown in Figure (4.38A) have more cracks in the oxide layer as compared with the surface of alloys with addition (In, Ta, Y_2O_3, and Zr) as shown in Figure (4.38 B, C, D, and E) respectively. This is mean that the oxide become more adhesive and has less brittleness. Therefore, that the alloys become more resistant to corrosion and more noble. The above results explained a decrease in corrosion current with alloys addition and ceramic particles (Y_2O_3).

4.9. Damping Test

Internal friction is one origin of the energy absorption of SMAs. It is considered that the damping effect resulting from internal friction is caused by the resistance to the movement of the martensitic and austenitic interface or the boundary between martensite variants in the narrow temperature range where the energy barriers to such

interface movement are quite low [142]. The interfaces, including twin boundaries, thermoelastic martensite variant interfaces, and stress- induced martensite variant interfaces, can move repeatedly under external alternating stress [143,144]. As the result of interfaces movement, the mechanical energy is dissipated. The variation of damping after sintering and after aging heat treatment with the grain refining additions is plotted in Figures (4.39-40) and Table (4.7-8) respectively from Figures plotted in appendix B. From Figure (4.39) and Table (4.7) can be noticed the damping capacity after sintering improved by adding these elements (Ta, Zr, and In) and Y_2O_3 ceramic particles.

Table (4.7): Damping capacity of alloys CuAlMn and CuAlMn-X (Ta, Zr, In and Y_2O_3 after sintering

Synthesized Composition	Code	logarithmic decrement δ
Cu-8Al-9Mn	A	0.081
Cu-8Al-9Mn-1%Ta	B1	0.091
Cu-8Al-9Mn-2%Ta	B2	0.1103
Cu-8Al-9Mn-3%Ta	B3	0.0536
Cu-8Al-9Mn-1%In	C1	0.1103
Cu-8Al-9Mn-2%In	C2	0.046
Cu-8Al-9Mn-3%In	C3	0.079
Cu-8Al-9Mn-0.6%Zr	D1	0.129
Cu-8Al-9Mn-1%Zr	D2	0.039
Cu-8Al-9Mn-2%Zr	D3	0.053
Cu-8Al-9Mn-1%Y_2O_3	E1	0.069
Cu-8Al-9Mn-2%Y_2O_3	E2	0.0883
Cu-8Al-9Mn-3%Y_2O_3	E3	0.121

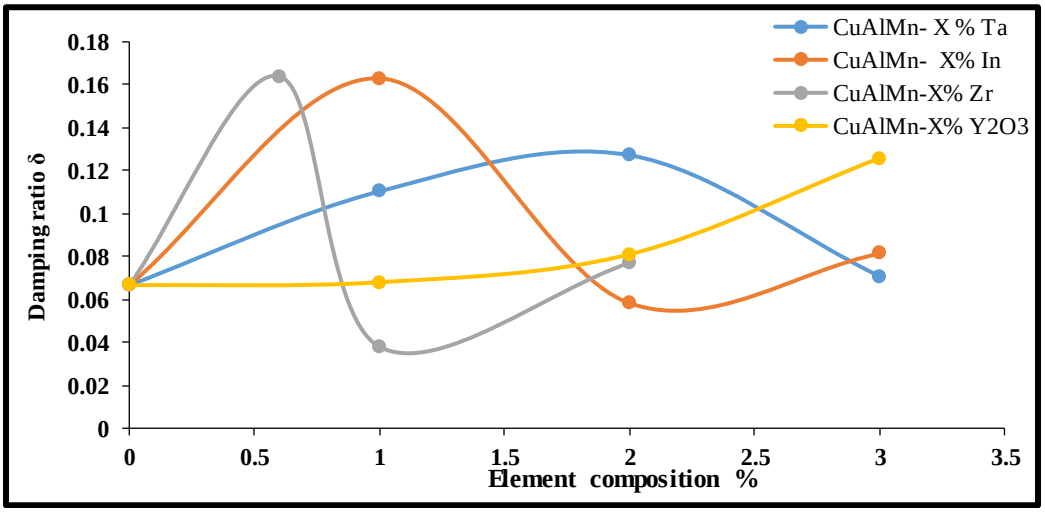

Figure (4.39): Damping ratio verse composition of alloys (A, B1…. E3) after sintering

Table (4.8): Damping capacity of alloys CuAlMn and CuAlMn-X (Ta, Zr, In and Y_2O_3 after Aging heat treatment

Synthesized Composition	Code	logarithmic decrement δ
Cu-8Al-9Mn	A	0.0666
Cu-8Al-9Mn-1%Ta	B1	0.1103
Cu-8Al-9Mn-2%Ta	B2	0.1272
Cu-8Al-9Mn-3%Ta	B3	0.0708
Cu-8Al-9Mn-1%In	C1	0.163
Cu-8Al-9Mn-2%In	C2	0.0583
Cu-8Al-9Mn-3%In	C3	0.0813
Cu-8Al-9Mn-0.6%Zr	D1	0.164
Cu-8Al-9Mn-1%Zr	D2	0.038
Cu-8Al-9Mn-2%Zr	D3	0.077
Cu-8Al-9Mn-1%Y_2O_3	E1	0.068
Cu-8Al-9Mn-2%Y_2O_3	E2	0.081
Cu-8Al-9Mn-3%Y_2O_3	E3	0.1258

From Figure (4.40) and Table (4. 8) can be noticed the damping capacity improved by adding these elements (Ta, Zr, In) and Y_2O_3 ceramic powder. The resulted was good agree with Naoki Koeda et. al. [157] and Zhixian Jiao [145].

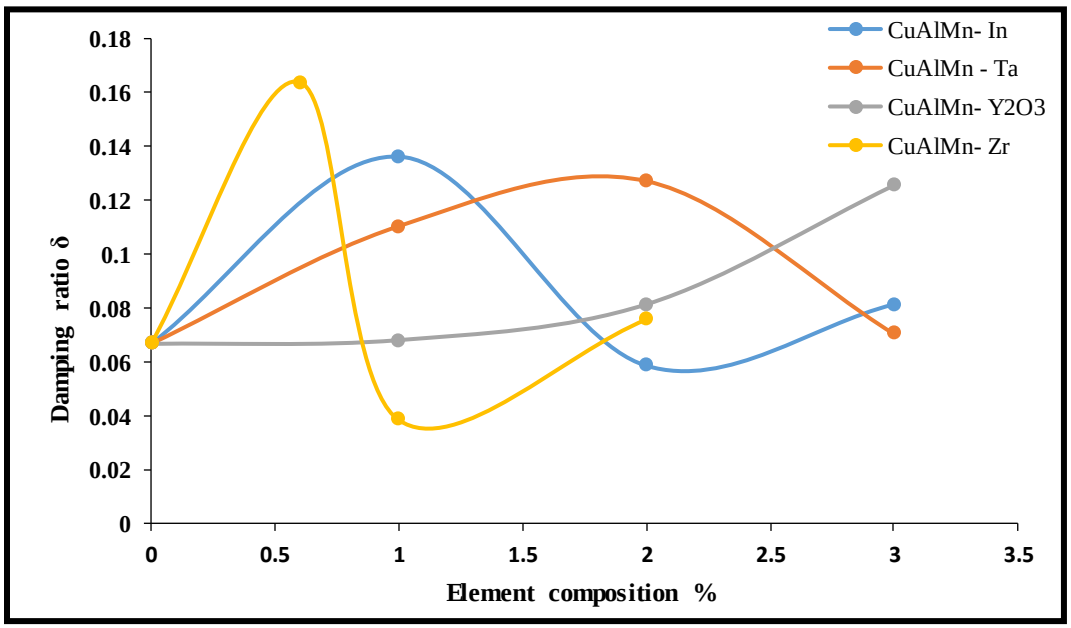

Figure (4.40): Damping ratio verse composition of alloys code (A, B1…. E3) after Aging

The increase of martensite and the disappearance of α-phase also explains why the damping capacity of Cu–8Al–9Mn alloy remarkably increased after Aging treated at 300°C. Note that the martensite plates were thicker after Aging, as shown in Figure (4.26 A-D).

The increase in the thickness of the martensite plates would decrease the amount of interfaces in the thermoelastic martensite variant. The above analysis indicates that the shape memory effect in Cu-based alloys was mainly dependent on the amount of

the martensite, while their damping capacity was dependent on not only the amount but also the thickness of the martensite plates [107].

The damping capacity is affected by alloy compositions, processing histories, and test methods [142,146].

The grain refinement has two opposite influencing factors on the damping of the CuAlMn SMA. The first one is the promoting factor for the enhancement of damping, which arises from the increase in the density of interfaces. The second one is the restraining factor, which arises from the decrease of the mobility of various interfaces due to grain constraint [147].

Generally, alloys with big grains have higher damping levels, but worse mechanical strength and ductility because grain boundaries pin other crystal defects. Therefore, grain coarsening cannot always be used to increase damping and it is important to achieve high damping also in small grained metals [148].

Figure (4.40) and Figure (4.27 A-E) from where it can be seen that the alloy with the biggest grains has the highest damping level for all strain amplitudes. This is reasonable because a smaller grain suppresses the martensitic transformation and leads to higher hysteresis between the transformation's temperature

4.10. Erosion-Corrosion

Erosion rate of CuAlMn and CuAlMn- X (Ta, Zr, In and Y_2O_3) after sintering in (950 °C for 4hr.) shown in Figures (4.41 A- D) and Table (4. 10).

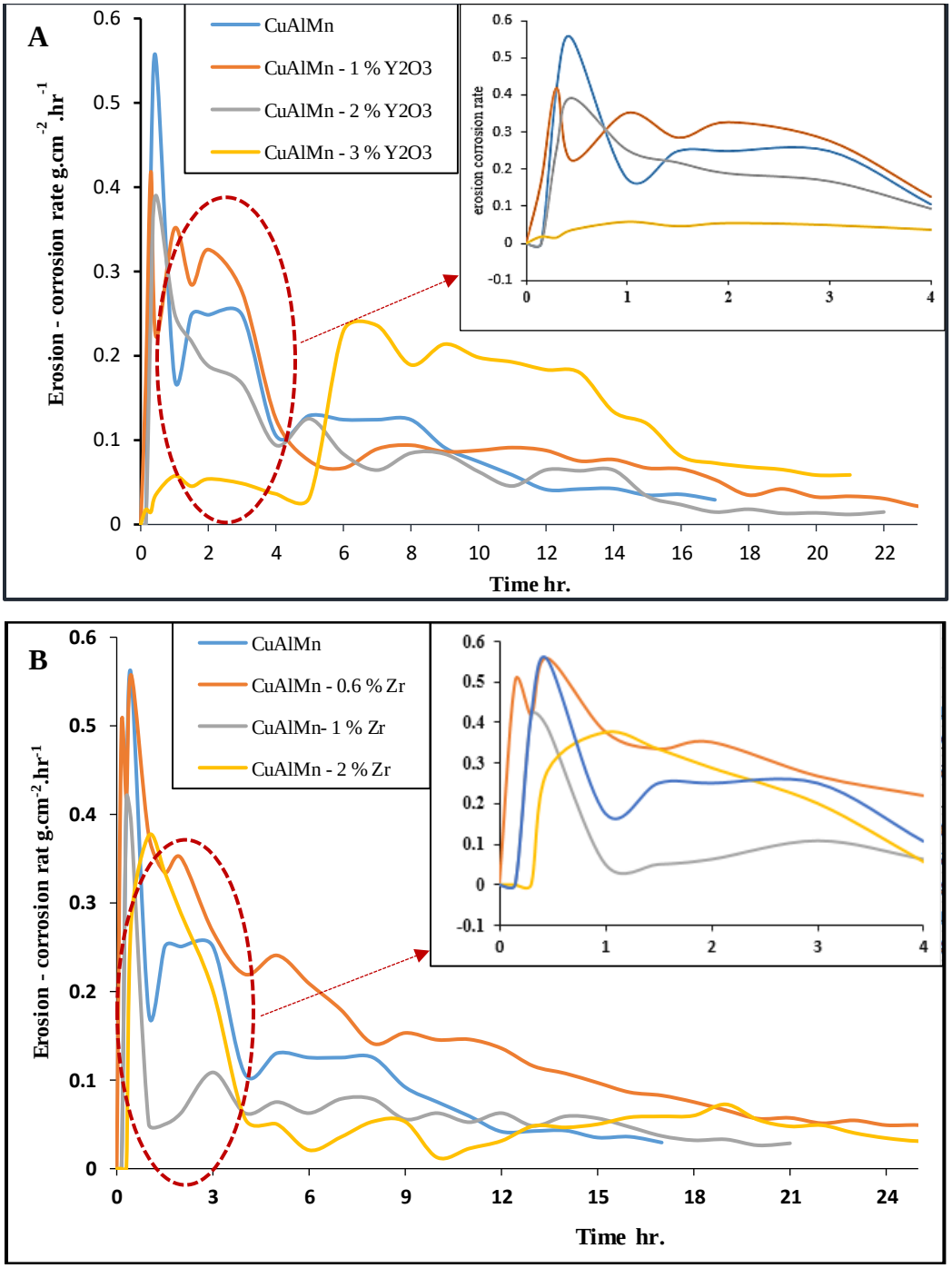

Figure (4.41): Erosion rate of alloys after sintering (A) CuAlMn-x% Y_2O_3, (B) CuAlMn-x% Zr, (C) CuAlMn-x%Ta, (D) CuAlMn-x% In

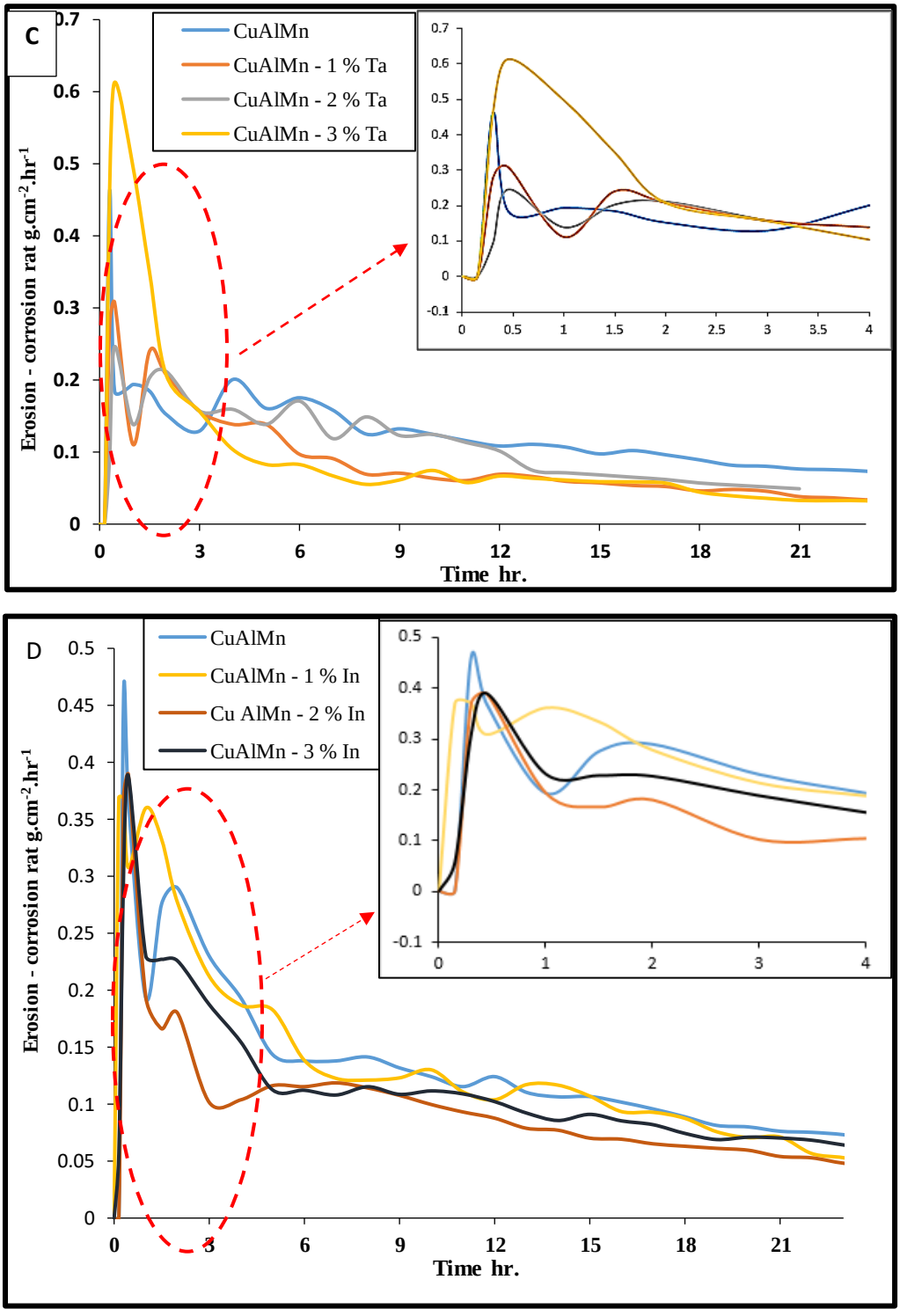

Figure (4.41): contend

Figure (4.41 A-D) indicates the results of erosion-corrosion of base alloy and base alloy with additives at a 4-hour cycle at an impact angle of 90°. It is evident that the curves have fluctuated and the reason behind this fluctuating is the repeated building and fracture of the protective surface layer. In case of the formation of this layer on the alloy's surface, the erosion-corrosion rate will decrease, whereas, the erosion-corrosion rate will increase as soon as the protective surface layer breaks down. This breaking down depends upon the impact force and the value of adhesion on the surface of the alloys. At the first time of immersion in the corrosive solution, the rate of corrosion was expected to be higher due to the simplicity of removing the created corrosion and the incidence of a new metal surface being in contact with the corrosive media. In addition, the area covered by deformed zones, produced by the impact of erodent, at the impact location on the surface of the specimen increased with increasing the exposure time, Nawal Dawood [159].

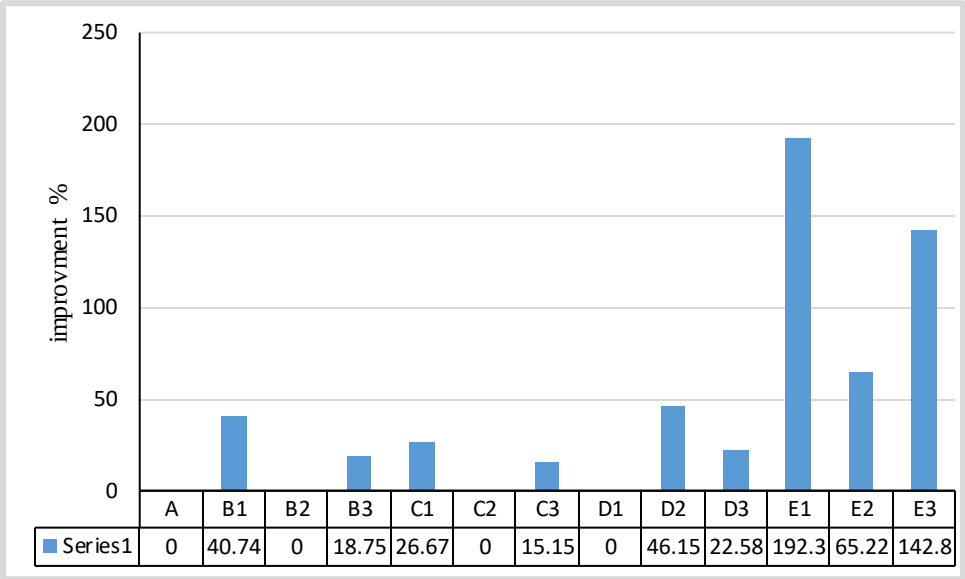

Figure (4.42): Improvement in erosion rate of Alloys (A, B1, B2, E3) after sintering

Table (4.9): Erosion rate - improvement of alloys after sintering treatment

Synthesized Composition	Code	Erosion rate	Improvement %
Cu-8Al-9Mn	A	0.038	-
Cu-8Al-9Mn-1%Ta	B1	0.027	40.7
Cu-8Al-9Mn-2%Ta	B2	0.054	0
Cu-8Al-9Mn-3%Ta	B3	0.032	18.75
Cu-8Al-9Mn-1%In	C1	0.030	26.6
Cu-8Al-9Mn-2%In	C2	0.038	0
Cu-8Al-9Mn-3%In	C3	0.033	15.15
Cu-8Al-9Mn-0.6%Zr	D1	0.049	0
Cu-8Al-9Mn-1%Zr	D2	0.026	46.15
Cu-8Al-9Mn-2%Zr	D3	0.031	22.58
Cu-8Al-9Mn-1%Y_2O_3	E1	0.023	192.30
Cu-8Al-9Mn-2%Y_2O_3	E2	0.016	65.21
Cu-8Al-9Mn-3%Y_2O_3	E3	0.015	142

From Figure (4.42) and Table (4.9) can be noticed that the maximum improvement in erosion rate (minimum erosion rate) after sintering belongs to Cu-8Al-9Mn-3%Y_2O_3 with erosion rate (0.015 g. $cm^{-2}.hr^{-1}$) and improvement % (142). The Y_2O_3 ceramic particle in alloy does not change the site of preferential attack but reduces the net surface area for erosion-corrosion due to an intrusion of reinforced particles. That is the reason composites depicts less material remove than alloy [153,154].

The corrosion rate, in the beginning, is increased due to the aggressive corrosion attack on the surface of the alloys [151].

The increase in erosion rate, in this case, is due to many factors as follows: The velocity of the flow of the corrosion solution produces cavitation and impingement which removed the oxide film during its formation. Therefore, there is not enough time for the oxide film to form, which does not produce passivity and nor protects the surface layer from corrosive media.

In other words, erosion-corrosion without slurry prevents the formation of the oxide film and thus passivity. Consequently, a naked surface is produced which open to the fast-flowing corrosive medium is resulting in cavitation and impingement. Therefore, corrosion is accelerated continuously [150].

It should be mentioned here that this type of corrosion results from two factors that act actively on one another. One is mechanical when the oxide film and surface layer are removed by the corrosive medium. The other is electro-chemical resulting from the corrosion process itself. This is in good agreement with that shown by Barik R.C. and others [149]. Also, Stephen M. McIntyre [152] pointed out that a corrosive fluid flowing at high -velocity impingement the metal surface, causing mechanical and / or electrochemical disruption of the protective oxide film then the localized metal

loss that occurs. Erosion rate of CuAlMn and CuAlMn- X (Ta, Zr, In and Y_2O_3) after Aging in (300 °C for 1 hr. and quenching) shown in Figure (4.43)

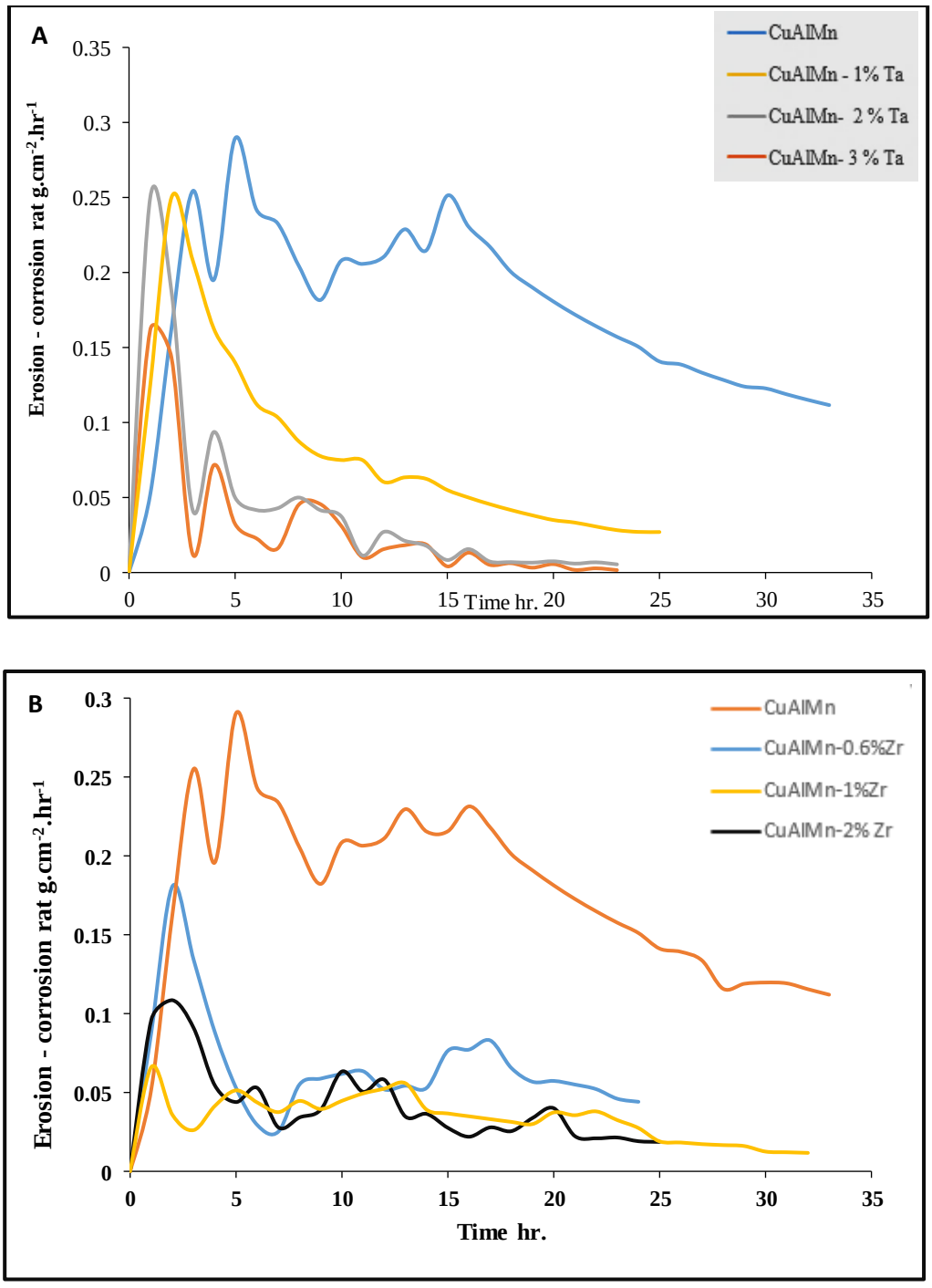

Figure (4.43): Erosion rate of alloys after Aging (A) CuAlMn-x% Ta, (B) CuAlMn-x% Zr, (C) CuAlMn-x%In, (D) CuAlMn-x% Y_2O_3

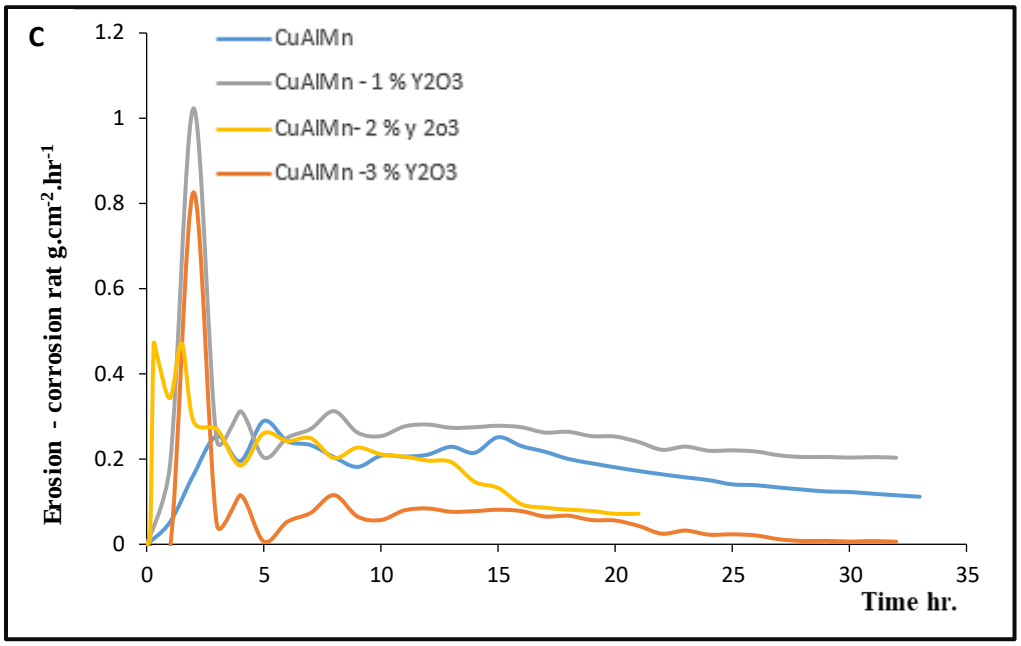

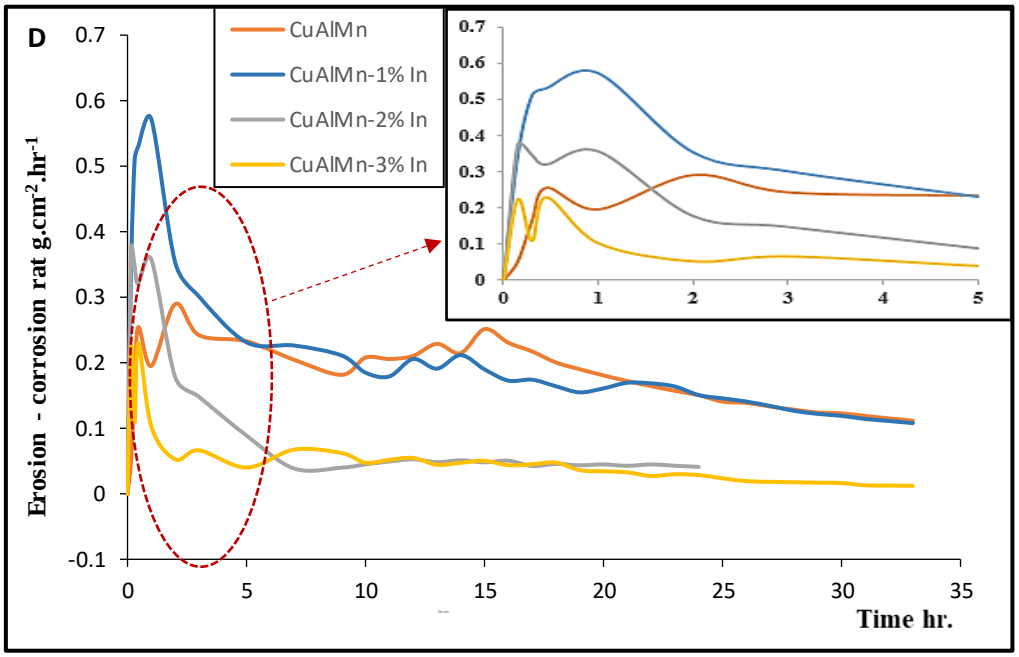

Figure (4.43): contend

Table (4.10): Erosion rate and improvement for alloys after aging heat

Synthesized Composition	Code	Erosion rate	Improvement %
Cu-8Al-9Mn	A	0.122	-
Cu-8Al-9Mn-1%Ta	B1	0.027	351.85
Cu-8Al-9Mn-2%Ta	B2	0.0017	706.4
Cu-8Al-9Mn-3%Ta	B3	0.0059	197.7
Cu-8Al-9Mn-1%In	C1	0.188	0
Cu-8Al-9Mn-2%In	C2	0.044	597.14
Cu-8Al-9Mn-3%In	C3	0.0175	177.27
Cu-8Al-9Mn-0.6%Zr	D1	0.0588	107.483
Cu-8Al-9Mn-1%Zr	D2	0.016	662.5
Cu-8Al-9Mn-2%Zr	D3	0.028	335.71
Cu-8Al-9Mn-1%Y_2O_3	E1	0.203	0
Cu-8Al-9Mn-2%Y_2O_3	E2	0.0819	48.96
Cu-8Al-9Mn-3%Y_2O_3	E3	0.0074	1548.6

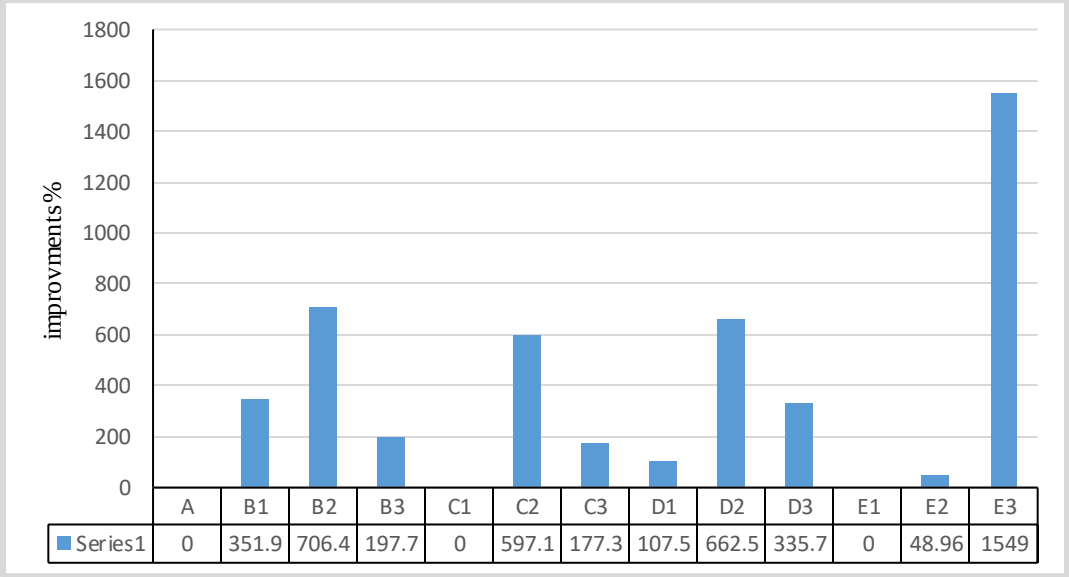

Figure (4.44): Improvement in erosion rate of Alloys (A, B1, B2, E3) after aging heat treatment

From Figure (4.44) and Table (4.11) can be noticed that the maximum improvement in erosion rate (minimum erosion rate) after aging heat treatment belong to Cu-8Al-9Mn-2%Ta with erosion rate (0.0017g. $cm^{-2}.hr^{-1}$) and improvement reach (706) % and then for 3% Y_2O_3 with improvement reach (1596)%.

The existence of hard Y_2O_3 particles within the matrix of CuAlMn alloy has more hardness resistance to erosion-corrosion than the matrix.

In general, aged specimens have higher hardness as the result of precipitation hardening.

Aging in martensite phase is associated with the diffusion and precipitation process of an intermetallic compound that is precipitated as fine particles and distributed equally in the microstructure which acts as obstacles prevent the dislocation movement, and the presence of the martensite phase (or mixture of both), while sintered specimens have low hardness due to the martensite phase doesn't form and presence of α phase[131].

The morphology of surface after erosion test for CuAlMn and CuAlMn-x (3% Ta, 3%In, 2 % Zr, and 3% $Y_2O_{3)}$ after aging is shown in Figure (4.45A-E).

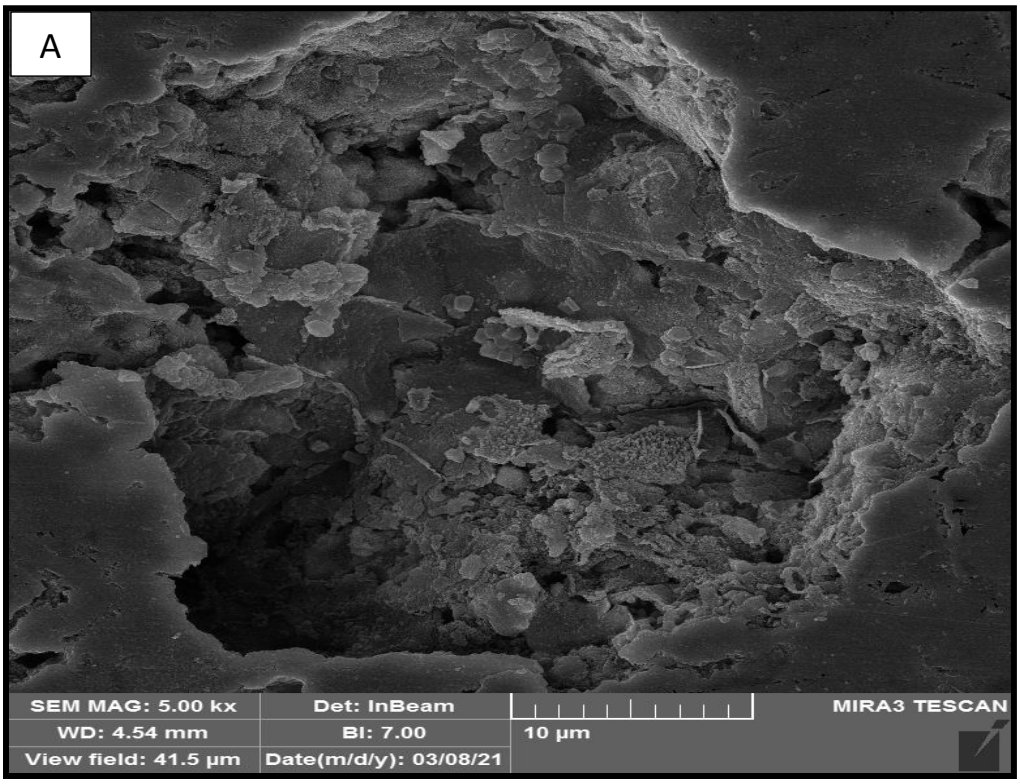

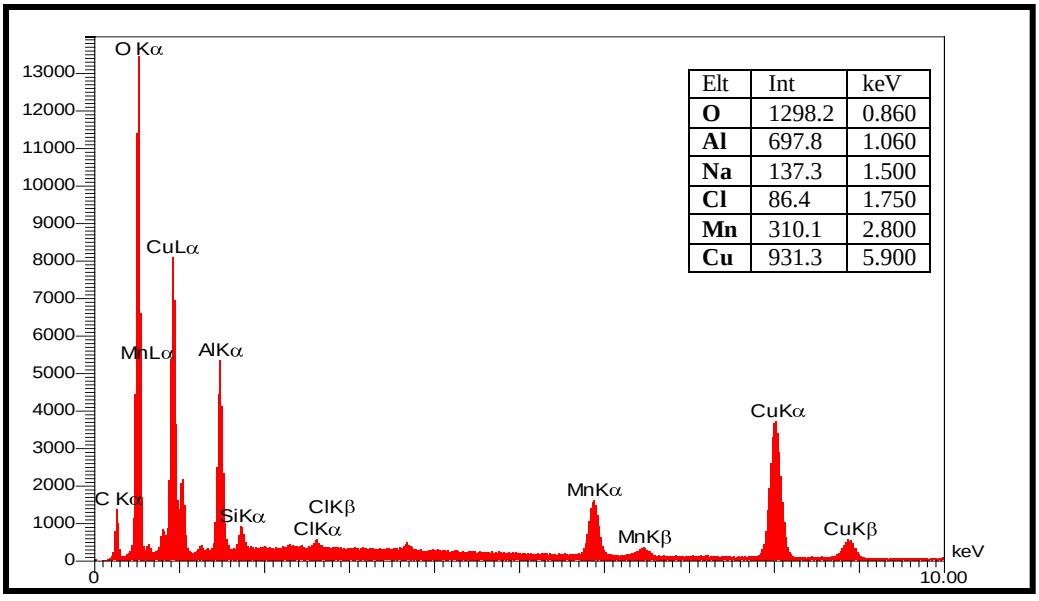

Figure (4.45 A): SEM and EDS analyses of surface morphology of CuAlMn after erosion corrosion test with magnifications (5.00KX)

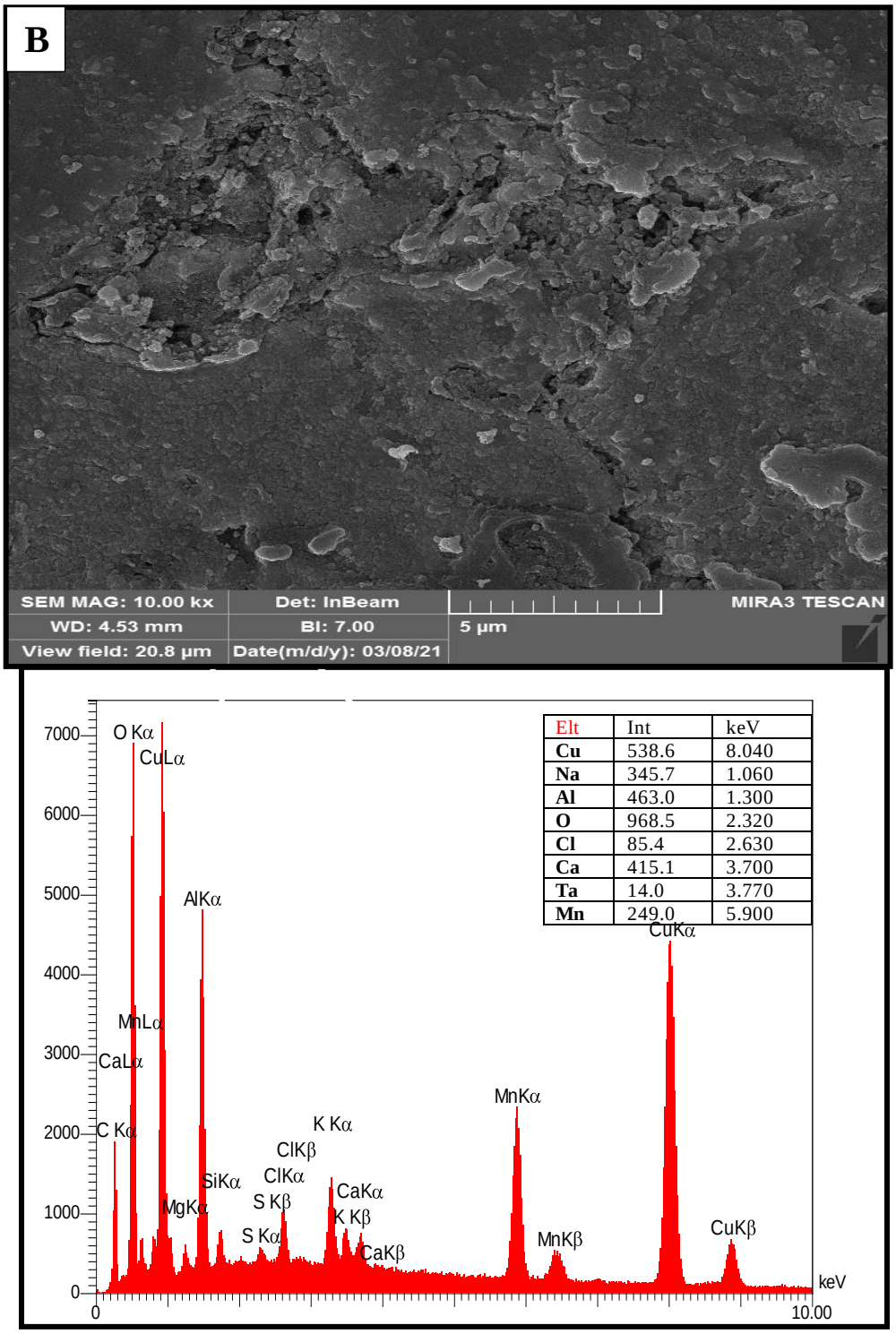

Figure (4.45 B): SEM and EDS analyses of surface morphology of CuAlMn- 3% Ta after erosion corrosion test with magnifications (5.00KX)

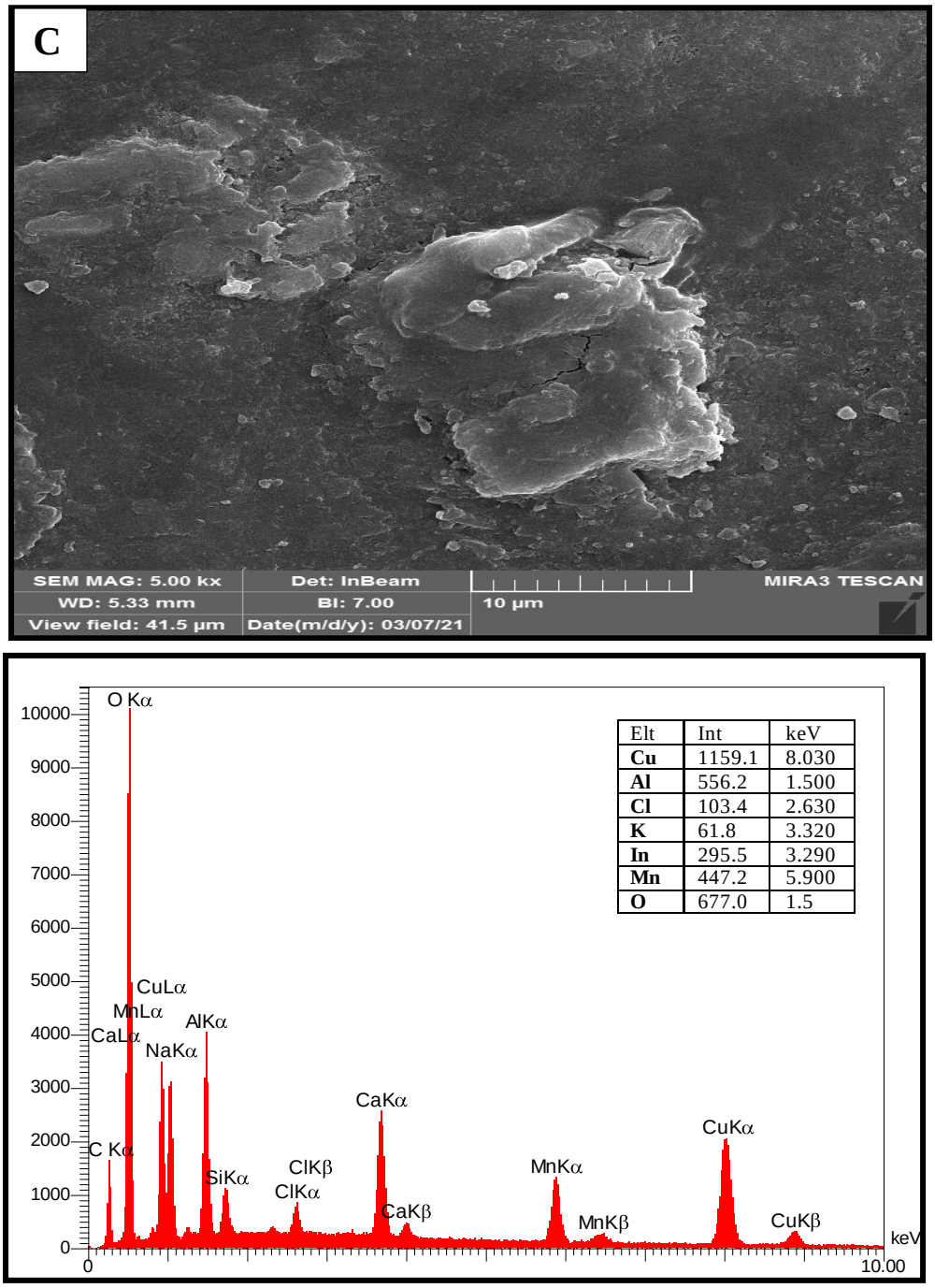

Elt	Int	keV
Cu	1159.1	8.030
Al	556.2	1.500
Cl	103.4	2.630
K	61.8	3.320
In	295.5	3.290
Mn	447.2	5.900
O	677.0	1.5

Figure (4.45 C): SEM and EDS analyses of surface morphology of CuAlMn- 3% In after erosion corrosion test with magnifications (5.00KX)

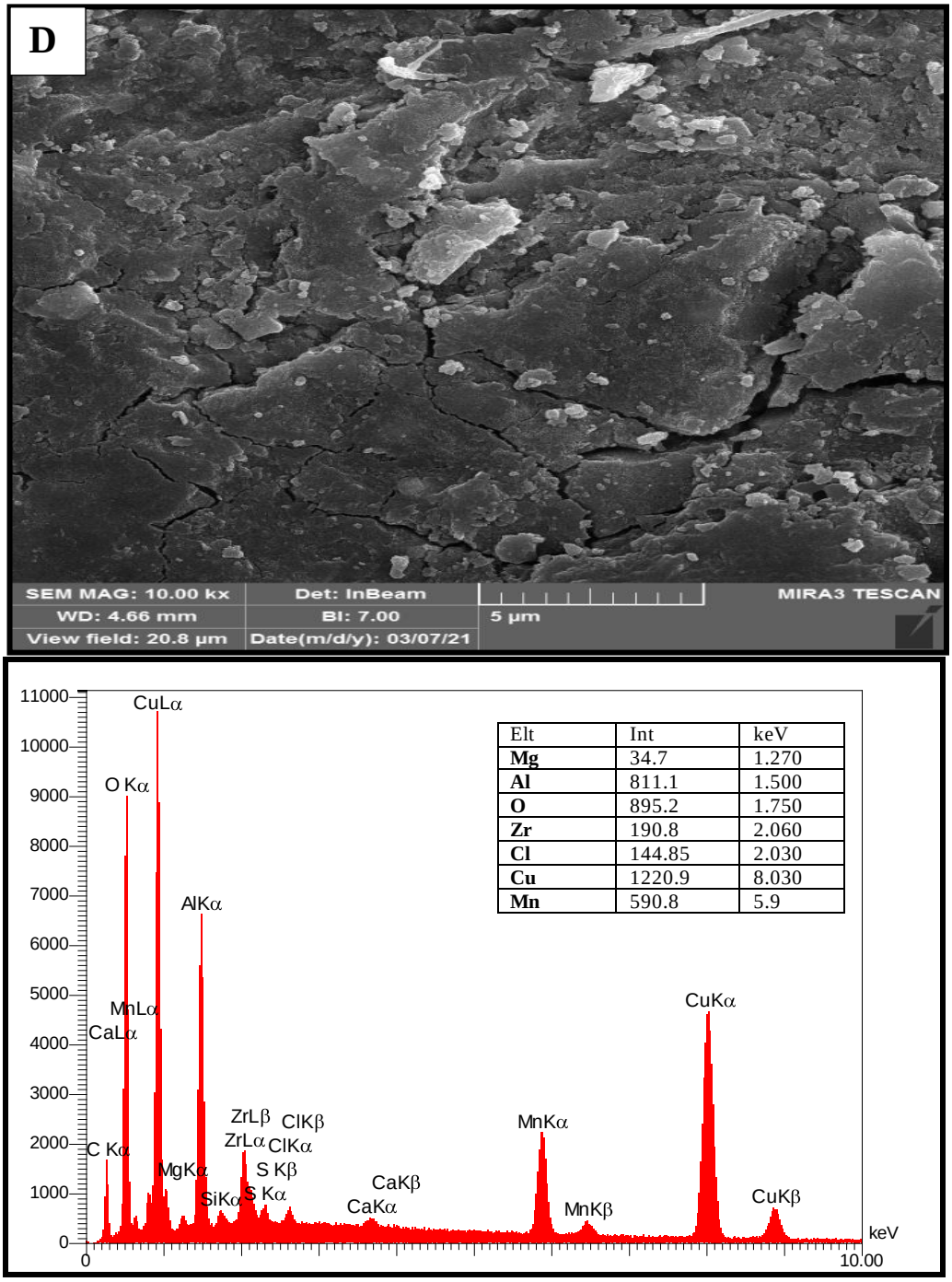

Elt	Int	keV
Mg	34.7	1.270
Al	811.1	1.500
O	895.2	1.750
Zr	190.8	2.060
Cl	144.85	2.030
Cu	1220.9	8.030
Mn	590.8	5.9

Figure (4.45 D): SEM and EDS analyses of surface morphology of CuAlMn- 2% Zr after erosion corrosion test with magnifications (10.00KX)

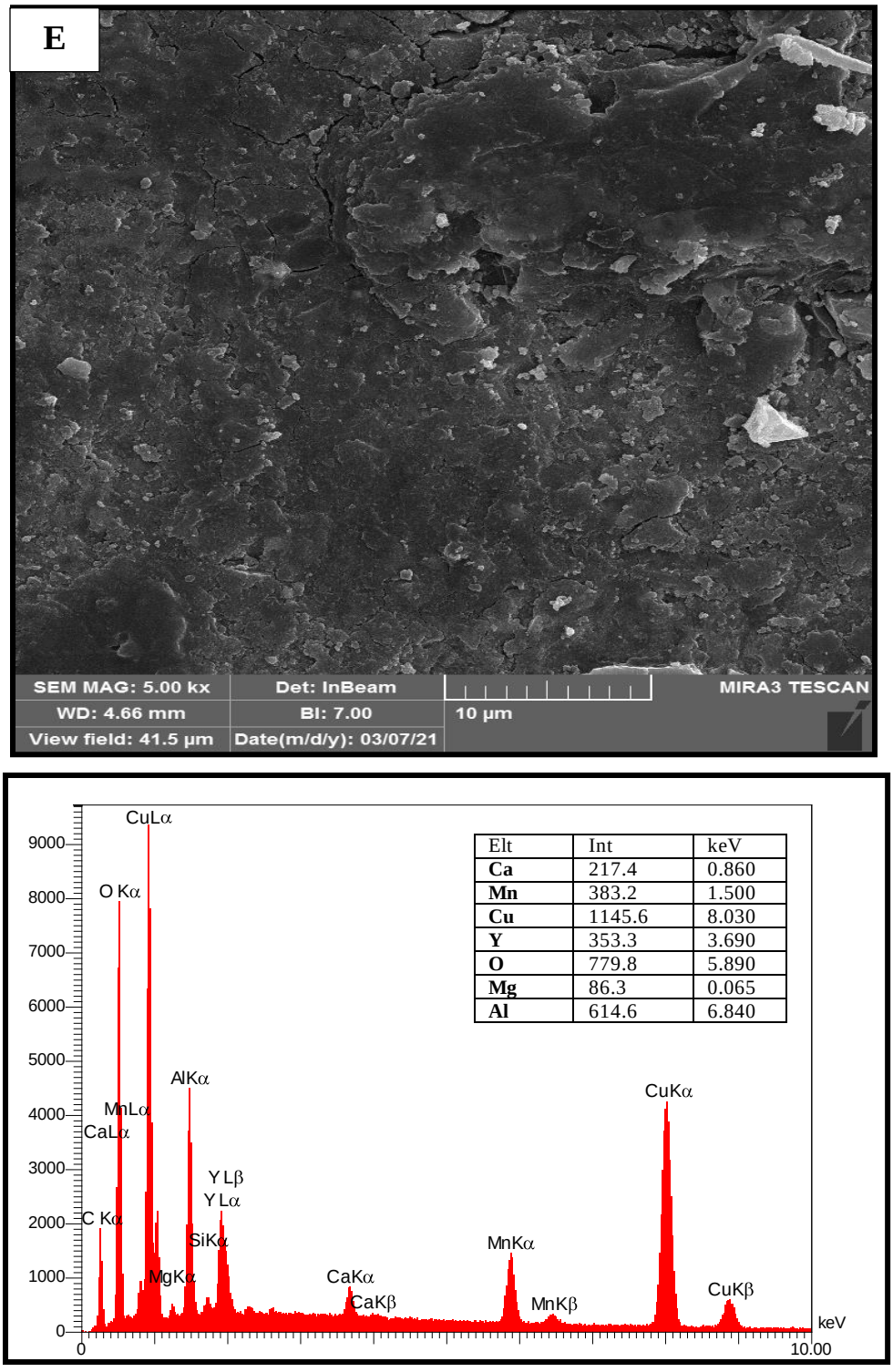

Elt	Int	keV
Ca	217.4	0.860
Mn	383.2	1.500
Cu	1145.6	8.030
Y	353.3	3.690
O	779.8	5.890
Mg	86.3	0.065
Al	614.6	6.840

Figure (4.45 D): SEM and EDS analyses of surface morphology of CuAlMn- 3% Y_2O_3 after erosion test

From Figures (4.45 A, B, C, D, and E) can be seen that the base alloy surface less resistance to erosion than the alloys with additive as the base alloy (CuAlMn) have less hardness (HV equal to 108.5) otherwise for CuAlMn-3%Ta, CuAlMn-3%In, CuAlMn-2%Zr, and CuAlMn-3%Y_2O_3) the microhardness measurement reach to 126.6, 132.9, 125.3, 143.8) respectively.

In general, aged specimens have higher hardness as the result of precipitation hardening. Ageing in the martensite phase is associated with the diffusion and precipitation process of an intermetallic compound that is precipitated as fine particles and distributed equally in the microstructure which acts as obstacles to prevent the dislocation movement, and the presence of martensite phase [131].

4.11 XRD after Linear Polarization Test

In this test X-Ray diffraction for specimens after corrosion test in 3.5% NaCl solution has been done for alloy A, B3, C3.

In Figure (4.46), the XRD test result showed that the formation of corrosion products on the specimen's surface in3.5 % NaCl solution. Figure (4.46.A, B, C) is the XRD result of alloy the corrosion products were Al_2O_3 and Cu_2O which represent the protective scales.

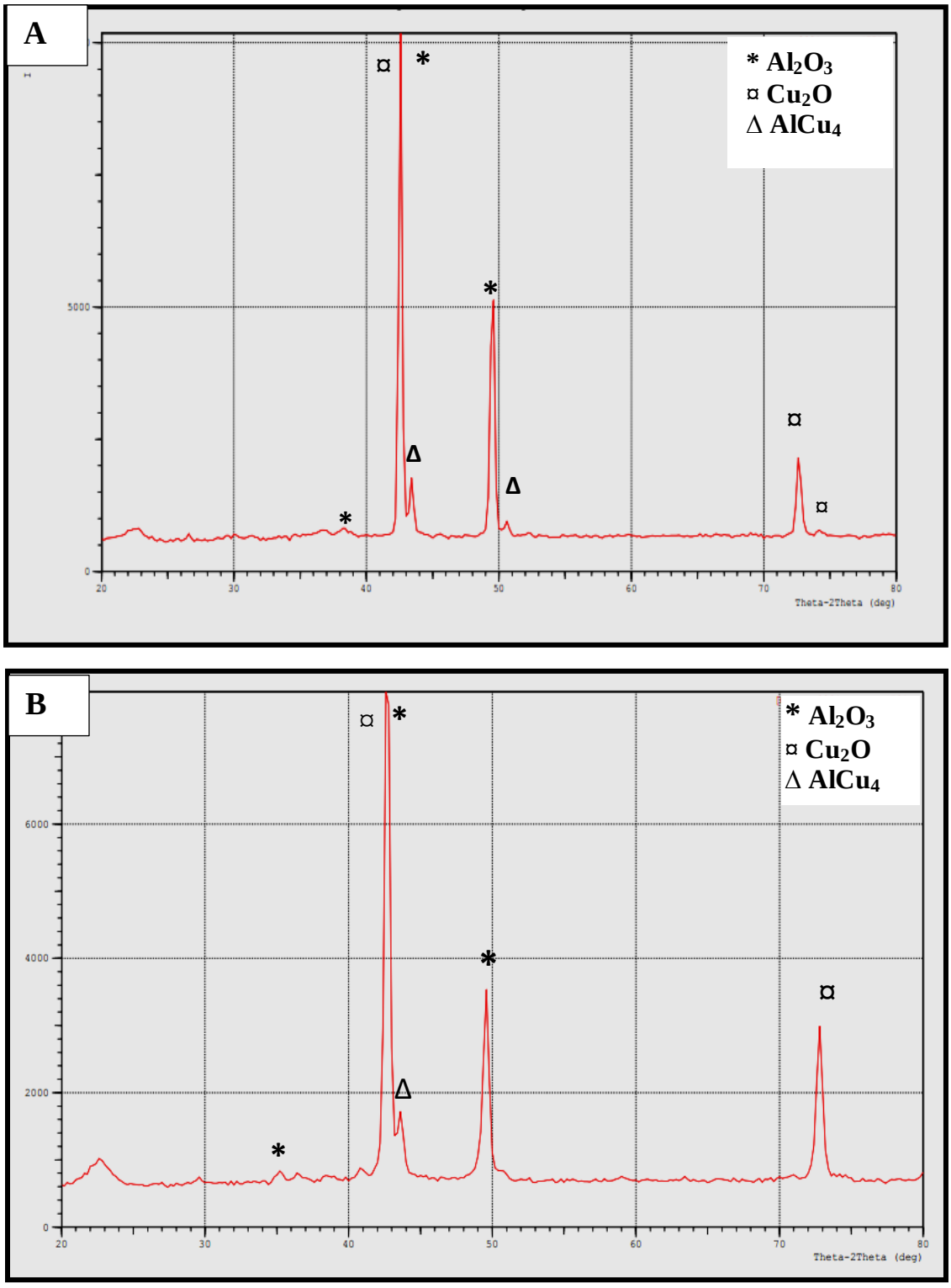

Figure (4.46): XRD Analysis for (A) Alloy A. (B) Alloy B3. (C) Alloy C3. in 3.5%NaCl Solution

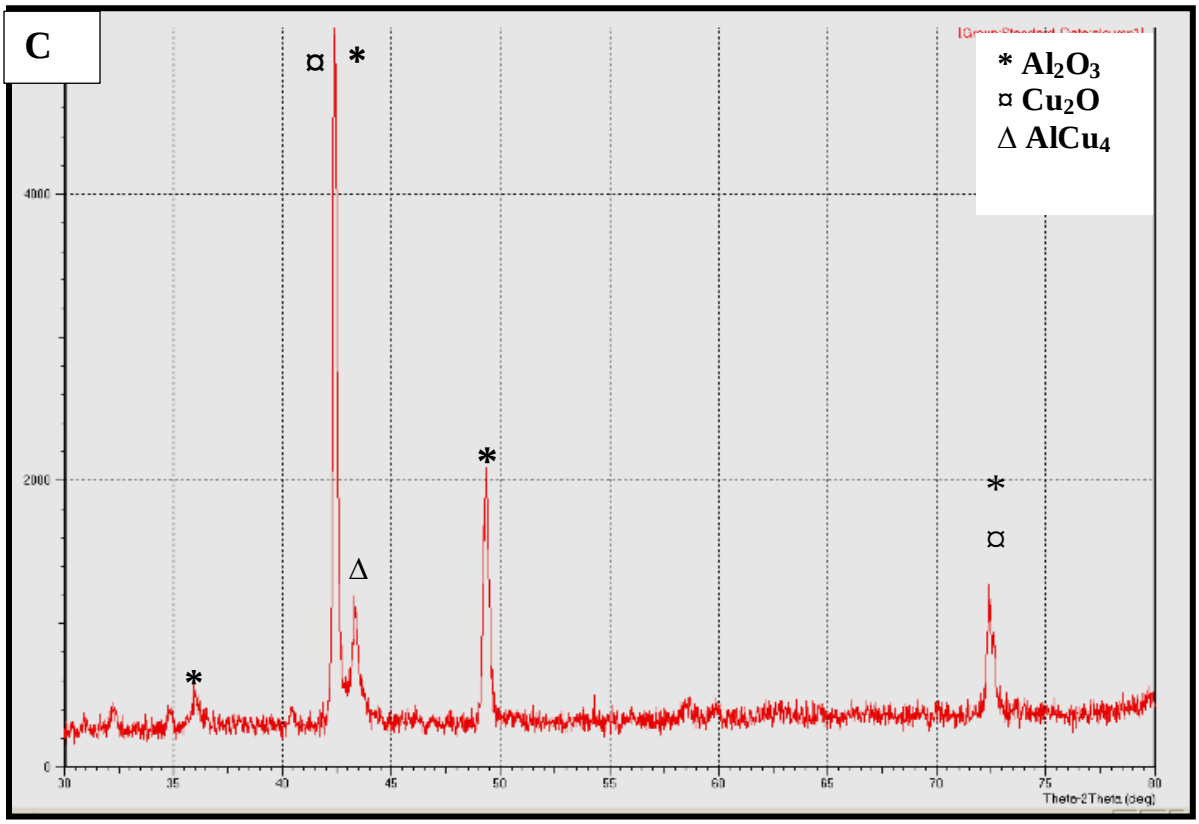

Figure (4.46): contend

The corrosion resistance of Cu-Al alloys is mainly because of the formation of a protective passive layer of Cu_2O and Al_2O_3 on the surface when exposed to a corrosion environment. The formation of these stable passive layers on Cu-Al alloys is mainly due to the higher affinity of Aluminum towards oxygen than Copper in salt solutions [86].

Chapter 5

Conclusions and Recommendations

5.1 Conclusions

These conclusions can be drawn from this work as following:

1. In the quenched ternary Cu–Al–Mn alloy, martensitic phase were precipitate as plate- or spear-like martensite [the zig-zag phase].
2. The Cu–Al–Mn SMAs transition temperatures change as the chemical composition of the alloy changes. Austinite started temperature decreases about (5-15) °C with addition grain refinement.
3. The addition of (Zr, In, and Y_2O_3) can increase the SME of ternary Cu-Al-Mn alloy by about 103 % with 3% Ta, 119% when addition 2% Zr and 35 when addition 3% Y_2O_3.
4. The alloy damping capacity, or IF, increases with addition alloying element (Ta, Zr, In), and Y_2O_3. Alloys exhibit maximum damping in 0.6% Zr and then decrease with addition 1% Zr, while the damping ratio increases with increasing the ratio of Y_2O_3 from (1 to 3) wt.%.
5. The best improvement in damping capacity ratio by the addition 0.6% Zr after sintering, while after aging heat treatment at 300°C by addition 1% In and 0.6% Zr.
6. The corrosion rate (mm/y) in 3.5% NaCl reduces by adding these elements (Ta, Zr, and In) and Y_2O_3 ceramic particles after sintering the best improvement belong to Cu-8Al-9Mn-2%Ta, otherwise after aging the best improvement belong to Cu-8% Al-9% Mn-2% Zr .
7. The addition of alloying elements (Ta, Zr, and In) and Y_2O_3 ceramic particles caused improved hardness.

8. The improvements in hardness of Cu-Al -Mn alloy after the addition of (Ta, In, Zr and Y_2O_3) can be attributed to the grain size reduction, solid solution strengthening.
9. The maximum improvement in erosion resistance after sintering belong to Cu-8Al-9Mn-1%Y_2O_3 with erosion rate (0.023 g. $cm^{-2}.hr^{-1}$) and improvement % (192) but after Aging heat treatment the minimum erosion rate belong to Cu-8Al-9Mn-3% Y_2O_3 with erosion rate (0.0074g. $cm^{-2}.hr^{-1}$) and improvement reach (1548) %.

Further recommendations

1. Mixing metallic elements (Tantalum, Zirconium, and Indium) with the ceramic particles (Y_2O_3) and investigate the mechanical properties and corrosive behavior of Cu (-8% Al -9% Mn) wt. shape memory alloy.
2. Study the synthesis and characterization of nanocrystalline CuAlMn SMAs .
3. Addition alloy elements such as Niobium or Cerium and observe its effects on the mechanical properties and corrosive behavior of CuAlMn shape memory alloy.

References

Reference

[1]. Mohammad H. Elahinia, "***Shape Memory Alloy Actuators Design, Fabrication, and Experimental Evaluation***", John Wiley & Sons, Ltd , First edition, 2016.

[2]. Marc Andre Meyers and Krishan Kumar Chawla, ***"Mechanical Behavior of Materials"*** First published, United States of America by Cambridge University Press, New York, 2009.

[3]. Corneliu Cismasiu "***Shape memory alloys"***, Sciyo, First published, India, 2010.

[4]. Z. WEI, R. Sandstro, "***Review Shape-memory materials and hybrid composites for smart systems, Part I Shape-memory material"***, Journal of Material science, Volume 33, Page 3743-3762, 1998.

[5]. Andrzej Zio łkowski***, "Pseudoelasticity of Shape Memory Alloys"***, Butterworth Heinemann, Elsevier, 2015.

[6]. NK Simha, ***"Shape-Memory Alloys"***, Materials Science and Materials Engineering. Oxford: Elsevier, pages. 1-37. ISBN: 978-0-12-803581-8, 2017.

[7]. Eren Kaya and Irfan Kaya, "***A review on machining of NiTi shape memory alloys: the process and post process perspective"***, The International Journal of Advanced Manufacturing Technology, 2018.

[8]. Darel E. Hodgson, Ming H. Wu, Robert J. Biermann***, "Shape Memory Alloys"*** ASM Handbook, Properties and Selection: Nonferrous Alloys and Special-Purpose Materials ASM Handbook Committee, Volume 2, pages 897-902, 1990.

[9]. Rupa Dasgupta, ***"A look into Cu-based shape memory alloys: Present scenario and future prospects"***, J. Mater. Res., Volume 29, Number 16, Aug 28, 2014.

Reference

[10]. Gabriella Faiella and Vincenza Antonuci, ***"Shape Memory Alloy Engineering",*** ISBN 978-0-08-099920-3, Elsavier, 2015

[11]. Sampath V. ***"Studies on the effect of grain refinement and thermal processing on shape memory characteristics of Cu–Al–Ni alloys. Smart Materials and Structures"***, Volume 14, Issue 5, Page 253-260, 2005.

[12]. Xinren Chen, Fan Zhang, Mengyuan Chi , Shuiyuan Yang , Cuiping Wang , Xingjun Liu, and Songsheng Zheng , ***"Microstructure, superelasticity and shape memory effect by stress-induced martensite stabilization in Cu–Al–Mn–Ti shape memory alloys"***, Materials Science and Engineering, Volume 236–237, Pges 10-17, 2018.

[13]. S. Takoka***, "Overview of the development of shape memory and superelastic alloy applications",*** Furukawa Electric, Woodhead Publishing Limited ,2011.

[14]. Worden K., Bullough W. A. and Haywood J., ***"Smart technologies"***, World Scientific, pages 109–135, 2003.

[15]. T. Maruyama, H. Kubo, ***"Ferrous (Fe-based) shape memory alloys (SMAs): properties, processing and applications",*** Woodhead Publishing Limited, 2011.

[16]. Jaronie Jani, Martin Leary, Aleksandar Subic, Mark Gibson,***"A review of shape memory alloy research, applications"***, J. Materials and Design, Volume 56 , Pages 1078–1113, 2014.

[17]. J. Cederstrom, J. van Humbeeck, ***"Relationship Between Shape Memory Material Properties and Applications"***, Journal de Physique, Volume 5, 1995.

Reference

[18]. Dominiek Reynaerts, Jan Peirs and Hendrik Van Brussel, ***"Design of a Shape Memory Alloy Actuated Implantable Drug Delivery System",*** Euro sensors X, Leuven, Belgium, 8-11, September 1996.

[19]. Ashish Agrawal and Ravindra Dube, ***"Methods of fabricating Cu-Al-Ni shape memory alloys"***, Journal of Alloys and Compounds ,2018. doi: 10.1016/j.jallcom.2018.03.390.

[20]. Jili Liu, Mohan Li , Xu Li, Wangxian Yan , Wei Huang, Shilin Yan, ***"The effect of superelastic strain on the damping capacity in columnar grained Cu-Al-Mn shape memory alloy"***, Journal of Alloys and Compounds, Volume 781 , PAGES. 621-628, 2019. https://doi.org/10.1016/j.jallcom

[21]. Bora Gencturk , Yoshikazu Araki , Tomoe Kusama , Toshihiro Omori , Ryosuke Kainum and Fernando Medina, ***"Loading rate and temperature dependency of superelastic Cu–Al–Mn alloys"***, Construction and Building Materials, Volume 53, Pages 555–560, 2014 .

[22]. Kshitij Shrestha, Yoshikazu Araki, Takuya Nagae and Yuji Koetaka, ***"Feasibility of Cu–Al–Mn superelastic alloy bars as reinforcement elements in concrete beams",*** Smart Mater. Struct., Volume 22, 2013. doi:10.1088/0964-1726/22/2/025025.

[23]. Alaa M. Sharabash, Bassem O. Andrawes, ***"Application of shape memory alloy dampers in the seismic control of cable-stayed bridges"***, Engineering Structures, Volume 31, PAGES. 607–616, 2009.

[24]. Y. Sutou, T. Omori, J.J. Wang, R. Kainuma, K. Ishida, ***"Characteristics of Cu–Al–Mn-based shape memory alloys and their applications"***, Materials Science and Engineering A, Volume 378 , PAGES. 278–282, 2004.

[25]. K. Yamauchi, I. Ohkata, K. Tsuchiya and S. Miyazaki, ***"Shape memory and superelastic alloys Technologies and applications",*** Woodhead Publishing Limited, 2011.

[26]. Jan Van Humbeeck, ***"Non-medical applications of shape memory alloys"***, Materials Science and Engineering A, Volume 273–275, Pages. 134–148,1999.

[27]. R. Desroches and B. SMITH, ***"Shape Memory alloys In Seismic Resistant Design and Retrofit: A Critical review",*** Journal of Earthquake Engineering, Volume 8, Number 3, issue 415-429, 2004.

[28]. Maria M., Paris G., Mauricio S., Aquiles S., ***"Use of copper base shape memory alloy in sesmic energy dissipation devices",*** 13th World Conference on Earthquake Engineering Vancouver, B.C., Canada, Number 3344, 2004.

[29]. Deepjyoti B., ***"Investigation of Cu based shape memory alloy as a reinforcement for metal matrix composite"***, Journal of Advancements in Material Engineering, Volume 3, Issue 3, 2018.

[30]. T. Gustmann, J. M. dos Santos, P. Gargarell, U. Kuhn, J. Van Humbeeck S. Pauly, ***"Properties of Cu-Based Shape-Memory Alloys Prepared by Selective Laser Melting"***, Shape Memory and Super elasticity, Volume 3, March 2017.

[31]. Kush Mehta, Kapil Gupta, ***"Fabrication and Processing of Shape Memory Alloys"***, Manufacturing and Surface Engineering, Springer International Publishing, 1st ed. 2019.

[32]. Haydn Chen and Hiroshi Kubo, ***"Martensitic phase transformations and shape memory alloys"***, Materials Science, Volume1, Pages. 349-354, 1996.

[33]. S. Montecinosa , A. Cuniberti, ***"Martensitic transformation and grain size in a Cu-Al-Be alloy",*** Procedia Materials Science, Volume 1 , Pages . 149 - 155, 2012.

[34]. Yusof Y. A., C. J., and Chin, N. L. , ***"Development of nutraceutical product",*** International Journal on Advanced Science, Engineering and Information Technology, Volume 5 (3), pages 201-206, 2015

[35]. O. Adiguzel, ***"Martensitic Transformation and Microstructural Characteristics in Copper Based Shape Memory Alloys"***, Key Engineering Materials, Volume 510-511, Pages 105-110, 2012.

[36]. L. E. TANNER, ***"Workshop on First-order Displacive Phase Transformations: Review and Recommendations",*** Materials Science and Engineering, Volume. A 127, Pages 137-144, 1990.

[37]. J.J. Zhu, K.M. Liew, ***"Description of deformation in shape memory alloys from DO3 austenite to 18R martensite by group theory",*** Acta Materialia, Volume 51, pages. 2443–2456, 2003.

[38]. T W Duerig, K N Melton, D Stockel ***"Engineering Aspects of Shape Memory"***, Butterworth-Heinemann, ISBN 0-750-61009-3, First published 1990.

[39]. Jeff Perkins, ***"Shape memory effects in alloys"***, Springer Science, New York, 1975.

[40]. Christian Lexcellent, ***"Shape-memory Alloys Handbook",*** First published, John Wiley & Sons, 2013.

[41]. L. Janke , C. Czaderski , M. Motavalli and J. Ruth , ***"Applications of shape memory alloys in civil engineering structures – Overview"***, Materials and Structures, Volume 38, Pages. 578-592, 2005.

Reference

[42]. Ghulam Abbas Gohar, Tareq Manzoor and Asad Naeem Shah, ***"Investigation of thermal and mechanical properties of Cu-Al alloys with silver addition prepared by powder metallurgy"***, Journal of Alloys and Compounds, Volume 735, pages 802-812, 2018.

[43]. Nwaeju C., J. U., Nnuka E. E, ***"Effect of niobium addition on the structure and mechanical properties of aluminum bronze"***, International Journal of Research in Advanced Engineering and Technology, Volume 1; Issue 2; Page Number 70-75, November 2015.

[44]. Jean-Marie Welter, ***"Copper",*** Proceedings of the International Conference Copper, Volume 06, ISBN: 978-3-527-31884-1

[45]. L. Vrsalovi , I. Ivani, S. Kozuh, S. Gudi , B. Kose and M. Goji, ***"Effect of heat treatment on corrosion properties of CuAlNi shape memory alloy"***, Trans. Nonferrous Met. Soc. China, Vol 28, PAGES. 1149−1156, 2018.

[46]. Safaa N. Saud, Esah Hamzah, Tuty Abubakar, Mustafa K. Ibrahim, and Abdollah Bahador, ***"Effect of a fourth alloying element on the microstructure and mechanical properties of Cu–Al–Ni shape memory alloys",*** J. Mater. Res., Volume 30, Number 14, 2015.

[47]. Diego Velazquez Ricardo Romero, ***"Calorimetric study of spinodal decomposition in β- Cu–Al–Mn",*** Journal of Thermal Analysis and Calorimetry, 2020.
https://doi.org/10.1007/s10973-019-09234-0.

[48]. E. Ercan, F. Dagdelen and I. N. Qade, ***"Effect of tantalum contents on transformation temperatures, thermal behaviors and microstructure of CuAlTa HTSMAs",*** Journal of Thermal Analysis and Calorimetry, Volume 139, pages 29–36 , 2020.

[49]. C. Aksu Canbay, S. Gudeloglu and Z. Karagoz Genc, ***"Investigation of the Enthalpy/Entropy Variation and Structure of Cu–Al–Mn–Fe Shape Memory Alloys",*** Int J Thermo phys, Volume 36, Pages 783–794, 2015. DOI 10.1007/s10765-015-1842-2

[50]. T. Grguric, D. Manasijevic, S. Kozuh, I. Ivanic, I. Anzel, B. Kosec, M. Bizjak, E. Govorcin Bajsic, Lj. Balanović, Mirko Gojic, ***"The effect of the processing parameters on the martensitic transformation of Cu-AlMn shape memory alloy"***, Journal of Alloys and Compounds, Volume 765, Pages 664-676, 15 October 2018.

[51]. U.S. Mallik and V. Sampath, ***"Influence of quaternary alloying additions on transformation temperatures and shape memory properties of Cu–Al–Mn shape memory alloy",*** Journal of Alloys and Compounds, Volume 469, Pages 156–163, 2009.

[52]. V. Sampath and U.S. Mallik***, "Influence of minor additions of boron and zirconium on shape memory properties and grain refinement of a Cu-Al-Mn shape memory alloy",*** EDP Sciences, 2009.

[53]. Emine Aldırmaz and Ilhan Aksoy, ***"Effects of Heat Treatment and Deformation on 2H and 18R Martensites in Cu–9.97 % Al–4.62 % Mn Alloy",*** Arab J Sci Eng, Volume 39, Pages 575–580, 2014

[54]. R. Kainuma, N. Satoh , X.J. Liu, I. Ohnuma and K. Ishida, ***"Phase equilibria and Heusler phase stability in the Cu-rich portion of the Cu–Al–Mn system",*** Journal of Alloys and Compounds, Volume 266, Pages 191–200, 1998.

[55]. J. P. Oliveira B. Panton, Z. Zeng, T. Omori, Y. Zhou, R.M. Miranda, F.M. Braz Fernande, ***"Laser welded superelastic Cu-Al-Mn shape memory alloy wire",*** 2015.
doi: 10.1016/j.matdes.2015.10.12.

[56]. Y. Sutou, T. Omori, T. Okamoto, R. Kainuma and K. Ishida, ***" Effect of grain refinement on the mechanical and shape memory properties of Cu-AI-Mn base alloys",*** J. Phys. IV France, Volume 11, Number 8, Pages 185-190, November 2001.

[57]. A. Mielczarek, W. Riehemann, S. Vogelgesann and B. Tonn, ***"Mechanical and fatigue properties of Cu - Al - Mn shape memory alloys with influence of mechanical cycling on amplitude dependence of internal friction at room temperature"***, Solid State Phenomena, Volume 137, pages 145-154,2008.

[58]. J. Dutkiewicz, J. Morgiel, T. Czepagese and E. Cesar, ***"Martensitic Transformation in CuAlMn and CuAlNi Melt Spun Ribbons",*** J. PHYS. IV FRANCE 7, 1997.

[59]. X. Liu, Q. Wang, S. Kondatev, P. J I, F. Yin, C. Cui and G. Hao, ***"Microstructural Mechanical and Damping Properties of a Cu-Based Shape Memory Alloy Refined by an In Situ LaB6/Al Inoculant",*** Metals & Materials Society and ASM International, 2310-Volume 50A, 2019

[60]. Eduard Obrado, Luıs Manosa, and Antoni Planes, ***"Stability of the bcc phase of Cu-Al-Mn shape-memory alloys"***, The American Physical Society ,Volume 56, Number 11, 1997.

[61]. N. Shajil, D. Das and L. Chandrasekaran, ***"Effects of cycling on the pseudoelastic properties of CuAlMnNi & TiNi based pseudoelastic alloys",***

international journal of structural changes in solids – Mechanics and Applications, Volume 1, Number 1, pages. 171-185, 2009.

[62]. Igor Altenberger, Stefanie Heinrichs, Hans-Achim Kuhn, ***"Microstructure and properties of ultra high strength high-alloyed and quasi-equiatomic Cu-Al-Mn alloys",*** Conference: EMC 2017, GDMB - European Metallurgical Conference At: Leipzig, 2017.

[63]. R. Amini, S. M. M. Mousavizad, H. Abdollahpour, M. Ghaffari, M. Alizadeh, Ali K. Okyay, ***"Structural and microstructural phase evolution during mechano-synthesis of nanocrystalline/amorphous CuAlMn alloy powders",*** Advanced Powder Technology, Volume 24, pages. 1048–1053, 2013.

[64]. S Barbarinol, E I Saavedra, Flores R M Ajaj, I Dayyani and M Friswe, ***"A review on shape memory alloys with applications to morphing aircraft",*** Smart Materials and Structures, Volume 23, Number 063001, 2014.

[65]. Matteo C., ***"Fundamentals on the use of Shape Memory Alloys in Soft Robotics",*** chapter X. ISTE Ltd

[66]. T. W. Duerig and K. Bhattacharya, ***"The Influence of the R-Phase on the Superelastic Behavior of NiTi"***, Shape Memory and Superelasticity, Volume 1, issue 2, 2015.

[67]. Lynette Ann Middleton, ***"The effect of ageing and thermal cyclic of ageing and thermal cycling on the shape memory properties of nickel-titanium***", MSc. Theses, University of Wollongong,1988.

[68]. Jose Maria Guilemany and J. Fernández, ***"Mechanism of Two Way Shape Memory Effect Obtained by Stabilised Stress Induced Martensite",*** Metallurgica et Materialia, Volume19, pages. 319-323, 1994.

[69]. M. Taha, M. B. Bahrom, O. Y. Taha, and M. S. Aris***, "Experimental study on two way shape memory effects training procedure for NiTiNOL shape memory alloy",*** ARPN Journal of Engineering and Apageslied Sciences, Volume 10, Number 17, 2015.

[70]. Yinong Liu, Yong Liu and J. Van H. ***, "Two way shape memory effects developed by martensite deformation in NiTi",*** Acta mater. Volume 47, Number 1, pages. 199-209, 1999.

[71]. Jose Maria Guilemany and J. Fernández, ***"Seismic Response Control Using Shape Memory Alloys: A Review",*** J. of INTELLIGENT MATERIAL SYSTEMS AND STRUCTURES, Volume. 22, pages. 1531-1549, 2014.

[72]. Islam A. , ***" Effect of Surface Porosity on Tribological Properties of Automotive Al-base Alloys ",*** August 2010.

[73]. M. Reza Rezvani and A. Shokuhfar, ***"Synthesis and characterization of nano structured Cu–Al–Mn shape memory alloy by mechanical alloying",*** Materials Science and Engineering A, Volume 532, pages. 282–286, 2012.

[74]. Z. Li , Z.Y. Pan, N. Tang, Y.B. Jiang, N. Liu, M. Fang and F. Zheng***, "Cu–Al–Ni–Mn shape memory alloy processed by mechanical alloying and powder metallurgy"***, Materials Science and Engineering A, Volume 417 ,page 225–229, 2006.

[75]. G. S. Upadhyaya, ***"Powder metallurgy technology"***, Cambridge International Science Publishing, First published, August 2002.

[76]. Philip A. Schweitzer, ***"metallic materials Physical, Mechanical, and Corrosion Properties",*** NEW York. BASEL, ISBN: 0-8247-0878-4, 2003.

Reference

[77]. Azim Gokcea, Fehim Fındıka, Ali Osman Kurtb, ***"Microstructural examination and properties of premixed Al–Cu–Mg powder metallurgy alloy"***, Materials characterizetion, Volume 62, Pages 730 – 735, 2011.

[78]. Bozzone, S. ***"Powder Blending "***, adopted from Solid Oral Dosage Forms, May 31, 2001.

[79]. Hoganas A. B., ***"Production of Sintered Components",*** Hoganas Handbook for Sintered Components, Sweden, 2013.

[80]. Groover M. P. ,***"Blending and Mixing of The Powders"***, Fundamentals of modern Manufacturing, Volume 352, 2010.

[81]. Aole D., Jain M.K. and Bruhis, ***" New characterization methods for powder die fill process for producing powder metallurgical components"***, Powder Technology, Volume 232, Pages 7-17, December 2012.

[82]. Seetharaman S., ***" Fundamentals of metallurgy"***, Pages. 486-490, 2005.

[83]. Colton,J.S. , ***"Metal Powder Processing"*** ,adopted from Manufacturing Processes and Engineering , 2009.

[84]. ASM Handbook, ***"Powder Metal Technologies and Applications"*** Volume 7, pages 1044.

[85]. Randall M. German, Pavan Suri, Seong Jin Park ***" Review: liquid phase sintering "*** J Material Science, Volume 44, pages. 1–39, 2009.

[86]. Mahammad Ali Shaik, Khader Hussain Syed and Brahma Raju Golla, ***"Electrochemical behavior of mechanically alloyed hard Cu-Al alloys in marine environment",*** Corrosion Science, Volume 153, Pages 249-257, June 2019.

DOI: https://doi.org/10.1016/j.corsci.2019.03.043

Reference

[87]. Nady H. El-Sayed and Mohamed M. El-Rabiei, ***"Effect of sulfide pollution on the stability of Cu–Al–5Ni alloy in 3.5% NaCl solution",*** Egyptian Journal of Petroleum, Volume 23, Pages. 163–168, 2014.

[88]. Mahammad Ali Shaik and Brahma Raju Golla, ***"Development of highly wear resistant Cu - Al alloys processed via powder metallurgy",*** Tribology International, Volume 136, Pages. 127–139, 2019.

[89]. F.P. Ijsseling, ***"General guidelines for corrosion testing of materials for marine applications",*** British Corrosion Journal, Pages. 53-78, 1989.

[90]. Schumacher, M. M., ***"Seawater corrosion handbook",*** 1979.

[91]. Kear, G., Barker, B. D., Walsh, F. , ***"Electrochemical corrosion of unalloyed copper in chloride media"***, Corrosion science, pages. 109-135, 2004.

[92]. Zaki Ahmad, ***"Principles of Corrosion Engineering and Corrosion Control"***, Butterworth-Heinemann/IChem E Series, First publish, 2006.

[93]. S. Montecinos and S.N. Simisona***, "Influence of the microstructure on the corrosion behaviour of a shape memory Cu–Al–Be alloy in a marine environment"*** Applied Surface Science, Volume. 257, pages. 2737–2744, 2011.

[94]. L.L. Shreir, R.A. Jarman and G.T. Burstein***, "Corrosion Metal Environment Reactions"***, Linacn House, Jordan Hill, Oxford, Vol 1, Third edition, 1994.

[95]. Mars G. Fontana and Greene, ***"Corrosion Engineering",*** McGraw-Hill book Co., Third edition, 1986.

[96]. Denny A. Jones, ***"Principles and Prevention of Corrosion",*** Prentice Hall, Upageser Saddle River, Second Edition, USA, 1996.

[97]. Kenneth R. Trethewey, ***"Corrosion for Science and Engineering",*** Longman Sc & Tech, Second edition, 1996.

Reference

[98]. S. Zhou, M.M. Stack, R.C. Newman, ***"Characterization of synergistic effects between erosion and corrosion in an aqueous environment using electrochemical techniques"***, Corrosion, Volume. 52, pages. 934-946, 1996.

[99]. Rao T. S. and Nair V. K., ***"Microbiologically influenced stress corrosion cracking failure of admiralty brass condenser tubes in a nuclear power plant cooled by freshwater"***, Corrosion Science, Volume 40, Issue11, Pages. 1821-1836, 1998.

[100]. Machuca, L. L Ginige, A. Kaksonen. K. Heidersbach, ***"Corrosion performance of offshore construction materials in the presence of active biofilms in seawater",*** Corrosion Science,2012.

[101]. Hackerman N. and Snavely E. "***Basic Corrosion Course"***, Chapter 9, Ed. NACE, Houston, Texas, 1970**.**

[102]. Uhlig H. H.**,** ***"Corrosion and Corrosion Control",*** Winston Revie. R., John Wiley and Sons, 3rd Edition, 1985.

[103]. J.R. Davis, ***"Corrosion, understanding the basic",*** ASM TECHNICAL BOOKS, ISBN: 978-1-62708-250-1, 2000.
https://doi.org/10.31399/asm.tb.cub.t66910049

[104]. C. Aksu Canbay and A. Keskin, ***"Effects of vanadium and cadmium on transformation"***, J. Thermal Analyses Colometry, 2014.
https://DOI 10.1007/s10973-014-4034-6.

[105]. Z. Xiao, M. Fang, Z. Li , T. Xiao , Q. Lei, ***"Structure and properties of ductile CuAlMn shape memory alloy synthesized by mechanical alloying and powder metallurgy"***, Materials and Design, Volume 58, pages 451–456, 2014.

[106]. Sh. Yang , F. Zhang, J. Wu, Y. Lu, Z. Shi, C. Wang, X. Liu, ***"Superelasticity and shape memory effect in Cu–Al–Mn–V shape memory alloys",*** Materials and Design, Volume 115, pages 17–25, 2010.

[107]. Y.Q. Jiao, Y.H. Wena, N. Lia, J.Q. Hea, J. Tenga, ***"Effect of solution treatment on damping capacity and shape memory effect of a CuAlMn alloy",*** Journal of Alloys and Compounds, Volume 491, pages 627–630, 2010.

[108]. Pravir Kumar, Ashish Kumar Jain, Shahadat Hussain, Abhishek Pandey, Rupa Dasgupta, ***"Changes in the properties of Cu-Al-Mn shape memory alloy due to quaternary addition of different elements"***, Revista Materia ,Volume 20, Number 1, Pages 284-292, 2015.

[109]. U.S. Mallik and V. Sampath, ***"Influence of aluminum and manganese concentration on the shape memory characteristics of Cu–Al–Mn shape memory alloys"***, Journal of Alloys and Compounds, Volume 459, pages 142–147, 2008.

[110]. U.S. Mallik and V. Sampath, ***"Effect of composition and ageing on damping characteristics of Cu–Al–Mn shape memory alloys"***, Materials Science and Engineering A, Volume 478, pages 48–55, 2008.

[111]. Restu Faizah and Akhmad Aminullah, ***"Simple Laboratory Test to Measure Damping Properties of Hardened Mortar or Concrete Elements",*** International Journal of Sustainable Construction Engineering and Technology, Volume. 11 Number 1, pages. 76-86, 2020.

[112]. C. Canbay and Z. Karagoz, ***"The effect of quaternary element on the thermodynamic parameters and structure of CuAlMn shape memory alloys",*** materials science and process, ISSN 0947-8396, 2013.
DOI 10.1007/s00339-013-7880-3

[113]. A. Benedeiti, P. Sumomof, K. Nobe P. Cabot and W. Proud, ***"Electrochemical studies of Copper, Copper Aluminum and Copper-Aluminum –Silver: impedance results in NaCl"*** , Electro chemical Acts. Volume 40, Number 16, pages. 2657-2668. 1995.

[114]. G. Abbas, T. Manzoorc, A. Naeem, ***"Investigation of Thermal and Mechanical Properties of Cu-Al alloys with silver addition prepared by Powder Metallurgy"***, Journal of Alloys and Compounds, Volume 11, Number l76, 2017.

[115]. X. Chen, F. Zhang, M. Chia, S. Yanga, C. Wang, X. Liu, S. Zheng, ***"Microstructure, super elasticity and shape memory effect by stress-induced martensite stabilization in Cu–Al–Mn–Ti shape memory alloys"***, Materials Science & Engineering B, Volume 236–237, pages 10–l7, 2018.

[116]. ASTM B-328, ***"Standard Test Method for Density, Oil Content, and Interconnected Porosity of Sintered Metal Structural Part and Oil-Impregnated Bearing"***, ASTM international, 2003.

[117]. ASTM G 5 – 94, ***"Standard Reference Test Method for Making Potentiostatic and Potentiodynamic Anodic Polarization Measurements",*** ASTM international, Reapproved 2004.

[118]. G.R. Argade, S.K. Panigrahi and R.S. Mishra, ***"Effects of grain size on the corrosion resistance of wrought magnesium alloys containing neodymium"*** Corrosion Science, Volume 58, pages. 145-151, 2012.

[119]. ASTM, ***"Powder metallurgy technologies and applications"***, Handbook, Volume 07, pages 23.

[120]. Jassim Mohammed Salman, Abdul Raheem K.Abid Ali and Huda Abbas Kheralla, ***"Corrosion study of CuAlZn Shape Memory Alloys in 3.5 NaCl***

Solution", International Journal of Current Engineering and Technology, Volume 4, Number 3, 2014.

[121]. K. A. Darling, A. J. Roberts, Y. Mishin, S. N. Mathaudhu, and L. J. Kecskes, ***"Grain size stabilization of nanocrystalline copper at high temperatures by alloying with Tantalum,"*** Journal of Alloys and Compounds, Volume. 573, pp. 142–150, 2013

[122]. Guofei Zhanga, Haiqing Yina, Cong Zhanga,c, Zhenghua Denga , Ruijie Zhanga, Xue Jianga, Xuanhui Qua, ***"Effect of Mn on Microstructure and Properties of Cu-12Al Powder Metallurgy Alloy",*** Mater. Res. Express. Vol 7, Number 1, 2020.

[123]. Ayad M. Takhakh, Raied Z. Alfay, Abdul Rahim K. Abid Ali, ***"Effect of Ta addition on hardness and wear resist of Cu-Al-Ni shape memory alloy fabricated by powder metallurgy"***, IEEE Business Engineering and Industrial Applications Colloquium (BEIAC),2013.

[124]. Jiao Yu, Wen Yu, Li Ning, He Jia. , Teng J., ***"Effect of environmental temperature on damping capacity of Cu-Al-Mn alloy"***, Trans. Nonferrous Met. Soc. China, Volume 19, pages. 616- 619, 2009.

[125]. A.T. Adorno, T.M. Carvalho, R.A.G. Silva, C.M.A. Santos, A.G. Magdalena, ***"Effect of Ag additions on the b phase formation reaction in the Cu–9 Wt. %Al–6 Wt. %Mn alloy"***, Journal of Alloys and Compounds, Volume 643, Pages. S275–S279, 2015.

[126]. Haydar H.J. Jamal Al-Deen, ***"Improvement of Corrosion Resistance of Aluminum – Bronze Alloys In (3.5%NaCL and 2m HCl) Solutions by Indium Additions"***, Journal of Mechanical Engineering Research and Developments, Volume 43, Number 2, pages. 218-225, 2020.

Reference

[127]. Tamara H. , Dragan M. , L. Balanovic ,Dusko M. , Stjepan K., Ivana I., Mirko G., ***"Microstructure and phase transformation of Cu based shape memory alloys",*** International science J. machines technologies materials, Volume10, pages. 419-422, 2018.

[128]. Safaa Najah Saud Al-Humairi, ***"Cu-Based Shape Memory Alloys: Modified Structures and Their Related Properties"***, Recent Advances in Engineering Materials and Metallurgy, 2013. http://dx.doi.org/10.5772/intechopen.86193.

[129]. Hussein Ali, ***"Effect of Some Alloying Elements on the Mechanical and Corrosion Behavior of Copper-Aluminum-Nickel Alloys",*** MSc. Thesis, Materials Engineering/University of Babylon, 2018.

[130]. S. Kozuh, M. Gojic, I. Ivanic, T. Grguric, Kosec, and I. Anzel, ***"The Effect of Heat Treatment on the Microstructure and Mechanical Properties of Cu-Al-Mn Shape Memory Alloy"***, KEM journal, Volume 67, issue 1-2, pages. 11−17, 2018.

[131]. Ladislav Vrsalovic, Ivana Ivanic, Stjepan Kozuh, Borut Kosec, Milan Bizjak, Janez Kovac, Urska Gabor and Mirko Gojic, ***"Influence of heat treatment on the corrosion properties of CuAlMn shape memory alloys",*** Corrosion Rev, Volume 37(6), pages. 579–589, 2019.

[132]. Mirko Gojic, Stjepan Kožuh, Ivana Ivanic, Magdalena Selanec, Tamara Holjevac Grguric, Borut Kosec, Diana Ćubela, Omer Beganovic ***"Microstructural characterization of Cu82.3Al8.3Mn9.4 shape memory alloy after rolling"*** Metallurgical and Materials Engineering, Volume 23 (3), pages. 281-289, 2017.

[133]. S. Mahammad Ali and G. Brahma Raju, ***"Densification, microstructure and properties of mechanically alloyed and hot pressed Cu-15wt.% Al alloy",*** Journal of Materials Science, J. Mater. Sci., Volume 53, pages. 14694–14712, 2018.

[134]. R. O. Ferreira , L. S. Silva , R. A. G. Silva, ***"Thermal behavior of as annealed CuAlMnAgZr alloys",*** Journal of Thermal Analysis and Calorimetry, 2020. https://doi.org/10.1007/s10973-020-10002-8.

[135]. C.B. Pilz, E.L. Matsumura, A. Paganotti, D.R. Cornejo, R.A.G. Silva, ***"Microstructure and phase stability of CuAlMnAgZr multi component alloys",*** Materials Chemistry and Physics, Volume 241, Number 122343, 2020.

[136]. C. Santos, A. Adorno, M. Stipcich, Cuniberti, J. Souza, C. Bessa, R. Silva, ***"Effects of Ag presence on phases separation and order-disorder transitions in Cu-xAl-Mn alloys",*** Materials Chemistry and Physics, Volume 227, pages. 184–190, 2019.

[137]. A. T. Adorno, M. R. Guerreiro and A. V. Benedetti, ***"thermal behaviour of CuAl alloy near the α-CuAl solubility limit"***, Journal of Thermal Analysis and Calorimetry, Volume 65, pages. 221–229, 2001.

[138]. Canan Aksu Canbay and Tercan Polat, ***"Thermal and structural alternations in CuAlMnNi shape memory alloy by the effect of different pressure applications",*** Physica B: Condensed Matter, Volume 521, Pages 331-338, 2017.

[139]. G. Kear, B.D. Barker, F.C. Walsh, ***"Electrochemical corrosion of unalloyed copper in chloride media - a critical review",*** Corrosion Science, Volume 46, pages. 109-135, 2004.

[140]. Mirko Gojic, Ladislav Vrsalovic, Stjepan Kozuh, Albert Kneiss, Ivan Anzel, Senka Gudic, Borut Kosec, Maja Kliski, ***"Electrochemical and microstructural study of Cu–Al–Ni shape memory alloy",*** Journal of Alloys and Compounds, Volume 509, pages. 9782–9790, 2011.

[141]. S. Montecinos and S. Simison, ***"Corrosion behavior of Cu–Al–Be shape memory alloys with different compositions and microstructures",*** Corrosion Science, Volume74, Pages 387-395, 2013.

[142]. Qiang Pan and Chongdu Cho, ***"Damping properties of shape memory alloys",*** Metal, Volume 5, pages. 13-15, 2008.

[143]. D.E. Hodgson, ***"Damping applications of shape- memory alloys",*** Material Science Forum, Volume 394–395, pages. 69–74, 2002.

[144]. J. Van Humbeeck, ***"Damping Properties of Shape Memory Alloys During Phase Transformation",*** Journal de Physique IV Colloque, 06 (C8), pages.C8- 371-C8-380, 1996,

[145]. Zhixian Jiao , Qingzhou Wang, Fuxing Yin , Chunxiang Cui , Jianjun Zhang, Chang Yao, ***"Effects of Cu51Zr14 inoculant and caliber rolling on microstructures and comprehensive properties of a Cu–Al–Mn shape memory alloy",*** Materials Science & Engineering A, Volume. 772, 2020.

[146]. Zhishan Yuan, Jingli Hu, Hengjin Zhang, Weidong Miao, and Ming Zhu, ***"Characterization of high damping TiNi shape memory alloy",*** Third International Conference on Smart Materials and Nanotechnology in Engineering, Volume 8409, 2012.

Reference

[147]. Qingzhou Wang, Xlaojnliu, Sergeyyu K. , Puguangi, Fuxing Y. , Chunxiang C., and Ganglighao, ***"Microstructural, Mechanical, and Damping Properties of a Cu-Based Shape Memory Alloy Refined by an In Situ LaB6/Al Inoculant"***, Metallurgical and materials transformation , Volume 50A, 2019.

[148]. Agnieszka Mielczarek, Werner Riehemann, Sonke Vogelgesang, Hennadiy Zak, Babette Tonn, ***"Amplitude Dependent Internal Friction of CuAlMn Shape Memory Alloys"***, Engineering Materials, Volume 319, pages. 45-52, 2006.

[149]. Barik R. C., Wood R. J. K. and Stokes K. R., ***" Erosion and Erosion-Corrosion Performance of Cast and Thermally Spread Nickel-Aluminum Bronze",*** Wear, Volume259, issue 1-6, 2005. http://handle.dtic.mil/100.2/ADA 442471.

[150]. Mohammed Abdullatef, ***"Evaluation of Erosion and Erosion Corrosion in 3.5 % NaCl for Steel Pip"***, A Thesis Submitted to the Department of Production and Metallurgy Engineering of the University of Technology, 2007.

[151]. R. Manikandan , S.P. Kumaresh Babu, M. Murali, A. Vallimanalan, ***"A study of corrosion enhanced erosion in Nickel Aluminium Bronze with Niobium and Yttrium"***, Materials Today: Proceedings, 2019. https://doi.org/10.1016/j.matpr.2019.10.083

[152]. Stephen M. McIntyre, ***"Metallurgical Examination of cooling water Equipment Failures",*** Journal of The analyst , Volume 7, Number 2, 2005.

[153]. Mohini Saxena, O. P. Modi, B. K. Prasad, A. K. Jha, ***"Erosion and corrosion characteristics of an Aluminium alloy-alumina fibre composite",*** Wear, Volume 169, Issue 1, Pages. 119-124, 1993.

[154]. Pradeep Kumar Yadav, Gajendra Dixit, ***"Investigation of erosion-corrosion of aluminium alloy composites: Influence of slurry composition and speed in a different mediums",*** Journal of King Saud University – Science, Volume 31, pages. 674 – 683, 2019. https://doi.org/10.1016/j.jksus.2019.02.003

[155]. Uwe Arlica, Hennadiy Zak, Bernd Weidenfeller, Werner Riehemanna, ***"Impact of Alloy Composition and Thermal Stabilization on Martensitic Phase Transformation Structures in CuAlMn Shape Memory Alloys",*** Materials Research, Volume 21, 2018. http://dx.doi.org/10.1590/1980-5373-MR-2017-0897.

[156]. Faisel A. M. Al-Bassam, Abd Al-Wahed K.R. Al-Bakry and Saif M. H. Al-Sharify, ***"Effect of Alloying Elements and Heat Treatment on Behavior of the Alloy (Cu, Al) Used in Marine Industries",*** The Iraqi Journal For Mechanical and Material Engineering, Volume10, Number 1, 2009.

[157]. Naoki Koeda, Toshihiro Omori, Yuji Sutou, Hidekazu Suzuki, Masami Wakita, Ryosuke Kainuma and Kiyohito Ishida, ***"Damping Properties of Ductile Cu-Al-Mn-Based Shape Memory Alloys"***, Materials Transactions, Volume. 46, Number. 1, pages. 118 to 122, 2005.

[158]. Nawal Mohammed Dawood and Abdul Raheem Kadhim AbidAli, ***"Influence of Titanium Additions on the Corrosion Behavior of Cu-Al-Ni Shape Memory Alloys",*** Materials Science Forum, ISSN: 1662-9752, Volume.1021, pages. 55-67, 2021.

Reference

[159]. Nawal Mohammed Dawood, ***"Erosion-Corrosion Behavior of Al-20%Ni-Al2O3 Metal Matrix Composites by Stir Casting",*** Materials Science Forum, ISSN: 1662-9752, Volume. 1002, pages. 161-174, 2020.

[160]. Abdulraheem Kadhim Abid Ali and Nawal Mohamed Dawood, ***"The Effect of Boron Addition on The Microstructure and Corrosion Resistance of Cu-Al-Ni Shape-Memory Alloys Prepared by Powder Technology"*** IOP Conf. Series: Materials Science and Engineering, Volume 987, 2020.

[161]. Dolce M. and Cardone D., ***"Mechanical behaviour of shape memory alloys for seismic applications"***, International Journal of Mechanical Sciences,2001.

[162]. J. Moraisa, P. Gil de Morais, C. Santos, A. Campos Costa, P. Candeias, ***"Shape Memory Alloy Based Dampers for Earthquake Response Mitigation",*** 2nd International Conference on Structural Integrity, ICSI 2017, 4-7 September 2017, Funchal, Procedia Structural Integrity, Volume 5, pages 705–712, 2017.

Appendix A
X-Ray Diffraction Cards

A.1. XRD Diffraction Card for Powder

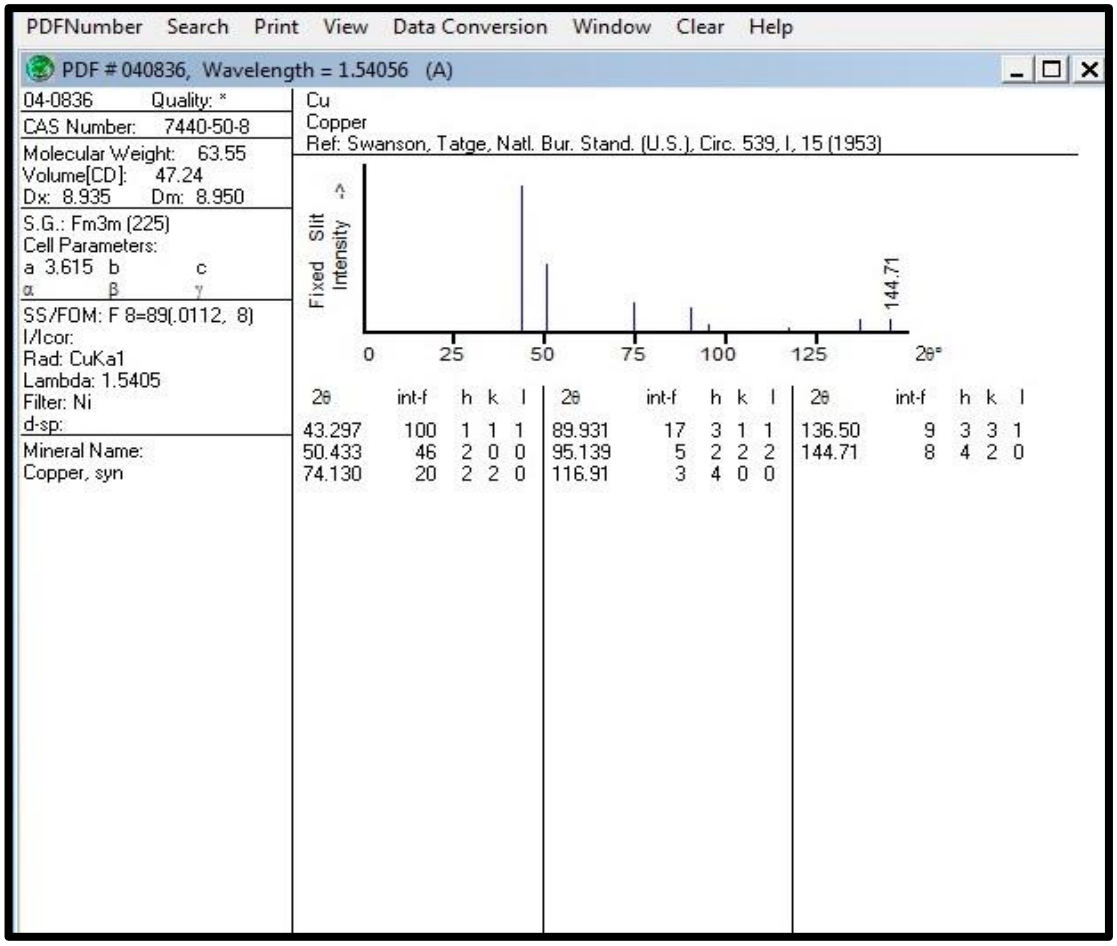

Figure (A.1): ***XRD card for*** **Cu**

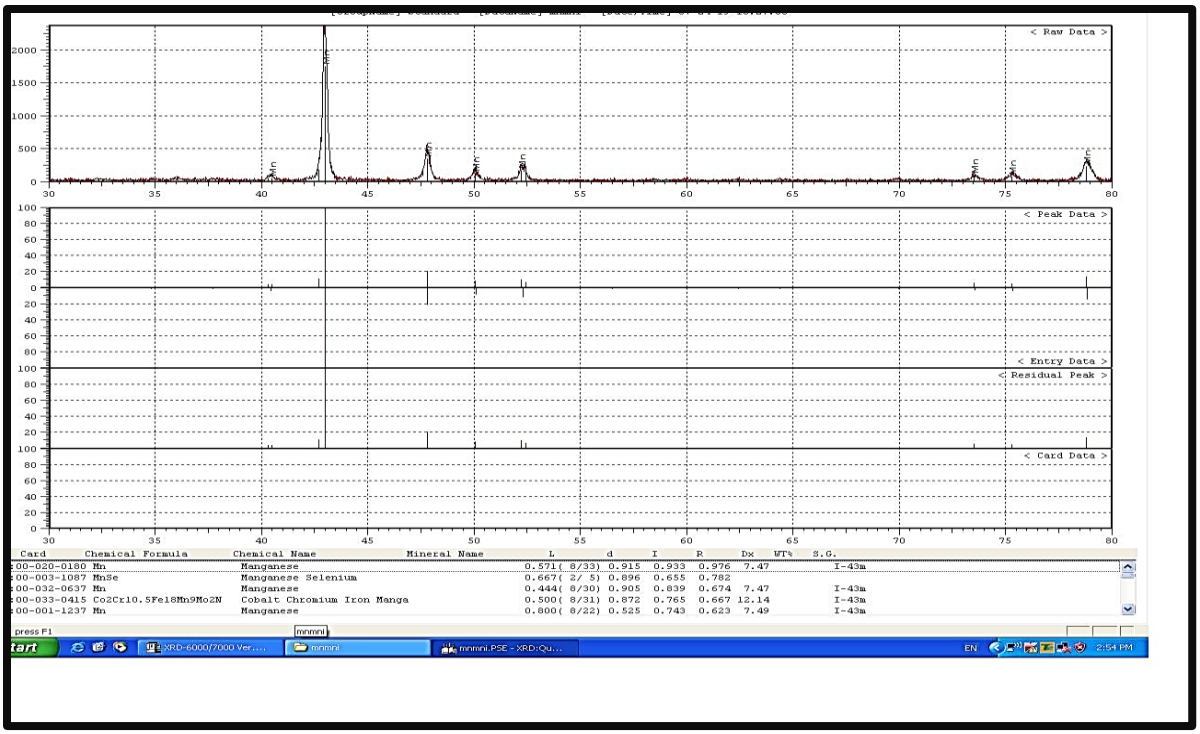

Figure (A.2): ***XRD card for*** **Mn**

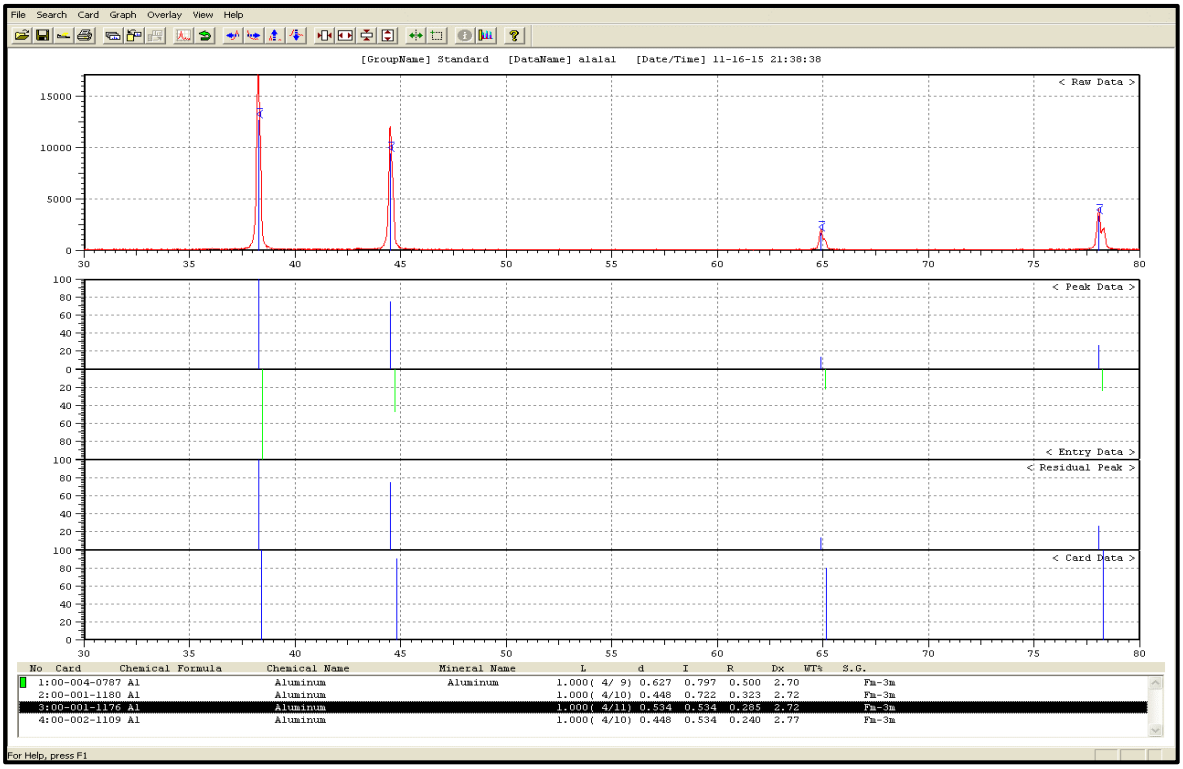

Figure (A.3): ***XRD card for*** **Al**

A.2. XRD Diffraction Card for Intermetallic Compounds

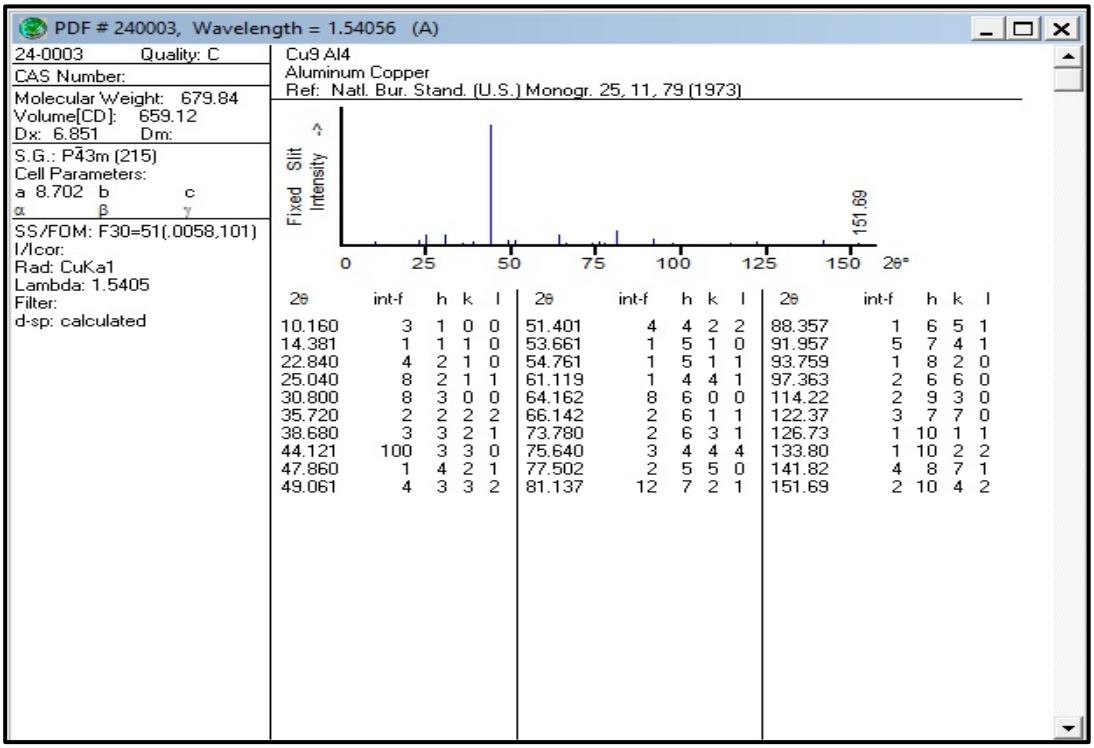

PDF # 240003, Wavelength = 1.54056 (A)

24-0003 Quality: C
CAS Number:
Molecular Weight: 679.84
Volume[CD]: 659.12
Dx: 6.851 Dm:
S.G.: P$\bar{4}$3m (215)
Cell Parameters:
a 8.702 b c
α β γ
SS/FOM: F30=51(.0058,101)
I/Icor:
Rad: CuKa1
Lambda: 1.5405
Filter:
d-sp: calculated

Cu9 Al4
Aluminum Copper
Ref: Natl. Bur. Stand. (U.S.) Monogr. 25, 11, 79 (1973)

Fixed Slit Intensity

0 25 50 75 100 125 150 2θ°

151.69

2θ	int-f	h	k	l	2θ	int-f	h	k	l	2θ	int-f	h	k	l
10.160	3	1	0	0	51.401	4	4	2	2	88.357	1	6	5	1
14.381	1	1	1	0	53.661	1	5	1	0	91.957	5	7	4	1
22.840	4	2	1	0	54.761	1	5	1	1	93.759	1	8	2	0
25.040	8	2	1	1	61.119	1	4	4	1	97.363	2	6	6	0
30.800	8	3	0	0	64.162	8	6	0	0	114.22	2	9	3	0
35.720	2	2	2	2	66.142	2	6	1	1	122.37	3	7	7	0
38.680	3	3	2	1	73.780	2	6	3	1	126.73	1	10	1	1
44.121	100	3	3	0	75.640	3	4	4	4	133.80	1	10	2	2
47.860	1	4	2	1	77.502	2	5	5	0	141.82	4	8	7	1
49.061	4	3	3	2	81.137	12	7	2	1	151.69	2	10	4	2

Figure (A.4): ***XRD card for*** **Cu_9Al_4 Intermetallic Compounds**

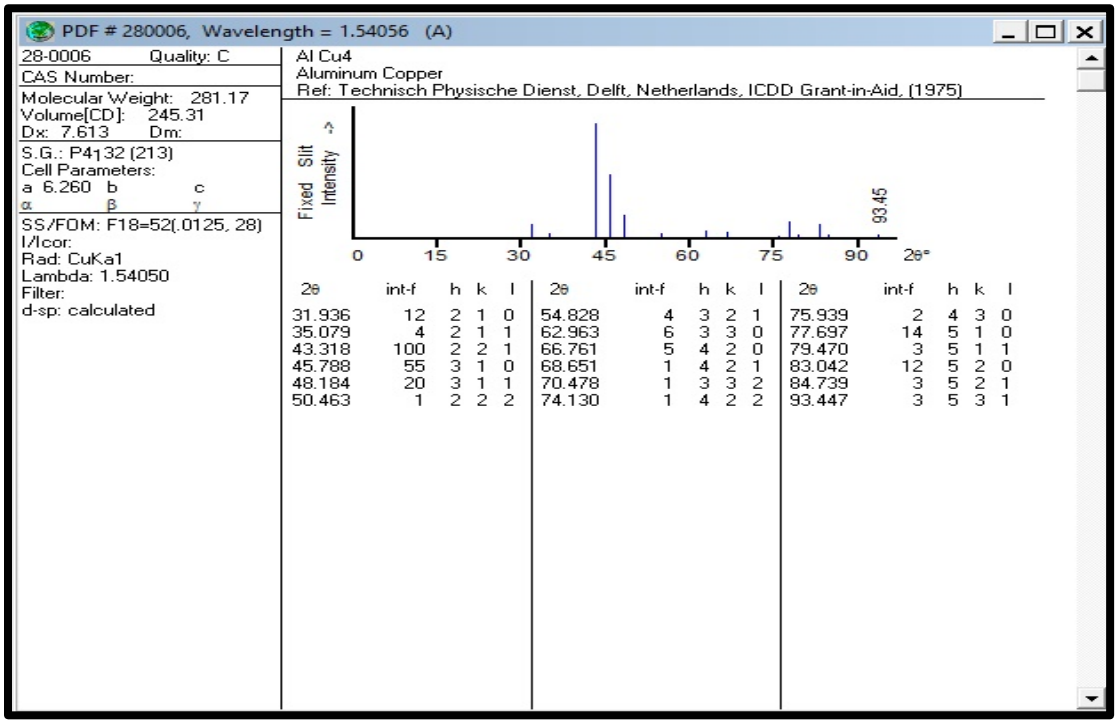

PDF # 280006, Wavelength = 1.54056 (A)

28-0006 Quality: C
CAS Number:
Molecular Weight: 281.17
Volume[CD]: 245.31
Dx: 7.613 Dm:
S.G.: P4$_1$32 (213)
Cell Parameters:
a 6.260 b c
α β γ
SS/FOM: F18=52(.0125, 28)
I/Icor:
Rad: CuKa1
Lambda: 1.54050
Filter:
d-sp: calculated

Al Cu4
Aluminum Copper
Ref: Technisch Physische Dienst, Delft, Netherlands, ICDD Grant-in-Aid, (1975)

Fixed Slit Intensity

0 15 30 45 60 75 90 2θ°

93.45

2θ	int-f	h	k	l	2θ	int-f	h	k	l	2θ	int-f	h	k	l
31.936	12	2	1	0	54.828	4	3	2	1	75.939	2	4	3	0
35.079	4	2	1	1	62.963	6	3	3	0	77.697	14	5	1	0
43.318	100	2	2	1	66.761	5	4	2	0	79.470	3	5	1	1
45.788	55	3	1	0	68.651	1	4	2	1	83.042	12	5	2	0
48.184	20	3	1	1	70.478	1	3	3	2	84.739	3	5	2	1
50.463	1	2	2	2	74.130	1	4	2	2	93.447	3	5	3	1

Figure (A.5): ***XRD card for*** **AlCu4 Intermetallic Compounds**

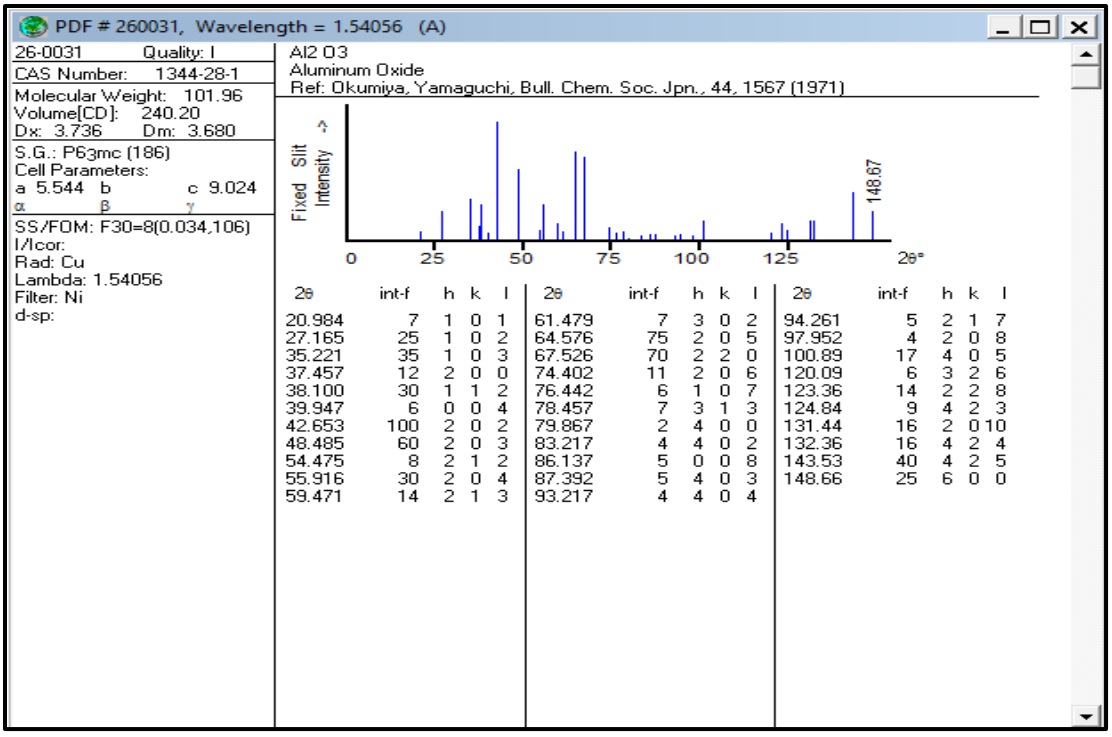

Figure (A.6): *XRD card for* Al_2O_3 Intermetallic Compounds

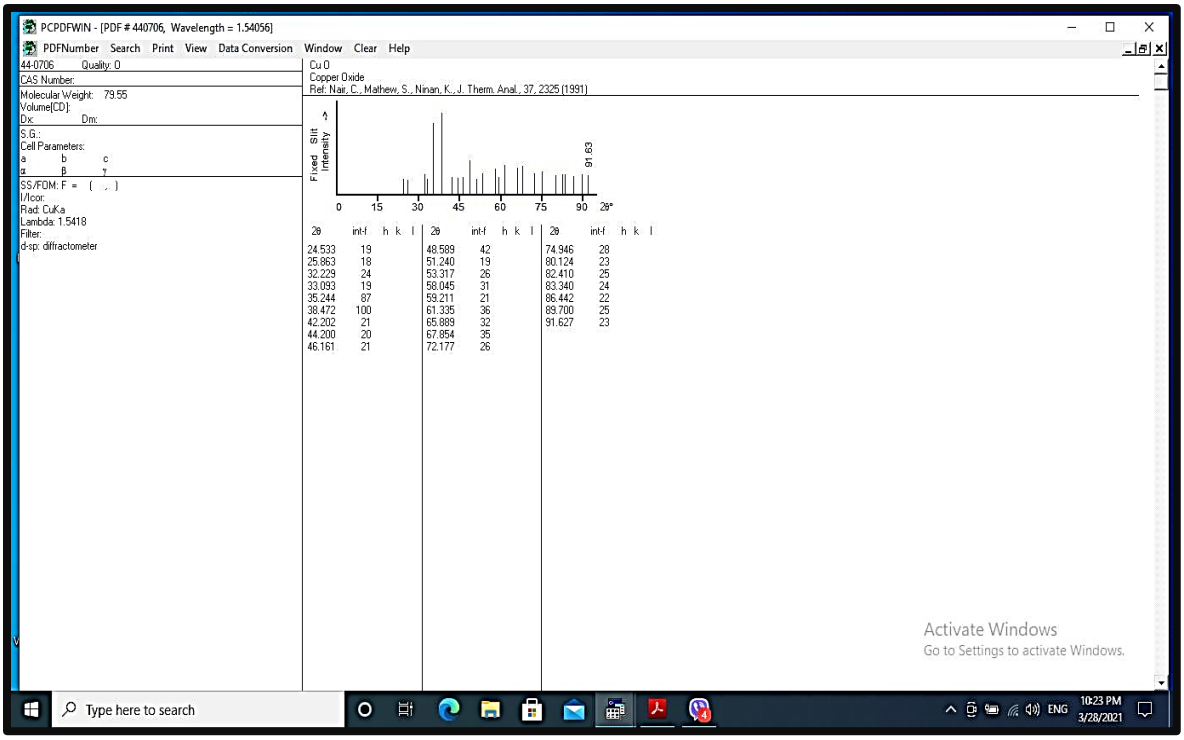

Figure (A.7): *XRD card for* CuO Intermetallic Compounds

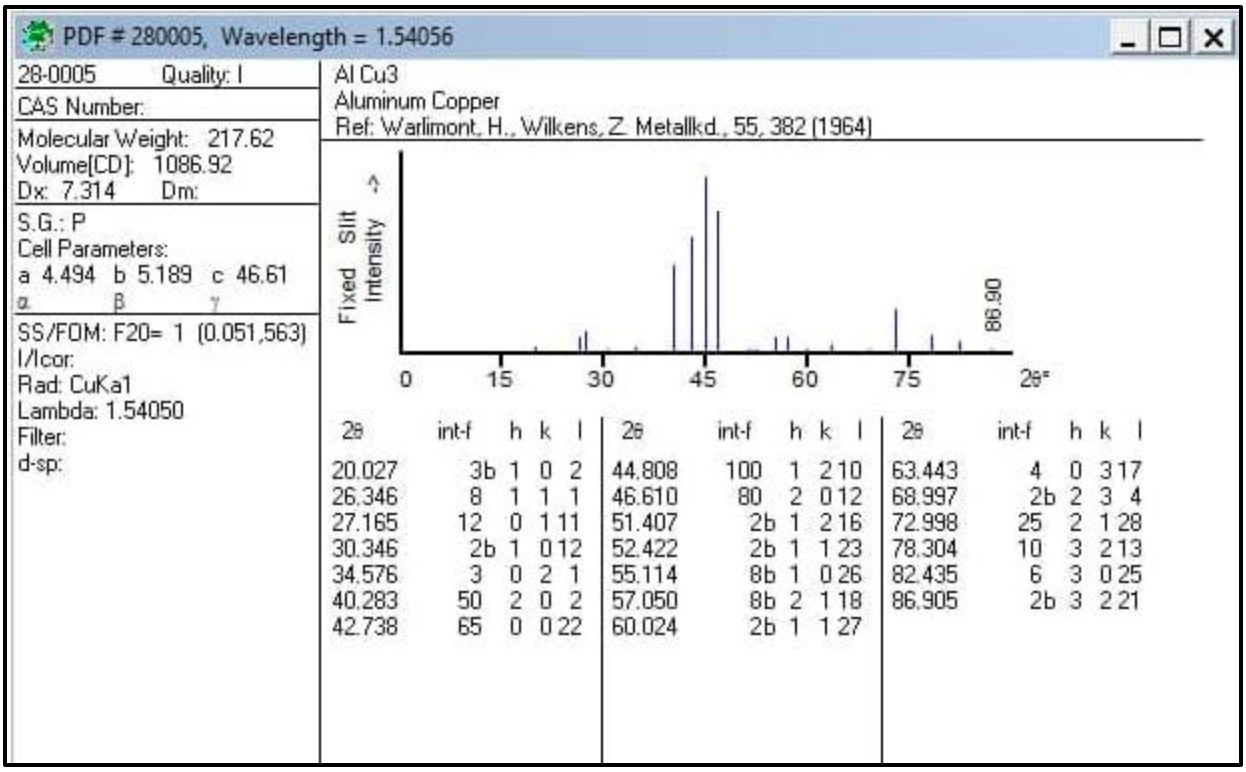

Figure (A.8): ***XRD card for*** **Cu_3Al Intermetallic Compounds**

Appendix B

Damping Capacity curves

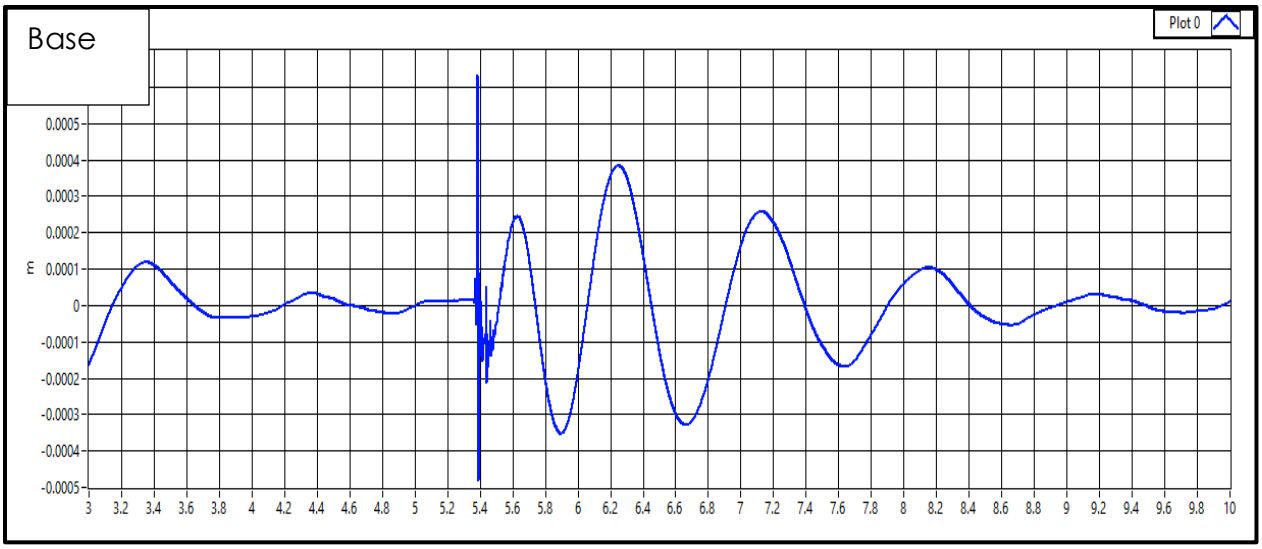
Base
Plot 0
m
0.0005
0.0004
0.0003
0.0002
0.0001
0
-0.0001
-0.0002
-0.0003
-0.0004
-0.0005
3 3.2 3.4 3.6 3.8 4 4.2 4.4 4.6 4.8 5 5.2 5.4 5.6 5.8 6 6.2 6.4 6.6 6.8 7 7.2 7.4 7.6 7.8 8 8.2 8.4 8.6 8.8 9 9.2 9.4 9.6 9.8 10

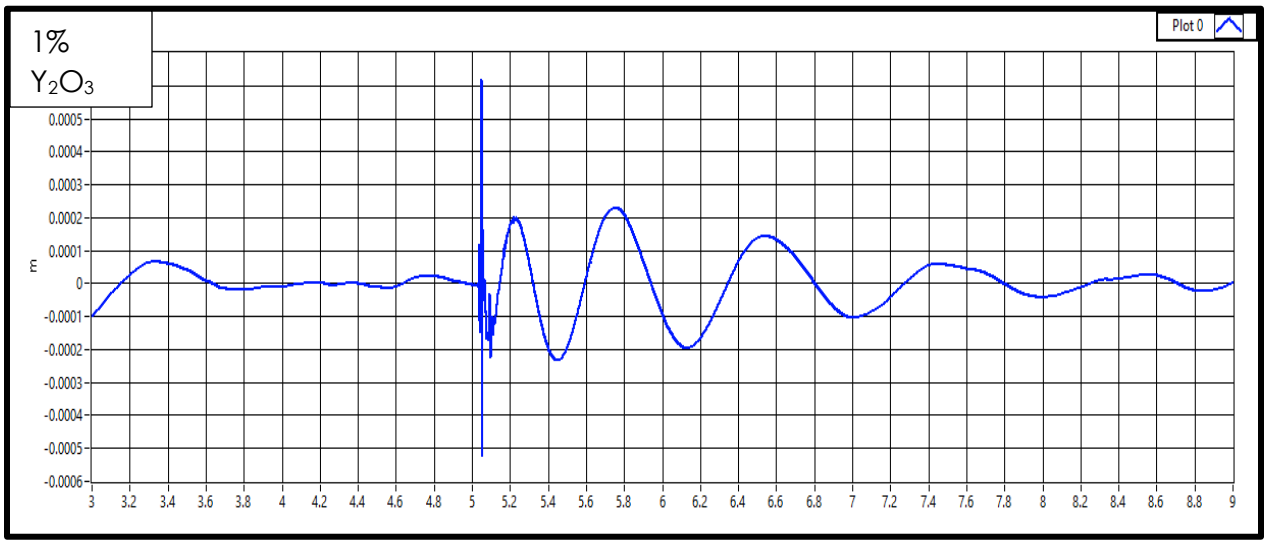
1%
Y_2O_3
Plot 0
m
0.0005
0.0004
0.0003
0.0002
0.0001
0
-0.0001
-0.0002
-0.0003
-0.0004
-0.0005
-0.0006
3 3.2 3.4 3.6 3.8 4 4.2 4.4 4.6 4.8 5 5.2 5.4 5.6 5.8 6 6.2 6.4 6.6 6.8 7 7.2 7.4 7.6 7.8 8 8.2 8.4 8.6 8.8 9

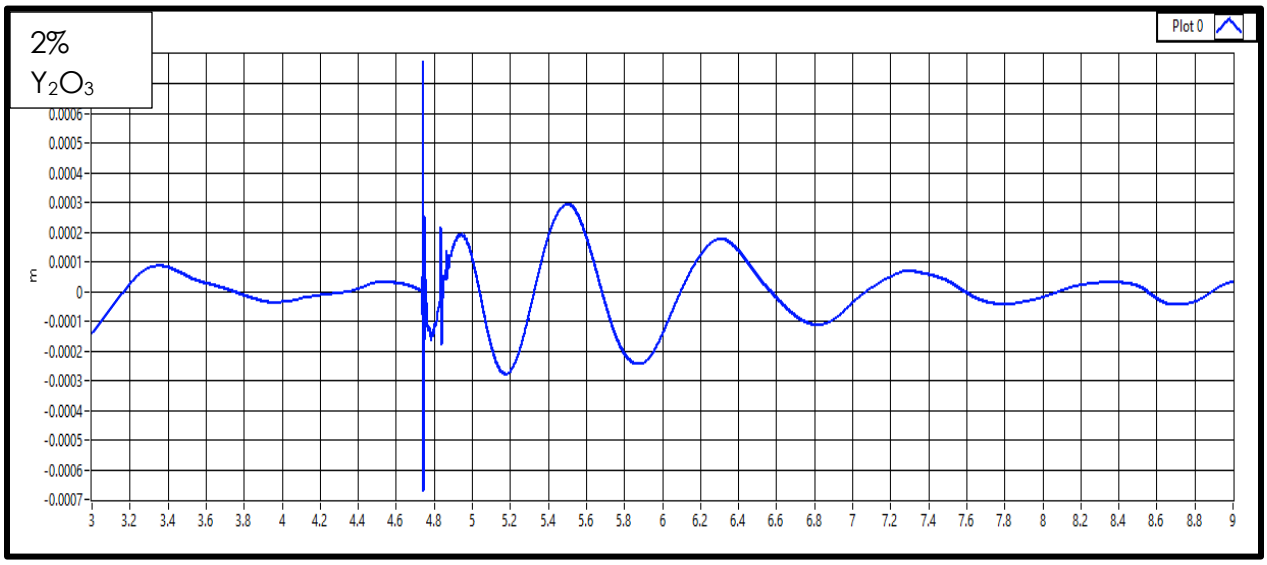
2%
Y_2O_3
Plot 0
m
0.0006
0.0005
0.0004
0.0003
0.0002
0.0001
0
-0.0001
-0.0002
-0.0003
-0.0004
-0.0005
-0.0006
-0.0007
3 3.2 3.4 3.6 3.8 4 4.2 4.4 4.6 4.8 5 5.2 5.4 5.6 5.8 6 6.2 6.4 6.6 6.8 7 7.2 7.4 7.6 7.8 8 8.2 8.4 8.6 8.8 9

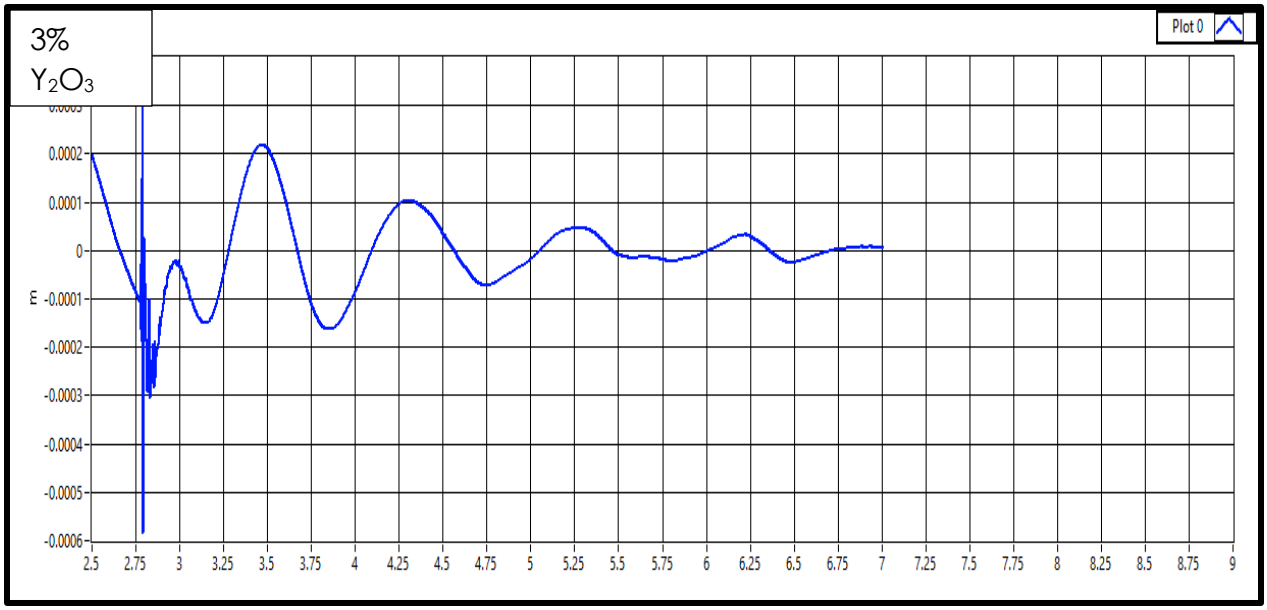
3%
Y_2O_3
Plot 0
m
0.0002
0.0001
0
-0.0001
-0.0002
-0.0003
-0.0004
-0.0005
-0.0006
2.5 2.75 3 3.25 3.5 3.75 4 4.25 4.5 4.75 5 5.25 5.5 5.75 6 6.25 6.5 6.75 7 7.25 7.5 7.75 8 8.25 8.5 8.75 9

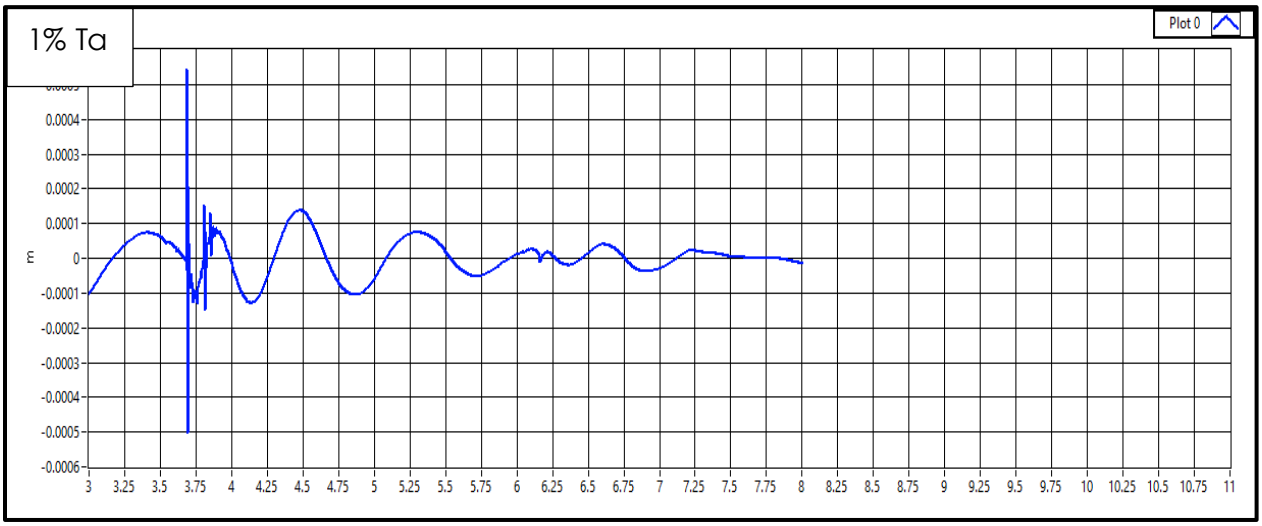
1% Ta
Plot 0
m
0.0004
0.0003
0.0002
0.0001
0
-0.0001
-0.0002
-0.0003
-0.0004
-0.0005
-0.0006
3 3.25 3.5 3.75 4 4.25 4.5 4.75 5 5.25 5.5 5.75 6 6.25 6.5 6.75 7 7.25 7.5 7.75 8 8.25 8.5 8.75 9 9.25 9.5 9.75 10 10.25 10.5 10.75 11

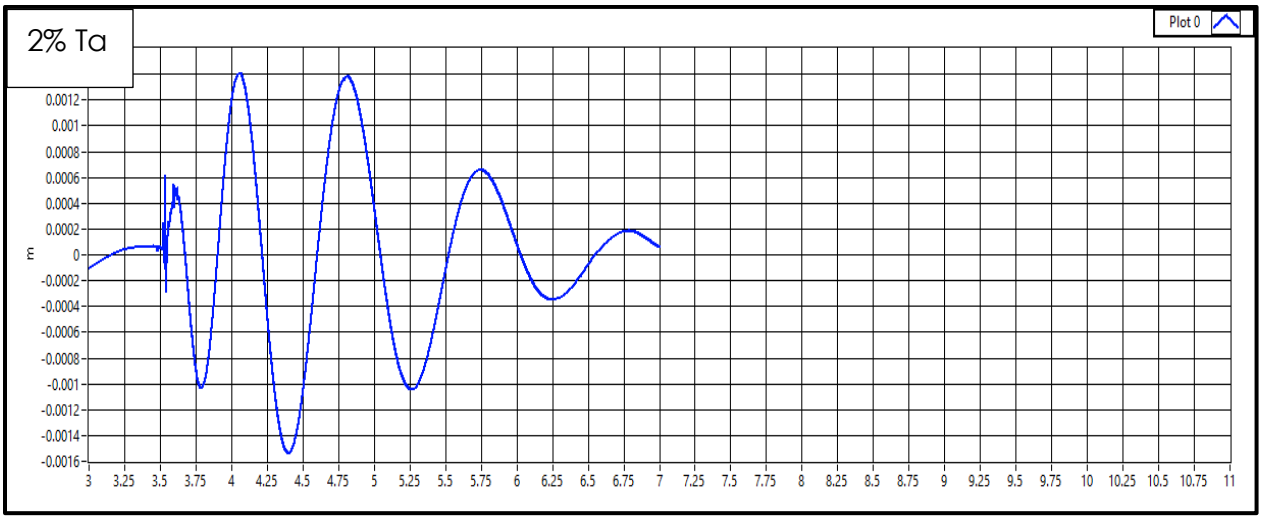
2% Ta
Plot 0
m
0.0012
0.001
0.0008
0.0006
0.0004
0.0002
0
-0.0002
-0.0004
-0.0006
-0.0008
-0.001
-0.0012
-0.0014
-0.0016
3 3.25 3.5 3.75 4 4.25 4.5 4.75 5 5.25 5.5 5.75 6 6.25 6.5 6.75 7 7.25 7.5 7.75 8 8.25 8.5 8.75 9 9.25 9.5 9.75 10 10.25 10.5 10.75 11

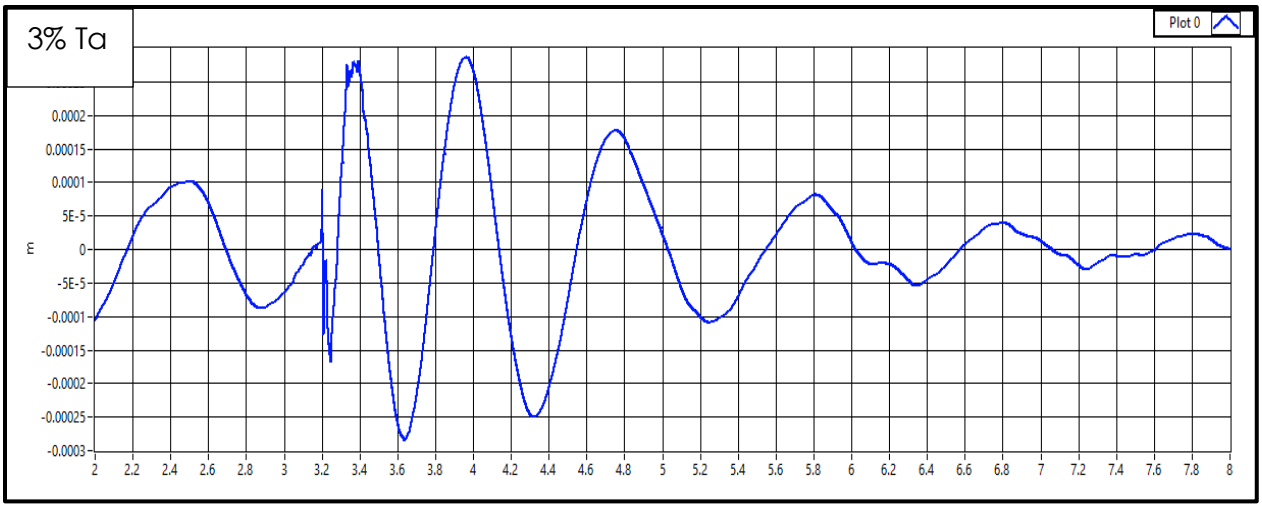
3% Ta
Plot 0
m
0.0002
0.00015
0.0001
5E-5
0
-5E-5
-0.0001
-0.00015
-0.0002
-0.00025
-0.0003
2 2.2 2.4 2.6 2.8 3 3.2 3.4 3.6 3.8 4 4.2 4.4 4.6 4.8 5 5.2 5.4 5.6 5.8 6 6.2 6.4 6.6 6.8 7 7.2 7.4 7.6 7.8 8

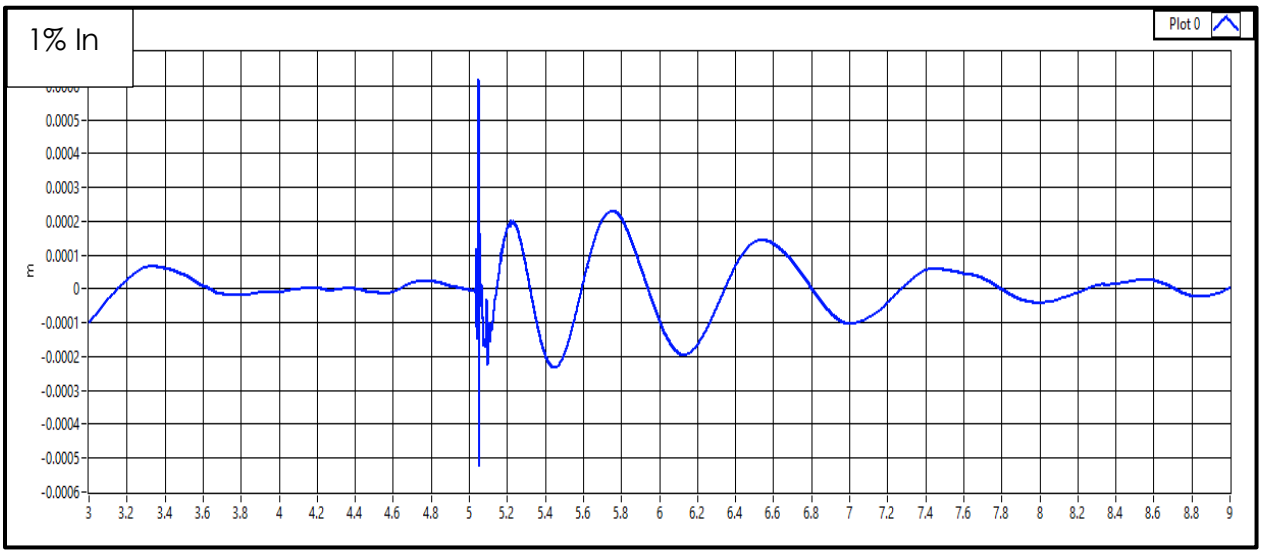
1% In
Plot 0
m
0.0005
0.0004
0.0003
0.0002
0.0001
0
-0.0001
-0.0002
-0.0003
-0.0004
-0.0005
-0.0006
3 3.2 3.4 3.6 3.8 4 4.2 4.4 4.6 4.8 5 5.2 5.4 5.6 5.8 6 6.2 6.4 6.6 6.8 7 7.2 7.4 7.6 7.8 8 8.2 8.4 8.6 8.8 9

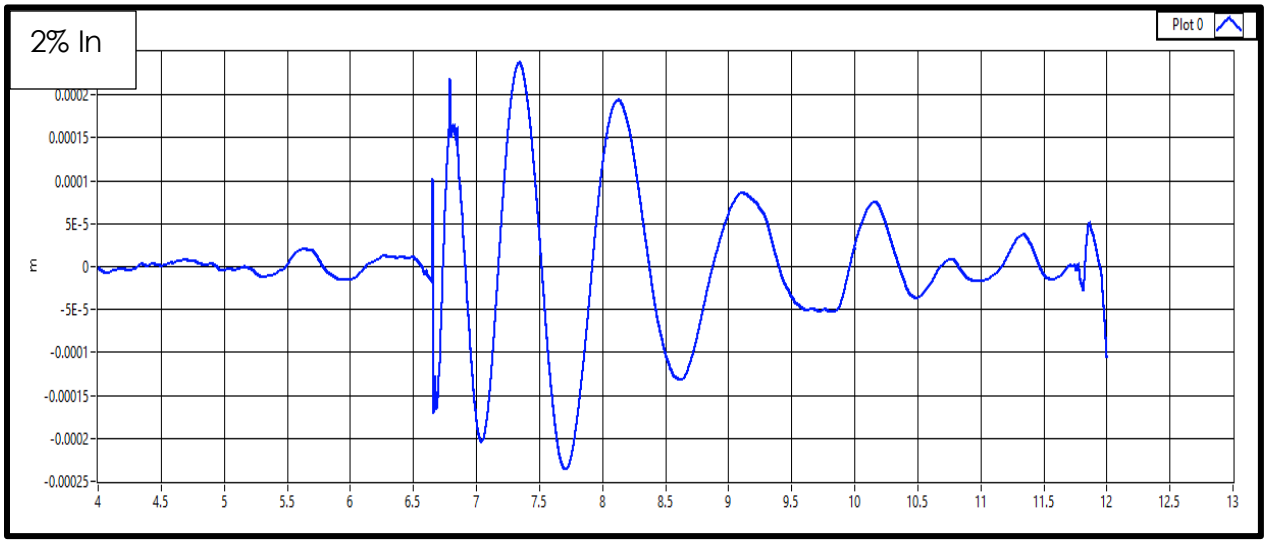
2% In
Plot 0
m
0.0002
0.00015
0.0001
5E-5
0
-5E-5
-0.0001
-0.00015
-0.0002
-0.00025
4 4.5 5 5.5 6 6.5 7 7.5 8 8.5 9 9.5 10 10.5 11 11.5 12 12.5 13

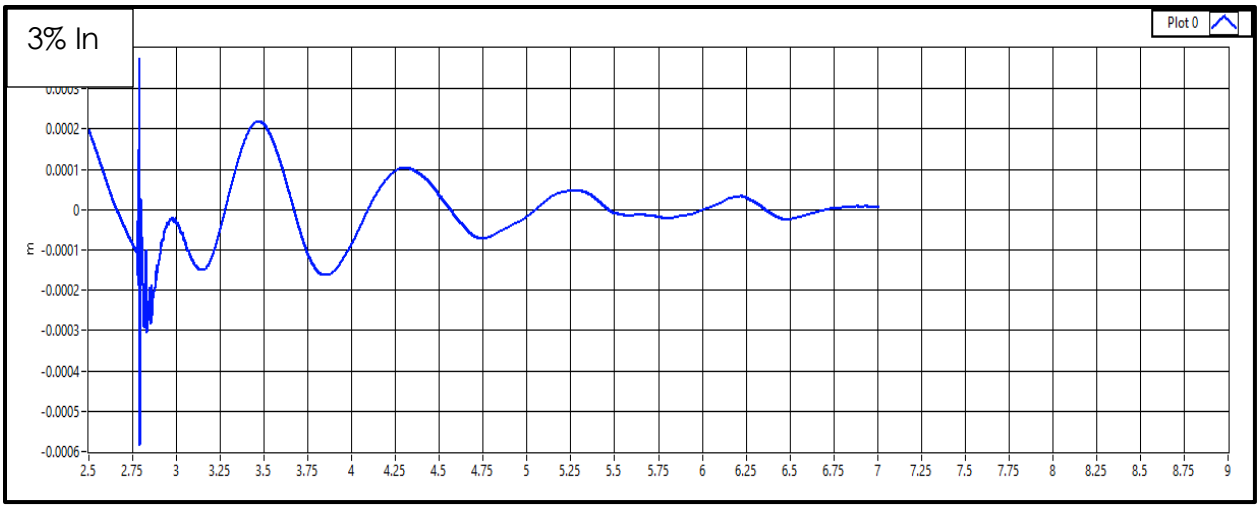
3% In
Plot 0
m
0.0002
0.0001
0
-0.0001
-0.0002
-0.0003
-0.0004
-0.0005
-0.0006
2.5 2.75 3 3.25 3.5 3.75 4 4.25 4.5 4.75 5 5.25 5.5 5.75 6 6.25 6.5 6.75 7 7.25 7.5 7.75 8 8.25 8.5 8.75 9

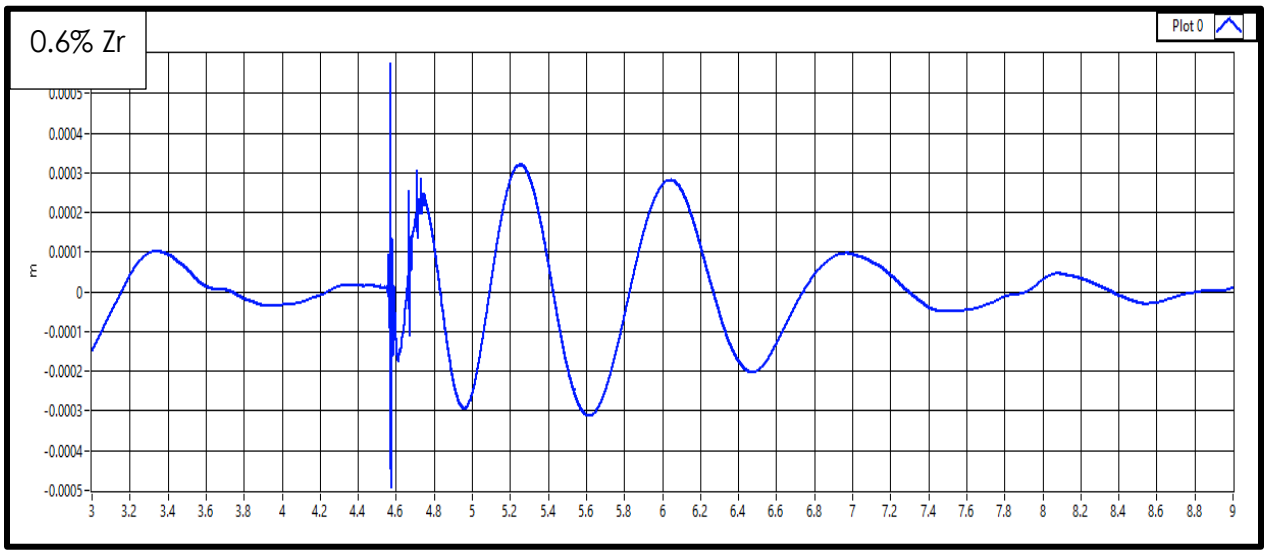
0.6% Zr
Plot 0
m
0.0004
0.0003
0.0002
0.0001
0
-0.0001
-0.0002
-0.0003
-0.0004
-0.0005
3 3.2 3.4 3.6 3.8 4 4.2 4.4 4.6 4.8 5 5.2 5.4 5.6 5.8 6 6.2 6.4 6.6 6.8 7 7.2 7.4 7.6 7.8 8 8.2 8.4 8.6 8.8 9

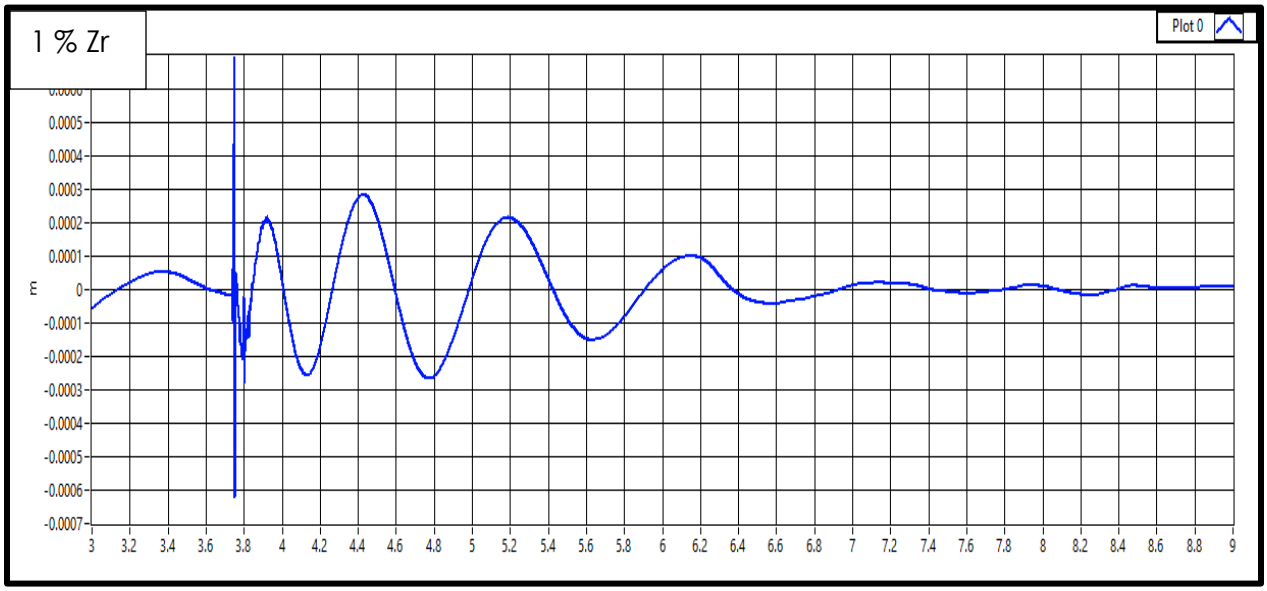
1 % Zr
Plot 0
m
0.0005
0.0004
0.0003
0.0002
0.0001
0
-0.0001
-0.0002
-0.0003
-0.0004
-0.0005
-0.0006
-0.0007
3 3.2 3.4 3.6 3.8 4 4.2 4.4 4.6 4.8 5 5.2 5.4 5.6 5.8 6 6.2 6.4 6.6 6.8 7 7.2 7.4 7.6 7.8 8 8.2 8.4 8.6 8.8 9

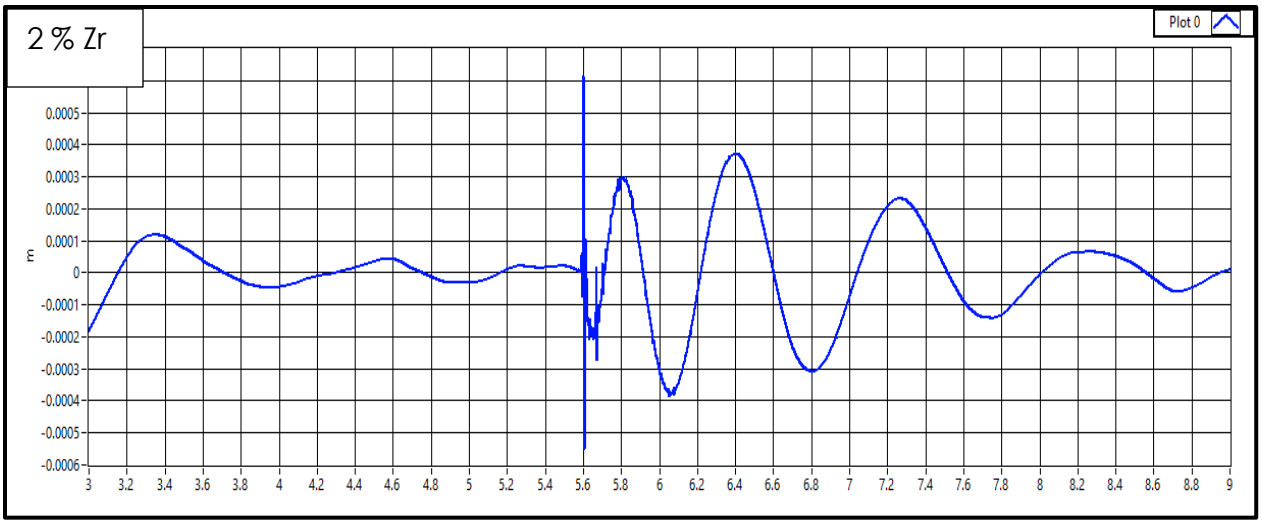

Figures B-1 : displacement Against time of :[(A) alloy A, (B,C,D) Alloy CuAlMn – (1,2,3) % Y_2O_3, (E,F,G) CuAlMn –(1,2,3) % Ta, (H , I , K) Alloy CuAlMn- (1, 2, 3)%In , (M,N,O) Alloy CuAlMn-(0.6,1,2) % Zr] respectively after Aging

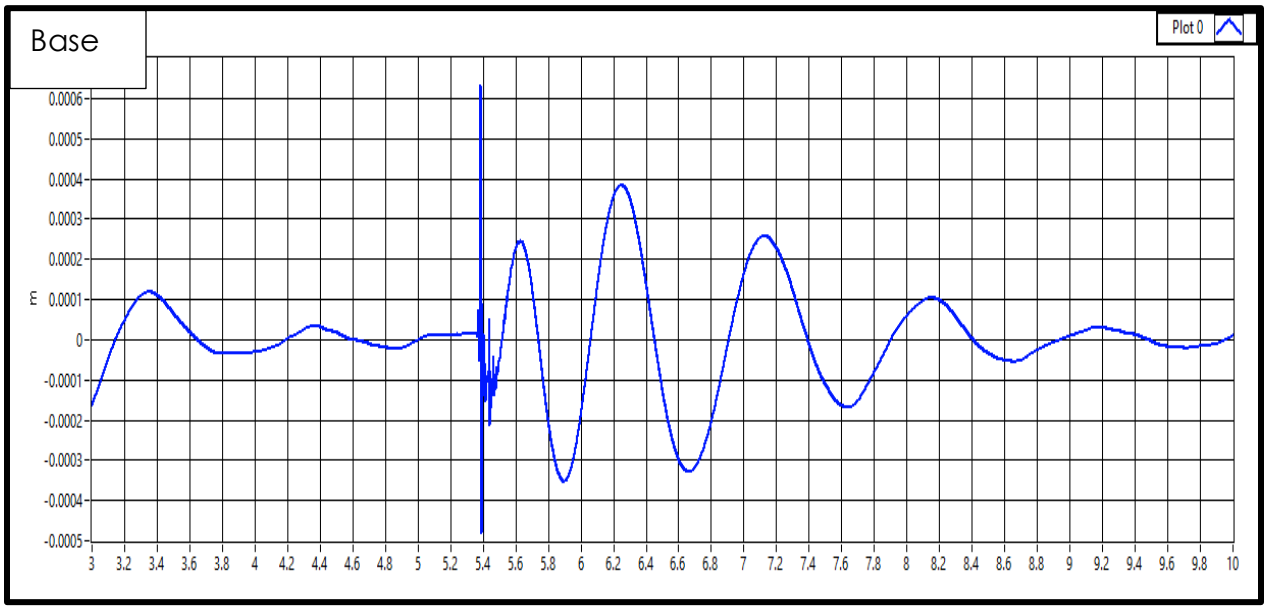

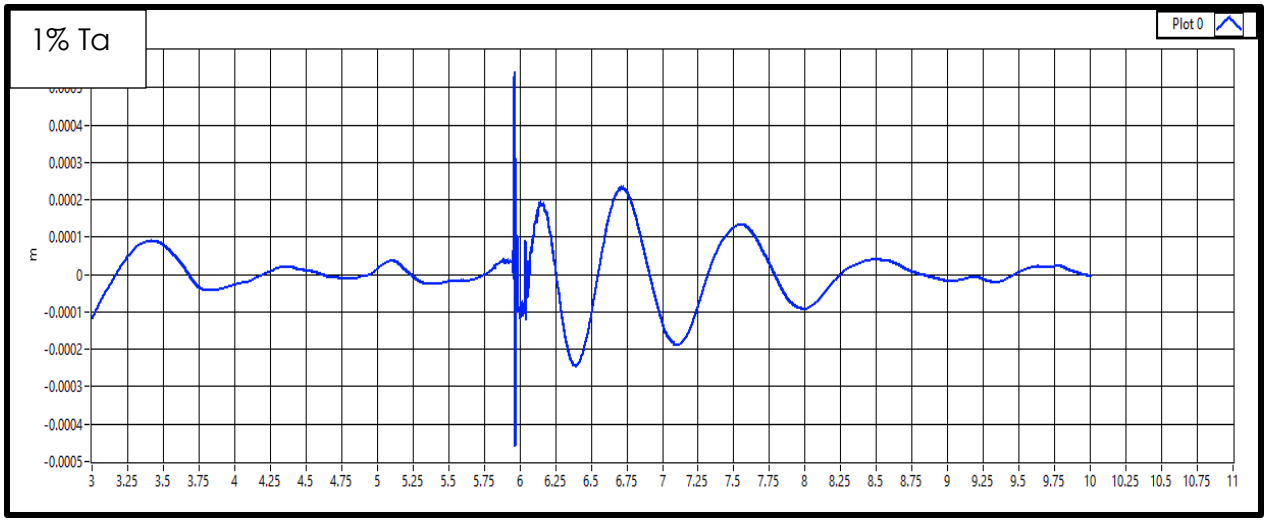
1% Ta
Plot 0
m
0.0004
0.0003
0.0002
0.0001
0
-0.0001
-0.0002
-0.0003
-0.0004
-0.0005
3 3.25 3.5 3.75 4 4.25 4.5 4.75 5 5.25 5.5 5.75 6 6.25 6.5 6.75 7 7.25 7.5 7.75 8 8.25 8.5 8.75 9 9.25 9.5 9.75 10 10.25 10.5 10.75 11

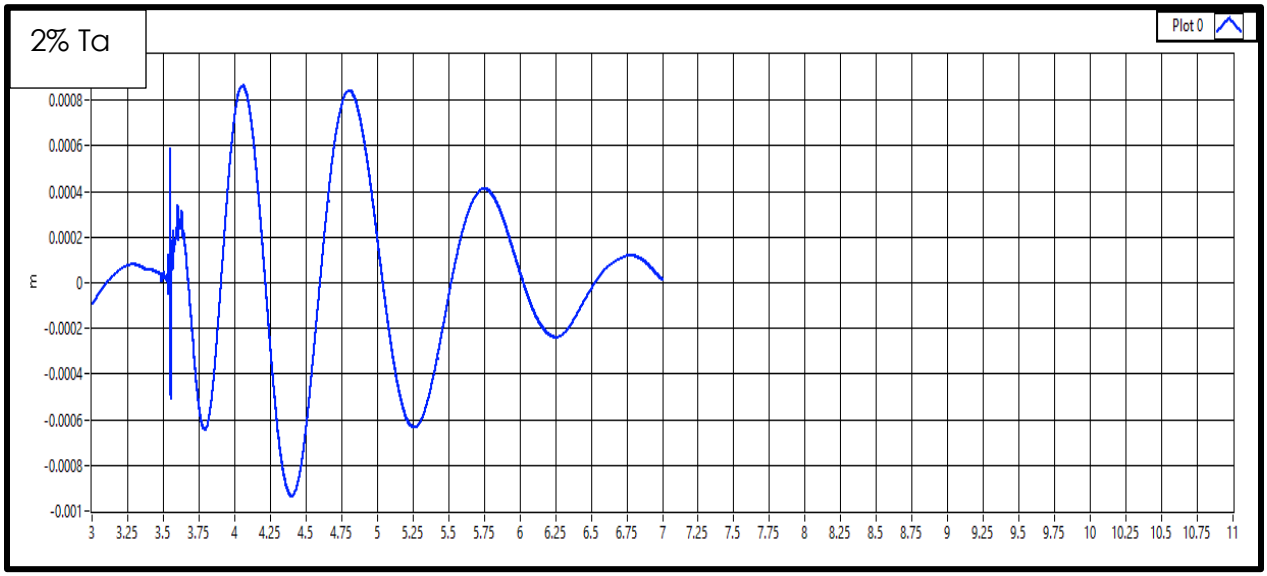
2% Ta
Plot 0
m
0.0008
0.0006
0.0004
0.0002
0
-0.0002
-0.0004
-0.0006
-0.0008
-0.001
3 3.25 3.5 3.75 4 4.25 4.5 4.75 5 5.25 5.5 5.75 6 6.25 6.5 6.75 7 7.25 7.5 7.75 8 8.25 8.5 8.75 9 9.25 9.5 9.75 10 10.25 10.5 10.75 11

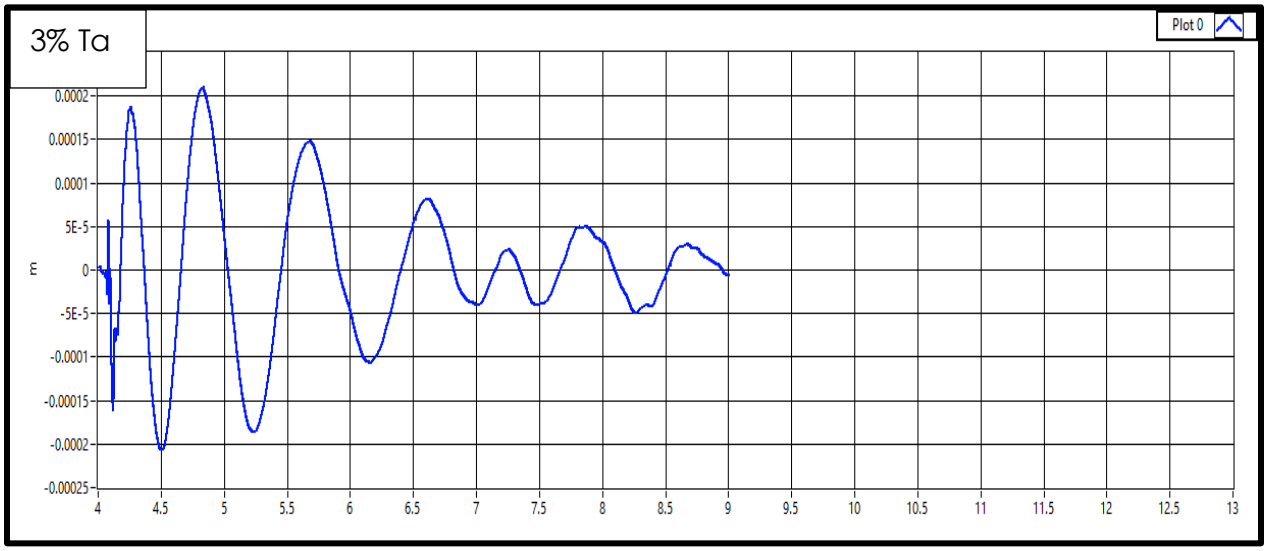
3% Ta
Plot 0
m
0.0002
0.00015
0.0001
5E-5
0
-5E-5
-0.0001
-0.00015
-0.0002
-0.00025
4 4.5 5 5.5 6 6.5 7 7.5 8 8.5 9 9.5 10 10.5 11 11.5 12 12.5 13

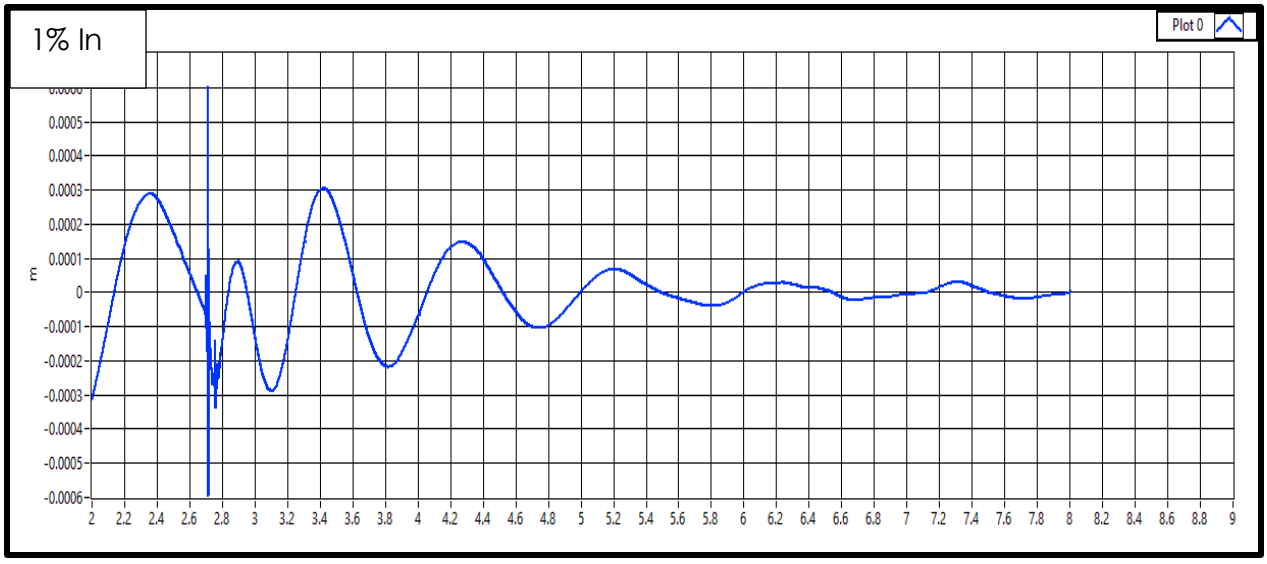
1% In
Plot 0
m
0.0005
0.0004
0.0003
0.0002
0.0001
0
-0.0001
-0.0002
-0.0003
-0.0004
-0.0005
-0.0006
2 2.2 2.4 2.6 2.8 3 3.2 3.4 3.6 3.8 4 4.2 4.4 4.6 4.8 5 5.2 5.4 5.6 5.8 6 6.2 6.4 6.6 6.8 7 7.2 7.4 7.6 7.8 8 8.2 8.4 8.6 8.8 9

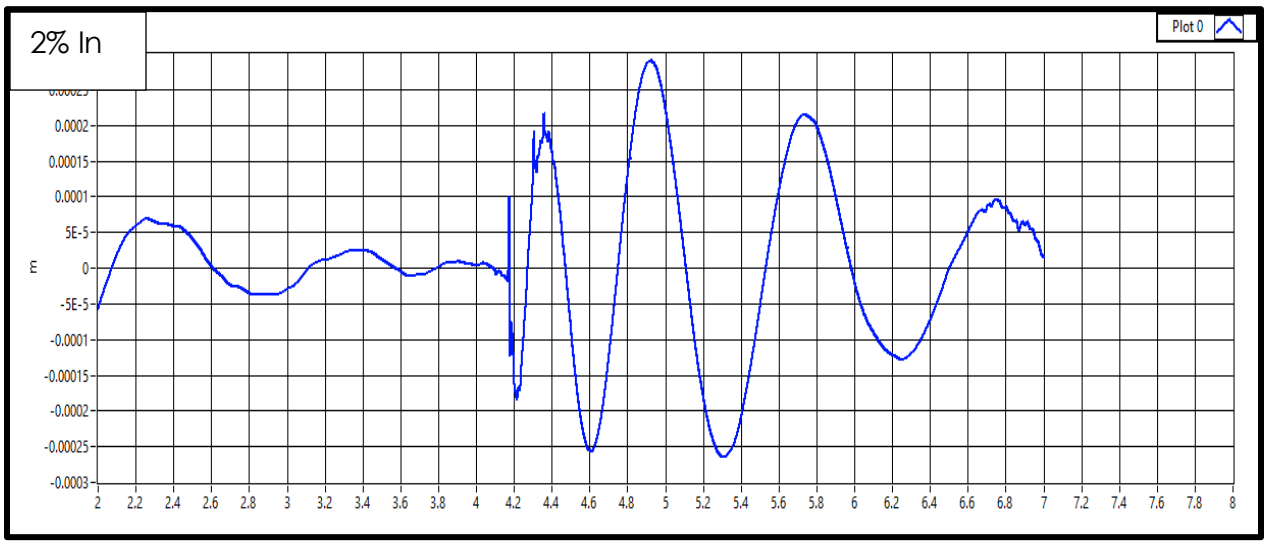
2% In
Plot 0
m
0.0002
0.00015
0.0001
5E-5
0
-5E-5
-0.0001
-0.00015
-0.0002
-0.00025
-0.0003
2 2.2 2.4 2.6 2.8 3 3.2 3.4 3.6 3.8 4 4.2 4.4 4.6 4.8 5 5.2 5.4 5.6 5.8 6 6.2 6.4 6.6 6.8 7 7.2 7.4 7.6 7.8 8

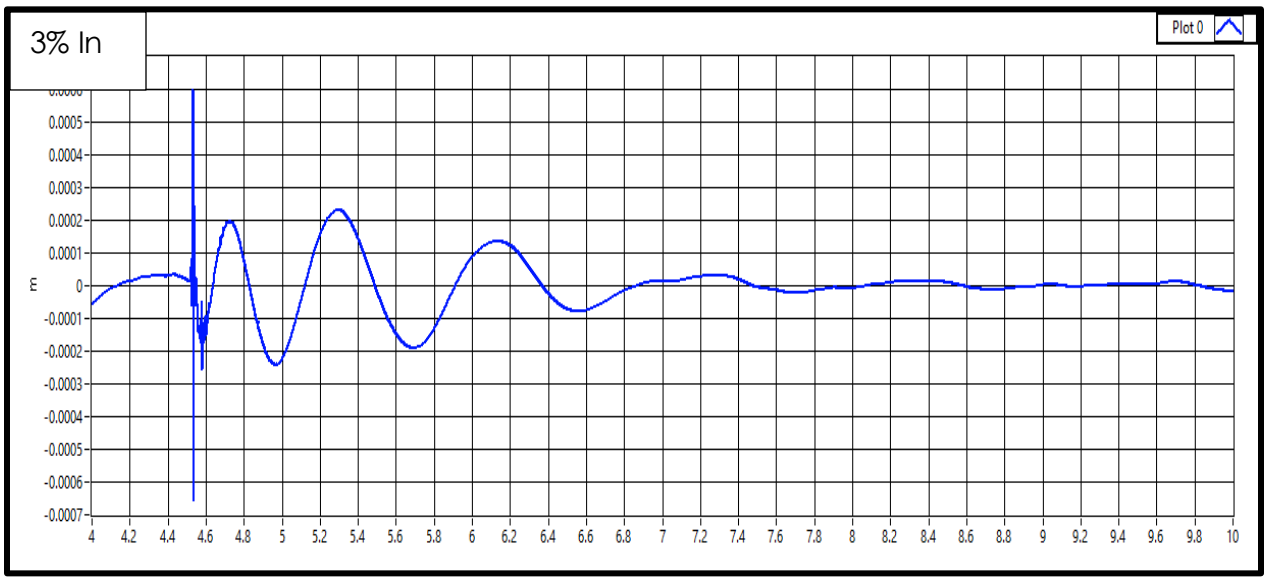
3% In
Plot 0
m
0.0005
0.0004
0.0003
0.0002
0.0001
0
-0.0001
-0.0002
-0.0003
-0.0004
-0.0005
-0.0006
-0.0007
4 4.2 4.4 4.6 4.8 5 5.2 5.4 5.6 5.8 6 6.2 6.4 6.6 6.8 7 7.2 7.4 7.6 7.8 8 8.2 8.4 8.6 8.8 9 9.2 9.4 9.6 9.8 10

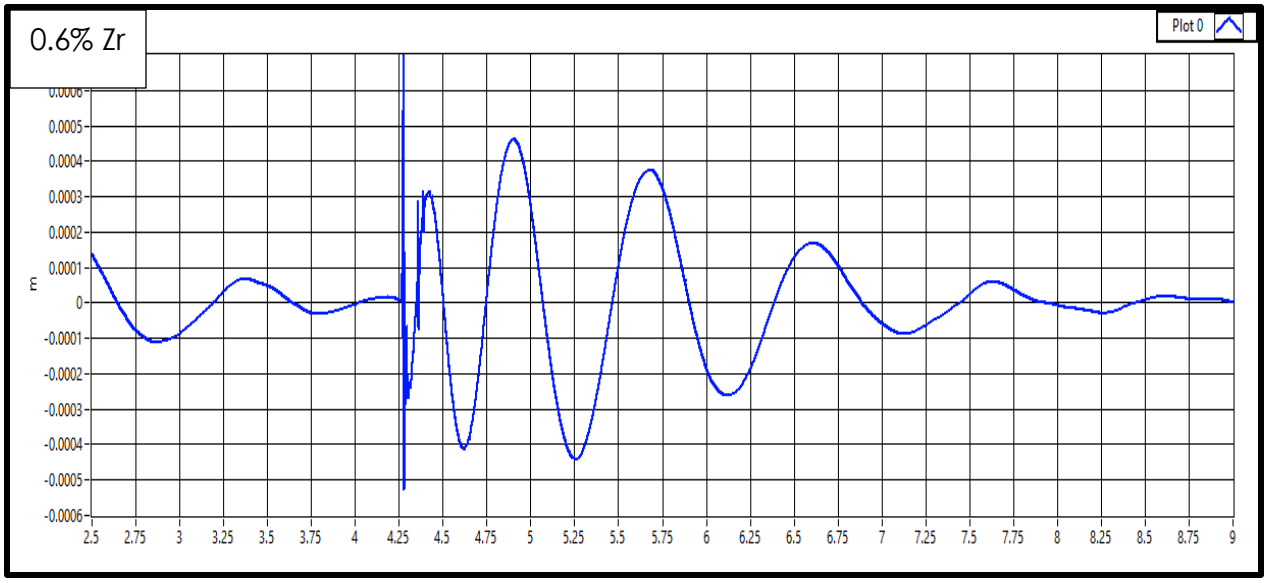
0.6% Zr
Plot 0
m
0.0005
0.0004
0.0003
0.0002
0.0001
0
-0.0001
-0.0002
-0.0003
-0.0004
-0.0005
-0.0006
2.5 2.75 3 3.25 3.5 3.75 4 4.25 4.5 4.75 5 5.25 5.5 5.75 6 6.25 6.5 6.75 7 7.25 7.5 7.75 8 8.25 8.5 8.75 9

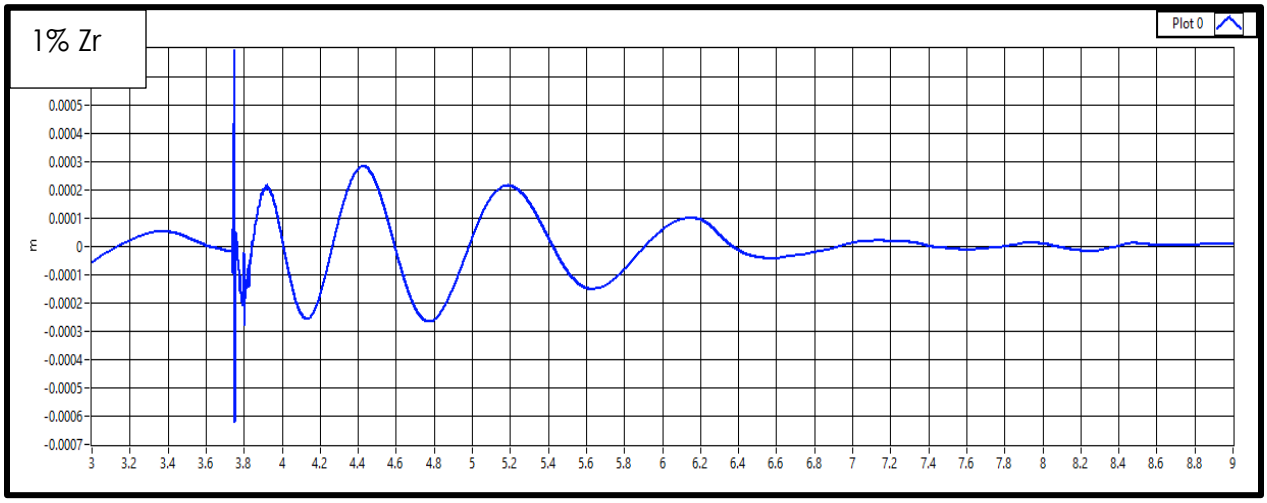
1% Zr
Plot 0
m
0.0005
0.0004
0.0003
0.0002
0.0001
0
-0.0001
-0.0002
-0.0003
-0.0004
-0.0005
-0.0006
-0.0007
3 3.2 3.4 3.6 3.8 4 4.2 4.4 4.6 4.8 5 5.2 5.4 5.6 5.8 6 6.2 6.4 6.6 6.8 7 7.2 7.4 7.6 7.8 8 8.2 8.4 8.6 8.8 9

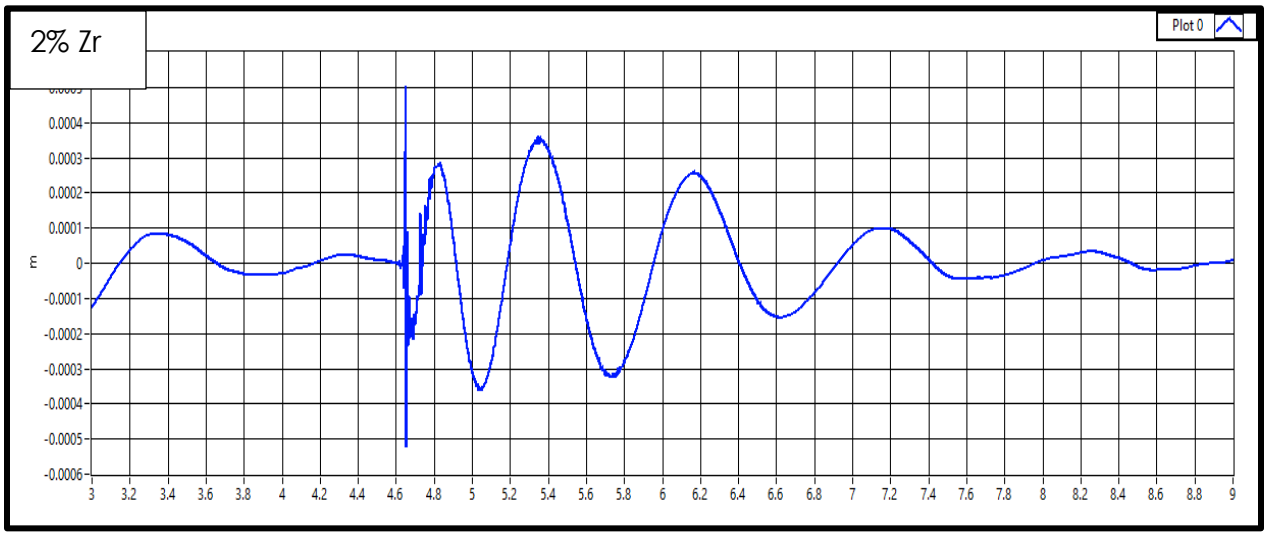
2% Zr
Plot 0
m
0.0004
0.0003
0.0002
0.0001
0
-0.0001
-0.0002
-0.0003
-0.0004
-0.0005
-0.0006
3 3.2 3.4 3.6 3.8 4 4.2 4.4 4.6 4.8 5 5.2 5.4 5.6 5.8 6 6.2 6.4 6.6 6.8 7 7.2 7.4 7.6 7.8 8 8.2 8.4 8.6 8.8 9

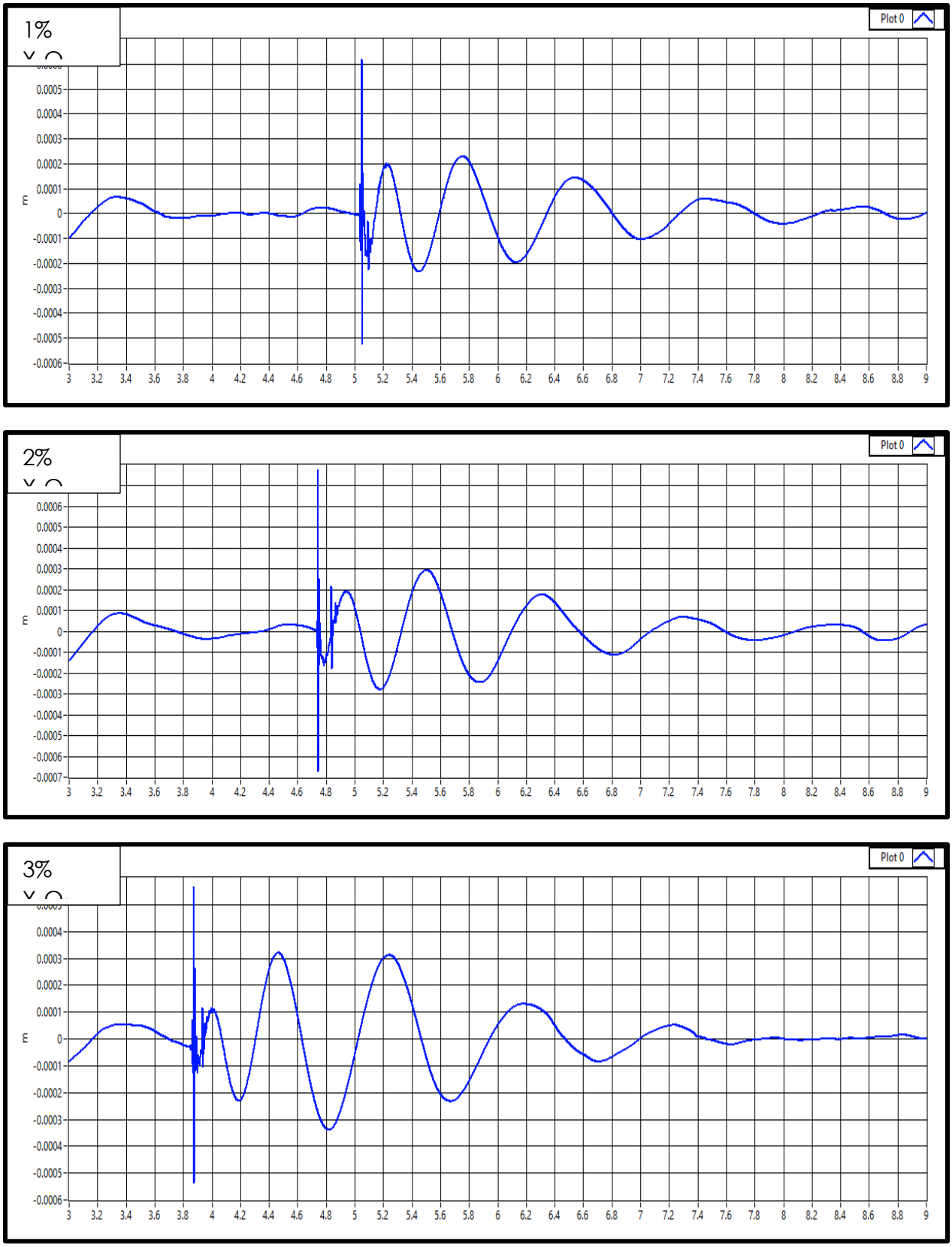

Figures B-2: displacement Against time of :[(A) alloy A, (B,C,D) Alloy CuAlMn –(1,2,3) % Ta, (E,F,G) CuAlMn –(1,2,3) % In, (H , I , K) Alloy CuAlMn- (0.6,1, 2)%Zr , (M,N,O) Alloy CuAlMn-(1,2,3) % Y_2O_3] respectively after sintering

Appendix C
X-Ray diffraction for aged specimens

A

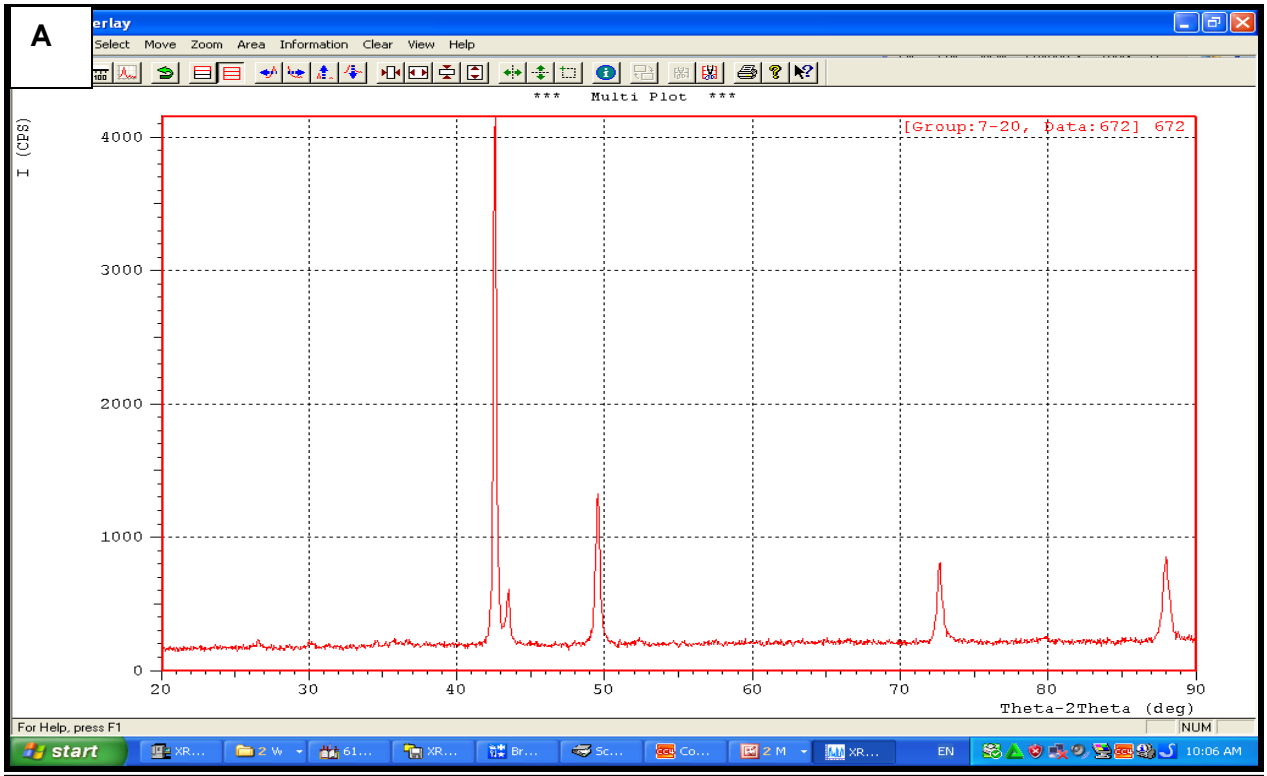
Select Move Zoom Area Information Clear View Help
*** Multi Plot ***
[Group:7-20, Data:672] 672
I (CPS)
4000
3000
2000
1000
0
20
30
40
50
60
70
80
90
Theta-2Theta (deg)
For Help, press F1
NUM
start
EN
10:06 AM

B

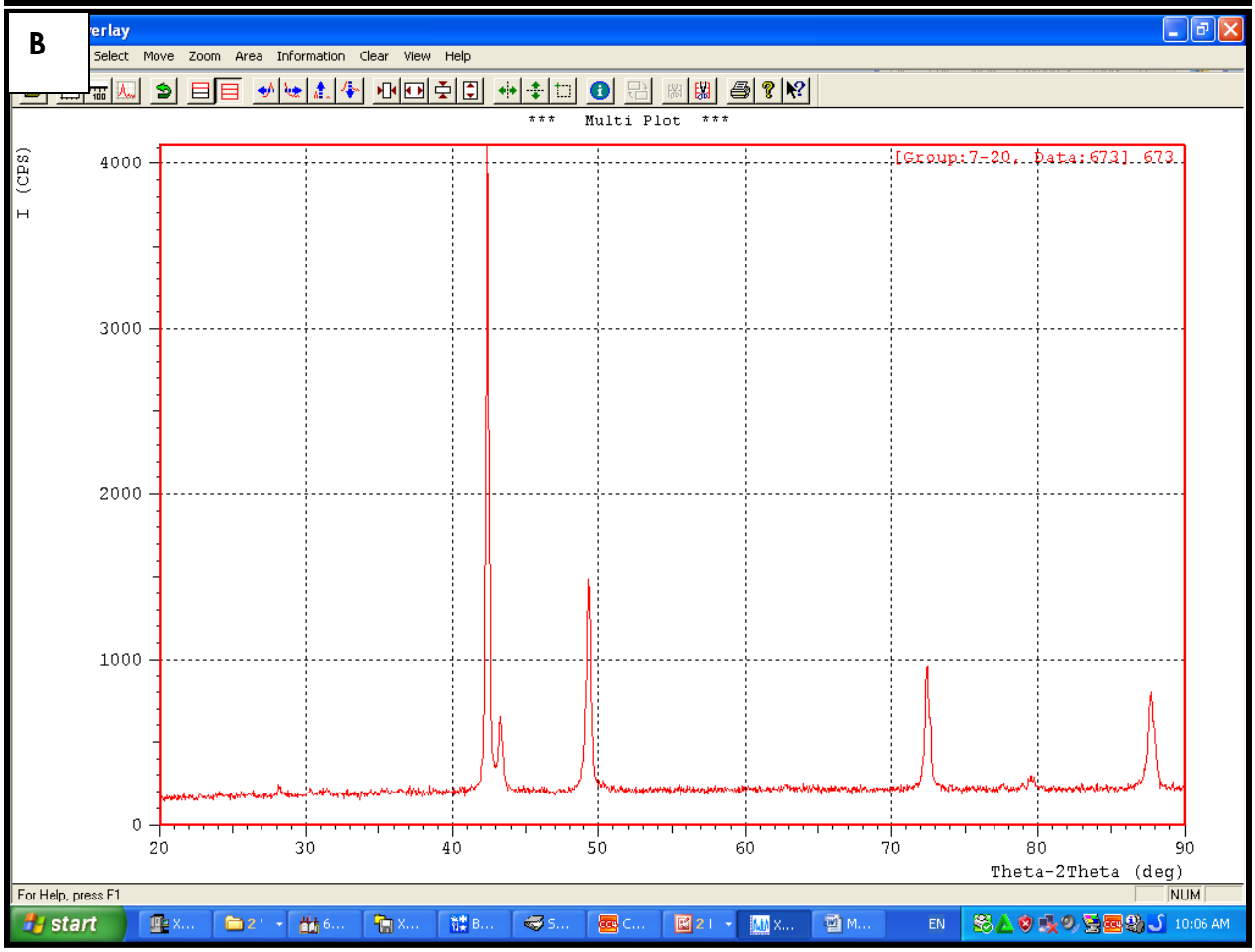
Select Move Zoom Area Information Clear View Help
*** Multi Plot ***
[Group:7-20, Data:673] 673
I (CPS)
4000
3000
2000
1000
0
20
30
40
50
60
70
80
90
Theta-2Theta (deg)
For Help, press F1
NUM
start
EN
10:06 AM

C

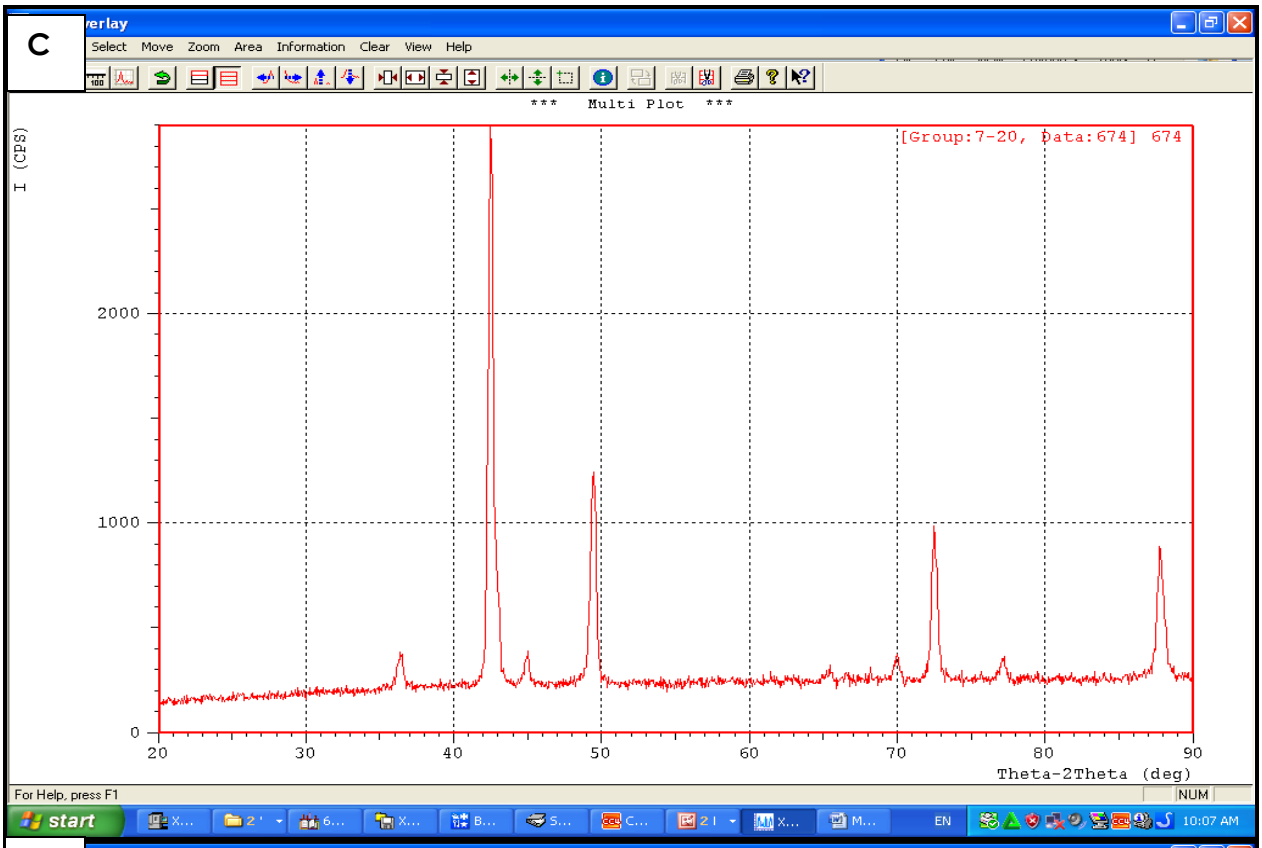
erlay
Select Move Zoom Area Information Clear View Help
*** Multi Plot ***
[Group:7-20, Data:674] 674
I (CPS)
2000
1000
0
20 30 40 50 60 70 80 90
Theta-2Theta (deg)
For Help, press F1
NUM
start
EN
10:07 AM

D

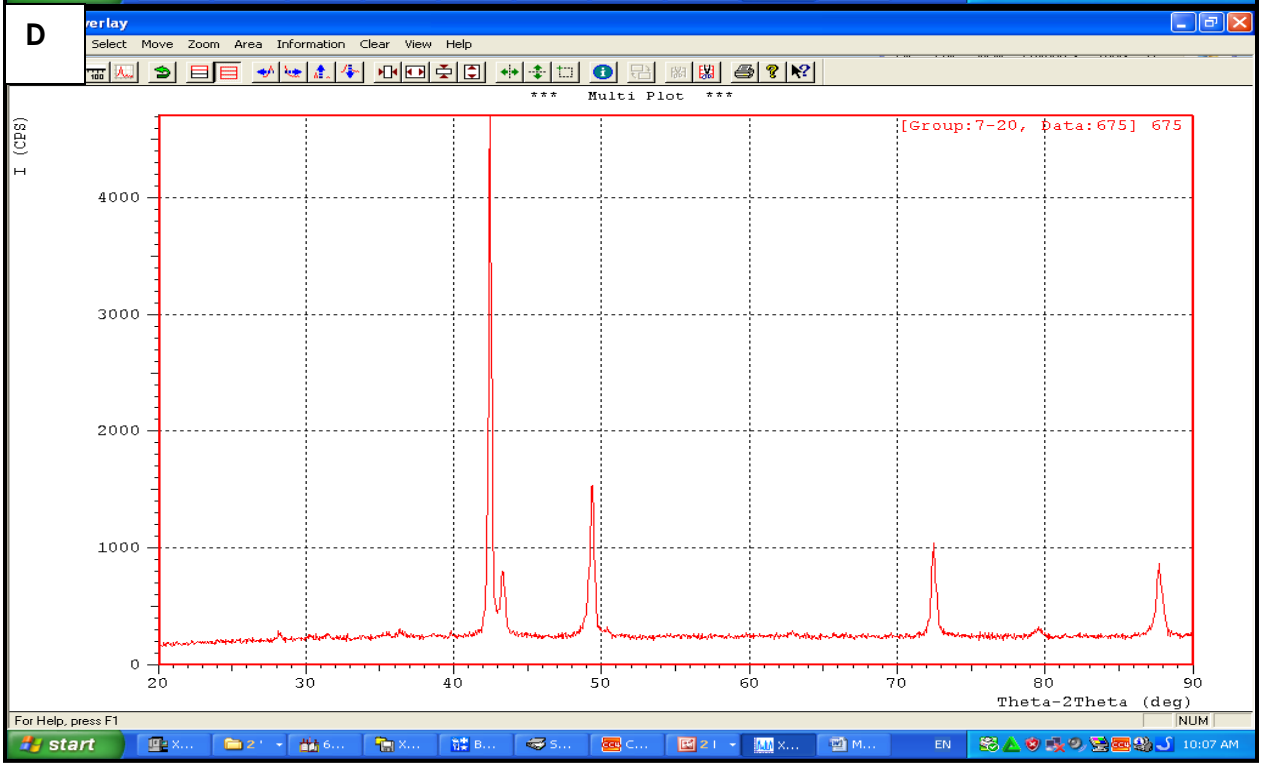
erlay
Select Move Zoom Area Information Clear View Help
*** Multi Plot ***
[Group:7-20, Data:675] 675
I (CPS)
4000
3000
2000
1000
0
20 30 40 50 60 70 80 90
Theta-2Theta (deg)
For Help, press F1
NUM
start
EN
10:07 AM

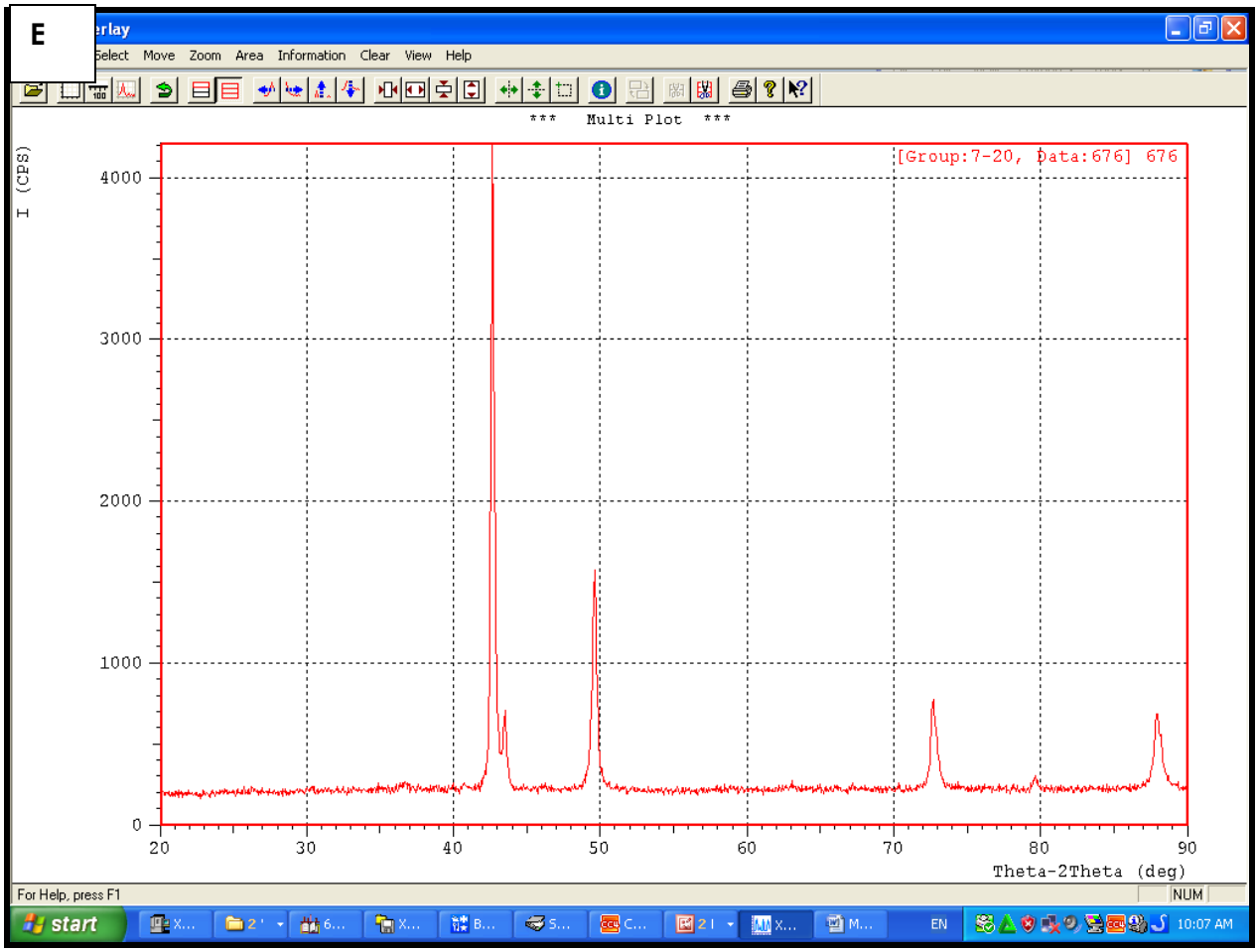

Figures C-1: A,B,C,D and E X-Ray diffraction for aged specimens (A, B3, C3, D3, E3) respectively

Physical properties of powders used in present work

Name	***Formula***	***Melting Point***	***Density***
Yttrium Oxide	Y_2O_3	2440 °C	5.0 g/cm^{-3}
Tantalum	Ta	2850 °C	16.69 $g.cm^{-3}$
zirconium	Zr	1,852 °C	6.49 $g.cm^{-3}$
Indium	In	156 °C	7.31 $g.cm^{-3}$
Copper	Cu	1083°C	8.94 g/cm^3
Aluminum	Al	667°C	2.7 $g.cm^{-3}$
Manganese	Mn	1246°C	7.26 g/cm^3